UNIVERSITAT POLITÈCNICA DE CATALUNYA BARCELONATECH

Modeling and identification of power electronic converters

Gabriel Esteban Rojas Dueñas

PhD program in Electrical Engineering

Modeling and Identification of Power Electronic Converters

Doctoral thesis by:

Gabriel Esteban Rojas Dueñas

Thesis advisor:

Jordi Roger Riba Ruiz

Manuel Moreno Eguílaz

Electrical Engineering Department

Terrassa, September 2021

ABSTRACT

Nowadays, many industries are moving towards more electrical systems and components. This is done with the purpose of enhancing the efficiency of their systems while being environmentally friendlier and sustainable. Therefore, the development of power electronic systems is one of the most important points of this transition. Many manufacturers have improved their equipment and processes in order to satisfy the new necessities of the industries (aircraft, automotive, aerospace, telecommunication, etc.). For the particular case of the More Electric Aircraft (MEA), there are several power converters, inverters and filters that are usually acquired from different manufacturers. These are switched mode power converters that feed multiple loads, being a critical element in the transmission systems. In some cases, these manufacturers do not provide the sufficient information regarding the functionality of the devices such as DC/DC power converters, rectifiers, inverters or filters. Consequently, there is the need to model and identify the performance of these components to allow the aforementioned industries to develop models for the design stage, for predictive maintenance, for detecting possible failures modes, and to have a better control over the electrical system.

Thus, the main objective of this thesis is to develop models that are able to describe the behavior of power electronic converters, whose parameters and/or topology are unknown. The algorithms must be replicable and they should work in other types of converters that are used in the power electronics field. The thesis is divided in two main cores, which are the parameter identification for white-box models and the black-box modeling of power electronics devices. The proposed approaches are based on optimization algorithms and deep learning techniques that use non-intrusive measurements to obtain a set of parameters or generate a model, respectively. In both cases, the algorithms are trained and tested using real data gathered from converters used in aircrafts and electric vehicles. This thesis also presents how the proposed methodologies can be applied to more complex power systems and for prognostics tasks. Concluding, this thesis aims to provide algorithms that allow industries to obtain realistic and accurate models of the components that they are using in their electrical systems.

SUMARIO

En la actualidad, el uso de sistemas y componentes eléctricos complejos se extiende a múltiples sectores industriales. Esto se hace con el propósito de mejorar su eficiencia y, en consecuencia, ser más sostenibles y amigables con el medio ambiente. Por tanto, el desarrollo de sistemas electrónicos de potencia es uno de los puntos más importantes de esta transición. Muchos fabricantes han mejorado sus equipos y procesos para satisfacer las nuevas necesidades de las industrias (aeronáutica, automotriz, aeroespacial, telecomunicaciones, etc.). Para el caso particular de los aviones más eléctricos (MEA, por sus siglas en inglés), existen varios convertidores de potencia, inversores y filtros que suelen adquirirse a diferentes fabricantes. Se trata de convertidores de potencia de modo conmutado que alimentan múltiples cargas, siendo un elemento crítico en los sistemas de transmisión. En algunos casos, estos fabricantes no proporcionan la información suficiente sobre la funcionalidad de los dispositivos como convertidores de potencia DC-DC, rectificadores, inversores o filtros. En consecuencia, existe la necesidad de modelar e identificar el desempeño de estos componentes para permitir que las industrias mencionadas desarrollen modelos para la etapa de diseño, para el mantenimiento predictivo, para la detección de posibles modos de fallas y para tener un mejor control del sistema eléctrico.

Así, el principal objetivo de esta tesis es desarrollar modelos que sean capaces de describir el comportamiento de un convertidor de potencia, cuyos parámetros y/o topología se desconocen. Los algoritmos deben ser replicables y deben funcionar en otro tipo de convertidores que se utilizan en el campo de la electrónica de potencia. La tesis se divide en dos núcleos principales, que son la identificación de parámetros de los convertidores y el modelado de caja negra (black-box) de dispositivos electrónicos de potencia. Los enfoques propuestos se basan en algoritmos de optimización y técnicas de aprendizaje profundo que utilizan mediciones no intrusivas de las tensiones y corrientes de los convertidores para obtener un conjunto de parámetros o generar un modelo, respectivamente. En ambos casos, los algoritmos se entrenan y prueban utilizando datos reales recopilados de convertidores utilizados en aviones y vehículos eléctricos. Esta tesis también presenta cómo las metodologías propuestas se pueden aplicar a sistemas eléctricos más complejos y para tareas de diagnóstico. En conclusión, esta tesis tiene como objetivo proporcionar algoritmos que permitan a las industrias obtener modelos realistas y precisos de los componentes que están utilizando en sus sistemas eléctricos.

ACKNOWLEDGEMENTS

First of all, I would like to thank my supervisors Jordi Riba and Manuel Moreno for all the help and guidance during my PhD study. Jordi, your tutelage, patience and support over the last three years was key in the development of my academic research. Manuel, thank you for your dedication and invaluable contribution in this thesis, especially in the experimental part.

Additionally, I am grateful to Jordi Riba, Manuel Moreno, Antoni Garcia and Santiago Bogarra for taking me as a student in the AEMS-IdFit project. I would have not made it this far without the knowledge and industry insights acquired in the completion of this exciting project.

Many thanks to all the former and present members of Amber research laboratory. Mainly to Akash, Carlos and Jimmy, we have shared ups and downs but in the end we have made it through. Yuming and Pau, I hope the best for you in the upcoming years, you still have a long way to go. I would like to acknowledge David, Ivan, Alvaro, Carles, Albert, Nabil, Marc and Victor, which in one way or another helped me during my stay in Amber.

I would not be in this position without the love and encouragement of my parents. For this, I am extremely grateful. They have been role-models and I have enjoyed so many opportunities because of them. I am so thankful to my brother Luis for guiding me into the academic path. The after-work time I spent with him, Zelda, Gabriel and Emilio during the course of my PhD studies was the perfect way to end the day. Special thanks to my brother Mauricio, who was always supportive despite the distance.

I am very grateful to Domenica for her unconditional support during these years. Thanks for bringing happiness and joy to my life even in the most adverse situations. All the trips we took were the best way to escape from the PhD routine I was in.

Finally, I want to thank all my friends and family that contributed to the accomplishment of this important goal for me.

INDEX

LIST OF FIGURES

LIST OF TABLES

1 INTRODUCTION

The use of power electronics has been extended in many electrical engineering applications. This technology is widely used in industrial, commercial, residential, aerospace, smart grids, automotive and military environments for different applications to allow the interconnection of HVDC transmission lines, machine drives, integration of renewable power generation, electrochemical processes, electric vehicles, harmonic filtering and much more [1]. Technology developments in generation technologies and an increase in the electricity demand require advances in the power electronics field in order to deliver all the energy generated to the final users. On the other hand, the aircrafts electrification and electric vehicles advances add new challenges to the power converters applications [2]. Particularly, the next generation of more electric aircrafts (MEA) are friendlier from an environmental point of view by maximizing the performance and reducing the weight of the airplanes [3]. Therefore, huge developments on power electronic devices, components and converters are expected for the next few years [4].

The first time that the concept of power electronics was introduced was in 1955, when the diode became commercially available [5]. Nowadays different power electronics systems such as DC/DC power converters, inverters, filters, rectifiers and AC-AC power converters are designed to work with a high efficiency that is almost 100%. This is mainly due to the used power semiconductor devices, where the most used are: thyristors, power MOSFETs, insulated gate bipolar transistors (IGBT), integrated gate commutated thyristors (IGCT) and wide bandgap devices [6]. Most of these devices work with high switching frequencies, which allow a very efficient energy conversion.

Essentially, power electronics devices transform energy from one state to another in order to meet some specific requirements [5]. For instance, DC-DC power converters step up or down the voltage at the output when compared to the input voltage, depending on the requirements of the grid or the electrical system at which they are connected. The converters consist of a combination of passive electronic components (resistors, capacitors, inductors), semiconductor devices, and in most of the cases, a controller that regulates the output of the system. These converters are usually governed by a pulse width modulated (PWM) signal that is in charge of switching the transistors according to the instructions received from the controller.

Different sectors of the industry are experiencing a transition to a more electric environment and a change in the primary sources of electricity generation. This is mainly driven by global climate change, which implies the necessity of using alternative and clean sources of energy in order to reduce the environmental impact derived from the generation of electrical energy. This transition represents technological challenges such as the integration of renewable energies to the grid,

electrification of cars and aircrafts, smart grids, batteries, HVDC transmission lines, etc. For the case of the aviation industry, the next generation of MEA is being developed with the objective of maximizing the electrical performance and reducing the environmental impacts [3]. One of the approaches to accomplish these goals is the use of novel power electronics technologies that allow a higher efficiency, size and weight reduction.

Currently, the sectors mentioned above are implementing complex systems that include switching mode power converters (SMPCs) and other elements associated with power electronics [7]. SMPCs offer interesting features, including higher conversion efficiency and compactness [8], [9], which are highly appreciated when designing power conversion systems. They are mostly applied in different applications, including domestic appliances [10], portable electronics, computers and motor drives [11], or in power conversion systems applied to renewable generation [12], among others. Currently, high-tech sectors such as aerospace, naval or automotive are based on complex power systems integrating multiple converters. Such complex power systems often consist of several SMPCs from various suppliers, which usually are reluctant to provide detailed information of the internal components [13]. Therefore, the information available usually is not sufficient to generate detailed discrete models, although models which are too exhaustive may require unacceptable computational resources [14]. These shortcomings make it difficult to generate accurate dynamic models, especially for the abovementioned high-tech sectors combining several models of SMPCs from different suppliers. This is an impediment for MEA and power system designers, as they require accurate models of the converters to execute planning, prevention, design and optimization tasks. The modelling of these elements is difficult due to their switching and nonlinear nature [15]. Furthermore, the data that can be acquired experimentally is limited to the input and output signals of the converter, since there is no access to the internal circuits of most converters [16]. A proper model should replicate the static and dynamic characteristics of the power converter, including the voltage and current mean value and ripple, the commutation frequency of the switches and the transient response to perturbations, among others.

Different approaches are available to model power electronic converters. They can be roughly classified into white-, black- and grey-box models. White-box models require a deep physical description of the converter through a set of algebraic or differential equations, which are able to reproduce its dynamics [17]. On the other hand, grey-box models consist of a data-driven approach where the prior knowledge about the system is available, but it is limited. Contrarily, black-box models do not assume any particular structure of the converter, so that they are able

to emulate or reproduce its behavior without describing its physical equations [18] when the internal topology is unknown, so that this model does not require internal data of the converter.

Available modelling and identification methods vary depending on the approach. Basically, white and grey box models are based on a parametric identification, where the values of the components are identified based on the measurements of the system. On the other hand, black-box system identification finds a model that has the same inputs and outputs of the device and it is able to reproduce the behaviour under different operating points, without assuming any specific model of the system. Different strategies to find these models can be applied, including neural networks, genetic algorithms, deep learning methods, optimization algorithms, mathematical formulation of the problem, etc. Consequently, this thesis is focused on implementing methods and techniques that are able to model with accuracy the behaviour of power electronic systems using white-box and black-box approaches.

This thesis is dedicated to develop algorithms that lead to an accurate modelling of different power electronic converters. It also focuses on the experimental implementation and data acquisition of converters used in aircrafts and electric vehicles. The obtained results are compared to several state-of-the-art techniques.

This document is divided into five chapters. The first chapter presents the introduction and the objectives of the thesis. The second chapter proposes two white-box parameter estimation algorithms, which are tested using real data gathered from different power electronic converters. The third chapter reviews three different algorithms that aim to obtain black-box models of power converters based on neural networks. The approaches are tested using converters that are used in aircrafts and electric vehicles. Chapter four presents two applications of the techniques proposed in chapters 2 and 3. They identify the parameters of a boost power factor corrector and estimate the remaining useful time of the output capacitor of the power converters. Finally, the conclusions derived from this thesis are presented in the last chapter.

1.1 Objectives

The objectives are oriented towards accomplishing a proper modelling and identification of different power electronic converters. They are separated into general and specific objectives. This scientific project has four general objectives which are presented as follows.

1 **Identify suitable identification and modelling methods for the chosen power electronic converters.**

Specific objectives:

1.1. Review the state of the art regarding the white-box and black-box system identification techniques and methods.

1.2. Understand the working principle of power electronic devices in an electrical system.

1.3. Choose different power electronic components which will be used to test the identification methods.

1.4. Comprehend and select the best methods to model the systems considering the nature of the problem.

2 **Acquire the data of the chosen power electronic converters considering the requirements of the parametric and non-parametric identification algorithms.**

Specific objectives:

2.1. Select the measurement equipment.

2.2. Identify commercially available converters and choose the best one regarding cost and benefits.

2.3. Identify the data requirements of each method and determine how each set of data should be introduced in the identification program.

2.4. Define a protocol to measure the data considering that a large set of data is needed when applying black-box models.

2.5. Define and perform the experiment(s) for the white-box and black-box identification methods in order to perform a correct data acquisition.

3 **Implement different algorithms for identifying and/or modelling the behaviour of different power electronic converters**

Specific objectives:

3.1. Understand the difference between the white-box and black-box estimation modelling techniques.

3.2. Design the circuits of the proposed converters in Simulink.

3.3. Develop a parameter identification method based on the non-linear least squares method taking into account the nature of the available data.

3.4. Define a strategy for modelling black-box systems from a deep learning point of view.

3.5. Optimize the proposed methods in order to make them converge faster and with higher accuracy.

3.6. Program in Matlab® the selected methods.

4 Validate the proposed methods and algorithms using simulation and experimental data acquired from real power electronic converters in the laboratory

Specific objectives:

4.1. Test the algorithms using the simulation data from the circuits designed in Simulink and check the accuracy of the methods.

4.2. Test the methods using the data measured in the laboratory.

4.3. Verify the replicability of the proposed methods by testing the power electronic converters under different operating conditions.

4.4. Analyse the results and draw the conclusions according to the accuracy of the methods proposed during the thesis.

1.2 Publications

1.2.1 Journals

- G. Rojas-Dueñas, J.-R. Riba, and M. Moreno-Eguilaz, “Non-Linear Least Squares Optimization for Parametric Identification of DC-DC Converters,” IEEE Trans. Power Electron., vol. 36, no. 1, pp. 654–661, Jan. 2021.
- G. Rojas Duenas, J.-R. Riba, and M. Moreno-Eguilaz, “A Deep Learning-Based Modeling of a 270 V -to- 28 V DC-DC Converter used in More Electric Aircrafts,” IEEE Trans. Power Electron., vol. 37, no. 1, pp. 509–518, Jan. 2022.
- G. Rojas-Duenas, J.-R. Riba, and M. Moreno-Eguilaz, “Black-Box Modeling of DC–DC Converters Based on Wavelet Convolutional Neural Networks,” IEEE Trans. Instrum. Meas., vol. 70, pp. 1–9, Jul. 2021.
- G. Rojas-Dueñas, J.R Riba, and M. Moreno-Eguilaz, “Modeling of a DC-DC bidirectional converter used in mild hybrid electric vehicles from measurements,” Measurement, vol. 183, p. 109838, Oct. 2021.
- G. Rojas-Dueñas, J. R. Riba, and M. Moreno-Eguilaz, “Parameter estimation of a single-phase boost pfc converter with emi filter based on an optimization algorithm,” Electron., vol. 10, no. 11, p. 1231, Jun. 2021.

- G. Rojas-Dueñas, J. R. Riba, and M. Moreno-Eguilaz, “Deep Learning-based Prognostics of Bidirectional Converters to Supply the Electric Machine in Electric Vehicles,” Sensors., *Under Review.*

1.2.2 Conferences

- G. Rojas-Duenas, J.-R. Riba, K. Kahalerras, M. Moreno-Eguilaz, A. Kadechkar, and A. Gomez-Pau, “Black-Box Modelling of a DC-DC Buck Converter Based on a Recurrent Neural Network,” in 2020 IEEE International Conference on Industrial Technology (ICIT), 2020, pp. 456–461.
- G. Rojas-Duenas, J. R. Riba, M. Moreno-Eguilaz, and C. Candelo-Zuluaga, “Non-Intrusive Parameter Identification of a Three-Phase Rectifier Based on an Optimization Approach,” IECON Proc. (Industrial Electron. Conf., vol. 2020-October, pp. 1389–1394, Oct. 2020.

1.2.3 Participation in conferences

- C. Candelo-Zuluaga, A. Garcia Espinosa, J. R. Riba, P. Tubert Blanch, and G. Rojas-Duenas, “Fast and Efficient PMSM Electromagnetic Parameter Identification Methodology from the Efficiency Map,” IECON Proc. (Industrial Electron. Conf., vol. 2020-October, pp. 1584–1589, Oct. 2020.
- Kadechkar, J. R. Riba, G. Rojas-Duenas, J. A. Martinez, and M. Moreno-Eguilaz, “Experimental study of the effect of aeolian vibrations on the contact resistance of substation connectors,” Proc. IEEE Int. Conf. Ind. Technol., vol. 2020-February, pp. 613–618, Feb. 2020.

2 WHITE-BOX PARAMETER ESTIMATION OF POWER ELECTRONIC DEVICES

2.1 Introduction

This chapter presents the state of the art of the different techniques used to model and identify white-box systems. It shows the latest techniques used in the identification of DC/DC converters and introduces novel methods which are used in other areas in order to obtain a more accurate representation of the behaviour of power electronic converters.

During the modelling and design stages of complex power systems involving different SMPCs, design engineers often do not know most of the parameters in advance [19]. A feasible possibility for parameter identification is to acquire the instantaneous values of the input and output currents and voltages [20] at the input/output terminals of the power converter. This approach is appealing since it is compatible with a non-invasive on-line monitoring of the input/output signals, so there is no need to disconnect or remove the converter from its location once installed. In addition, conventional methods for modeling power converters involve a thorough analysis of the power converter configuration. Different inaccuracy sources such as poor load description, sudden external disturbances, tolerances or ageing of key components or diverse ambient conditions may alter the behavior of the power converter throughout its lifetime. By applying a white-box system identification approach, these issues can be partially overcome [21].

White-box models are fully derived from known physical laws, and all the equations and parameters are determined by theoretical modeling. Models whose structure is completely derived from first principles fall under the white-box category, even if some parameters are estimated from data. White-box models do not depend on data (or only to a minor degree), and their parameters have a direct interpretation using physical principles [17].

White-box models are usually based on a specific set of equations that define the physical behavior of the analyzed system. White-box models represent theoretical models which require a deep physical “a priori” knowledge of the problem, providing a global structural representation of the system. The equations describing the models tend to be very complex, especially when the models are highly non-linear. Therefore, white-box methods assume a known structure for the electric/electronic system. Although white-box models can reproduce system behavior from a theoretical point of view, they sometimes present a limited scope, since they have difficulty in representing unknown noises, nonlinearities and unseen dynamics that often appear as lumped modelling errors.

This chapter proposes to identify the model parameters of different commercial power converters (DC-DC Buck, Boost and Buck-Boost converters) by applying two different approaches. The first

one is based on the analytical equations of the converter, while the second one estimates the parameters by means of an optimization approach. Both methods are tested using real data and the results of the estimations are compared to the actual measurements of the converters.

2.2 Background

Different strategies are found in the technical bibliography to solve this problem, including off-line and on-line methods, or methods based on the time- or frequency-domain. In [8] the parameters of a DC-DC converter are identified by solving the differential equations governing the dynamics of the converter, although this approach requires measuring the current in the inductor. In [22] the parameters of a voltage source converter are estimated using artificial neural networks, thus requiring a large dataset of training and test signals under different load conditions. In [10] the parameters of a synchronous buck converter are identified by means of a Kalman filter, together with an adaptive tuning technique, which is applied to improve the tracking performance of the proposed method. In [23] an online identification of the voltage transfer function parameters of a DC-DC converter is carried out by applying a dichotomous coordinate descent method together with an infinite impulse response adaptive filter to model the plant. In [24] the frequency response and the transfer function of a buck converter were determined by means of auto-regressive models with exogenous inputs. In [25] the passive components of a boost converter were identified by applying an approach based on wavelet denoising and recursive least squares (RLS). A continuous time model based method is presented in [26], where a polynomial interpolation is applied to calculate the time derivatives involved, together with the least squares algorithm to estimate the passive and parasitic parameters of the converter. The closed loop parameters are estimated in [27] by means of state space models, taking into account the parasitic elements of the DC-DC converter. In [28] the behavior of the converter is approximated by means of a transfer function that is identified using a discrete-time model of the DC-DC converter. Reference [29] reviews different techniques for system and parameter identification of DC-DC power converters. However, all reported methods are invasive, i.e., they require external excitation signals for an effective parameter estimation.

From the literature review it is deduced that most of the papers either identify the converter by means of a transfer function, from which it is not feasible to obtain the real parameters (passive elements and control parameters) of the converter, or only determine some of the parameters. Therefore, there is a need to identify all real parameters of the converter from simple acquisitions of the voltages at the input/output terminals of the converter, since in most cases they are the only accessible sources of information.

2.3 Analytical Equations of the DC-DC Converter

This method consists of the identification of the open loop parameters of the converter based on steady-state signals (input and output voltages, and inductor and output currents). The equations derived from this method are not generic and change according to the converter topology. The proposed method consists of obtaining a set of equations that describe the performance of the power converters, allowing a parameter estimation based on measurements. It is worthy to mention that these models require a fixed duty cycle of the converter and depend on the operating point. Thus, the transient response of the converter cannot be reproduced.

2.3.1 Buck converter

Figure 2.1 shows the model of a simple Buck converter. The parameters to identify are the values of the passive components: L (inductor/coil inductance), R_L (inductor/coil resistance), C (capacitor capacitance), $R_{C,}$ (capacitor equivalent series resistance) and R_S (switch resistance).

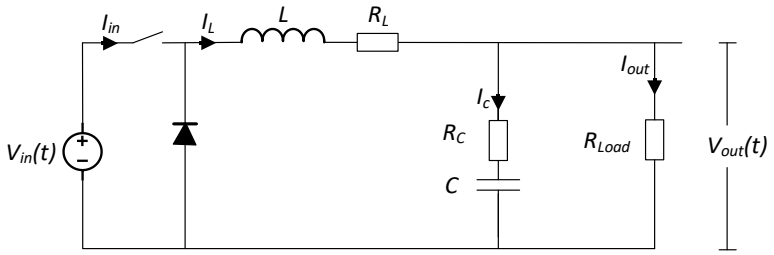

Figure 2.1. White-box model of a DC-DC buck converter.

To identify the aforementioned passive components, the steady state response is analyzed, since it is almost not affected by the controller. To this end, the model of the converter during T_{ON} is analyzed in detail, that is, when the switch is in its ON state. Figure 2.2 shows the equivalent circuit of the step down converter during the ON state of the transistor.

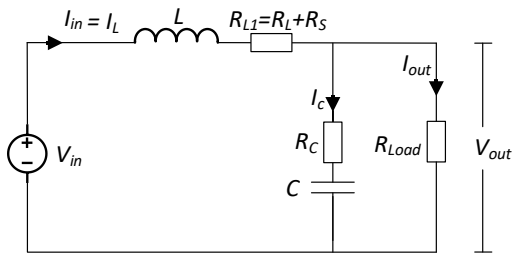

Figure 2.2. Equivalent circuit of a buck converter during T_{on}.

The next step is to obtain a set of equations that describe the behavior of the buck converter. First of all, the L and $R_{L1} = R_L + R_s$ values can be calculated as follows,

$$V_{input} - V_{output} = I_{input} \cdot R_L + L \cdot \frac{dI_{input}}{dt} \quad (1)$$

next, (1) is integrated.

$$\begin{aligned} L \cdot \frac{dI_{input}}{dt} &= V_{input} - V_{output} - I_{input} \cdot R_L \\ L \cdot \int dI_{input} &= \int V_{input}.dt - \int V_{output}.dt - R_L \int I_{input}.dt \\ \int dI_{input} &= \int \frac{V_{input}.dt}{L} - \int \frac{V_{output}.dt}{L} - \frac{R_L}{L} \int I_{input}.dt \end{aligned} \quad (2)$$

Equation (2) can be discretized by considering two discrete time instants T_1 and $T_2 = T_1 + \Delta T$, ΔT being the considered discrete time step. Once discretized, the trapezoidal rule allows calculating the integral, thus obtaining (3).

$$\begin{aligned} & I_{input,T_2} - I_{input,T_1} \\ &= \frac{(V_{input,T_2} - V_{output,T_2} + V_{input,T_1} - V_{output,T_1}) \cdot (T_2 - T_1)}{2 \cdot L} - \frac{(I_{input,T_2} + I_{input,T_1}) \cdot (T_2 - T_1) \cdot (R_L + R_s)}{2 \cdot L} \end{aligned} \quad (3)$$

Finally, L and R_{L1} can be obtained by means of the following equations system, which considers four time instants T_1, $T_2 = T_1 + \Delta T$, $T_3 = T_2 + \Delta T$, $T_4 = T_3 + \Delta T$.

$$\begin{bmatrix} I_{input,T_2} - I_{input,T_1} \\ I_{input,T_4} - I_{input,T_3} \end{bmatrix} = \begin{bmatrix} \frac{(V_{input,T_2} - V_{output,T_2} + V_{input,T_1} - V_{output,T_1}) \cdot (T_2 - T_1)}{2} & \frac{(-I_{input,T_2} - I_{input,T_1}) \cdot (T_2 - T_1)}{2} \\ \frac{(V_{input,T_4} - V_{output,T_4} + V_{input,T_3} - V_{output,T_3}) \cdot (T_4 - T_3)}{2} & \frac{(-I_{input,T_4} - I_{input,T_3}) \cdot (T_4 - T_3)}{2} \end{bmatrix} \cdot \begin{bmatrix} \frac{1}{L} \\ \frac{R_L + R_S}{L} \end{bmatrix} \quad (4)$$

On the other hand, during the OFF state, the model of the buck converter is represented as shown in Figure 2.3. This results in the disconnection of the DC source and a new equivalent circuit during T_{OFF}.

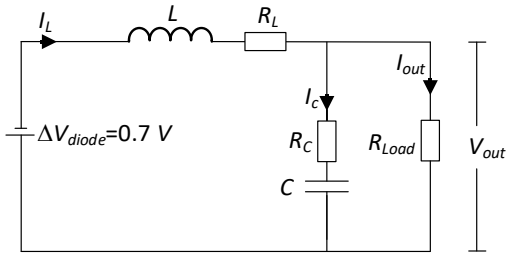

Figure 2.3. Equivalent circuit of a buck converter during T_{OFF}.

Similarly to (1), the equations governing the dynamic behavior during the OFF state can be expressed as in (5).

$$-\Delta V_{diode} - V_{out} = I_L \cdot R_L + L \cdot \frac{dI_L}{dt} \tag{5}$$

Therefore, the solution is similar to (4), so it can be expressed as in (6).

$$\begin{bmatrix} I_{L,T_2} - I_{L,T_1} \\ I_{L,T_4} - I_{L,T_3} \end{bmatrix} = \begin{bmatrix} \frac{(-\Delta V_{diode,T_2} - V_{out,T_2} - \Delta V_{diode,T_1} - V_{out,T_1}) \cdot (T_2 - T_1)}{2} & \frac{(-I_{L,T_2} - I_{L,T_1}) \cdot (T_2 - T_1)}{2} \\ \frac{(-\Delta V_{diode,T_4} - V_{out,T_4} - \Delta V_{diode,T_3} - V_{out,T_3}) \cdot (T_4 - T_3)}{2} & \frac{(-I_{L,T_4} - I_{L,T_3}) \cdot (T_4 - T_3)}{2} \end{bmatrix} \cdot \begin{bmatrix} \frac{1}{L} \\ \frac{R_L}{L} \end{bmatrix} \tag{6}$$

It is noted that $R_{L1} = R_L + R_S$ is calculated during the ON state, R_S being the ON resistance of the switch. Since R_L is calculated during the OFF state, the switch resistance can be obtained by applying $R_S = R_{L1} - R_L$. Once the parameters of the inductor and the switch are known, those of the capacitor must be obtained. According to [26], the equivalent series resistance (ESR) of the output capacitor in a buck converter can be calculated as,

$$\begin{aligned} I_{input} &= I_c + I_{output} \\ I_c &= C \cdot \frac{dV_c}{dt} \\ V_{output} &= V_c + V_{R_c} \\ R_c &= \frac{\Delta V_{out} \cdot R_{load}}{\Delta I_L \cdot R_{load} - \Delta V_{out}} \end{aligned} \tag{7}$$

ΔV_{out} and ΔI_L being, respectively, the output voltage and current ripples. During T_{ON}, the inductor current can be written as,

$$I_L = C \cdot \frac{dV_c}{dt} + I_{out} \tag{8}$$

whereas the voltage in the capacitor is expressed as in (9).

$$V_c = V_{out} - (I_L - I_{out}) \cdot R_c \tag{9}$$

By replacing (8) into (9) and integrating, it results in (10).

$$C \cdot \int dV_c = \int (I_L - I_{out}) \cdot dt \tag{10}$$

Equation (10) can be discretized by considering two discrete time instants T_1 and T_2, where $T_2 = T_1 + \Delta T$, ΔT being the discrete time step considered. Once discretized, the trapezoidal rule allows calculating the integral, thus obtaining,

$$C \cdot (V_{c,T_2} - V_{c,T_1}) = \frac{T_2 - T_1}{2}(I_{L,T_2} - I_{out,T_2} + I_{L,T_1} - I_{out,T_1}) \tag{11}$$

next, (9) is substituted into (11), thus obtaining (12).

$$C \cdot [V_{out,T_2} - (I_{L,T_2} - I_{out,T_2}) \cdot R_c - V_{out,T_1} + (I_{L,T_1} - I_{out,T_1}) \cdot R_c] = \frac{T_2 - T_1}{2}(I_{L,T_2} - I_{out,T_2} + I_{L,T_1} - I_{out,T_1}) \tag{12}$$

By isolating the capacitance C in (12), its value is obtained as in (13).

$$C = \frac{\frac{T_2 - T_1}{2}(I_{L,T_2} - I_{out,T_2} + I_{L,T_1} - I_{out,T_1})}{V_{out,T_2} - (I_{L,T_2} - I_{out,T_2}) \cdot R_c - V_{out,T_1} + (I_{L,T_1} - I_{out,T_1}) \cdot R_c} \tag{13}$$

Equations (7) and (13) provide, respectively, the ESR and the capacitance of the output capacitor, R_C and C, respectively. The values of parameters L, R_L, C, R_C and R_S, are calculated at every time step T_i from (4), (6) and (13) under steady state conditions and at the end of the process the average value of each vector is calculated to obtain the identified values.

2.3.2 Boost converter

This section describes the same process introduced in the previous section. Figure 2.4 presents a simple topology of a synchronous boost DC-DC converter. It is appreciated that the model consists of two transistors.

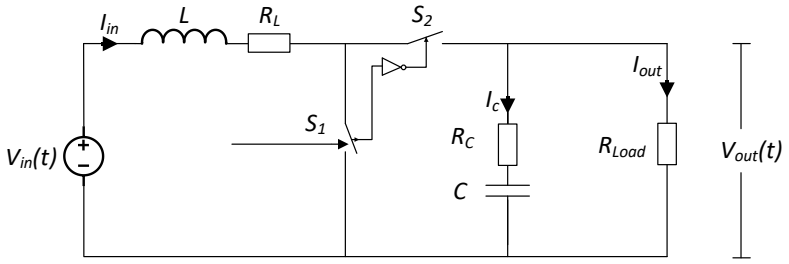

Figure 2.4. Synchronous boost DC-DC converter.

As done with the buck converter, the steady state response must be analyzed to identify the values of the passive components of the boost converter (L, R_L, C, R_C, R_{S1} and R_{S2}), since it is almost not affected by the controller. To this end the model of the converter during T_{ON} is analyzed

in detail, that is, when the switch is in its ON state. Figure 2.5 presents the equivalent circuit of the boost converter during the ON state.

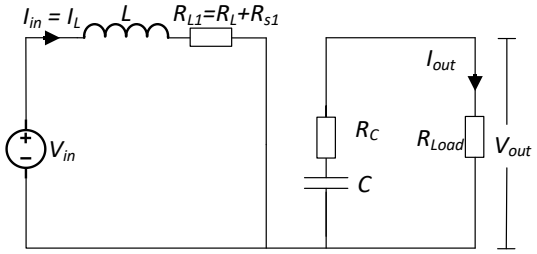

Figure 2.5. Equivalent circuit of the boost converter during T_{on}.

The L and $R_{L1} = R_L + R_{S1}$ values are calculated from (14) and (15).

$$V_{in} = L \cdot \frac{dI_L}{dt} + R_{L1} \cdot I_L \tag{14}$$

$$\int V_{in} dt = L \int dI_L + R_{L1} \int I_L dt \tag{15}$$

By applying the trapezoidal rule of integration and considering four time instants T_1, $T_2 = T_1 + \Delta T$, $T_3 = T_2 + \Delta T$, $T_4 = T_3 + \Delta T$, (15) results in (16).

$$C = \frac{\frac{T_2 - T_1}{2}(I_{L,T_2} - I_{out,T_2} + I_{L,T_1} - I_{out,T_1})}{V_{out,T_2} - (I_{L,T_2} - I_{out,T_2}) \cdot R_c - V_{out,T_1} + (I_{L,T_1} - I_{out,T_1}) \cdot R_c} \tag{16}$$

Finally, the L and R_L values are obtained by solving the following system of equations.

$$\begin{bmatrix} (V_{in,T_2} + V_{in,T_1}) \cdot \frac{T_2 - T_1}{2} \\ (V_{in,T_4} + V_{in,T_3}) \cdot \frac{T_4 - T_3}{2} \end{bmatrix} = \begin{bmatrix} I_{L,T_2} - I_{L,T_1} & \frac{(I_{L,T_2} + I_{L,T_1}) \cdot (T_2 - T_1)}{2} \\ I_{L,T_4} - I_{L,T_3} & \frac{(I_{L,T_4} + I_{L,T_3}) \cdot (T_4 - T_3)}{2} \end{bmatrix} \cdot \begin{bmatrix} L \\ R_{L1} \end{bmatrix} \tag{17}$$

The next step is to obtain the analytical equations of the boost converter during the OFF state. Figure 2.6 shows the equivalent circuit of the boost converter during this state.

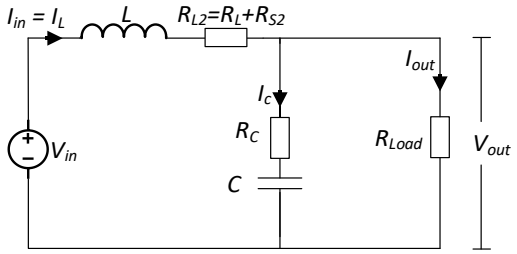

Figure 2.6. Equivalent circuit of the boost converter during T_{off}.

Similarly to (14), the equations governing the dynamic behavior during the OFF state can be expressed as in (18).

$$V_{in} - V_{out} = L \cdot \frac{dI_L}{dt} + R_{L2} \cdot I_L \tag{18}$$

The solution is similar to (17), so it can be expressed as in (19).

$$\begin{bmatrix} (V_{in,T_2}+V_{in,T_1}-V_{out,T_2}-V_{out,T_1})\cdot\dfrac{T_2-T_1}{2} \\ (V_{in,T_4}+V_{in,T_3}-V_{out,T_4}-V_{out,T_3})\cdot\dfrac{T_4-T_3}{2} \end{bmatrix} = \begin{bmatrix} I_{L,T_2}-I_{L,T_1} & \dfrac{(I_{L,T_2}+I_{L,T_1})\cdot(T_2-T_1)}{2} \\ I_{L,T_4}-I_{L,T_3} & \dfrac{(I_{L,T_4}+I_{L,T_3})\cdot(T_4-T_3)}{2} \end{bmatrix} \cdot \begin{bmatrix} L \\ R_{L2} \end{bmatrix} \quad (19)$$

It is noted that $R_{L1} = R_L + R_{S1}$ is calculated during the ON state, R_{S1} being the ON resistance of switch 1 (see Figure 2.5). Similarly, $R_{L2} = R_L + R_{S2}$ is calculated during the OFF cycle, R_{S2} being the ON resistance of switch 2. Since there are three unknowns R_L, R_{S1} and R_{S2} a third equation is required, which can be obtained by means of a suitable assumption, such as $R_{S1} = 2R_{S2}/3$ [31]. Once the parameters of the inductor and switches are identified, the parameters of the capacitor must be obtained. According to [26], the ESR of the output capacitor can be calculated as,

$$R_c = \frac{-[V_{out,t=0.5\cdot D\cdot T_{switch}} - V_{out,average}]\cdot R_L}{V_{out,average}} \quad (20)$$

D being the duty cycle or time period in which the inductor is charged, T_{switch} is the inverse of the switching frequency, and $V_{out,average}$ is the average value of the output voltage in a period T_{switch}. The currents in the equivalent circuit during T_{OFF} accomplish (21).

$$I_C = C\cdot\frac{dV_c}{dt} = I_L - I_{out} \quad \rightarrow \quad C\cdot\int dV_c = \int (I_L - I_{out})\cdot dt \quad (21)$$

Next, the voltage in the capacitor is calculated as,

$$C = \frac{\frac{T_2-T_1}{2}(I_{L,T_2}-I_{out,T_2}+I_{L,T_1}-I_{out,T_1})}{V_{out,T_2}-(I_{L,T_2}-I_{out,T_2})\cdot R_c - V_{out,T_1}+(I_{L,T_1}-I_{out,T_1})\cdot R_c} \quad (22)$$

and considering two point time instants T_1 and $T_2 = T_1 + \Delta T$, and applying the trapezoidal rule for approximating the integral in (21), it results in (23).

$$C\cdot(V_{C,T_2}-V_{C,T_1}) = \frac{T_2-T_1}{2}(I_{L,T_2}-I_{out,T_2}+I_{L,T_1}-I_{out,T_1}) \quad (23)$$

Substituting V_C from (22) in (23) it results in (24).

$$C\cdot[V_{out,T_2}-(I_{L,T_2}-I_{out,T_2})\cdot R_c - (V_{out,T_1}-(I_{L,T_1}-I_{out,T_1})\cdot R_c] = \frac{T_2-T_1}{2}(I_{L,T_2}-I_{out,T_2}+I_{L,T_1}-I_{out,T_1}) \quad (24)$$

Finally, the capacitance can be calculated from (25) by isolating C in (24).

$$C = \frac{\frac{T_2-T_1}{2}(I_{L,T_2}-I_{out,T_2}+I_{L,T_1}-I_{out,T_1})}{V_{out,T_2}-(I_{L,T_2}-I_{out,T_2})\cdot R_c - V_{out,T_1}+(I_{L,T_1}-I_{out,T_1})\cdot R_c} \quad (25)$$

Based on the previous equations, the main parameters can be obtained using the measured signals of the power converter. For this case, the parameters are estimated for several time steps during the corresponding state of the converter and the average value is obtained in the final step of the estimation process.

2.3.3 Buck-boost converter

The process of identifying the parameters of the Buck-boost converter is the same as in the buck and boost converter. The topology used to estimate the parameters is shown in Figure 2.7.

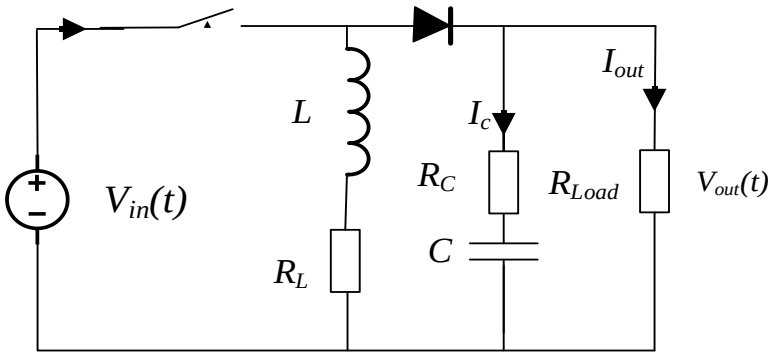

Figure 2.7. Equivalent circuit of an inverting buck-boost DC-DC converter.

The open loop model is used to estimate the values of the inductance (L), capacitance (C), inductive resistance (R_L) and the capacitive resistance (R_c). The open loop model during the T_{on} state is shown in Figure 2.8.

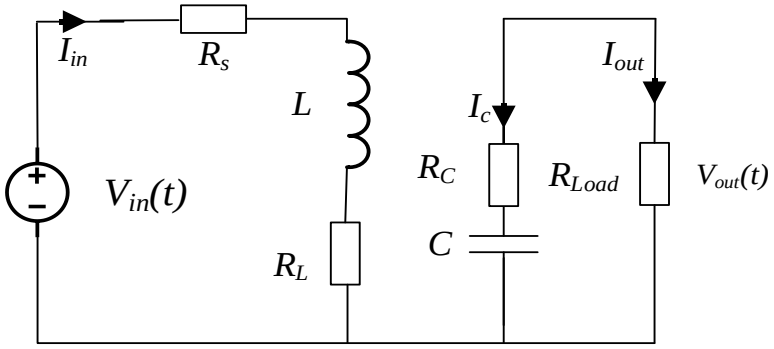

Figure 2.8. Equivalent circuit of the inverting buck-boost converter during T_{on}.

The *L*, R_L and *Rs* values are calculated from (26) and (27).

$$V_{input} - i_{input} \cdot \left(R_L + R_s\right) - L \cdot \frac{di_{input}}{dt} = 0$$
$$V_{input} - i_{input} \cdot \left(R_L + R_s\right) = L \cdot \frac{di_{input}}{dt} \quad (26)$$

$$\int V_{input} \cdot dt = L \cdot \int di_{input} + \left(R_L + R_s\right) \cdot \int i_{input} \cdot dt \quad (27)$$

By applying the trapezoidal rule of integration in points T_1, T_2, T_3 and T_4, it results in,

$$(V_{input,T_2}+V_{input,T_1})\cdot\frac{T_2-T_1}{2}=L\cdot(I_{input,T_2}-I_{input,T_1})+\frac{(I_{input,T_2}+I_{input,T_1})\cdot(T_2-T_1)\cdot(R_L+R_s)}{2} \quad (28)$$

$$\begin{bmatrix}(V_{input,T_2}+V_{input,T_1})\cdot\frac{T_2-T_1}{2}\\(V_{input,T_4}+V_{input,T_3})\cdot\frac{T_4-T_3}{2}\end{bmatrix}=\begin{bmatrix}I_{input,T_2}-I_{input,T_1} & \frac{(I_{input,T_2}+I_{input,T_1})\cdot(T_2-T_1)}{2}\\ I_{input,T_4}-I_{input,T_3} & \frac{(I_{input,T_4}+I_{input,T_3})\cdot(T_4-T_3)}{2}\end{bmatrix}\cdot\begin{bmatrix}L\\R_L+R_s\end{bmatrix} \quad (29)$$

The next step is to find the capacitance parameters.

$$\begin{aligned}V_{output}&=V_{R_c}+V_c\\V_c&=V_{output}-V_{R_c}\\V_{R_c}&=I_{output}\cdot R_c\\V_c&=V_{output}-I_{output}\cdot R_c\end{aligned} \quad (30)$$

$$\begin{aligned}-C\cdot\frac{dV_c}{dt}&=I_{output}\\-C\cdot\int dV_c&=\int(I_{output})\cdot dt\end{aligned} \quad (31)$$

Considering two time steps T_1, T_2 and applying the trapezoidal rule for approximating the integration,

$$C\cdot(V_{C,T_2}-V_{C,T_1})=\frac{T_2-T_1}{2}(I_{output,T_2}+I_{output,T_1}) \quad (32)$$

Substituting the value of V_C from equation (30)

$$\begin{aligned}&-C\cdot((V_{output,T_2}-I_{output,T_2}\cdot R_c)-(V_{output,T_1}-I_{output,T_1}\cdot R_c))=\frac{T_2-T_1}{2}(I_{output,T_2}+I_{output,T_1})\\&C=\frac{-\frac{T_2-T_1}{2}(I_{output,T_2}+I_{output,T_1})}{V_{output,T_2}-I_{output,T_2}\cdot R_c-V_{output,T_1}+I_{output,T_1}\cdot R_c}\end{aligned} \quad (33)$$

Where the resistance is calculated from equation (34).

$$R_c=\frac{-(V_{output,t=t_{on}/2}-\langle V_{output}\rangle)\cdot R_{load}}{\langle V_{output}\rangle} \quad (34)$$

The next step is to estimate the parameters in the OFF state of the DC-DC converter. The equivalent circuit during this state is shown in Figure 2.9.

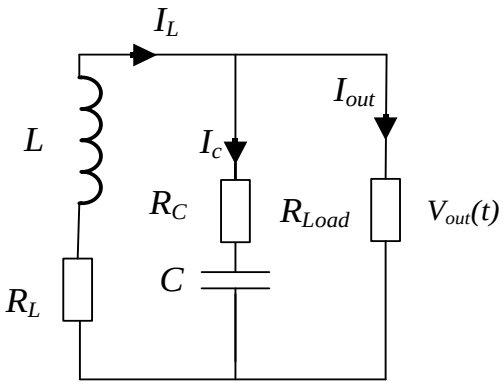

Figure 2.9. Equivalent circuit of the inverting buck-boost converter during T_{off}.

To obtain L and R_L parameters in T_{off}

$$\begin{aligned} V_L + V_{R_L} &= V_{output} \\ V_L &= L \cdot \frac{dI_L}{dt} \\ V_{R_L} &= I_L \cdot R_L \\ L \cdot \frac{dI_L}{dt} &= V_{output} - I_L \cdot R_L \end{aligned} \tag{35}$$

$$L \cdot \int dI_L = \int V_{output} \cdot dt + R_L \cdot \int I_L \cdot dt \tag{36}$$

By applying the trapezoidal rule of integration in points T_1, T_2, T_3 and T_4, it results in,

$$(V_{output,T_2} + V_{output,T_1}) \cdot \frac{T_2 - T_1}{2} = L \cdot (I_{L,T_2} - I_{L,T_1}) + \frac{(I_{L,T_2} + I_{L,T_1}) \cdot (T_2 - T_1) \cdot R_L}{2} \tag{37}$$

$$\begin{bmatrix} (V_{output,T_2} + V_{output,T_1}) \cdot \frac{T_2 - T_1}{2} \\ (V_{output,T_4} + V_{output,T_3}) \cdot \frac{T_4 - T_3}{2} \end{bmatrix} = \begin{bmatrix} I_{L,T_2} - I_{L,T_1} & \frac{(I_{L,T_2} + I_{L,T_1}) \cdot (T_2 - T_1)}{2} \\ I_{L,T_4} - I_{L,T_3} & \frac{(I_{L,T_4} + I_{L,T_3}) \cdot (T_4 - T_3)}{2} \end{bmatrix} \cdot \begin{bmatrix} L \\ R_L \end{bmatrix} \tag{38}$$

Based on the equations presented above and the measured signals of the converter, the parameters of the buck-boost converter are identified. Similar to the identification of the buck and boost converters, the parameters are identified for multiple time steps and the average value of each parameter is obtained.

2.3.4 Six-pulse diode rectifier

This subsection presents the identification process of the main parameters of a six-pulse diode rectifier by obtaining its analytical equations. The model of the rectifier considered in the estimation of the parameters is shown in Figure 2.10

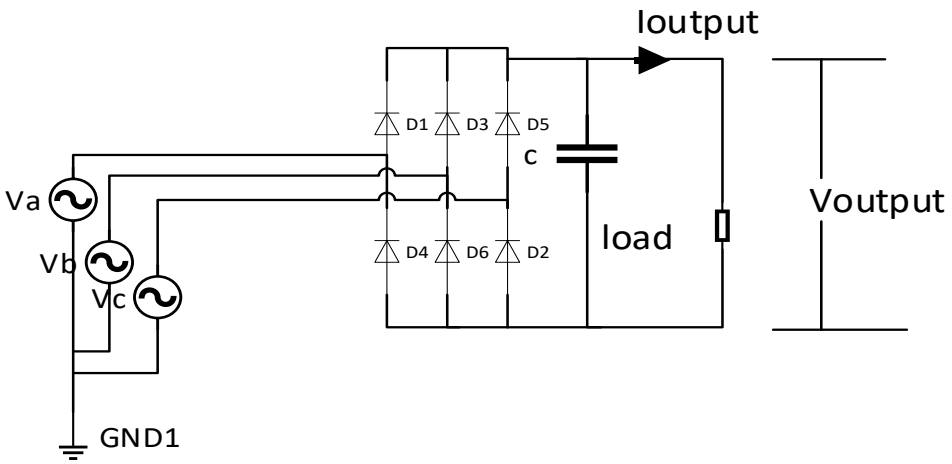

Figure 2.10. Six-pulse diode rectifier.

Considering that it is a six-pulse rectifier, Figure 2.11 shows the corresponding equivalent circuit when just two of the diodes are conducting. In general, this model works for every pulse, it just changes the voltages and currents.

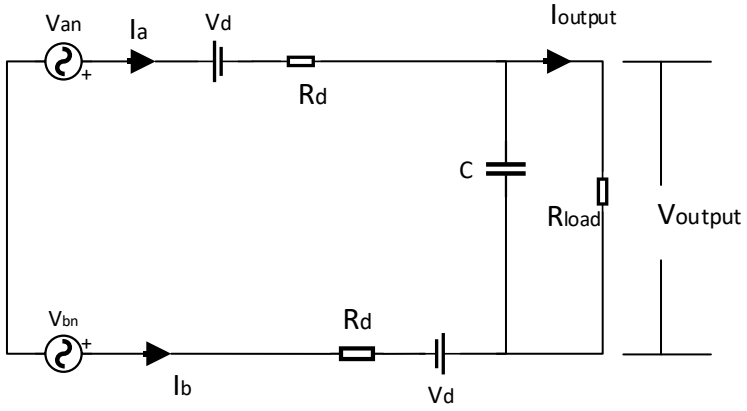

Figure 2.11. Equivalent circuit of a six-pulse rectifier when just two diodes are conducting.

Each pulse must be treated separately because the voltages and currents are different. However, in the end, the electrical parameters (diode voltage, diode resistance, capacitance and load resistance) are the same for each one. Thus, just one analysis is needed in order to estimate the values of the elements. For this project purpose, the final values are the average of the identified parameters for each pulse.

It is important to mention that the model presented in Figure 2.11 is only valid when the diode is considered as ideal and it is represented as a voltage source in series with a resistance. For the case of the exponential model of the diode, the topology presented is not valid and other parameters must be estimated.

The equations to obtain the values of the electrical parameters are shown below:

$$\begin{aligned} &V_{an} - V_{bn} = V_{output} + I_a \cdot R_d + 2V_d - I_b \cdot R_d \\ &I_b = -I_a \\ &V_{an} - V_{bn} = V_{output} + (I_a \cdot R_d + 2V_d + I_a \cdot R_d) = V_{output} + 2(I_a \cdot R_d + V_d) \\ &V_{an} - V_{bn} - V_{output} = 2 \cdot \Delta V_{diode} \end{aligned} \tag{39}$$

$$\begin{aligned} \Delta V_{diode} &= \frac{V_{an} - V_{bn} - V_{output}}{2} \\ \Delta V_{diode} &= I_a \cdot R_d + V_d \end{aligned} \tag{40}$$

From equation (40), the voltage across the diode V is calculated. The slope of the straight line defining V represents the diode resistance (R_d). The point at which the I_{input} will be zero represents the forward voltage of the diode (V_d).

$$\begin{aligned} &I_a = I_{cap} + I_{output} \\ &I_{cap} = I_a - I_{output} \\ &C \cdot \frac{dV_{output}}{dt} = (I_a) - I_{output} \end{aligned} \tag{41}$$

By applying the trapezoidal rule within the time instants T_1, T_2

$$C = \frac{(I_{a,T_2} - I_{output,T_2} + I_{a,T_1} - I_{output,T_1}) \cdot (T_2 - T_1)}{2 \cdot (V_{output,T_2} - V_{output,T_1})} \tag{42}$$

It is important to state that for a low output current, the equations do not identify the parameter of the diode resistance. Then, an appropriate load is needed in order to correctly estimate this parameter from the experiments.

2.4 Non-linear least squares algorithm

This section introduces a methodology that aims to identify the parameters of power converters based on non-intrusive measurements and an optimization algorithm. Due to the limitations of the method based on the analytical equations exposed in Section 2.3, another method is required. These limitations are mainly due to the difficulty to model complex power converters by means of differential equations, and the need to measure the current flowing through the inductor, thus the measurement being intrusive.

To overcome these limitations, an optimization approach is proposed in this section. The non-linear least squares (NLS) algorithm is applied to minimize the error, i.e., the objective function, by estimating step by step the value of the different parameters in the NLS sense, thus continuously minimizing the error function until achieving the optimal solution. The main advantage of the proposed approach is the ability of identifying the full set of parameters of the converters, including the passive, parasitic and control loop elements. Parasitic elements must be considered to model the performances of the DC-DC converters [30]. This method is based on acquiring the input/output voltage and current signals at the terminals of the converter, in both steady state (open loop), and transient state (closed loop). It is shown that once the parameters have been identified, the behavior of the converters can be simulated accurately when operating under different conditions by means of a suitable discrete circuit.

2.4.1 Methodology

This section presents the parameter identification methodology that estimates the open loop and the closed loop parameters of the power converters. This methodology is based on the trust-region reflective non-linear least squares (TRRNLS) algorithm, and it uses the measured signals of the converter and a Simulink model to find the parameter values of the Simulink model. Therefore, a circuit topology must be defined and implemented in Simulink prior to applying the approach presented in Figure 2.12.

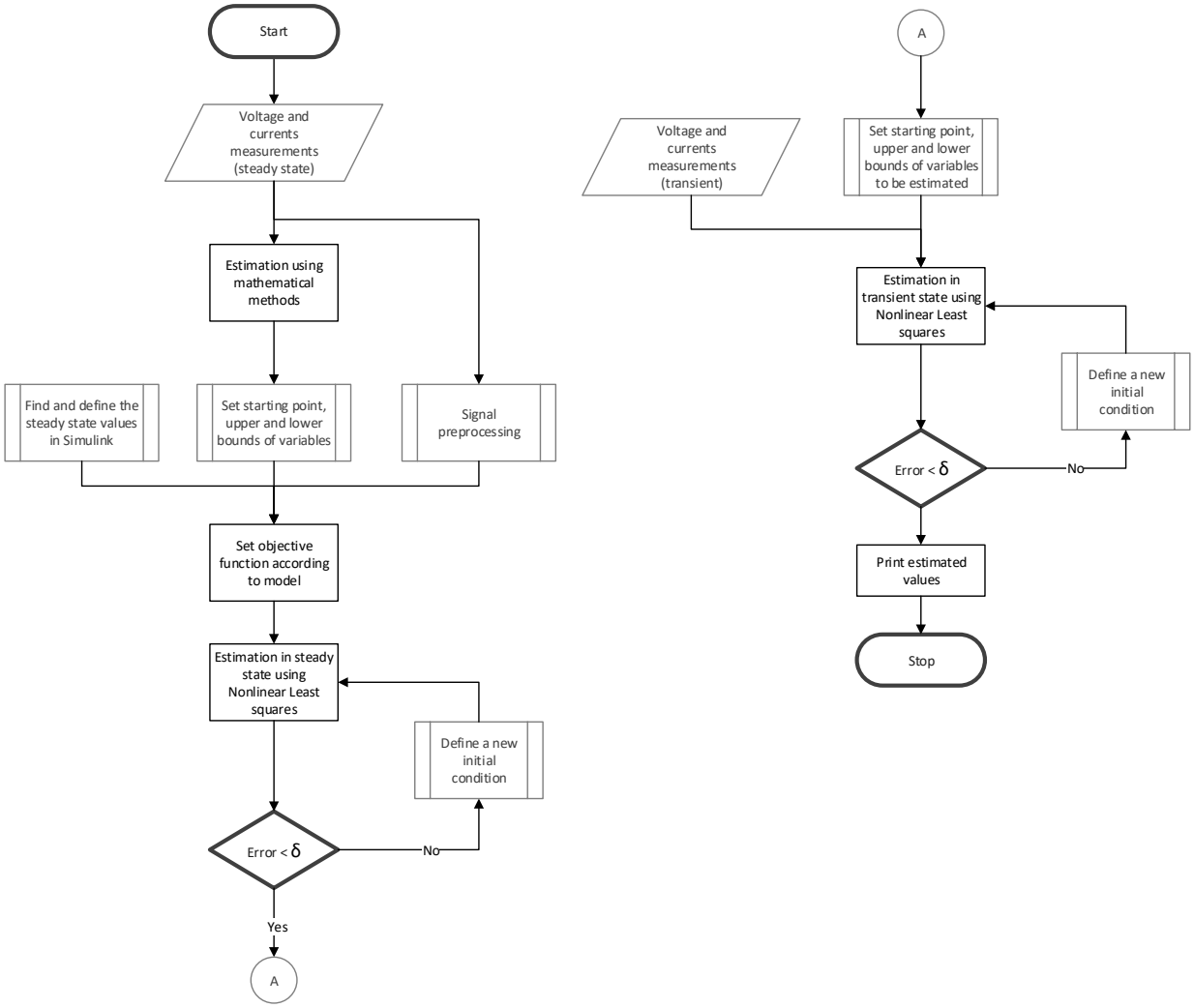

Figure 2.12. Parameter estimation methodology based on NLS.

The flowchart shown in Figure 2.12 details the proposed method to estimate the unknown parameter values of a power converter based on a model and measurements. Next, each block is described:

- Voltage and currents measurements: is the experimentally measured data of the power converter, which is the reference for the minimization problem. There are two different sets: the first one is measured under steady state conditions, whereas the second one is measured under a transient that occurs when a new load is connected to the converter.
- Estimation using mathematical methods: it is the first step of this algorithm and consists of estimating the open loop parameters of the power converter by applying the method of analytical equations depicted in Section 2.3. The parameters are estimated if the inductor current measurement is available. Otherwise, a vague estimation is performed, which is based on the a-priori knowledge of the converter that is being identified.

- Find and define the steady state values in Simulink: based on the Simulink model, the steady state space variables are estimated in order to start the simulations from the operating point, which implies a shorter simulation time.
- Set the starting point, and the upper and lower boundaries of the variables based on the results obtained from the estimation of the parameters using the mathematical model. The constraints and starting point of the problem are defined according to the following equation.

$$\begin{aligned} x_{\min} \le x \le x_{\max} \\ 0.2x_0 \le x \le 5x_0 \end{aligned} \tag{43}$$

  The starting point of the problem is the one obtained as a solution from the mathematical model and the limits are the starting point divided and multiplied by a factor, which in this case is 5.
- Signal synchronization: this step is fundamental in order to obtain accurate results. The main purpose is to synchronize the measured signal with the simulated one, so both signals are comparable and the error vector calculated is reliable.
- Set the objective function according to the model: the cost function is assigned by the user and it depends on the simulated outputs and the measured ones. In some cases, it is not necessary to include all signals in the optimization process.
- Estimation of parameters: the parameters are estimated by solving the nonlinear least squares problem. This is done for the steady state data and the load change scenarios.
- Error > δ: with the obtained parameters, the error is calculated according to the following equation

$$error = \left| \frac{V_{output,measured} - V_{output,estimated}}{V_{output,measured}} \right| \tag{44}$$

  If the error is greater than a given δ, a new starting point is defined with different lower and upper bounds for the different variables.
  This criterion is applied for steady state and transient state parameter identification.
- Define a new initial condition: this process is executed when the error is greater than δ. A new initial state and new limits are assigned randomly.

The algorithm estimates the model parameters so that the input/output signals provided by the simulation model are very similar to the experimental ones. The procedure summarized in Figure 2.12 is performed in two stages. The first one is based on steady state data, whereas the second one is based on transient data, which is obtained by applying a sudden connection of a new load

to the output terminals of the converter. From the steady state signals, the passive and parasitic components of the equivalent circuit of the converters are identified, whereas the closed-loop parameters are identified from the transient (load change) signals. The execution of this algorithm may lead to a feasible solution with an error lower than δ.

2.4.2 Trust region reflective least squares method

This section describes the optimization approach based on the nonlinear least squares method (NLS) to identify the parameters of DC-DC converters from experimental data. NLS is a technique well suited for identifying parameters of nonlinear systems, i.e., those not satisfying the superposition principle [32] by applying an optimization approach. The NLS algorithm adopted in this section is based on the trust-region reflective least squares (TRRLS) method, which is a powerful tool to solve constrained bound nonlinear minimization problems [33].

In general, the least squares problem consists of finding a vector x that minimizes a sum of squares function e(x) [34],

$$\min_x\left(\|e(x)\|^2\right)=\min_x\left(\sum_{i=1}^{n}e_i^2(x)\right)=\min_x\left(e_1(x)^2+e_2(x)^2+\ldots+e_n(x)^2\right) \tag{45}$$

subjected to linear inequalities $A\cdot x \le b$ and linear equalities $A_{eq}\cdot x = b_{eq}$, A and A_{eq} being matrixes, b and b_{eq} vectors, $e(x)$ the objective function to be minimized and x a vector, which can have upper and lower bound constraints, ub and lb, respectively, with $lb \le x \le ub$. The optimization approach consists of minimizing $e(x)$, which returns scalar values, the inputs of the function being vector arguments x. The optimization approach consists of minimizing $e(x)$, which returns scalar values, the inputs of the function being vector arguments x. The objective function is minimized by the identification of a surrounding point that minimizes the value of this function [35].

Under the trust-region optimization approach, and supposing the algorithm centered at a point $x \in \Re^n$, to improve the solution it is required to move to a point providing a lower value of $e(x)$. The algorithm is based on approximating $e(x)$ by a quadratic function $q(s)$, which reproduces the behavior of $e(x)$ in a region N around x, called the trust-region. The objective of the TRRLS method is to calculate $q(s)$ and to find the trust-region. To this end, the TRRLS computes trial steps s to minimize $q(s)$ over N, defining the trust-region subproblem,

$$\min_s\left(q(s),\ s\in N\right) \tag{46}$$

The method calculates s step-by-step by minimizing the area of N. A successful step accomplishes $e(x+s) < e(x)$, so that the current point x is updated by $x + s$ and the trust-region N remains for the next step. In case of an unsuccessful step, i.e., $e(x+s) \ge e(x)$, the vector x remains unchanged, and in the next step the trust-region N will be reduced. To this end, the interior

reflective method generates iterations x_k within the interior of *N* by applying a reflective line search algorithm that ensures convergence at each iteration. The interior of *N* is expressed as int(*N*) and it is defined by *ub* and *lb*, Once the scaling transformation is applied to the quadratic function *q(s)*, the standard trust-region subproblem is defined as [36],

$$\min_s\left(q(s)\right)=\min_s\left(\nabla e(x^k)^T s+\frac{1}{2}sB_k s\right) \text{ with } \left\|D_k^{-1}s\right\|\le\Delta_k \tag{47}$$

∇ being the partial derivative operator, $\nabla e(x^k)^T$ the gradient of function *e*(*x*) at the current point *x*, $B_k=H_k+D_k^{-1}\text{diag}\left(\nabla f(x^k)\right)J_x(x^k)D_k^{-1}$ a symmetric approximation of the Hessian matrix $H_k=\nabla^2 e(x^k)$, where ∇^2 is the Laplacian operator, $J_x(x^k)=\left(\nabla|v_1|^T\ \nabla|v_2|^T\ldots\nabla|v_n|^T\right)^T$ is the *n* x *n* Jacobian matrix and $D_k=\text{diag}\left(\sqrt{|v(x^k)|}\right)$ is a diagonal scaling matrix. *D* is calculated by means of a vector function, which is defined by $v(x)=[v_1(x),v_2(x),\ldots,v_n(x)\,]^T$ and it is obtained according to the gradient of the error function, the boundaries (*ub* and *lb*), and the actual state x_k [16]. It is calculated as,

$$\begin{aligned}
v_i &= x_i - ub_i \text{ if } \nabla\left(e(x)\right)_i<0 \text{ and } ub_i<\infty\\
v_i &= x_i - lb_i \text{ if } \nabla\left(e(x)\right)_i\ge 0 \text{ and } lb_i<\infty\\
v_i &= -1 \text{ if } \nabla\left(e(x)\right)_i<0 \text{ and } ub_i=\infty\\
v_i &= +1 \text{ if } \nabla\left(e(x)\right)_i\ge 0 \text{ and } lb_i=-\infty
\end{aligned} \tag{48}$$

Next, by applying a certain x^k, equation (47) is solved to define s^k, so that $x^{k+1}=x^k+\alpha_k s^k$ is obtained, α_k being a step length, which depends on the distance between the boundary of int(*N*) and x^k+s^k. Since the region int(*N*) is limited by *lb* and *ub*, the iterations are reflected into int(*N*) when they lie on the boundary, which is known as the reflective line search (RLS). To accelerate the convergence of the optimization, the space int(*N*) is limited to a subspace *V* of two dimensions. This restriction enhances the speed of the algorithm because the mathematical calculations of the eigenvectors and eigenvalues are easier due to the low dimension of the subspace [35]. Also, by using a 2-D subspace, the problem can be solved with well-known and less complex algorithms such as the preconditioned conjugate gradient method. Furthermore, the Jacobian matrix *J(x)* approximates the Hessian matrix *H(x)* and it is calculated by means of the efficient finite differencing method [37]. The initial or seed point defined prior to the optimization process plays an important role in the trust-region reflective algorithm, since it determines the step length and how the trust-region reduces after each iteration. Therefore, the local minimum reached after the NLS optimization is conditioned by the initial value of the variables x_0.

On the other hand, the user defines the objective function according to the nature of the problem. For example, for the case of power converters or other electrical circuits, the error is the objective

function and it is defined as the difference between the predicted and simulated data. The function is as follows,

$$\min_{x}\left(\sum_{i=1}^{n}\left(\left[V_{in}^{est}(t)-V_{in}^{meas}(t)\right]^2+\left[I_{in}^{est}(t)-I_{in}^{meas}(t)\right]^2+\left[V_{out}^{est}(t)-V_{out}^{meas}(t)\right]^2+\left[I_{out}^{est}(t)-I_{out}^{meas}(t)\right]^2\right)\right), t=iT \quad (49)$$

V and *I* refer, respectively, to the normalized values of the voltage and current, the subscripts denoting the port where the signals are obtained, the superscripts indicate whether the signal is estimated by the model or acquired in the laboratory, *n* represents the total number of time steps considered, *T* is the length of the time step, and *t* is the time instant at which the error function is evaluated. To ensure that all signals have the same importance, the input/output currents and voltages are standardized as follows,

$$v^*(t)=(v(t)-v_{mean})/\sigma_v \quad (50)$$

where $v(t)$ is an input/output voltage or current, v_{mean} the mean value, and σ_v the standard deviation. Therefore, the TRRNLS algorithm tries to find iteratively the values of the model parameters minimizing the objective function in (47), although the algorithm ends when reaching a predefined tolerance value of the objective function.

The minimum and maximum values of the parameters to be identified define the trust-region *N* of the NLS optimization. However, if all the variables of the power converter being studied are identified at once, *N* would be too large and the problem too complex to solve. Then, it is necessary to define an estimation methodology that uses the TRRNLS algorithm but does not rely entirely on it.

2.5 Validation and results

The proposed methodology is tested with four types of power electronic converters, where three of them are DC-DC and the remaining one is an AC-DC. As mentioned in the previous section, the topologies must be defined and implemented in Simulink based on a real power converter. The following subsections present the topologies, the Simulink models and the actual converters used in the laboratory.

The DC/DC converters presented in this section were chosen according to the problem specifications and to the capabilities of the measurement equipment available in the laboratory. Therefore, the converters must work at voltages, power and frequencies where there is no problem to measure the input and output voltages and currents. In some cases, it is also required to measure the current flowing through the inductor.

To select each device, different considerations were taken into account:

- Cost and availability: The converter should not be expensive and widely known because in case of an accident, where the converter stops working, ordering another one must be fast and not expensive.
- Available information: The information about the converters and their parameters should be clear in order to compare the results obtained with the theoretical values given in the datasheet.
- Control loop: The response time of the control loop should not affect the measurements when a load change occurs.
- Working range: The DC/DC converter should work under continuous and discontinuous conduction modes with a wide range of operational states to test it under a broad range of operating conditions.

The converters used in the validation of the proposed methods are the same as the ones presented in section 0of this document, which are buck, boost, buck-boost and a six-pulse diode rectifier. The entire estimation process is depicted for the buck converter, while for the other DC-DC converters the final results are presented.

This section presents the parameters identified in open loop for the two proposed methodologies. However, the closed loop parameters are identified just by the methodology proposed in section 2.4.

The commercial converters described in this section have been selected because the manufacturer provides most of the values of the parameters. The full set of parameters are divided in three types, namely passive, parasitic and control loop elements. Whereas the first two types

are identified from steady state data, the last ones are identified from transient data, which is generated under a sudden load change.

2.5.1 Power supply filter

Before identifying the parameters of the converters it is necessary to define the input filter of the system. Ideally, the topology of a DC-DC converter does not include an input filter stage. However, when sensing the input current and voltage of the DC-DC converters (buck, boost and buck boost), the signals are not completely accurate and differ from simulation data. This happens mainly because a real converter has a series of elements such as filters at the input, which alters the measurements of these ports.

To overcome this problem, a model of the input stage is proposed based on the main characteristics of the converters. The manufacturer does not provide any information about this input stage or parasitic elements that may affect the performance of the circuit. However, there are elements that are inherent to the behavior of a converter, which are the following:

- Voltage source resistance: this element represents the resistance of the voltage source and the cables that connect the voltage source to the converter. In general, the manufacturers do not provide this value.
- Input capacitance: the manufacturer (in some cases) provides the value of this element, whose function is to reduce the input ripple voltage.
- ESR of the input capacitance.
- Resistance that models the power consumption of the circuit (R_{cc}): since the controller requires energy to operate, there is a power consumption, which in this particular case is modelled by a resistance in parallel.
- Parasitic capacitances in parallel.
- Parasitic inductance in series: it is the most important element of this circuit because it is responsible for the change in the input current. Due to the switching frequency of the PWM, the inductance effect on the measurement is considerable. However, the mean value of the measured current remains the same.

The proposed input filter is shown in Figure 2.13.

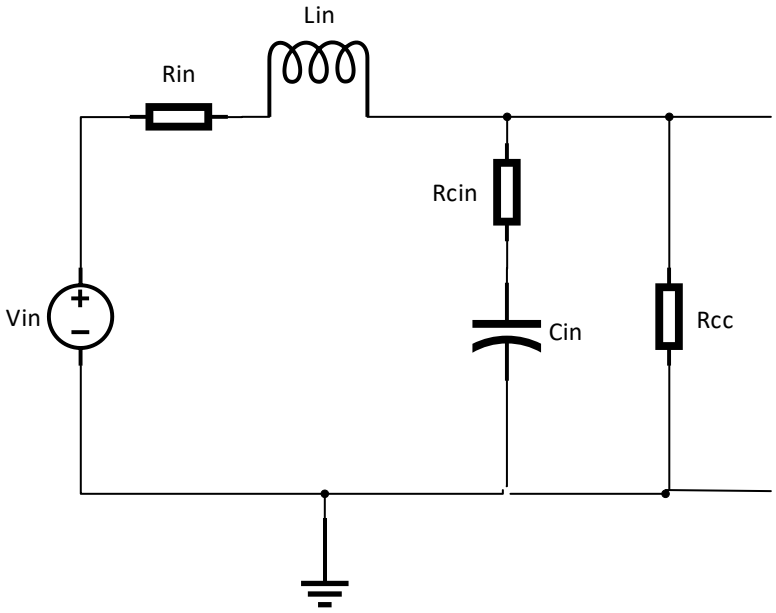

Figure 2.13. Equivalent circuit of a power supply connected to the input filter of a power converter.

The filter stage presented in Figure 2.13 is implemented in the converter model and helps to obtain more accurate results.

2.5.2 Buck converter

A buck converter (step-down converter) steps down the voltage (or steps up the current) from the input (supply) to the output (load) [26].

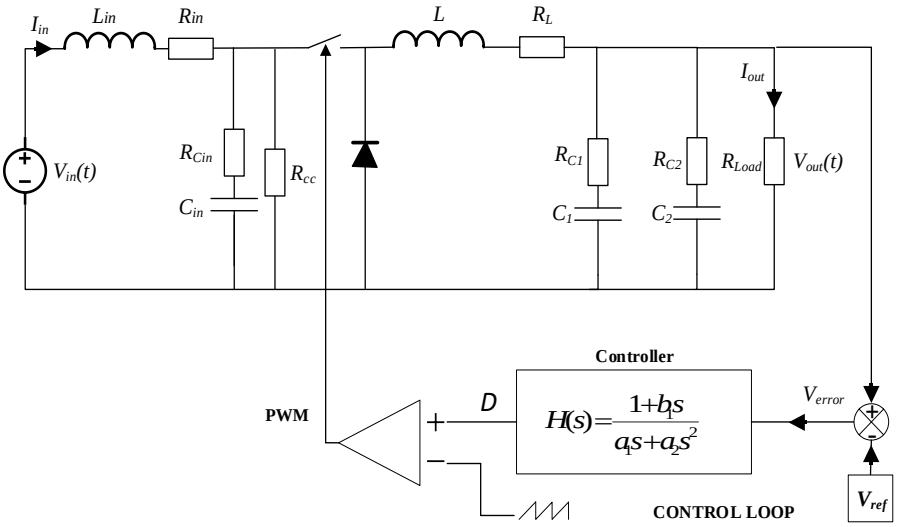

Figure 2.14. Model of the analyzed buck converter.

Due to the high switching frequency of the buck converter, some parasitic elements must be considered in the input stage of the discrete simulation models, which are not provided by the manufacturer, although they may affect the performance of the circuit. The parasitic components

are the MOSFET on resistance R_s, the ESR of the inductor R_L, the ESR of the output capacitor R_C, and the input capacitor, which is modelled as a capacitance C_{in} in series with the ESR R_{Cin} [38].

It is worth noting that Figure 2.14 depicts two capacitors connected in parallel with the load. This is because commercial SMPCs habitually include several parallel connected capacitors to ensure that the converter performs appropriately. The output capacitors can be modelled by an equivalent large electrolytic capacitor connected in parallel to a smaller ceramic one. In general, the small capacitor affects the ripple of the output signals, while the electrolytic capacitor has a direct impact on the transient response of the circuit.

The commercial buck converter used to identify the electrical parameters is the model TPS40200EVM-002, manufactured by Texas Instruments. This converter fulfils the specifications listed in the introduction of this section. Figure 2.15 shows the circuit board of the buck converter and Table 2.1 presents its main characteristics. According to the information provided by the manufacturer, the control loop is governed by a Type III compensator [39] transfer function of second order and the parameters are estimated accordingly.

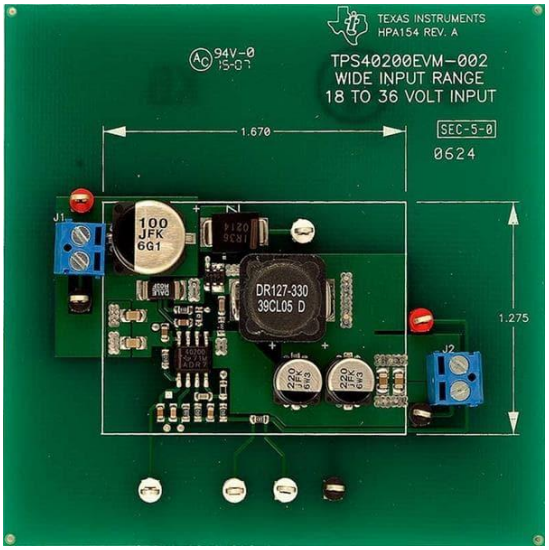

Figure 2.15. TPS40200EVM-002 commercial buck converter circuit board [40]**.**

Table 2.1. TPS40200EVM-002 specifications [40]

Parameter	Value
Input voltage	18 V – 36 V
Output voltage	3.3 V
Maximum current	2.5 A
Switching frequency	198 kHz
Efficiency	92%

Type	Nonsynchronous

The steady state and transient voltages and currents at the input and output terminals of the buck converter were acquired by means of the experimental setup presented in Figure 2.16. It shows that the buck converter is fed with a fixed voltage from the DC power supply and the signals are measured using an oscilloscope. Two resistors are placed at the output of the converter. One is used to acquire the steady state data, while the other is connected suddenly in order to measure the transient response of the converter.

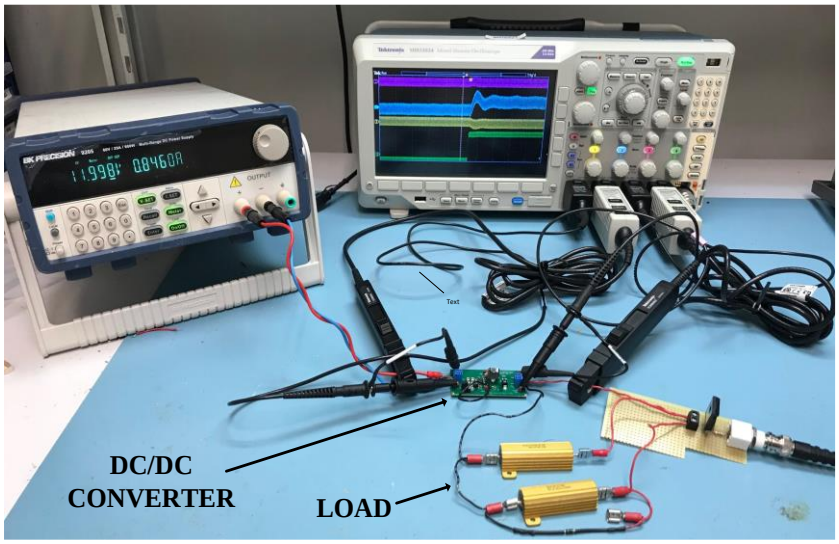

Figure 2.16. Experimental setup of the analyzed commercial Buck converter.

2.5.2.1 Parameter estimation procedure

This section presents the identification results from experimental data acquired from the TPS40200EVM-002 Buck converter. A step-by-step demo of the procedure is presented, detailing the evolution of the algorithm described in Figure 2.12. First, the upper and lower boundaries and the seed point of the parameters are set. These values are defined based on a priori knowledge of the converters, which are shown in Table 2.2.

Table 2.2. Upper and lower bounds for the optimization algorithm

	Minimum	**Maximum**	**Seed point**
Inductors	1 nH	1 mH	Random value between the *ub* and *lb*
Capacitors	1 nF	10 mF	
Resistors	0.1 mΩ	10 Ω	
TF coefficients	10^{-12}	10^{-3}	

The objective function is set as the difference between the measured and estimated signals. The output current is not considered in the optimization because its value is equal to the output voltage

divided by the load resistance. Thus, by neglecting this signal from the parameter estimation stage, the computation speed increases without compromising the accuracy of the methodology. The objective function is expressed as,

$$\min\left(\sum_{i=1}^{n}\left(\left(V_{in}^{est}(t)-V_{in}^{meas}(t)\right)^2+\left(V_{out}^{est}(t)-V_{out}^{meas}(t)\right)^2+\left(I_{in}^{est}(t)-I_{in}^{meas}(t)\right)^2\right)\right) \quad (51)$$

Then, the process of identifying the open loop parameters is executed. Figure 2.17 compares the measured signals and the system simulated using the seed point as the converter parameters

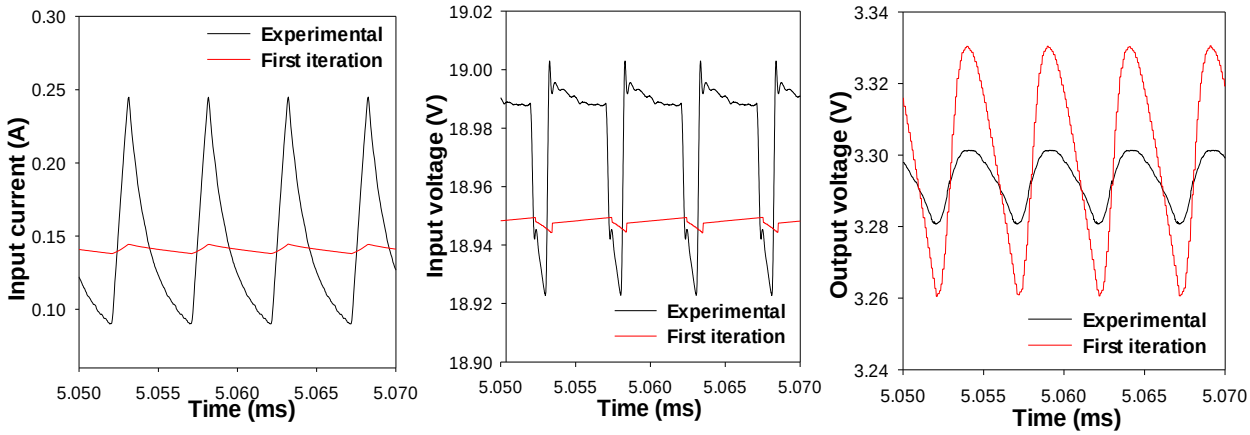

Figure 2.17. Initial point of the first stage of the optimization process. a) Input current. b) Input voltage. c) Output voltage.

The values of the obtained parameters of the first optimization process were: $L = 39.88\mu H$, $C_1 = 17.1\mu F$, $C_2 = 560.4\mu F$, $R_L = 73.1m\Omega$, $R_{C_1} = 59.5m\Omega$, $R_{C_2} = 0.36\Omega$, $R_s = 53m\Omega$ $L_{in} = 0.213\mu H$, $C_{in} = 4.87\mu F$, $R_{C_{in}} = 75m\Omega$, $R_{in} = 0.16\Omega$ and $R_{CC} = 2.57k\Omega$. To estimate the closed loop parameters, the previous values were used as the seed point, and the parameters of the controller (transfer function coefficients) were included in the optimization process. The transient state dataset was used in this stage. Figure 2.18 compares the measured signal and the starting point of the second stage and the optimization.

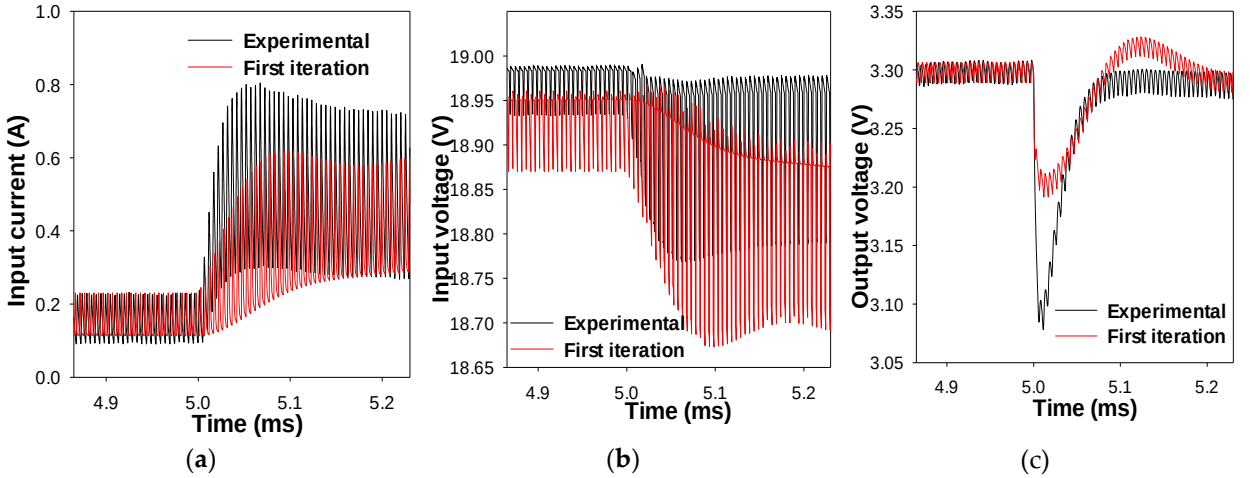

Figure 2.18. Initial point of the second stage of the optimization process. a) Input current. b) Input voltage. c) Output voltage.

Figure 2.19 shows the convergence process for the two optimization stages. Compared to the second stage, due to the lower number of parameters involved, the first stage requires less iterations to achieve the minimum and also the value of the cost function is lower. Finally, once the algorithm reaches the minimum, it finishes and stores the estimated values.

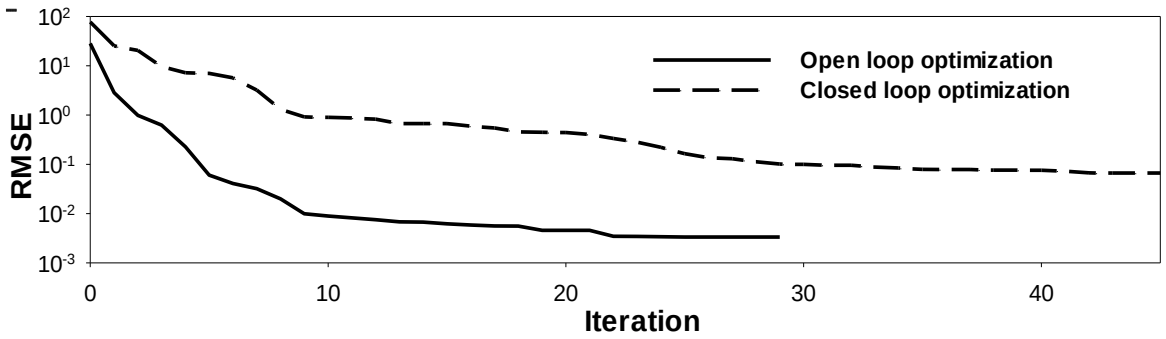

Figure 2.19. Buck converter. Convergence process of the two stages of the NLS-TRRLS.

The final estimated parameters are shown in Table 2.3, and they are compared to the results obtained with the method that uses the analytical equations of the converter. It is seen that both approaches resemble the actual values of the converter in steady state. It is worth noting that the strategy based on TRRNLS is also capable of estimating the filter parameters and the transfer function coefficients of the control loop.

Table 2.3. Actual and identified parameters of the analyzed Buck converter

	Value	Identified TRRNLS	Identified Analytical Equations.
L	33 µH	35.4 µH	35.2 µH
C_1	20 µF	16.5 µF	16.8 µF
C_2	440 µF	494.3 µF	490 µF
R_L	60 mΩ	73.13 mΩ	55.8 mΩ
R_{C1}	65 mΩ	59.5 mΩ	60.9 mΩ
R_{C2}	300 mΩ	207 mΩ	280 mΩ
R_s	<40 mΩ	31 mΩ	39.1 mΩ
C_{in}	100 µF	96.4 µF	-
L_{in}	-	0.40 µH	-
R_{cc}	-	2.57 kΩ	-
R_{Cin}	-	75 mΩ	-
R_{in}	-	0.160 Ω	-

a_0	0	0	-
a_1	$4.7 \cdot 10^{-4}$	$5.3 \cdot 10^{-4}$	-
a_2	$1.6 \cdot 10^{-9}$	$2.8 \cdot 10^{-9}$	-
b_0	1	1	-
b_1	$4.7 \cdot 10^{-4}$	$8.7 \cdot 10^{-4}$	-
b_2	0	0	-

Figure 2.20 and Figure 2.21 compare experimental and estimated data under steady state conditions and under a sudden load change against the results obtained from the discrete simulation model using the identified parameters (TRRNLS) and the results derived from the analytical equations of the converter. However, since the analytical equations based method does not estimate the closed loop parameters of the buck converter, the results displayed in Figure 2.21 only show the estimation performed by means of the TRRNLS method.

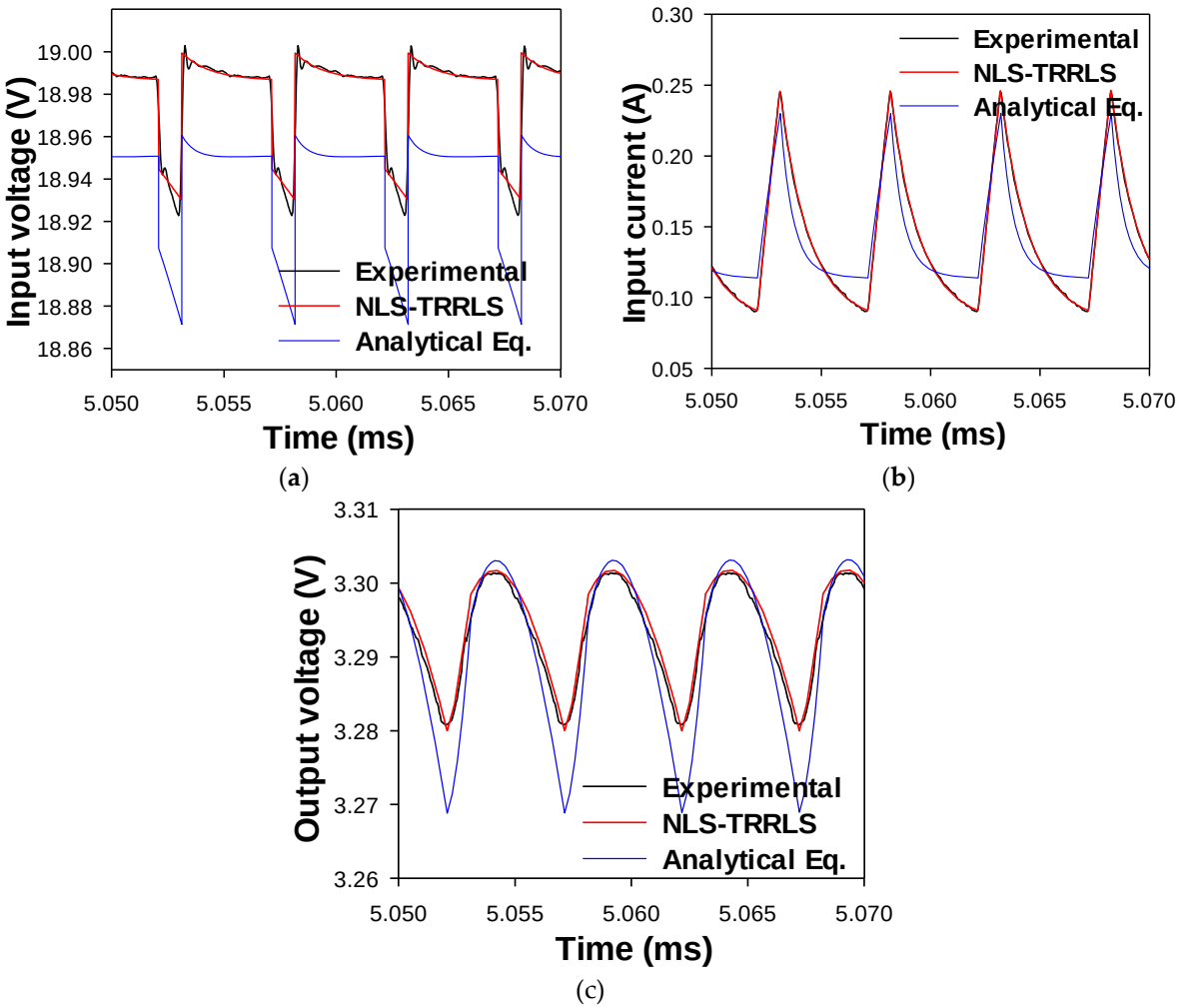

Figure 2.20. Commercial buck converter operating under steady state. Experimental versus simulated data using the identified parameters a) Input voltage. b) Input current. c) Output voltage.

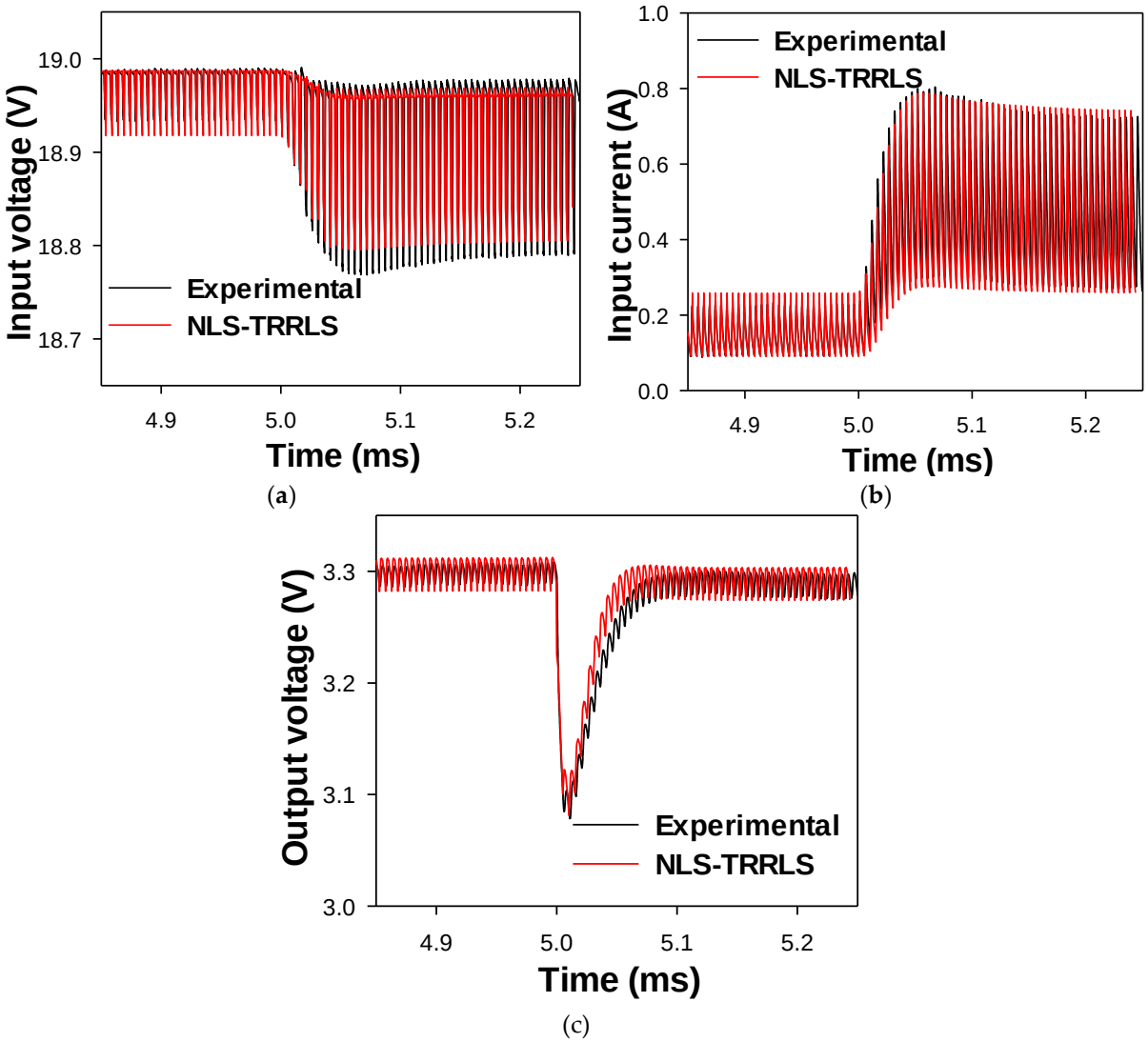

Figure 2.21. Commercial buck converter operating under transient condition. Experimental versus simulated data using the identified parameters a) Input voltage. b) Input current. c) Output voltage.

The results show a good match between experimental data and simulated results with the identified parameters of the commercial TPS40200EVM-002 buck converter, thus validating the parameter identification approach proposed in this chapter. It can be seen that method based on the analytical equations is less accurate in reproducing the ripple of the voltages and currents of the converter.

2.5.3 Boost converter

A boost converter (step-up converter) steps up the voltage (or steps down the current) from the input (supply) to the output (load) [26]. Figure 2.22 presents the synchronous topology used in the parameter estimation process.

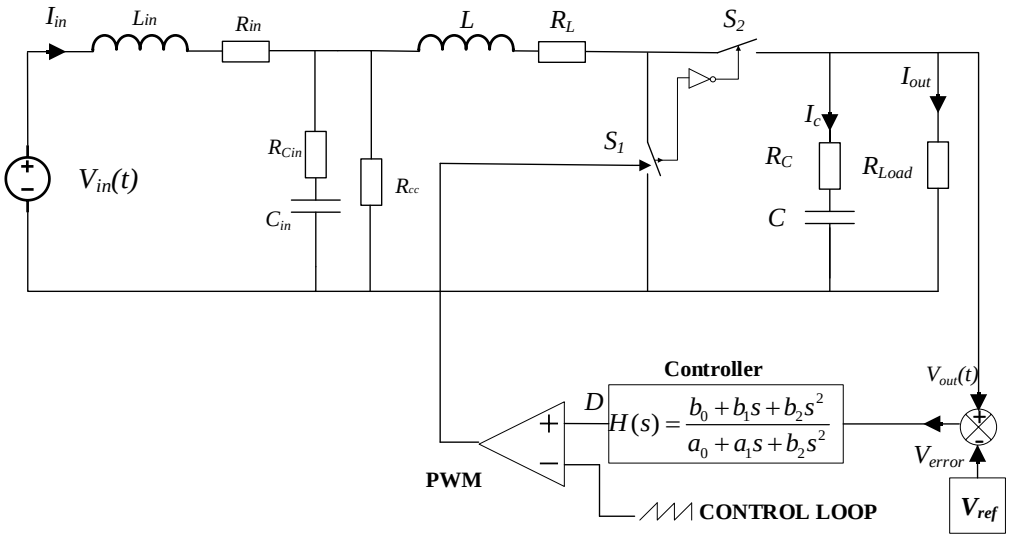

Figure 2.22. Model of the analyzed synchronous boost converter.

Similar to the case of the buck converter, the parasitic components and the input filter are included in the topology of the boost converter. On the other hand, the model just includes one capacitor at the output of the boost converter since the evaluation module used in the laboratory only has ceramic capacitors. Also, the boost converter controller is based on a type III compensator. The commercial Boost converter used to identify the electrical parameters is the model TPS61089EVM-742, manufactured by Texas Instruments.

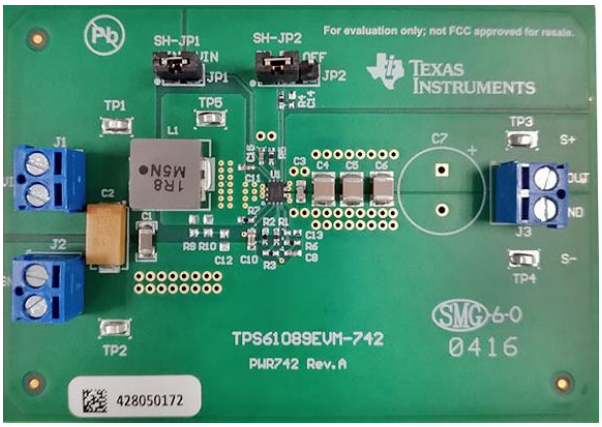

Figure 2.23. TPS61089EVM-742 commercial boost converter circuit board [41]**.**

Table 2.4. TPS61089EVM-742 specifications [41]

Parameter	Value
Input voltage	3 V – 5 V
Output voltage	9 V
Maximum current	2 A
Switching frequency	480 kHz

Efficiency	93%
Type	Synchronous

The experimental setup is the same as the one presented in Figure 2.16. The difference is the converter and the resistors used in the data acquisition process. After measuring the signals from the boost converter, the next step is to identify the parameters in open loop and in closed loop conditions following the same procedure proposed in Section 2.4.

Table 2.5 presents the results of the estimation of the converter parameters after applying the TRRNLS and after solving the analytical equations. These results show that the TRRNLS outperforms the analytical equations method since it estimates a larger number of parameters with a higher accuracy.

Table 2.5. Actual and identified parameters of the boost converter

	Value	Identified TRRNLS	Identified Analy. Eq.
L	1.8 μH	1.7 μH	1.9 μH
C	67 μF	65.6 μF	47.9 μF
R_L	12.6 mΩ	10.6 mΩ	7.5 mΩ
R_C	0.65 mΩ	0.60 mΩ	1.06 mΩ
R_{s1}	<31 mΩ	38.3 mΩ	10.92 mΩ
R_{s2}	-	412.6 mΩ	16.38 mΩ
C_{in}	-	40 μF	-
L_{in}	-	0.35 μH	-
R_{cc}	-	2.90 kΩ	-
R_{Cin}	-	5.42 mΩ	-
R_{in}	-	0.1 mΩ	-
a_0	0	0	-
a_1	$4.7 \cdot 10^{-9}$	$9 \cdot 10^{-10}$	-
a_2	-	$7 \cdot 10^{-17}$	-
b_0	1	1	-
b_1	$8.18 \cdot 10^{-5}$	$1.42 \cdot 10^{-4}$	-
b_2	-	$1.05 \cdot 10^{-9}$	-

Figure 2.24 and Figure 2.25 compare experimental input/output data under steady state conditions and under a sudden load change, respectively, against the results obtained from the

discrete simulation model using the identified parameters (TRRNLS) and the results derived from the analytical equations of the converter.

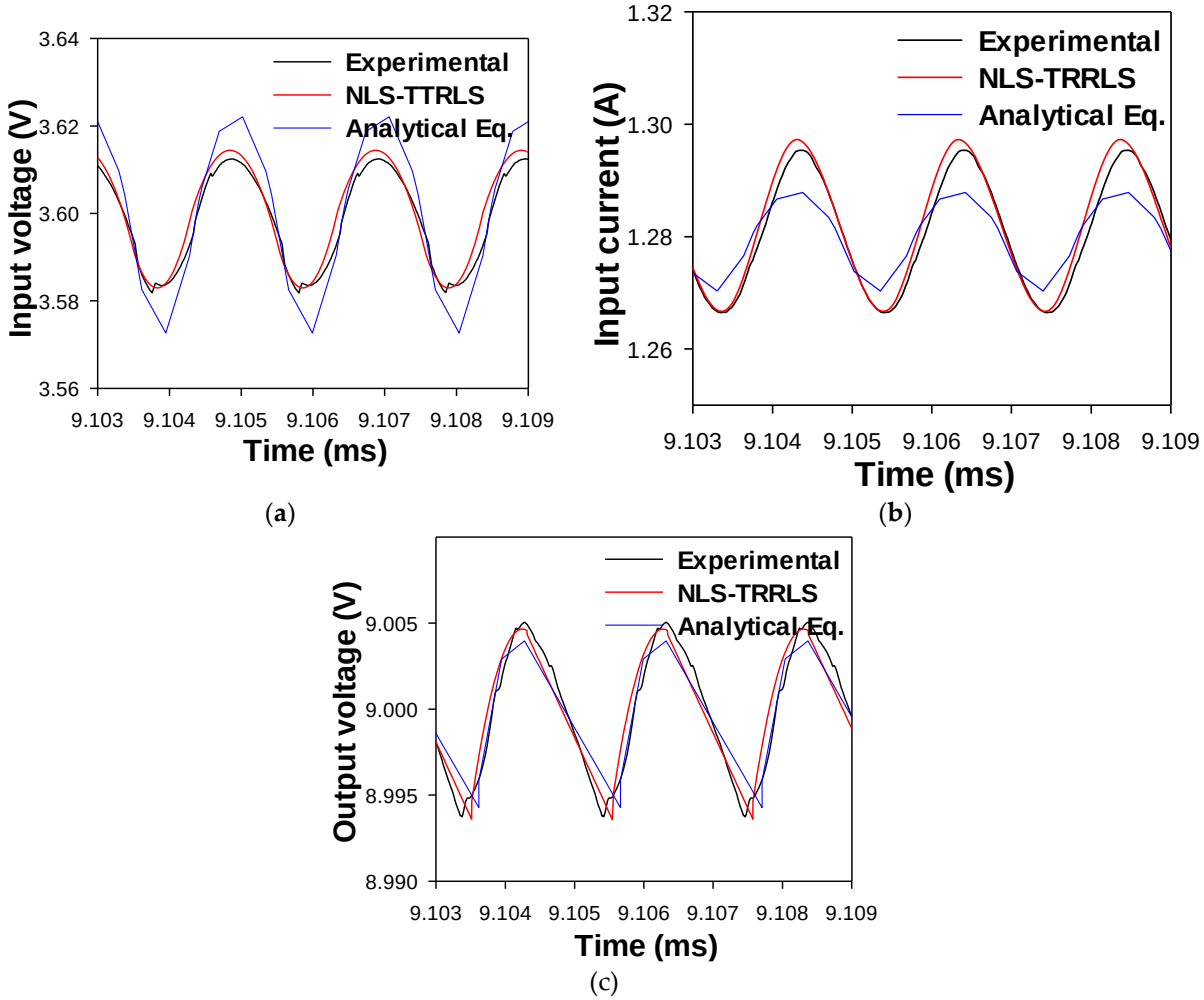

Figure 2.24. Commercial boost converter operating under steady state. Experimental versus simulated data using the identified parameters a) Input voltage. b) Input current. c) Output voltage.

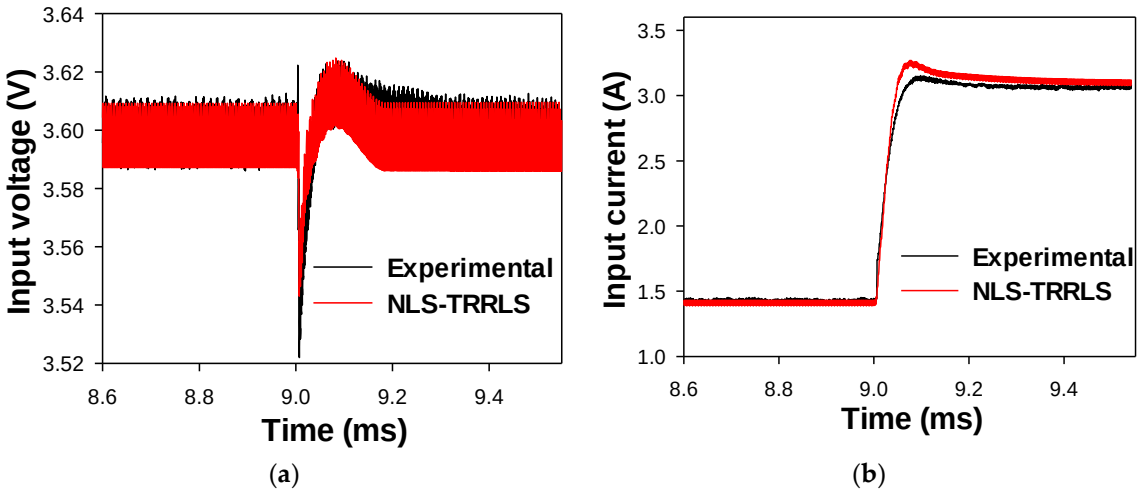

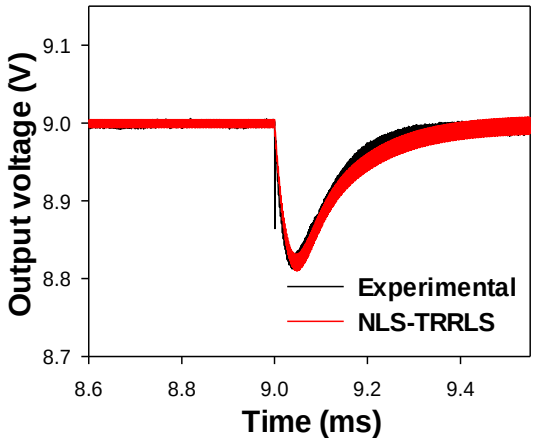

(c)

Figure 2.25. Commercial boost converter operating under a transient condition. Experimental versus simulated data using the identified parameters a) Input voltage. b) Input current. c) Output voltage.

Once again, from the results presented in Figure 2.24 and Figure 2.25, it can be deduced a close agreement between experimental data and simulated results with the identified parameters of the proposed method. It is seen that the TRRNLS method is able to replicate the converter behavior both in steady and transient conditions with high accuracy, while the method based on analytical equations cannot reproduce the converter response to perturbations.

2.5.4 Buck-boost converter

The buck–boost converter has an output voltage magnitude that can be either less than or greater than the magnitude of the input voltage. Figure 2.26 presents the inverting buck-boost converter topology used in the parameter estimation process.

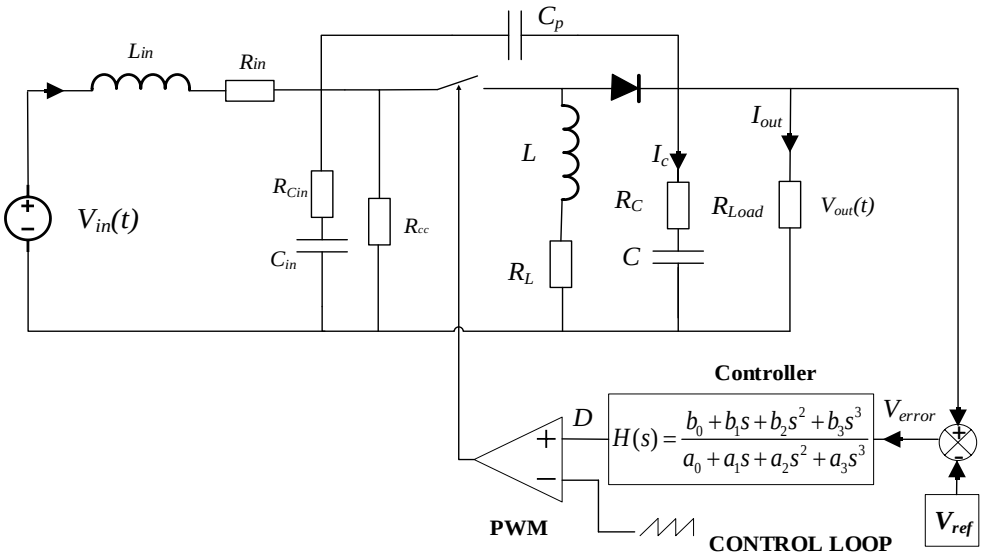

Figure 2.26. Model of the analyzed inverting buck-boost converter.

As it occurs in the models of the buck and boost converters, the topology of the inverting buck-boost converter includes the parasitic elements and an input filter. It also includes a capacitor C_p that creates a link between the input and output terminals of the converter. According to literature, this capacitor is used to reduce the output voltage ripple by means of a continuous AC path from the input voltage to the output voltage during the switching states of the converter [42]. The commercial inverting buck-boost DC-DC converter used in the laboratory is the model TPS5430EVM-342, manufactured by Texas Instruments. The TPS5430 chip is configured as an inverting buck-boost, thus, the output voltage is negative. The controller consists of a compensator that can be modeled as a third order transfer function.

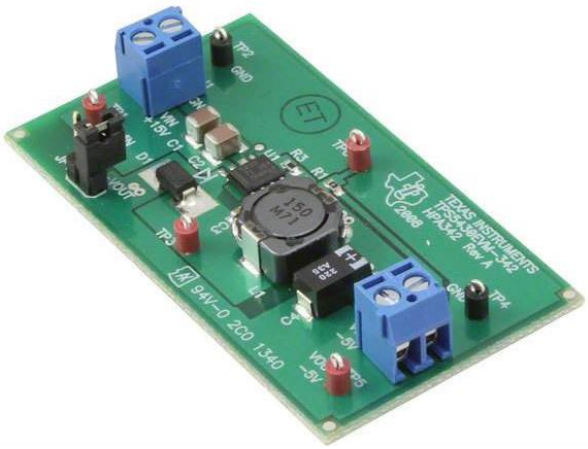

Figure 2.27. TPS5430EVM-342 commercial inverting buck-boost converter circuit board. Source: [42]**.**

Table 2.6. TPS5430EVM-342 specifications [42]

Parameter	Value
Input voltage	10.8 V – 19.8 V
Output voltage	-5 V
Maximum current	2.25 A
Switching frequency	493 kHz
Efficiency	93%
Type	Nonsynchronous

The experimental setup is the same as the one presented in Figure 2.16. The difference is the converter and the resistors used in the data acquisition process. After measuring the signals from the buck-boost converter, the next step is to identify the parameters under open loop and closed loop conditions following the same procedure proposed in Section 2.4. Table 2.7 presents the results of the estimation of the converter parameters after applying the TRRNLS and after solving the analytical equations. The results show a good match between the parameters provided by the

manufacturer and the ones estimated using the proposed methods. Despite of being the converter with most parameters, the TRRNLS identifies the parameter values with good precision.

Table 2.7. Actual and identified parameters of the Buck-boost converter

	Value	Identified TRRNLS	Identified Analy. Eq.
L	15 μH	15.41 μH	15.09 μH
C	220 μF	292 μF	193.2 μF
R_L	41 mΩ	42.26 mΩ	51.1 mΩ
R_C	40 mΩ	50.2 mΩ	56.2 mΩ
R_s	40 mΩ	46.8 mΩ	28.8 mΩ
C_{in}	-	0.354 μF	-
L_{in}	-	0.232 μH	-
R_{cc}	-	0.27 kΩ	-
R_{Cin}	-	2.8 mΩ	-
R_{in}	-	48.3 mΩ	-
C_p	10 μF	9.31 μF	-
a_0	0	0	-
a_1	$7.35 \cdot 10^{-5}$	$2.78 \cdot 10^{-5}$	-
a_2	$7.0 \cdot 10^{-10}$	$3.75 \cdot 10^{-10}$	-
a_3	$1.4 \cdot 10^{-15}$	$1.56 \cdot 10^{-15}$	-
b_0	1	1	-
b_1	$1.4 \cdot 10^{-4}$	$1.2 \cdot 10^{-4}$	-
b_2	$4.5 \cdot 10^{-9}$	$4.3 \cdot 10^{-9}$	-
b_3	0	0	-

Figure 2.28 and Figure 2.29 compare experimental input/output data under steady state conditions and under a sudden load change, respectively, against the results obtained from the discrete simulation model with the identified parameters (TRRNLS) and the results derived from the analytical equations of the converter. These figures show a close similitude between experimental data and simulated results with the identified parameters using the method based on an optimization algorithm.

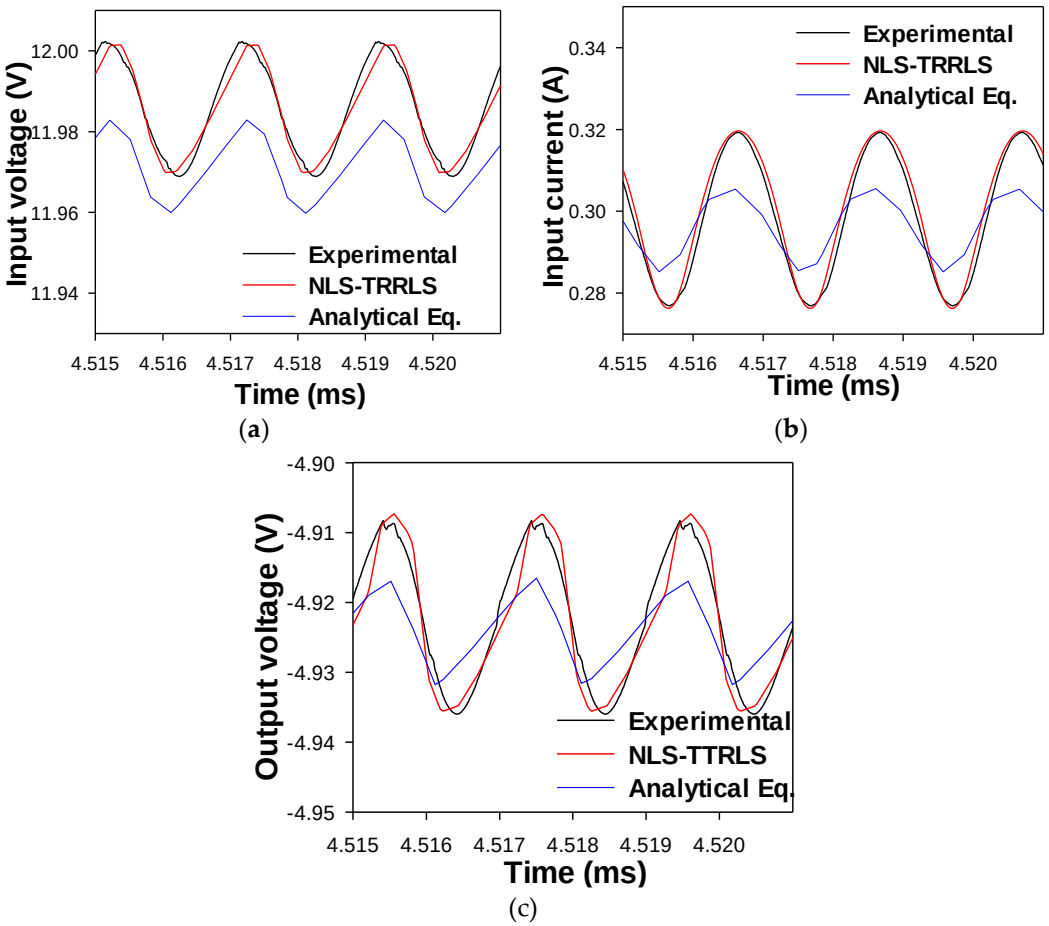

Figure 2.28. Commercial buck-boost converter operating under steady state. Experimental versus simulated data using the identified parameters a) Input voltage. b) Input current. c) Output voltage.

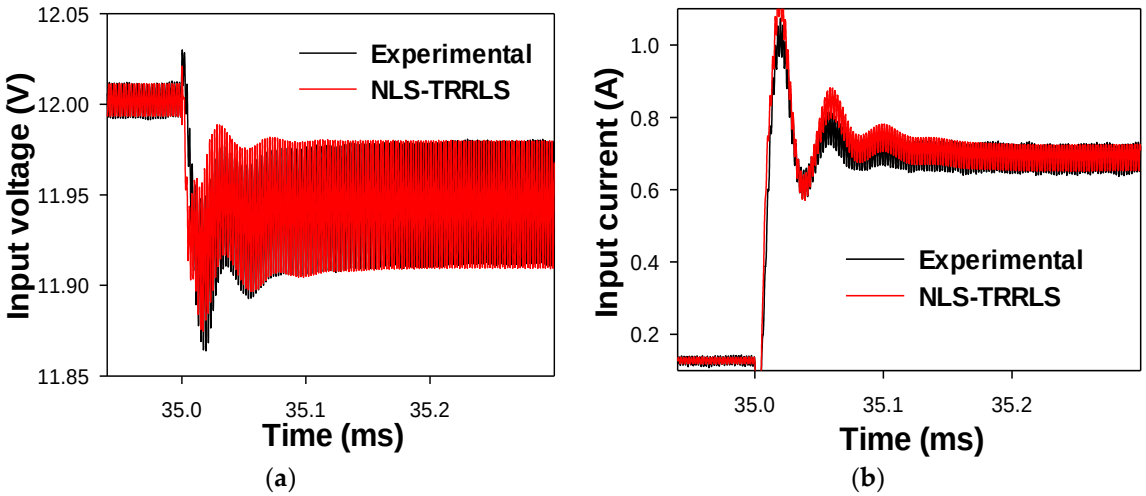

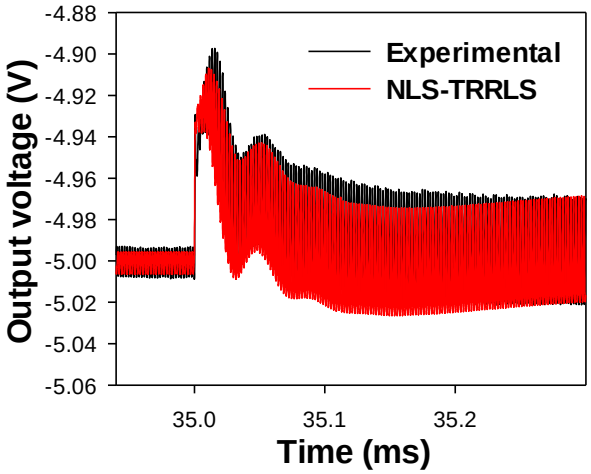

(c)

Figure 2.29. Commercial buck-boost converter operating under transient condition. Experimental versus simulated data using the identified parameters a) Input voltage. b) Input current. c) Output voltage.

It is noted that the method based on analytical equations fails to reproduce with high accuracy the ripple of the converter signals, while the TRRNLS shows a good match in the estimations in open and closed loop.

2.5.5 Six-pulse diode rectifier

This section presents the estimation of the rectifier parameters. Since the rectifier does not have a control loop, the methodology based on TRRNLS presented in Figure 2.12 is modified and the second part of the process is not required. A new step was added at the beginning, consisting in defining the operating points of the rectifier. This phase defines the number of load conditions that should be specified in order to apply the experimental part. Figure 2.30 presents the methodology to estimate the parameters of the rectifier.

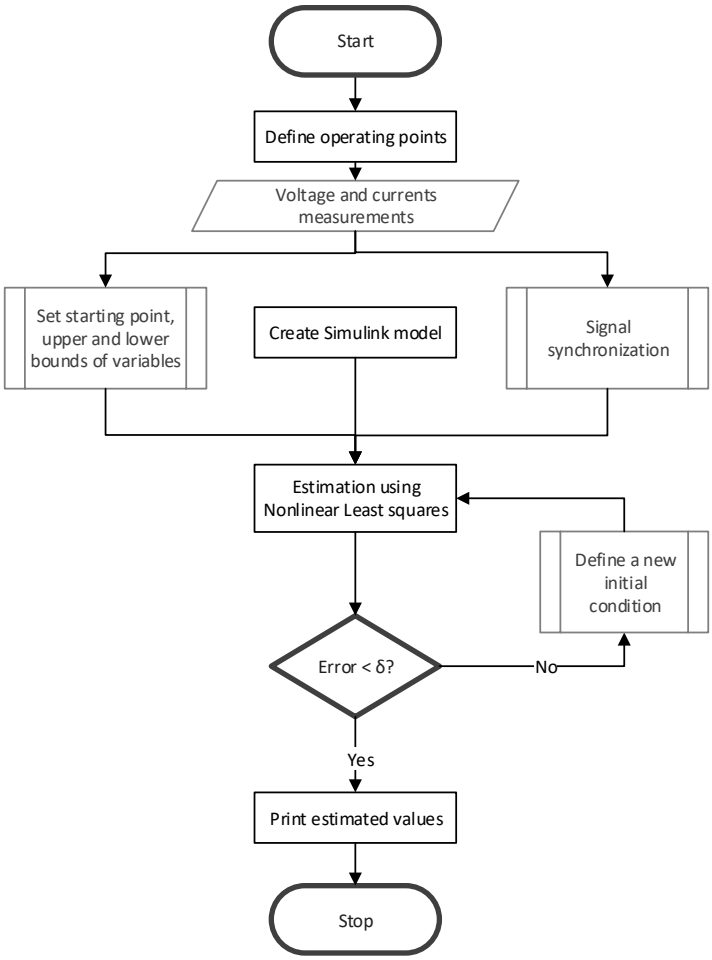

Figure 2.30. Parameter estimation methodology of a six-pulse rectifier based on TRRNLS.

The objective function of the TRRNLS is based on the input and output voltages and currents of the rectifier. However, it is necessary to consider the data from more than one operating point because the current flowing through the diodes changes depending on the voltage drop across its terminals. Therefore, in order to find the parameters that describe the nonlinear characteristics of a diode, different experiments with different loads at the output should be considered. The total number of experiments affects the accuracy and time that the optimization process requires to find an optimal point. The error function is calculated as follows:

$$\min_x\left(\left\|e(x)\right\|^2\right)=\min_x\left(\sum_{i=1}^{n}e_i^2(x)\right)=\min_x\left(e_1(x)^2+e_2(x)^2+\ldots+e_n(x)^2\right)$$

$$e(t)=\sum_{k=1}^{n}\begin{bmatrix}\left(V_{out}^{est}(t)+I_{out}^{est}(t)\right)_k\\-\left(V_{out}^{\exp}(t)+I_{out}^{\exp}(t)\right)_k\end{bmatrix} \tag{52}$$

where *V* and *I* refer to the output voltage and current respectively, while *n* is the total number of operating conditions considered in the optimization process. It is worth to note that the three

phase input signal is not considered in the objective function because the model of the power source is well-known. However, in the case of an unknown power source, the input signals should also be included in the objective function.

As mentioned before, the only constraints of the problem are the lower and upper bounds of the variables that are estimated during the process. Consequently, these parameters must be defined according to the topology of the rectifier and the physical knowledge about it. Figure 2.31 shows the topology of the applied six-pulse diode rectifier. There are three elements of the circuit that affect the performance of the system, which are the diode, the smoothing or output capacitor and the load. The parameters of each of these elements are described as follows:

- Diode: this is the most important element in the identification process of the rectifier. In Section 2.3.4it was mentioned that the ideal model of the diode was considered when applying the analytical equations method. However, the TRRNLS algorithm uses the exponential model of the diodes. The model of the diode determines which variables are used in the optimization process, while affecting the accuracy of the identification. The exponential model relates the diode junction voltage drop *V* and the current *I* across the diode [43]. The following equation describes the I-V characteristic curve:

$$I = I_s \cdot \left(e^{qV/(NkT_m)} - 1 \right) \tag{53}$$

  I_s being the reverse saturation current, *k* the Boltzmann constant, *N* the emission coefficient, T_m the working temperature and *q* the elementary charge of an electron. Since *q* and *k* are known constant values, the parameters to identify are *N*, T_m and I_s. In addition, the series ohmic resistance of the diode R_{diode} is also identified. It is assumed that the six diodes of the rectifier have the same I-V characteristics.

  Other diode models could be used for the estimation, such as the linear or piecewise linear model, which are different approaches. In these cases, the objective function may change.

- Smoothing capacitor: the parameter to be identified is C_{out}. However, when an electrolytic capacitor is used, the equivalent series resistance (ESR) R_C is considered in the estimation.
- Load: this estimation process considers a resistive load at the output of the rectifier. Then, the parameters to be identified are $R_{LOAD,1}, R_{LOAD,2}, \ldots, R_{LOAD,NL}$ where *NL* is the total number of experiments.

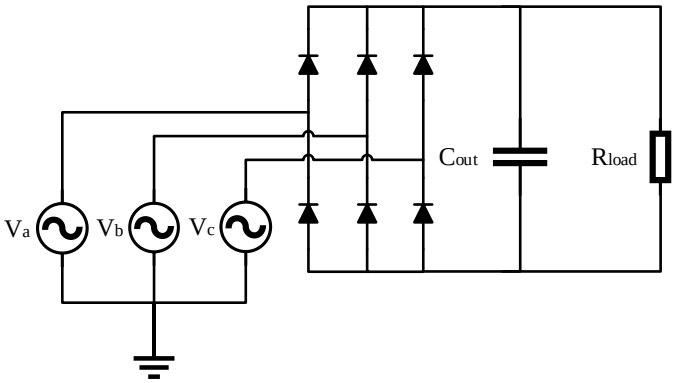

Figure 2.31. Three phase six-pulse rectifier topology.

The rectifier used to identify the electrical parameters is the commercial model SKD 30/16A1, manufactured by Semikron. It has a maximum input voltage range of 1600 V and a maximum output current of 30 A. It is worth to note that the manufacturer just provides the operating curves of the diodes at certain conditions. The rectifier receives the three-phase 50 Hz signal from a transformer with a relation of 380 Vrms / 24 Vrms. Therefore, the peak voltage of the signal that feeds the rectifier is of 40 V. Figure 2.32 and Figure 2.33 show the three phase rectifier and the system implemented in the laboratory to measure the signals, respectively.

Figure 2.32. SKD 30/16A1 monolithic rectifier [44]**.**

Figure 2.33. Experimental setup of the three-phase six-pulse rectifier.

The rectifier was forced to work under three steady state conditions, the first one by connecting at the output terminals of a 55 Ω load resistance, the second condition applying a 38 Ω resistance and the third one a 38 Ω resistance connected in parallel with the 55 Ω load resistance. After measuring and pre-processing the data, the parameters of the three phase rectifier were identified, which are shown in Table 2.8. Since the two methods consider different diode models, the estimated parameters differ.

Table 2.8. Estimated parameters of three phase rectifier

Parameter	Theoretical	Identified TRRNLS	Identified Analy. Eq.
I_S	-	1 pA	-
T_m	-	322.5 K	-
N	-	1.0985	-
R_{diode}	-	9.59 mΩ	-
V_d	< 2.2 V	-	1.2227 V
C_{out}	1000 μF	1048.7 μF	1419 μF
R_C	21 mΩ	21.6 mΩ	11.6 mΩ
$R_{LOAD,1}$	55 Ω	54.21 Ω	56.99 Ω
$R_{LOAD,2}$	38 Ω	38.6 Ω	-
$R_{LOAD,3}$	22.47 Ω	22.9 Ω	-

From the results presented in Table 2.8 it can be seen a good match between the theoretical values of the parameters and the parameters estimated using TRRNLS. The mean error of all estimations is 2.53%, which is low considering that a total of 9 parameters were estimated. On the other hand, the parameters identified by means of the analytical equations resemble to the values provided by the manufacturer, but they are less accurate than the ones obtained with TRRNLS optimization algorithm.

In order to prove the suitability of the parametric identification process performed in this section, Figure 2.34 compares the experimental and simulated values from the identified parameters of the output voltage and current under two loading conditions.

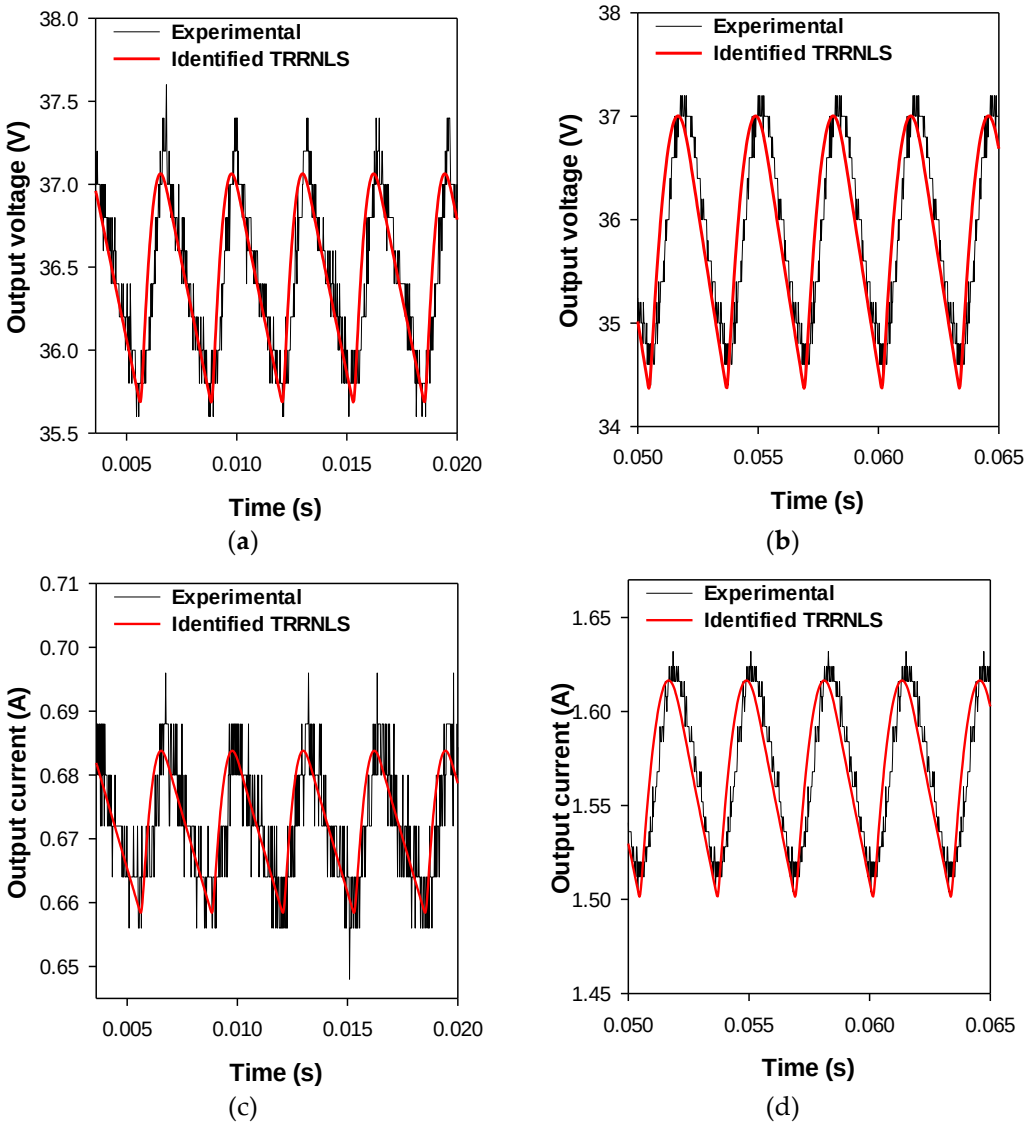

Figure 2.34. Commercial three-phase six-pulse diode rectifier with smoothing capacitor. Experimental versus simulated data using the identified parameters. a) Output voltage 55 Ω load; b) Output voltage 55//38 Ω load. c) Output current 55 Ω load; d) Output current 55/38 Ω load.

Results shown in Figure 2.34 show a good agreement between experimental and simulated results taking into account the identified values of the parameters. There is almost no visible difference between the estimation and the measurements and it can be seen that the error is less than 2%. Figure 2.35 shows the forward curves of the diodes provided by the manufacturer at 25 ºC and 150 ºC and the simulated curve that considers the identified parameters.

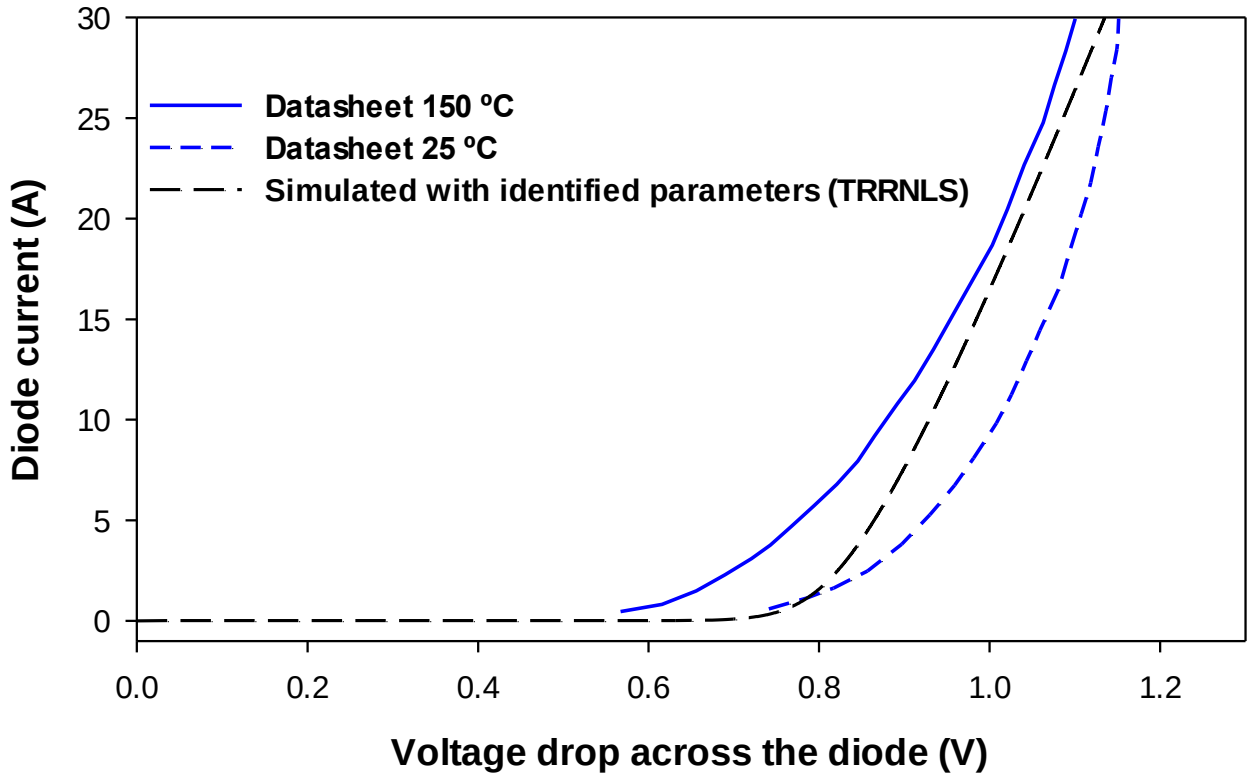

Figure 2.35. Forward curves of the diodes. Data provided by the manufacturer (25 ºC and 150 ºC) and simulated values obtained from the identified parameters.

From the results obtained and presented in the previous figures and tables, it is evident that the proposed TRRNLS algorithm is able to identify with a high accuracy the parameters of a six pulse diode rectifier. Even if the manufacturer does not provide the value of the diode parameters, the forward curve resembles the ones given in the datasheet of the rectifier. It is important to note that it is not exactly the same because the diodes were working at different temperatures.

2.6 Discussion

Section 2.5 compares the parameters provided by the manufacturer of the four converters analyzed with those identified by means of the approaches presented in sections 2.3and 2.4. Results summarized in Table 2.3, Table 2.5, Table 2.7 and Table 2.8 show a good match between the values of the parameter provided by the manufacturer and those identified by means of the TRRNLS approach. The parameters estimated in open loop show a higher accuracy than those estimated in closed loop. This also can be seen in Figure 2.21, Figure 2.25 and Figure 2.29, where there are slight differences between experimental and estimated data when a load change occurs. One of the main causes is that in closed loop the optimizer considers more parameters, thus hindering the parameter identification process. Furthermore, even if the manufacturer provides the transfer function of the control loop, there are different elements of the electronic board that may affect the transient response. Also, the TRRNLS optimization is affected by the noise present in the measurements, even when applying a low-pass filter. Finally, there are elements such as the output impedance of the voltage source and different parasitic components of the DC/DC converters, which were considered in the parameter estimation but not provided by the manufacturer which could affect the identification.

It is noted that the parameters identified using the proposed method show a greater accuracy than the ones identified by solving the analytical equations of the converters. As shown in Figure 2.21, Figure 2.25 and Figure 2.29, the TRRNLS method is able to estimate a large set of parameters that lead to an accurate representation of the DC-DC converter's transient behavior. Contrarily, other approaches in the literature are unable to make an accurate estimation of the controller parameters, where the identified values significantly differ from the ones given by the manufacturer. In addition, most approaches do not consider the input filter of the converters, since they use the current flowing across the inductor to make the estimations.

To measure the accuracy of the identification methods, Table 2.9 shows the coefficients of determination R^2 between measured and estimated data, which were calculated for the different signals estimated by the four converters. It can be observed that in all cases the values of R^2 are close to 1, thus indicating that the estimation fits the experimental data [45]. The mean value of R^2 for all the cases shown in Table 2.9 is 0.9863. This indicates that the TRRNLS methodology proposed in this thesis is able to reproduce the performance of the power converters with high accuracy.

Table 2.9. Coefficient of Determination Between Measured and Estimated Data

Converter	Operating mode	Coefficient of determination R^2			
		Input voltage	Input current	Output voltage	Output current
Buck	Steady State	0.9964	0.9998	0.9981	-
	Transient	0.9890	0.9951	0.9861	-
Boost	Steady State	0.9864	0.9902	0.9847	-
	Transient	0.9785	0.9993	0.9811	-
Buck-boost	Steady State	0.9810	0.9918	0.9792	-
	Transient	0.9749	0.9721	0.9705	-
Rectifier	Steady State	-	-	0.9901	0.9874

Table 2.10 summarizes some relevant information about the signals analyzed and the optimization process. The sampling frequency depends on the switching frequency of the converter and whether it works under transient or steady state conditions. It also depends on the used instrumentation.

Table 2.10. Sampling Frequency of The Input/Output Signals, Time Range, Time Required and Number of Iterations during the Optimization

Converter	Operating mode	Sampling frequency	Identification time*	Iterations	Load
Buck	Steady State	5 GHz	44 minutes	29	5 Ω
	Transient	1 GHz	132 minutes	45	5 + 2.6 Ω
Boost	Steady State	5 GHz	107 minutes	21	18.7 Ω
	Transient	250 MHz	111 minutes	16	18.7 + 18.7 Ω
Buck-boost	Steady State	5 GHz	112 minutes	34	8 Ω
	Transient	250 MHz	368 minutes	54	25 + 4 Ω
Rectifier	Steady State	250 MHz	51 minutes	35	55 Ω, 38 Ω

The used oscilloscope (Tektronix MDO3024 200 MHz 2.5 GS/s; Tektronix, Beaverton, OR, USA) allows a maximum sampling frequency of 5 GHz and 10^5 points per sample, which is enough to deal with switching frequencies in the range 100-500 kHz. Transient and steady state data must have the same number of data points to be compatible with the applied algorithms. Since transient data requires more periods than steady state data, we had to adapt the sampling frequency to deal with these constraints. Finally, the buck-boost converter requires more identification time, since it has more parameters than the others, thus making the identification process more complex.

3 BLACK-BOX SYSTEM IDENTIFICATION OF POWER CONVERTERS

3.1 Introduction

Black-box modeling is a useful tool for fitting experimental data (inputs and outputs) of the real system regardless of a particular mathematical structure of the model, that is, when such structure is unknown. Therefore, black-box models do not assume any particular structure of the analyzed system. The relationships between inputs and outputs are not based on physical equations as for analytical models, since they are deduced from experimental data.

These models do not assume any particular structure of the converter, so that they are able to emulate or reproduce its behavior without describing its physical equations [18] when the internal topology is unknown, so that black-box models do not require internal data of the converter. Therefore, black-box models prevent disclosure of manufacturer's confidential data [15], [16]. In addition, once the model is trained, it requires low computational burden. Black-boxes have been applied to model different types of devices, such as DC-DC converters [46], battery chargers [47] or permanent magnet generators [48], among others.

Different mathematical methods based on linear and nonlinear black-box model structures have been traditionally applied to represent the dynamics of electrical and electronic systems. These methods vary in complexity depending on flexibility and accuracy required to account for the dynamics and noise of the system under analysis. When applying black-box models, physical significance or structural information of the system is lost, since the mapping between a black-box model and the set of ordinary differential equations (ODEs) defining the behavior of a nonlinear system are not bijective or equivalent.

This unclear system representation restricts the analysis of the system to the conditions represented by the available data. Mathematical tools such as AR (auto-regressive), ARX (auto-regressive with exogenous inputs) models for linear predictions or ARMA (nonlinear auto-regressive moving average) and ANN (artificial neural network) models for nonlinear predictions can be used to model or approximate the behavior of both linear and nonlinear systems.

In particular, linear regression techniques are often more efficient than most non-linear techniques. Experimental data sets are often split in three different sets: the calibration set, which is dedicated to calibrate or train the identification procedure; the remaining data constituting the validation and test sets, which are dedicated to validate the identification procedure using data different that the used during the calibration stage [49].

This chapter presents three different black-box approaches based on neural networks. These methodologies are tested using real data that is gathered from experiments carried out in the laboratory. The results are compared to several state-of-the-art techniques and its robustness is tested.

3.2 Background

Several black-box approaches to model power converters are found in the technical literature, most of them being based on transfer functions, which are parametrized in the frequency domain. However, this approach presents several drawbacks, because of the errors due to the conversion from frequency to time domains or vice versa, or the need to use expensive measuring devices and complex tests, particularly when analyzing high power converters [16]. In [46], [50] it is presented a black-box approach based on a two-port equivalent circuit, which is parametrized in the frequency domain. The four parameters of the two-port matrix are transfer functions, which are obtained by using a high-frequency impedance analyzer. However, these works assume that the average value of the output voltage is known, which is used to build the model; only the continuous conduction mode is analyzed and the presented results are based only on two/three load conditions. A similar approach is applied in [51] and [52], where the black-box model of a three-phase AC-DC converter is obtained from frequency-domain response data. An electromagnetic compatibility black-box model of a DC-DC converter operating in open-loop configuration based on wavelet transform and support vector regression is presented in [15]. The Hammerstein model is presented in [53], where it models the non-linear and the linear dynamic characteristics separately and generates an overall transfer function based on these two models. It results in a simple and accurate model, although it is subjected to the operating point of the DC-DC converter. A black-box model based on time-domain measurements is presented in [16], which identifies the transfer function coefficients from input voltage and current steps. However, this approach requires to select a predetermined candidate transfer function and the posterior application of a suitable optimization algorithm [14]. Considering the modeling of MEA converters, in [16] a DC-DC converter of a fuel cell unit of an aircraft is modeled using a polytopic model that is based on local transfer functions of the converter [54]. It obtains the small signal G-parameter models to determine the linear response of the converter at each operating point. The results are accurate, although its efficiency is quite limited because it requires a model for each operating point. This approach cannot accurately reproduce changes from continuous conduction mode (CCM) to discontinuous conduction mode (DCM) of the converter. This method is based on an input current control, which implies that different current steps are needed, adding complexity to the experimental setup. In [55], [56] a modeling technique based on the state-space average equations of the converter is explained. It uses a known topology of the converter to generate a transfer function that is tuned with measured data.

In [29] a review of different white-box and black-box modelling techniques of SMPCs is presented. Two of the main black-box identification methods analyzed are the Hammerstein and Steiglitz IIR

models, which perform a real time estimation based on an external excitation applied to the duty cycle of the SMPCs [57]. Although these approaches allow replicating the SMPC black-box model, they are complex, time consuming and of limited robustness. In [58] a terminal characterization of a DC-DC converter is presented by generating a model based on the frequency response functions of the converter, which are acquired by means of a network analyzer. Despite its accuracy, the model cannot replicate the DCM of the converter, while requiring expensive equipment to measure the signals.

Neural networks (NN) have been used lately to identify and estimate different variables of electrical systems. For example, in [59] a parameter fault detection of DC-DC converters is performed by using NNs. They are also used to estimate the remaining useful life (RUL) [60]. In [61] a traditional recursive neural network (RNN), specifically a nonlinear autoregressive exogenous neural network (NARX NN), is used to identify the behavior of a DC-DC buck converter. Although this method provides accurate results, it is time consuming, as it trains more than 100 NNs. RNNs are typically applied to time-series because their architecture is a cyclic connection that allows the RNN to update the actual state using the information from past states and training data [62]. Another approach is based on feed-forward wavelet artificial neural networks (WANNs), which apply a wavelet transform to the input signals to extract time-frequency features [63]. WANNs are mostly used in classification and fault diagnosis problems that deal with multi-frequency time-series [64].

In [65] an identification method based on recursive neural networks is presented. However, it fails to replicate with high-fidelity the behavior of the converter and it just uses data gathered from simulation. However, the hyper-parameters are not optimized, the ripple of the signals is not estimated and the immediate transient response is not replicated with accuracy. The authors of [66] propose a dynamic system identification method of a DC-DC bidirectional converter used in automobiles. It is based on three different techniques, each one being applied in a certain condition of the converter. It uses the state space averaging method, which is also applied in [67] to obtain the model of a buck converter. Although the error obtained is very low, it was just tested under the buck mode, and the operating point of the converter must be known in order to apply one of the three techniques. In [68] the authors use neural networks for predictive control and fault diagnosis of power converters, respectively. However, a model that replicates the behavior of the converter is not obtained.

3.3 Problem definition

First of all, it is necessary to define the main characteristics of a DC-DC power converter in order to explain how the NN is used to generate the corresponding model. Considering that there is no prior knowledge about the internal structure of the converter, the only accessible information are the measurements at the input and output terminals, which are the voltages and currents. Since the proposed methodologies aim to model the static (ripple) and dynamic characteristics of the converter, the sampling frequency needs to be higher that the commutation frequency of the converter. A deeper explanation regarding the DC-DC power converters and its data acquisition system is given in the following sections.

The inputs of the black-box are the input voltage and output current, because these are the variables that can be controlled externally by changing the voltage input level or the output load, respectively. Whereas, the outputs are the input current and output voltage. Consequently, the modeling of the power converter is considered a regression problem, since it aims to generate two numeric and dependent output variables as a function of the inputs. The length of the data is determined by the number of points recorded in the measurements. The NN depth and its hyper-parameters are adjusted based on the dataset characteristics, as it is described in the following subsections. The data used to train the NN is organized in three different groups, i.e., training, validation and test datasets. The first two ones are used for the training process and the last one to test the accuracy. Each dataset has a certain number of experiments, each experiment consisting of a load change. Figure 3.1 shows the experiments corresponding to the different datasets.

After the NN is trained, the RMSE and the R^2 are calculated for different operating conditions of the converter and their mean value is calculated. A value of R^2 equal or similar to 1 is pursued, since it indicates a strong correlation between the measurements and the model output.

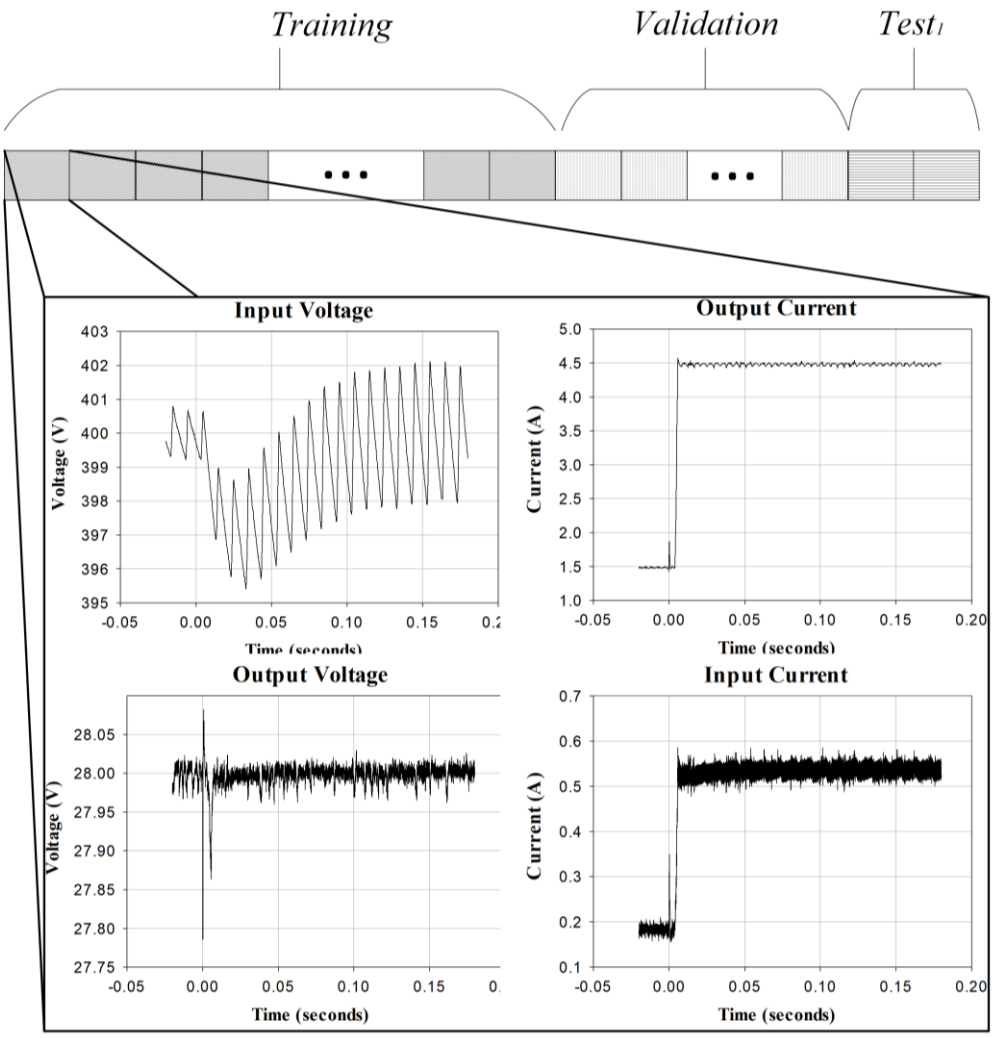

Figure 3.1. Distribution of experiments (training, validation and test).

3.4 Non-linear Autoregressive Exogenous Neural Network (NARX-NN)

Nonlinear systems are usually defined as any system which is not linear, i.e., it does not satisfy the superposition principle [32]. Most systems encountered in the real world are nonlinear in nature, but linear models cannot capture the rich dynamic behavior associated with nonlinear systems. It is imperative to have identification techniques which are specific for nonlinear systems. A recurrent NARX NN (or NARX-RNN) arises as a solution for the identification of a black-box system performance. It can predict the output of a nonlinear system based on the expansion of past inputs and outputs. The model depends on the configuration of the system, and it can be defined either by one of the two following equations [70]:

$$y(t) = f_N[y(t-1),\ldots,y(t-n_a),u(t-1),\ldots,u(t-n_k)] \tag{54}$$

$$y(t) = f_N[y(t-1),\ldots,y(t-n_a),u(t-1),\ldots,u(t-n_k)] \tag{55}$$

where $y(t)$ and $\hat{y}(t)$ refer to the black-box actual and simulated outputs (autoregressive) respectively, $u(t)$ is the system input (exogenous variable), n_a refers to the number of output delays and n_k the number of input delays [71].

The two architectures of the NARX-RNN system, defined by equations (54) and (55), depend on whether or not the output feeds-back the actual output information. The first one is the open loop (or series) architecture, which is mostly used for designing and training the neural network, because it uses *a priori* target information (known) to estimate the output of the system (predicted). On the other hand, the closed loop architecture uses the actual estimated output as an input of the black-box, so there is no need to have the target data beforehand, which is useful for predictions [71]. Figure 3.2 shows both architectures.

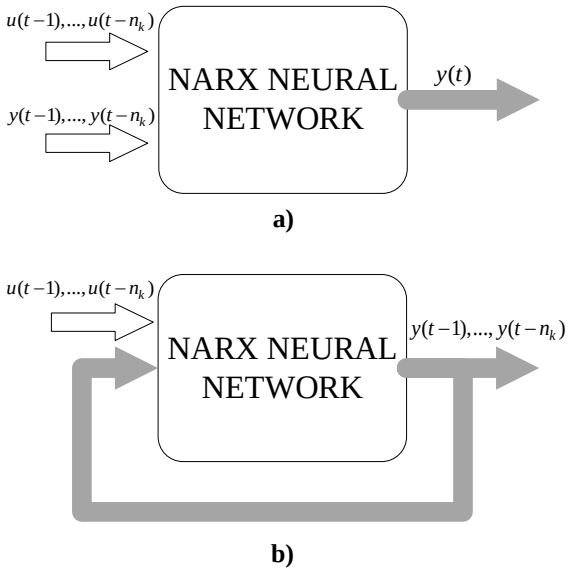

Figure 3.2. NARX architecture in a) Open loop and b) Closed loop.

The structure of a neural network consists of one input layer, one output layer and several hidden layers, whose number is difficult to determine, and depends on the type of problem, so it may change depending on the application and the nature of the input data.

The NARX model is essentially an expansion of past inputs, outputs, and a noise term. The functional description of an actual system can be very complex and the explicit form of this functional is usually unknown. Therefore, the practical modeling of real signals must be based upon a chosen set of the unknown functions. For example, a NARX model as,

$$y(i) = -a_1 \underbrace{y(i-1)}_{x1} - a_2 \underbrace{y(i-2)y(i-3)}_{x2} + b_{11} \underbrace{u_1(i-3)u_1(i-2)}_{x3} + b_{12} \underbrace{u_1(i-1)u_1(i-2)}_{x4} + b_{21} \underbrace{u_2(i-3)u_2(i-2)u_2(i-1)}_{x5} + e(i) \quad (56)$$

Leads to

W_i = [-y(i-1),-y(i-2)y(i-3),u_1(i-3)u_1(i-2),u_1(i-1)u_1(i-2),u_2(i-3)u_2(i-2)u_2(i-1)]^T with dim =(5,1)

P = [a_1,a_2,b_{11},b_{12},b_{21}]^T is the vector of parameters with dim= (5,1)

Processes with nonlinear dynamics often offer challenging difficulties to obtain accurate results using classic autoregressive methods. Alternative methods based on neural networks (NN) are being used for this purpose. NN-based approaches can deal with the nonlinear processes based on experimental data. Figure 3.3 shows a three-layer feed-forward neural network, since, in general, three layers are sufficient, although to improve convergence during the learning process

additional hidden layers can be required at the expense of increasing the computational burden [72]. The basic structure, having one hidden layer with sigmoid function, is known to be powerful enough to produce an arbitrary mapping among variables [73].

Figure 3.3 shows the series-parallel architecture of the NARX neural network. It means that the output is considered also as an input but with a certain delay specified by the user. This is particularly beneficial for training datasets where the output is well known. It gives more precision to the training and the resulting network is purely feedforward, and the common algorithms of training networks can be used. Another advantage is that the time it takes to train the network is less. After training the network, it needs to be converted to a parallel configuration (closed loop) in order to predict step-ahead outputs of the system considering a set of input values.

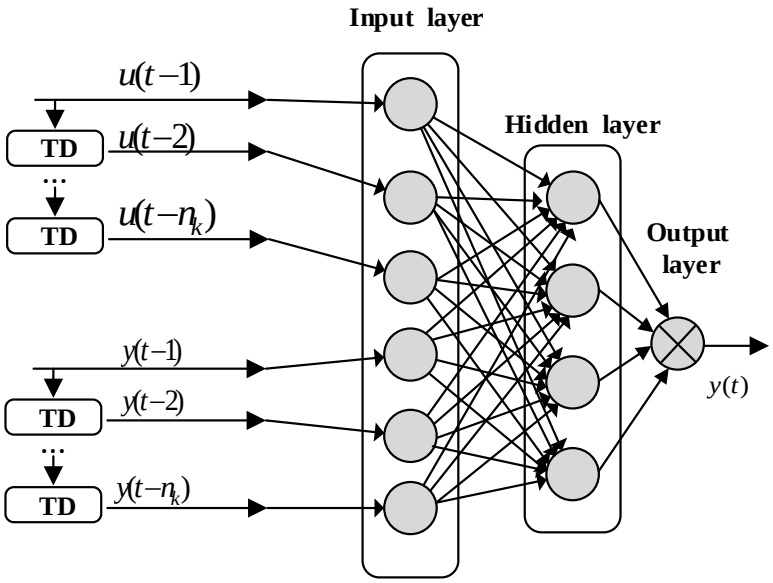

Figure 3.3. The structure of a neural network NARX model with a hidden layer. TD: Tapped Delay.

The mapping function of the neural network depends on the inputs and outputs of the net and when it has a series parallel configuration (open loop) the function is the following:

$$y(t) = f_N[y(t-1),...,y(t-n_a),u(t-n_k),...,u(t-n_k-n_b+1)]+e(t) \quad (57)$$

Equation (57) differs from equations (54) and (55) since it introduces the moving average variable or white noise e(t), i.e. $E_t[e(t)]=0$ and $E_t[e(t)e(t-i)]=\delta_i\sigma_a^2$, where n_a and n_b, refer to the autoregressive and exogenous orders, respectively.

The following steps explain the calculation of the NN output based on the input vector.

- Step 0: Before starting the calculation of the weights in the neural network, it is important to normalize the input and output variables.
- Step 1: Assign $w^T(i)$ to the input vector $x^T(i)$, where $w^T(i)$ is the data vector given by (29). $w^T(i) = [y(i-1), y(i-2),\dots y(i-n_a), u(i-n_k), u(i-n_k-1),\dots, u(i-n_k-n_b+1), e(i-1), e(i-2),\dots, e(i-n_c)]$. The initial values of e (-1), e (-2) … and e(-n) are set to zero.
- Step 2: Calculate the input of the hidden (h) layer units as,

$$net_j^h(i) = \sum_{k=1}^{p} w_{jk} x_k(i) + b_j^h \tag{58}$$

  $p = n_a+n_k+n_c$ being the number of input nodes of the network, j is the j-th hidden unit, w_{jk}^h is the connection weight between k-th input unit and j-th hidden unit and b_j^h is the bias term of the j-th hidden unit.
- Step 3: Calculate the output from a node in the hidden layer $z_j = f_j^h[net_j^h(i)] = f[\sum_{k=1}^{p} w_{jk} x_k(i) + b_j^h]$ where f_j^h can be a sigmoid function defined by

$$f_j^h[net_j^h(i)] = \frac{1}{1+\exp[-net_j^h(i)]}$$

- Step 4: Calculate the input to the output nodes as, $net_l^o(i) = \sum_{m=1}^{h} W_{lm}(i) z_m(i)$, where l is the l-th output unit, $W_{lm}^o(i)$ is the connection weight between m-th hidden unit and l-th output unit.
- Step 5: Calculate the outputs from the output nodes as, $zz(i) = f_l^o[net_l^q(i)]$, where f_l^o is the linear activation function defined by $f_l^o[net_l^o(i)] = net_l^o(i)$

From the previous algorithm, it can be seen that the process to calculate the output of the neural network depends on the weights assigned to the connections. Therefore, it is fundamental to choose an iterative algorithm that calculates the weights of the neural network, because an incorrect estimation of these weights may lead to an inaccurate prediction of the output value by the black-box model.

3.4.1 Levenberg-Marquardt algorithm

The Levenberg-Marquardt algorithm, also known as the damped least-squares method [74], is applied in this thesis to train the dataset and to find the weights of the neurons. This algorithm works specifically with loss functions in the form of a sum of squared errors, which is the case of this problem, when the target and the estimated data are compared. The criteria used to choose the algorithm was the computational time required in the training stage, which is the lowest

amongst other existing algorithms [74]. Considering equation **¡Error! No se encuentra el origen de la referencia.**, the error function and the objective function are the following,

$$e_i(t) = y_i(t) - y_i(t) \tag{59}$$

$$Obj = \sum e_i(t)^2, i = 0,1,...,m \tag{60}$$

where *m* is the number of outputs of the neural network. The algorithm works with the gradient vector and the Jacobian matrix of the loss function expressed in the equation (60). These elements are calculated according to the equations shown below.

$$J_{ij}(w) = \frac{de_i(t)}{dw_j} \tag{61}$$

$$\nabla f = 2J^T \cdot e \tag{62}$$

The term *e* is the vector including all error terms. Finally, the Hessian matrix is estimated and the new weights of the system are chosen as presented in the equations below.

$$H \approx 2J^T J + \lambda I \tag{63}$$

$$w_{i+1} = w_i - \left(J_i^T J_i + \lambda_i I\right)^{-1} \left(2J_i^T e_i\right) \tag{64}$$

The parameter λ refers to the damping factor, which ensures that the Hessian matrix is positive definite [74]. This parameter is adjusted at each iteration, and when the loss function decreases, the damping parameter also decreases; this enables an acceleration in the convergence to the minimum. Figure 3.4 depicts the process of the Levenberg-Marquardt algorithm to find the new weights of the neurons and their connections.

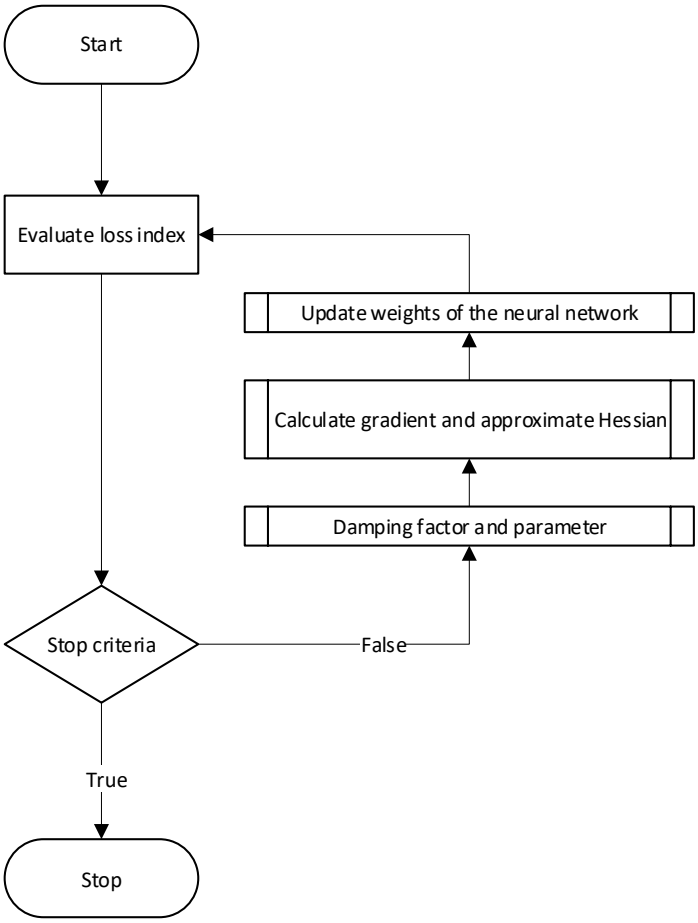

Figure 3.4. Levenberg-Marquardt algorithm to estimate weights of the neural network.

The stopping criteria depend on the minimum error, minimum gradient, maximum training gain, maximum number of epochs and maximum validation failures. These values are set depending on the dataset to be trained. The main drawback of the Levenberg-Marquardt algorithm is that for big data sets and networks, the Jacobian matrix is significantly big, so it requires a significant amount of memory.

3.4.2 Training algorithm

It is difficult to know *a priori* the exact configuration of a NARX-NN that fits the black-box dynamic characteristics, because it depends on different parameters of the dataset. Thus, a training algorithm is needed in to obtain a NARX-RNN that suits the characteristics of the problem and predicts the values of the output variables based on the input variables of the model. Figure 3.5 shows the flowchart of this algorithm.

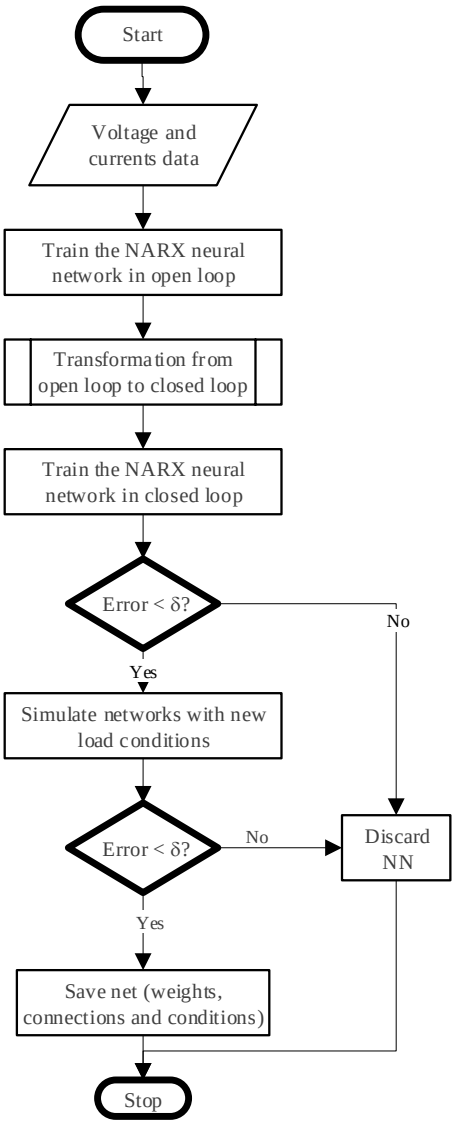

Figure 3.5. Training algorithm of a NARX-NN.

It is important to state the specifications of the measured data because they determine the accuracy and effectiveness of the training algorithm. The data set must consider different load scenarios in order to cover all the space of possible outputs. In addition, the time step must be the same for all sets of values. Interpolation is required when the time step is not constant.

Many neural networks were tested by varying their parameters, and the one with the lowest error was chosen. The parameters and their importance in the neural network are described as follows,

- Number of delays: this is the parameter that defines the number of previous time steps to be considered in order to calculate the present value of the output variables. It directly affects the time required to train the network since it adds inputs to the black-box.
- Number of neurons in the hidden layer: it results difficult to determine the exact number of neurons of the hidden layer, leading to a trial and error process. It greatly depends on the

architecture and parity of the network [75]. Furthermore, the computational time required to train the model is lower with neural networks with a small number of neurons, which is desirable for this work.

- Length of the dataset: it is one of the most important parameters because too low or too large number of points may lead to underfitting or overfitting, respectively. It is noted that each point represents a time step of the signal. The dataset consists of *n* number of experiments, where each experiment presents a load change.
- Training ratio: this parameter determines the percentage of the dataset that is designated for training, validation and testing. If the training ratio is x%, the validation and test percentage corresponds to $(100 - x)/2\,\%$. This value tends to change with the length of the dataset.

3.4.3 Buck converter

First of all, the type of converter chosen to perform the experiments and train the neural networks is the buck converter (step-down converter). It consists of a DC/DC power converter that steps down the voltage (or steps up the current) from the input (supply) to the output (load) [26]. Figure 3.6 presents how the buck converter is modeled as a black-box.

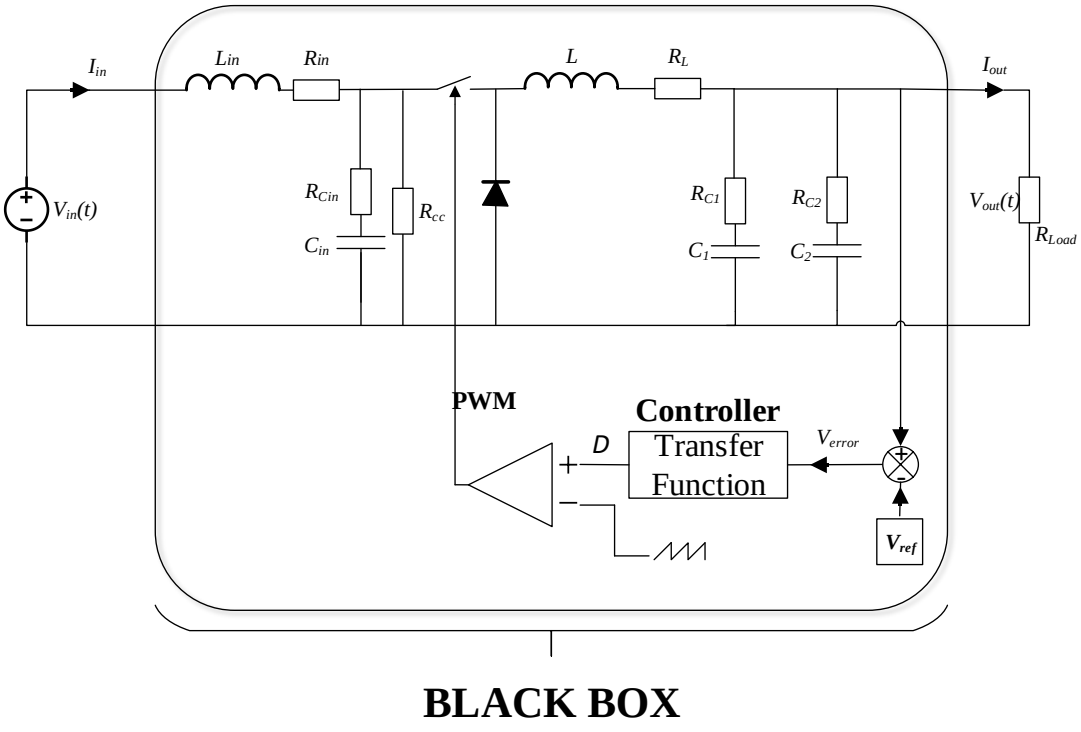

Figure 3.6. Black-box model of the buck converter used to test the NNs.

Considering that the input voltage and the output load may change every experiment and that the number of experiments should be considerable, the acquisition of the experimental data was automated and controlled externally using a computer. The general scheme of the acquisition system is shown in Figure 3.7.

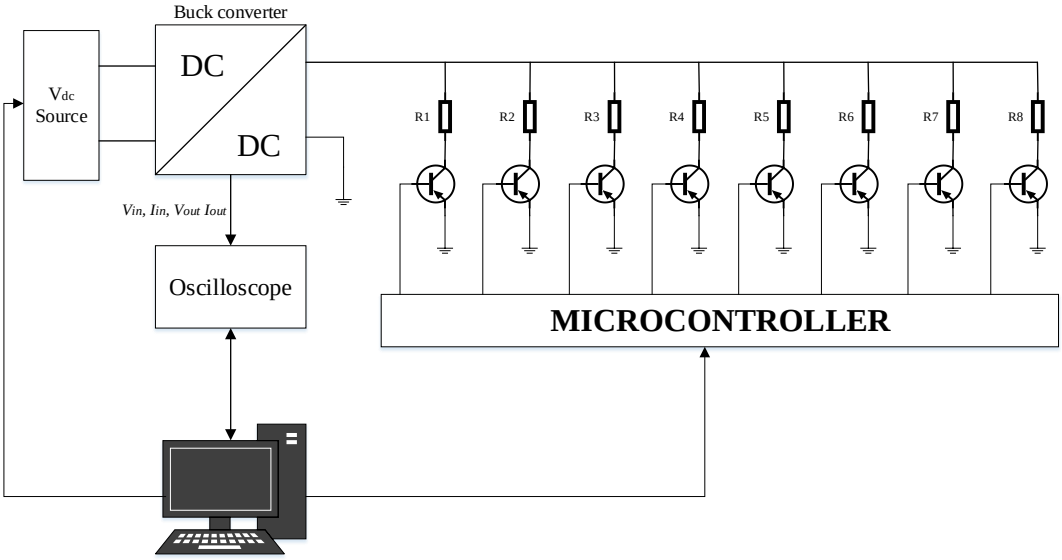

Figure 3.7. Data acquisition setup of the analyzed buck converter.

Since there was no availability of an electronic load to do the experiments, the output load consists of eight resistors that are connected in parallel, each being connected to a transistor that switches them on or off according to the signal received from an Arduino microcontroller. This microcontroller, at the same time, receives the instructions from a computer. The voltage source is also controlled externally by the computer, so that the voltage delivered to the buck converter depends exclusively on the received signal. The oscilloscope acquires the electric signals of the converter depending on the configuration (scales, coupling, trigger) of the measurement that is given from the computer for each experiment, and the measured data is sent to the computer and stored.

The data acquisition system was programmed using Python. For the case of the output load, the output voltage, the minimum and maximum currents, and the resistors connected to the converter are introduced as inputs in the code. Then, a configuration of the resistors is chosen randomly, assuring that the equivalent resistance is within the limits $V_{out}/I_{max} < R_{eq} < V_{out}/I_{min}$. The computer sends the configuration to the microcontroller, which sends the signals to switch on or off the transistors associated with each resistor. It is important to recall that each experiment considers a load change, then the total number of possible experiments is of $2^8 \times 2^8 = 65536$. The voltage provided by the voltage source is controlled by the computer using a code

programmed in Python. For each experiment, it generates a random DC voltage within a range that is specified in the code.

The used converter was the commercial nonsynchronous DC/DC buck converter model TPS40200EVM-002, manufactured by Texas Instruments. Figure 2.15 and Table 2.1 present the circuit board and the specification of the converter, respectively. The experimental setup in the laboratory is shown in Figure 3.8.

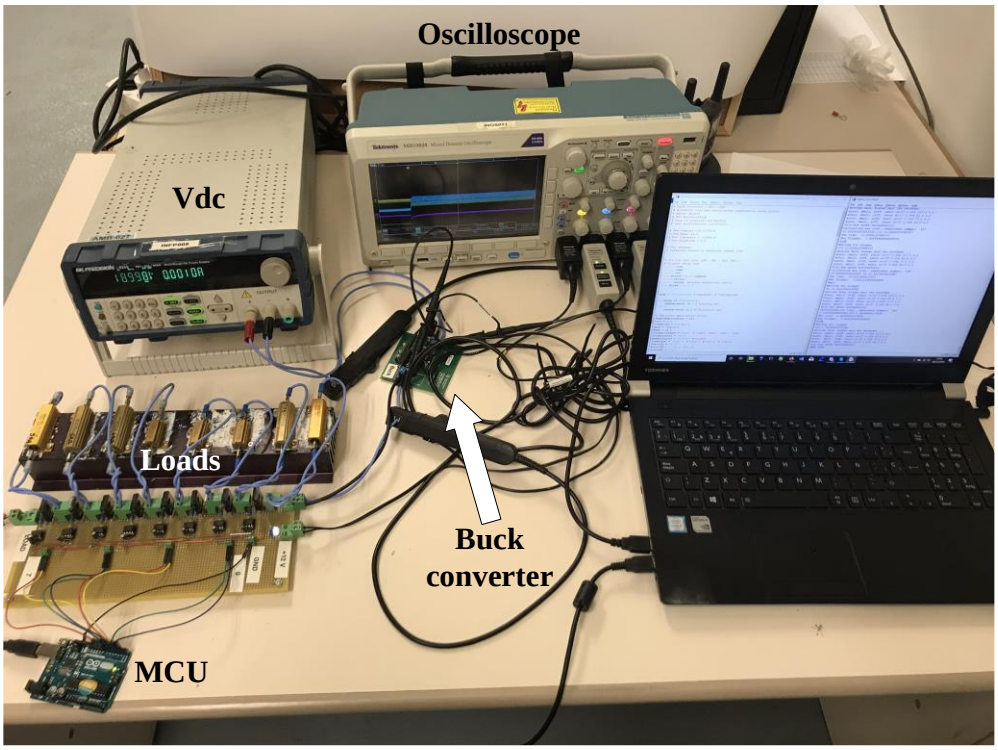

Figure 3.8. Experimental setup of the buck converter data acquisition

The data was measured with the following equipment: DC power supply (Figure A.2); four channel oscilloscope (Figure A.2); two high-frequency current probes (Figure A.2) and two high-frequency voltage probes (Figure A.2). Figure 3.9 presents the data acquired from one experiment where a load disconnection occurs at the output of the buck converter. It can be seen that the transient response and the ripple of the signals are acquired properly.

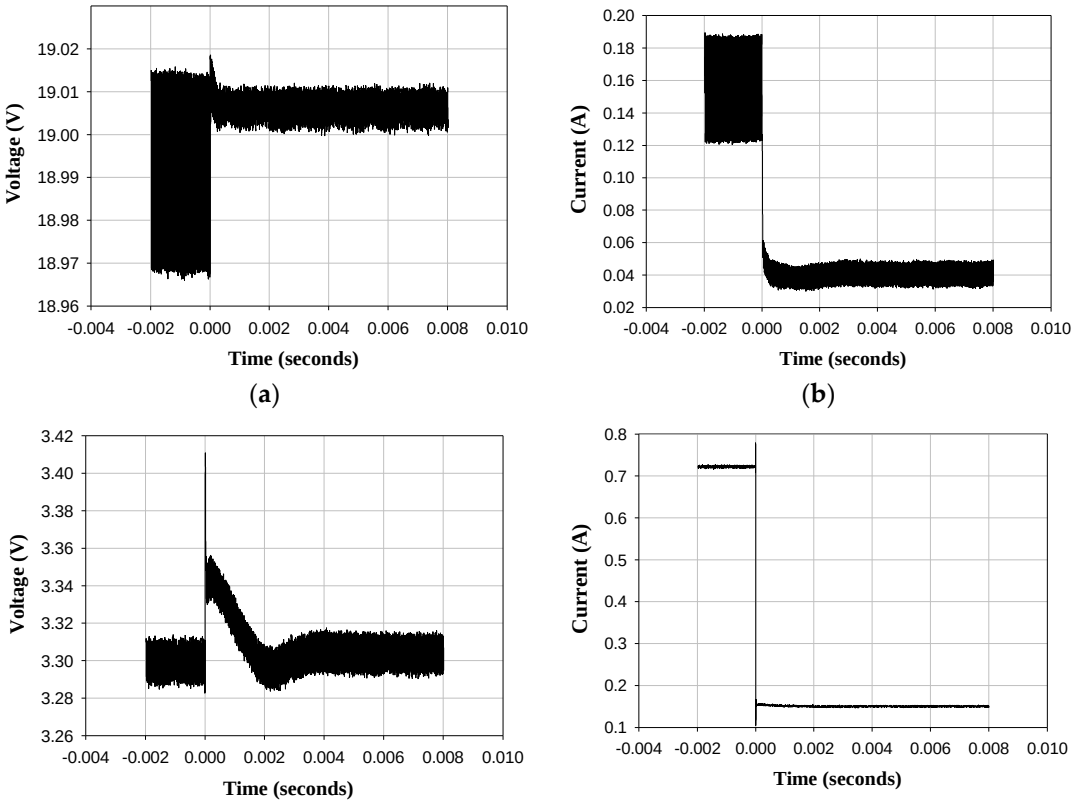

Figure 3.9. Commercial DC-DC buck converter measurements per experiment. (a) Input voltage, (b) Input current, (c) Output voltage and (d) Output current

3.4.3.1 Testing the method

After obtaining a rich dataset of the input and output variables of the black-box model, the next step is to specify the fixed and changing parameters of the neural networks to be trained. For this particular case, the hyper-parameters of the NARX-NN are tuned using a grid search algorithm. It trains various NARX-NNs by varying the hyper-parameters in each operation. The neural network with the lowest RMSE is chosen. The delays are fixed and the varying parameters are the number of neurons, length of the dataset and the percentage assigned to training, validation and test. Table 3.1 shows the aforementioned parameters.

Table 3.1. NARX NN grid search configuration

Parameter	Value
Maximum number of epochs	1000
Maximum time	3 hours
Minimum error	1e-7
Maximum number of validation failures	6

Neurons in the hidden layer	5, 6, 7, 8, 9, 10, 14, 20, 30
Length (number of experiments)	100, 120, 140, 150, 160, 180,200, 210, 220, 230, 240, 250
Training ratio (percentage)	40, 45, 50, 60, 65,70, 75, 80. 85, 90, 100

A total of 176 NARX-RNN were trained, requiring four days of computation, using an Intel Xeon CPU E5-1650 v2 @3.5 GHz, which means an average simulation time of 45 minutes per network. In open loop configuration, all networks were trained so that the error value was below 0.0001, calculated as the root mean square error (RMSE). However, after the transformation to closed loop, the error increased and just seven of them (3.98% of the proposed neural networks) presented an RMSE value below 0.001.

Considering the neural networks with the lowest error, there is not a clear relationship between their training parameters. The only clear conclusion that may be derived from the training of the 176 networks is that the ones with more neurons (more than 10) failed to reproduce correctly the target values of the variables, thus providing a relatively high error. In addition, the error value of the neural networks trained with more than 230 points and less than 140 points was higher due to overfitting and underfitting, respectively. On the other hand, there is not a clear pattern regarding the training ratio, mainly because it is strongly related to the length of the training dataset.

To determine the neural network that best approximates the performance of the buck converter, the networks were tested under a new set of load values. Ten new load profiles were simulated, as the one shown in Figure 3.9. For the ten cases, the outputs of the neural networks and the estimated outputs were compared to the ones obtained from the Simulink simulations. The network that best fitted the ten scenarios consisted of 10 neurons in the hidden layer and was trained with 200 experiments and a training ratio of 50%, thus obtaining a RMSE of $2.15 \cdot 10^{-4}$. The structure is shown in Figure 3.10.

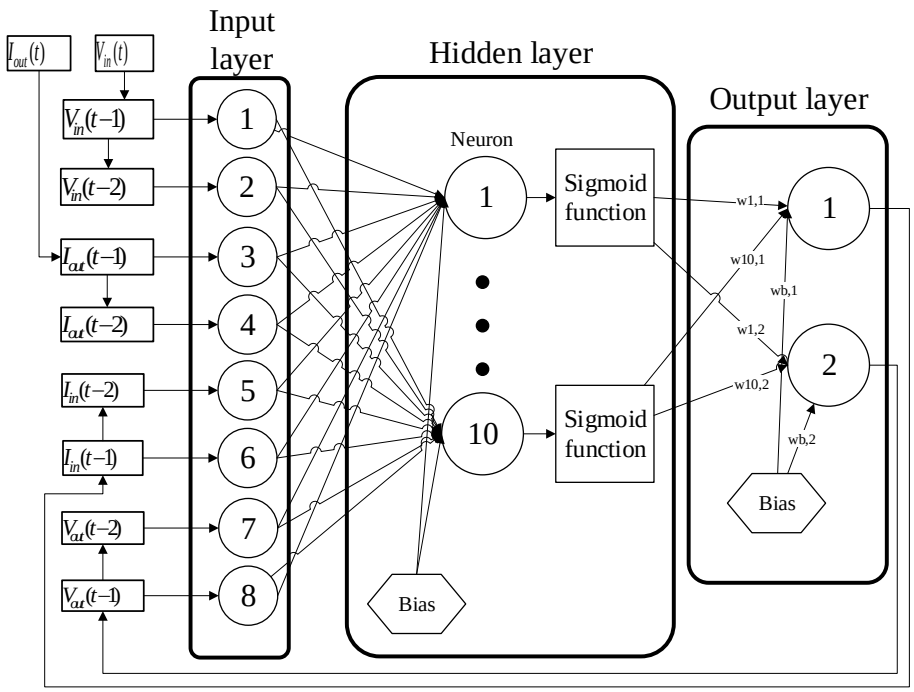

Figure 3.10. Resulting NARX NN.

Since the ten tests have multiple load conditions and 2 million of points each, it is necessary to focus on the steady state and a load change in order to compare the actual and estimated output values. Figure 3.11 shows the estimated and simulated outputs when the load is set to 1.204 Ω (steady state) and Figure 3.12 shows the comparison when there is a load change from 1.204 Ω to 0.791 Ω (transient state).

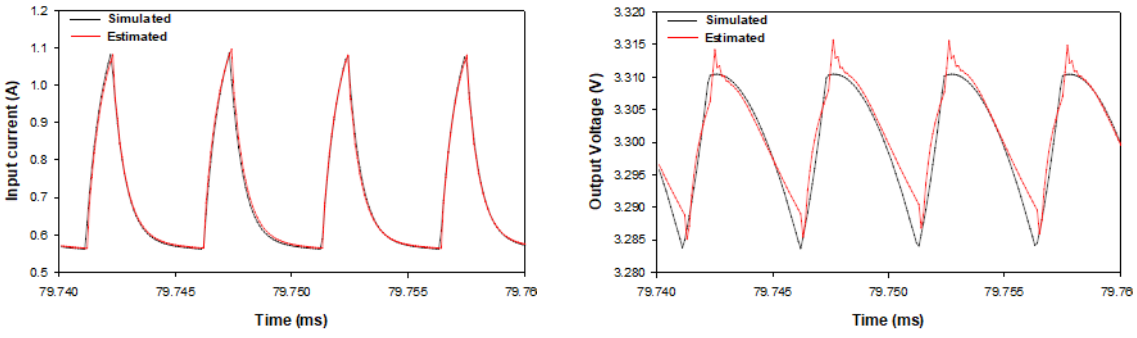

(a) (b)

Figure 3.11. Actual and estimated response in steady state. a) Input current. b) Output voltage.

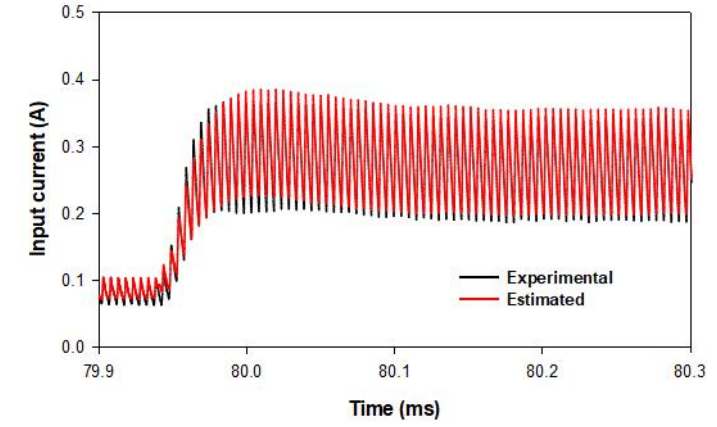

(a)

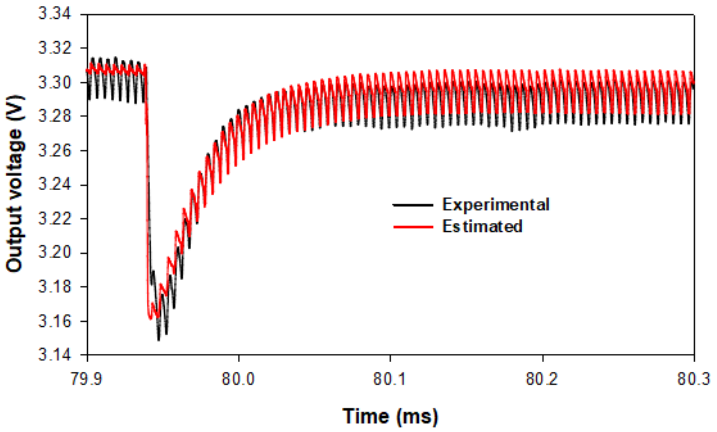

(b)

Figure 3.12. Actual and estimated response during a load change. a) Input current. b) Output voltage.

Figure 3.11 and Figure 3.12 show a significant resemblance between the measured and the curves predicted by the NARX-NN. This is just one of the 250 experiments where the net was tested after the training. To have a better understanding of the trained NARX net accuracy, the coefficient of determination R^2 between measured and estimated data was calculated for the 250 test experiments. Table 3.2 and Figure 3.13 show the results.

Table 3.2. Coefficient of Determination R^2 for the 250 Test Experiments

Variable	$\overline{R^2}$	$min(R^2)$	$max(R^2)$
I_{in}	0.9876	0.9464	0.9967
V_{out}	0.9815	0.9322	0.9938

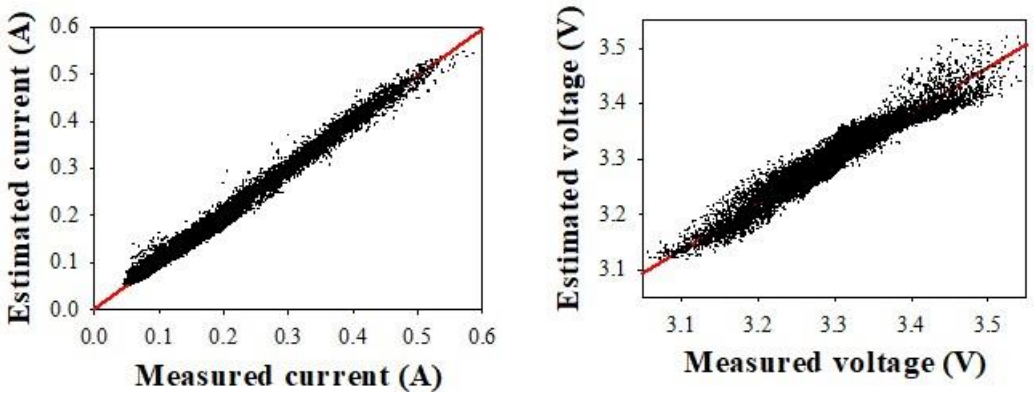

(a) (b)

Figure 3.13. Scatter plot between measured and estimated data. a) Input current; b) Output voltage.

From the results presented above it is evident that there exists a good correlation (R^2 is close to 1) between the measured and estimated data when the dataset is tested with new operating points.

3.5 Convolutional Neural Networks (CNN)

The basic CNN framework was first introduced in [76] to recognize hand-written digits by using back-propagation networks. One of the main characteristics of CNNs is that the information only flows from the inputs to the outputs [77] and there are no feedback connections as occurs with the RNNs. CNNs allow reducing the total number of parameters to be learned using a weight sharing approach [78], thus reducing the computational effort. CNNs are used primarily in image classification problems by applying filters to the input data, which are represented by numerical matrices. The convolution operation applies the filter to the input data to produce an output. The user defines the number of layers based on the requirements and specifications of the problem. The main difference between CNNs and other types of NNs is the number of connections between adjacent layers. This implies that only the closest nodes of one layer are connected to the next. This approach is more accurate than classic NNs and identification methods, thus allowing the detection of patterns in the images that are generally not identified [79].

Figure 3.14 shows a basic representation of a CNN, where the input is a set of images (or videos) to be trained and the output is a set of numerical values assigned to the image. In general, CNN includes three main parts, i.e., the input, hidden and output layer [80]. The most important is the hidden layer, because it determines how the NN generates an output based on the input values, so it is necessary to define an appropriate architecture for this layer. The hidden layer of the CNN consists of multiple sequential sublayers connected to each other. The depth of the network (number of sublayers) depends on the complexity of the problem. The typical structure includes a set of convolutional and pooling layers, and a fully-connected layer that generates the output values, as seen in Figure 3.14.

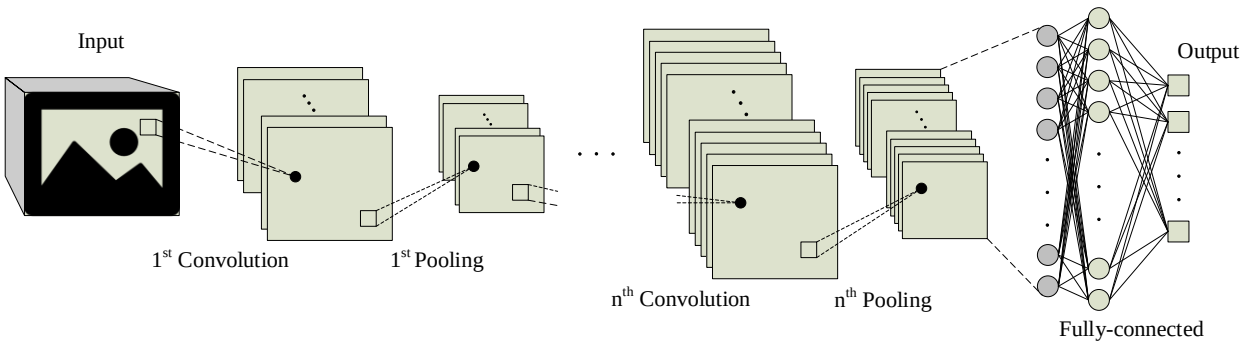

Figure 3.14. Convolutional neural network architecture.

To define the architecture of CNNs, it is important to review the different types of layers that could be included in the network:

- Convolutional layer: it is the most important part of the CNN, as it extracts the relevant features from the input images [77]. Typically, the input is a two dimensional object (for example an image) or an array. The weights applied to these matrices are called filters or kernels. The following equation describes the process that takes place in this layer:

$$C_k = W_k * x \tag{65}$$

  where C_k refers to the convolution between the feature map considered W_k and the input image x, whereas the k term refers to the feature map number [77]. The filters of a convolutional layer are used to extract a feature map of the input data to detect the strength and relevance of a certain part of this data. The size and number of filters determine the characteristics of the output feature map obtained after the convolutional layer. The number of filters and their size is often selected according to the size of the input dataset.
- Pooling layer: the main goal of this layer is to reduce the computational effort by decreasing the size of the spatial dimension data. It removes irrelevant data of the NN training process while retaining the useful information, thus increasing training speed. This occurs because pooling layers reduce the resolution of the feature maps obtained in convolutional layers by propagating the maximum (Max pooling) or average (average pooling) value of a feature set, this step helping the NN to extract the important details of a feature map [77].
- Fully connected layer: it receives the abstract representation of the input data from the convolutional or pooling layers. It uses different operators to generate accurate output values [77].

There are vital operations applied within the hidden layer, which are important to get an accurate result during CNN training and to enhance training efficiency. One of them is related to the activation function, whose main purpose is to avoid divergence problems. It changes the output value of the convolutional layer, thus ensuring a range of values that depends on the selected function. The most relevant activation functions are the sigmoid, hyperbolic tangent, rectified linear unit (ReLU) and Maxout, although the ReLU activation function is the most widely applied in CNNs. This layer can be described as,

$$Y_k = f\left(C_k\right) \tag{66}$$

where C_k is obtained from (1) and Y_k refers to the k^{th} output of the activation layer.

A batch normalization is also performed. It reduces the internal covariate shift during NNs training [82] and normalizes each input channel across a mini-batch during the training stage. According to [83], the batch normalization is based on calculating the mean and the variance of its inputs, and normalizing, shifting and scaling the activations. The mathematical expression that represents the normalized activations is as follows,

$$\widehat{x_i} = \frac{x_i - \mu_B}{\sqrt{\sigma_B^2 + \varepsilon}} \tag{67}$$

x_i being the input, μ_B the mean of the inputs, σ_B^2 the variance of the inputs and ε an added term to improve numerical stability. Then, the output of the batch normalization layer is calculated as follows,

$$y_i = \gamma \widehat{x_i} + \beta \tag{68}$$

γ and β being the scale and the offset factors of the normalization, respectively. These parameters are updated at each iteration during the training process.

3.5.1 Architecture

This section defines the CNN architecture to best suit the nature of the problem. Considering that the black-box NN to be identified consists of a DC-DC power converter, the inputs and outputs of the CNN are defined as follows:

- Inputs: they represent the variables that can be controlled externally by the user, which are the input voltage (V_{in}) and the output current (I_{out}) of the step-down converter. The second one is controlled by changing the output load. Despite the fact that the input voltage is not controlled externally, it is treated as an input, because its response to a load change is useful to predict the transient part of the output variables.
- Outputs: the output variables of the CNN are the input current (I_{in}) and output voltage (V_{out}) of the converter.

The inputs and outputs of the CNN are time-series with constant time steps. This determines how the data are entered into the neural network and how the output values are generated. Since the CNN does not accept sequential data in the hidden layers, a data transformation like the one shown in Figure 3.15 is required. Figure 3.15 shows how the input data are transformed into a 3D object, where the *x*-axis refers to the time vector of the measured data, the *y*-axis represents the features or input variables (input voltage and output current) and the *z*-axis depends on the total

number of experiments. This transformation is applied during the training process, and thus, the *z*-axis is not considered when predicting the output of a single experiment when the network is already trained. The data transformation performed at the output of the neural network is the same shown in Figure 3.15, but in the opposite direction.

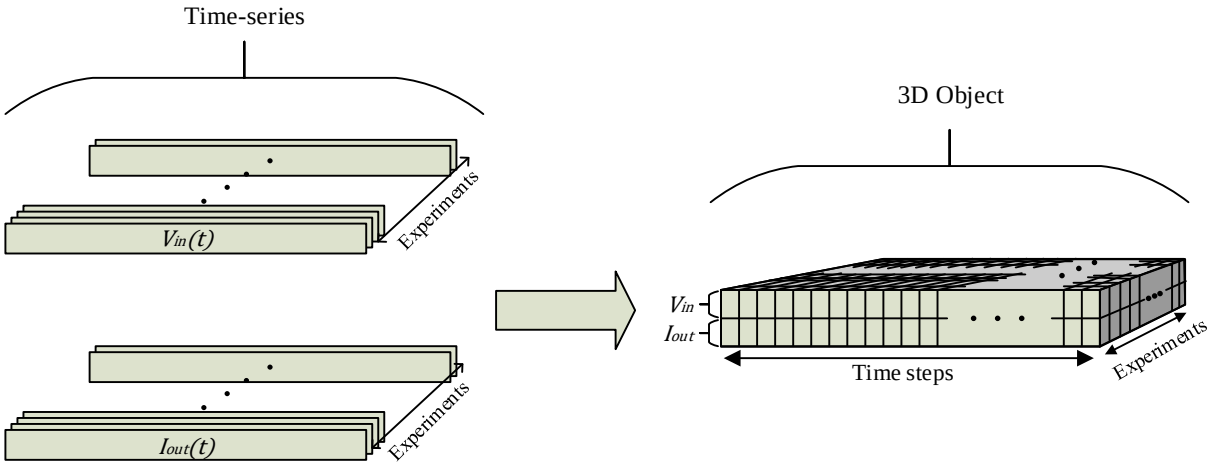

Figure 3.15. Data transformation from time-series to a 3-D object.

Figure 3.16 summarizes the proposed architecture. The input layer is represented by the object generated after applying the data transformation explained above. The output layer consists of an object that is transformed into two time-series variables. Figure 3.16 shows that the hidden layer has a total of six layers, which are divided into two convolutional layers, two pooling layers, a fully connected layer and a regression layer.

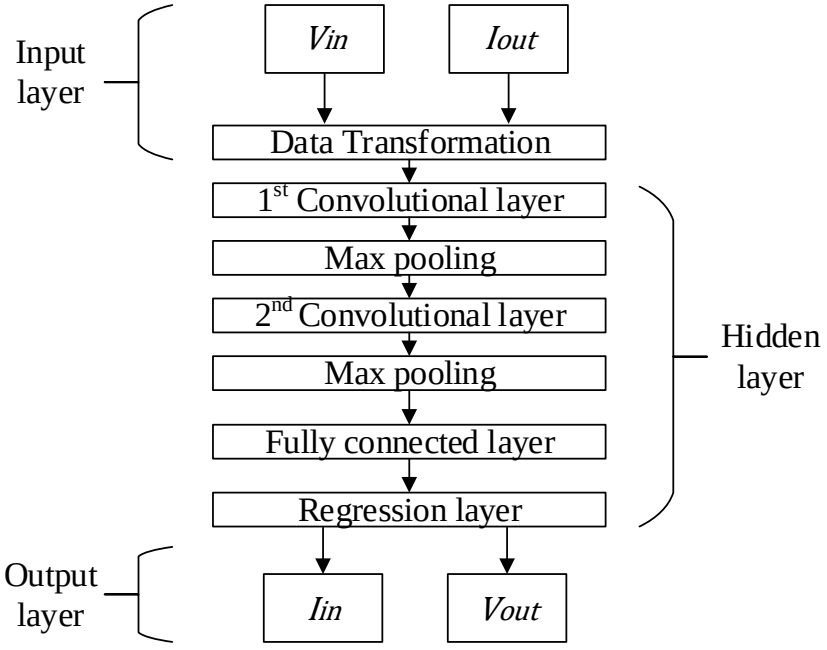

Figure 3.16. Proposed architecture of the CNN.

The number of convolutional layers was determined by training CNNs with different number of layers. The configuration offering the best balance between accuracy and computational burden was the CNN with two convolutional layers. The max-pooling layer was selected instead of the average pooling layer because it offers better performance [77].

The dimensions of the batch normalization layer are given by the parameters of the previous layers and the size of the input data. The ReLU function was selected for the activation layer. It sets to zero all negative values coming from the previous layer, thus avoiding saturation issues. This is done to ease the training stage of the NN and to increase its performance. The ReLU function is as follows,

$$f(x) = \begin{cases} x & x \geq 0 \\ 0 & x < 0 \end{cases} \tag{69}$$

A fully connected and a regression layer are included after the second convolutional layer. The length of these layers depends on the size of the convolutional filters and the Max- pooling layers.

3.5.2 Discrete Wavelet Transform (DWT)

The objective of this research is to model the steady-state (ripple) and the transient responses accurately. Thus, a wavelet convolutional neural network (WCNN) is proposed to identify the behavior of a step-down DC-DC power converter, which is a time-series problem. Because wavelets are used to obtain a multi-resolution representation of high frequency signals and CNNs are used to solve pattern recognition and classification problems, the application of the WCNN to a time-series problem allows the identification of more complex patterns in the converter signals, thus increasing the efficiency and the robustness of the proposed approach compared to RNNs. Considering the nature of switched mode power converters, which involves high-frequency switching of the transistors and low-frequency transient response, it is important to perform a system identification based on capturing all significant frequency components. If CNNs are able to learn and predict based on these components, prediction accuracy will improve [84].

The DWT is a method that extracts the multi-frequency characteristics of a time-series signal by calculating the wavelets [85]. This study aims to perform a wavelet decomposition (multilevel DWT) of the data acquired from the DC-DC converter in order to extract low- and high-frequency features. The DWT is calculated as,

$$DWT(j,k) = \frac{1}{2^j} \int f(t) \psi \left(\frac{t - k2^j}{2^j} \right) dt \tag{70}$$

where $f(t)$ is the time series signal, $\psi(t)$ is the mother wavelet, *j* is a scale coefficient and *k* the translation coefficient. A multiresolution analysis is performed to obtain the different decomposition levels of the original time-series signals, where in each level the low and high frequency components are filtered and obtained in the form of scaling and wavelet coefficients, respectively. These coefficients lead to the final result of the decomposition, which is an approximation signal (A_0) and the detail signals (D_0, D_1,…,D_n) of the raw data [85].

The Daubechies 10 (db10) was chosen as the mother wavelet since it enhances the computational speed and it is able to represent the features of the disturbances [85]. The decomposition level of the DWT was chosen based on the sampling frequency of the measuring equipment, switching frequency of the DC-DC converter and its transient response. Thus, the decomposed signals represent accurately the ripple frequency and the load change without compromising the simulation time [85].

The implementation of the wavelet decomposition of the measured data leads to a different transformation than the one presented in Figure 3.15 and to a different architecture of the CNN than the one introduced in Figure 3.16. This is mainly because the DWT transforms time series data into a frequency-based dataset. Figure 3.17 presents how the measured data is transformed into the approximation and detail signals of the wavelet decomposition and then, the decomposed signals are stacked into a 3D object that is the input of the CNN. Consequently, Figure 3.18 shows the modified architecture of the wavelet convolutional neural network (WCNN). It is seen that two layers are added to the structure and refer to the DWT at the first stage of the process and an inverse DWT at the end. The second one is used to obtain the response of the power converter in a time-series format.

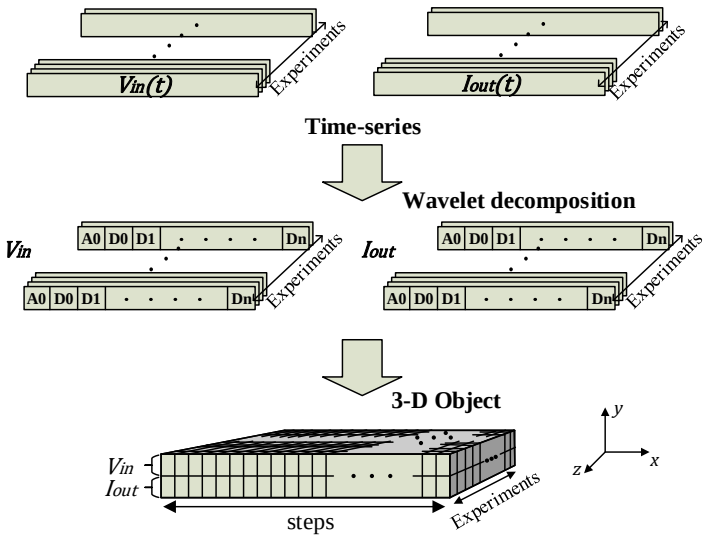

Figure 3.17. Data transformation from time-series to a 3-D object using DWT.

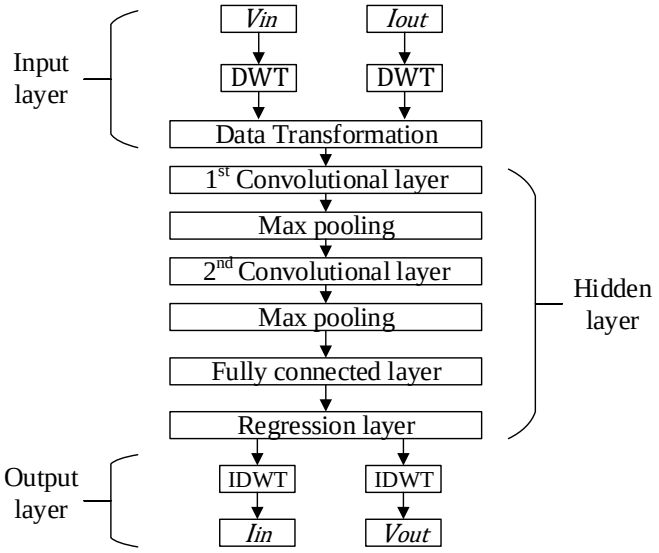

Figure 3.18. Proposed architecture of the CNN with DWT.

3.5.3 Training process

The next step consists of establishing the training procedure, hyper-parameters, dataset characteristics and simulation parameters of the neural network in order to obtain the most accurate results. The process described in this section is based on a WCNN architecture. However, it can be extended to a simple CNN without DWT by removing the stages related to the discrete wavelet transformation of the data.

The signals acquired experimentally are pre-processed by applying a low-pass filter to reduce the noise of the measurements. The next step is to normalize the values of the input and output variables. The total number of experiments must be defined and split into three different sets, which are the training, validation and test datasets. The first two sets are used during the WCNN

training process, whereas the test dataset is used to check the accuracy of the network once trained. These datasets are separated based on the measurements. It is necessary to correctly distribute the experiments among the three datasets because it directly affects the performance of the training procedure.

The Adam solver was selected. It is an extension of the stochastic gradient descent, offering good performance because it updates the weights of the neural network more efficiently than other solvers [86]. The Adam solver has more than 15 hyper-parameters. However, this section focuses only on the most important ones, i.e., the learning rate (LR), the gradient decay factor (GDF), the L_2 regularizer and the size of the mini-batch. The first two hyper-parameters are the most relevant ones because they determine how fast the algorithm moves towards the closest local minimum value of the optimization function, thus greatly impacting the NN training time. A Bayesian optimization algorithm (BOA) [87] was used to select the convolutional layer filter parameters (quantity and size) and the hyper-parameters of the training process. This method is thoroughly explained in Section 3.7.2 of this document. The BOA generates a surrogate function and reduces the problem uncertainty by evaluating the WCNN with different parameters [88]. The BOA was used to tune the values of five hyper-parameters, i.e., the learning rate, GDF, number of filters per layer, and width and height of each filter. For the L_2 regularizer, a hyper-parameter that is used to prevent overfitting, its value was set to 10^{-4}, which is typical in CNNs. The mini-batch size was adjusted to the number of experiments.

Figure 3.19 shows the general procedure to train the WCNN. There are different sequential tasks that led to an accurate training of the NN. The final outcomes of the procedure shown in Figure 3.19 are the WCNN architecture and its weights, the root mean square error (RMSE) and the coefficient of determination (R^2) of the test dataset. The RMSE and R^2 coefficients are used to assess the accuracy of the trained WCNN.

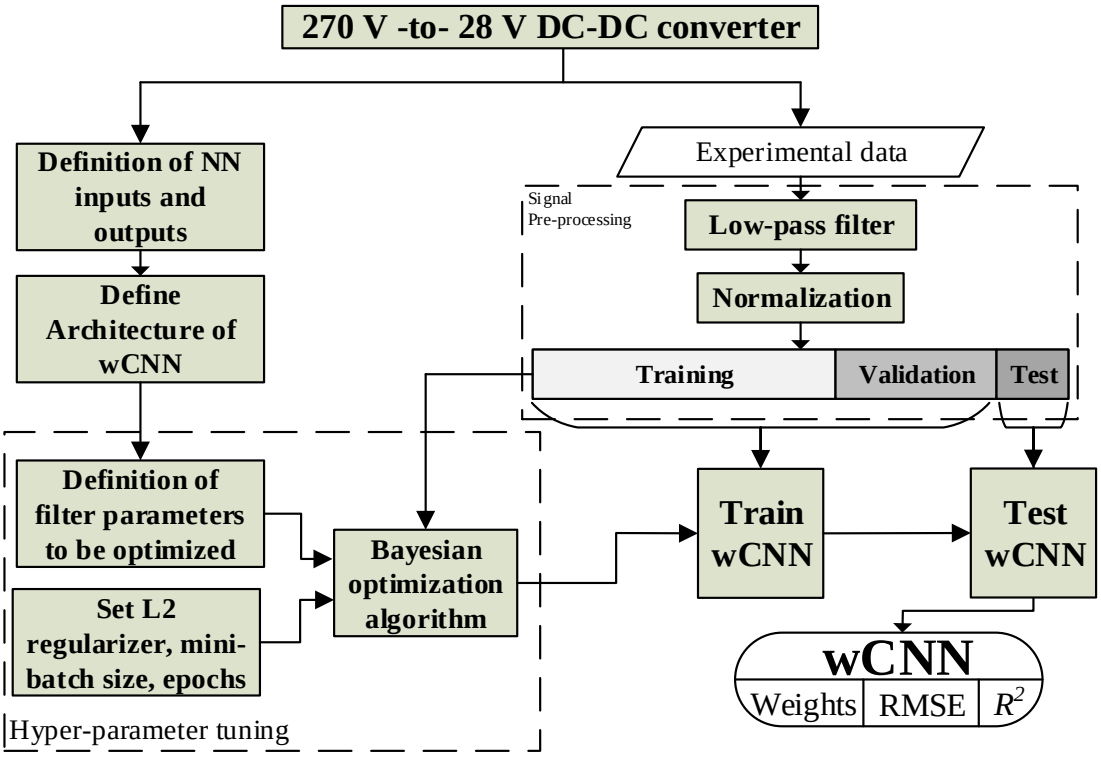

Figure 3.19. Training procedure of the CNN.

3.5.4 270 V to 28 V step down DC-DC converter

DC distribution systems of More Electric Aircrafts consist of several motors, power electronics devices, batteries, constant power loads (CPL) and others [89]. The high voltage (HV) DC bus usually operates at 270 V, whereas the low voltage DC bus operates at 28 V [90]. Therefore, the DC-DC converter to be identified in this subsection is an aeronautic step-down converter, where the input voltage is 270 V and the output level is 28 V. The loads are modeled as CPL, which result from connecting a resistive load to a DC-DC power converter.

Figure 3.20 shows the schematic of a typical on-board distribution system of an aircraft. It can be seen that the signal generated by the synchronous generator (G) is rectified to a DC signal with a voltage level of 270 V. The 270 V bus feeds different loads, where one of them is the isolated and regulated DC-DC converter. This converter represents the black-box to be identified by using the training algorithms explained in the previous sections. Several CPLs (DC-DC power converter with a resistive load) are connected to the 28 V bus at the output of the aforementioned converter.

The input voltage of the system is considered to be 270 V for all experiments because it is unlikely that the 270 V level undergoes considerable voltage changes [90]. The high voltage bus usually

withstands minor perturbations, which do not have a considerable impact on the performance of the converter and the on-board distribution system. Furthermore, the transient response of the control loop of the converter is faster than the time the source requires to change from one voltage level to another. Consequently, the system identification method just considers load changes, which can be due to sudden load connections or disconnections. All experiments in the dataset must contain a perturbation (load change) acquired at high resolution until the steady state in order to have an accurate training set, providing a full representation of the steady-state and transient response of the power converter.

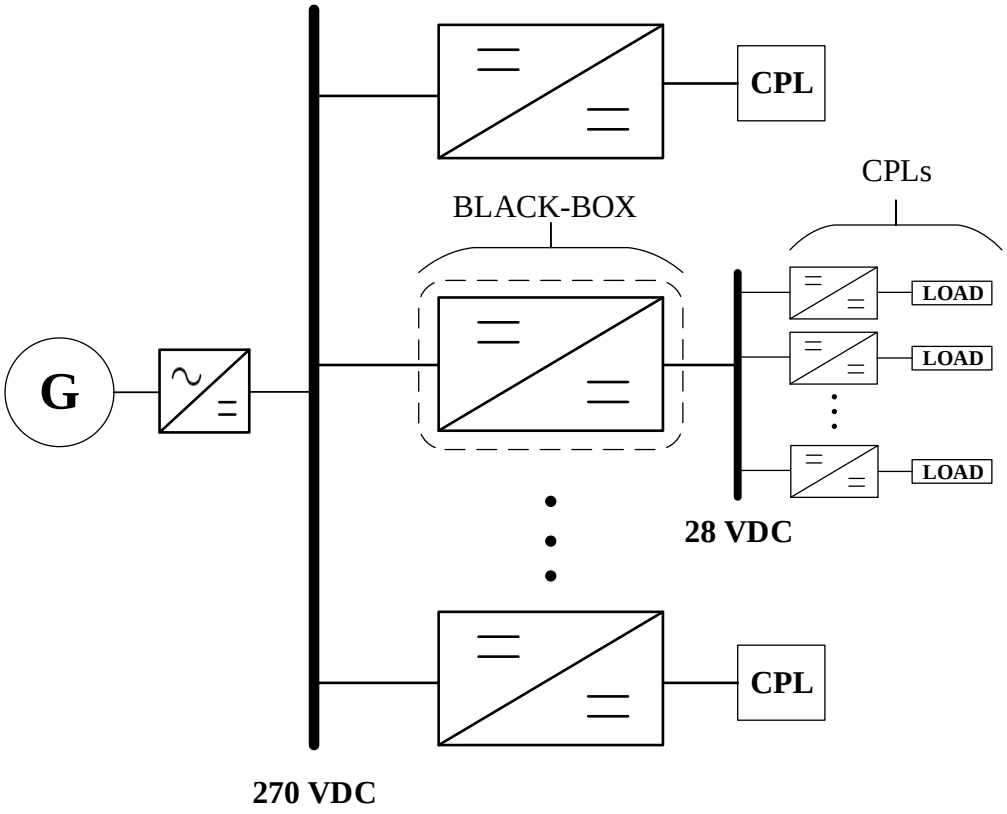

Figure 3.20. MEA on-board distribution system.

Considering that the manufacturer usually does not provide relevant information about the conduction modes of the power converter, it is not possible to know whether the DC-DC power converter is operating in continuous conduction mode (CCM) or discontinuous conduction mode (DCM). To overcome this problem, the experiments must cover a wide range of operating points of the DC-DC step-down converter, from almost no power consumption to its rated power.

As already explained, a large dataset is required to train a robust NN that is capable of representing the different operating points of the converter. All experiments must have a load change, and thus, the measuring device must acquire the whole transient response of the

converter. Figure 3.21 shows the acquisition system implemented in the laboratory. It shows the eight CPLs connected to the 28 V bus and how they are externally controlled by a microcontroller. The microcontroller sends a signal to the eight transistors, which switch their respective DC-DC converters on and off, based on the indications sent by the computer. At the same time, the computer controls the oscilloscope to acquire the electrical signals from the 270 V-to-28 V power converter. The main parameters (scale, coupling, trigger) of the oscilloscope are modified in each experiment, based on the specific features of each measurement, and they are synchronized with the signal sent to the microcontroller.

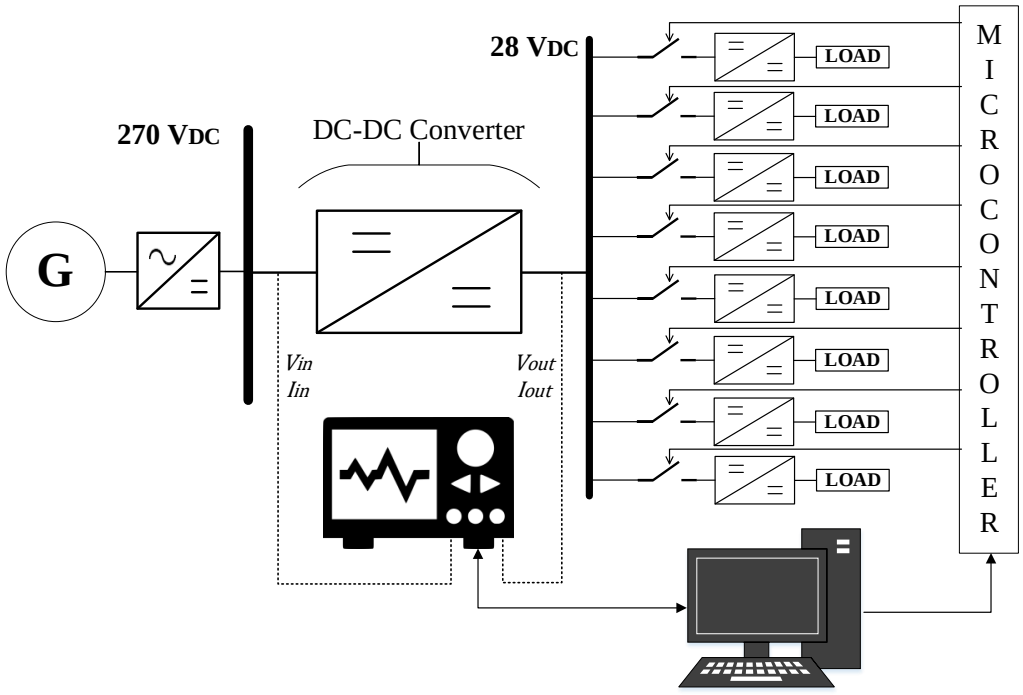

Figure 3.21. Experimental setup of the on-board distribution system.

The output load consists of eight CPLs (DC-DC converter with a resistor), which are connected in parallel. Each CPL is connected in series with a power transistor. By this way the CPLs can be switched on and off according to the signal received from the microcontroller, which is commanded by a personal computer. The voltage source consists of a 50 Hz AC signal that is rectified to 270 V-DC, reproducing the high voltage bus of the aircrafts. The voltage at the input presents a transient response when the DC-DC converter is subjected to a perturbation or a load change at the output. The oscilloscope acquires the electrical signals of the converter depending on the configuration (scale, coupling, trigger) settled by the computer for each experiment. The measured data is sent to the computer and stored. The data acquisition system was programmed using Python. The 270 V-to-28 V DCM3714xD2K31E0yzz DC-DC power converter, manufactured by Vicor and analyzed in this work, is a commercial converter already used in aircraft on-board

distribution systems. Figure 3.22 presents the packaged circuit of the converter and Table 3.3 summarizes the main specifications of this power converter.

Figure 3.22. Vicor DCM3714xD2K31E0yzz converter.

Table 3.3. Vicor DCM3714xD2K31E0yzz parameters

Parameter	Value
Input voltage	160 V – 420 V
Output voltage	27.86 V – 28.14 V
Output voltage ripple	220 mV
Rated output power	500 W
Rated output current	17.86 A
Switching frequency	700 kHz
Efficiency	90% - 93.7%

The eight DC-DC converters connected to the 28 V bus were chosen according to the voltage and power delivered by the 270 V-to-28 V converter. To realistically reproduce the distribution system, different types of converters were selected. They operate at different frequencies, have different rated powers and generate different output voltages.

Table 3.4 summarizes the basic information of each commercial DC-DC converter and Figure 3.23 shows the experimental setup implemented in the laboratory. All elements in this setup can be associated with the items presented in Figure 3.21. As can be seen, the system has a high complexity and a considerable number of elements. The equipment used to acquire the experimental data consists of a 4 channel oscilloscope (Figure A.2), two high-frequency current probes (Figure A.2) and two high-frequency isolated voltage probes (Figure A.2).

Table 3.4. 28 V bus DC-DC converters specifications

Type	Units	Reference	V_{out}(V)	P_{nom} (W)	f (kHz)	R_{load} (Ω)
Buck	2	TPS40200EVM-002 (Texas Instruments)	3.3	8.25	200	1.5
Buck-boost	2	PI3741-01-EVAL1 (Vicor)	48	150	750	30
Forward	2	MAX17599 (Maxim Integrated)	5	40	350	0.68
Flyback	2	LM5161PWPBKEVM (Texas Instruments)	12	12	300	16

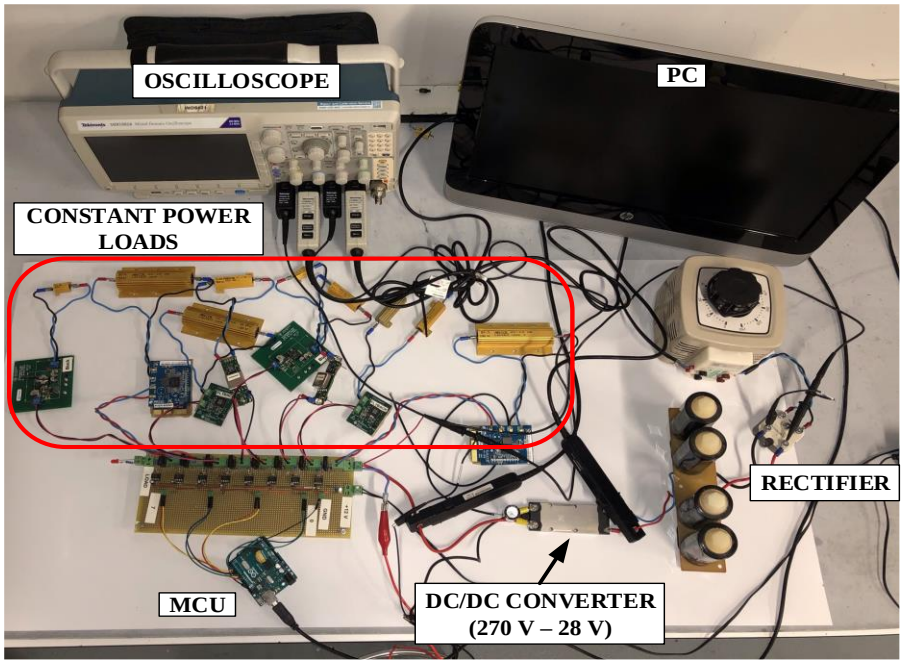

Figure 3.23. Data acquisition setup of the step-down converter.

A total of 1000 experiments were conducted, where half of them were assigned to the training set, a quarter to the validation dataset and the remaining quarter to the test set. Each experiment acquires five vectors, i.e., time, input voltage, input current, output voltage and output current. The sample frequency of each experiment was set to 2.5 MHz to ensure an optimal resolution.

3.5.4.1 Results

This section presents the procedure to design and train a WCNN and a CNN that replicates the behaviour of the step-down converter used in aircrafts. The procedure depicted is for the WCNN, since it presents the DWT as well as the training of the CNN. The results are compared to those of other approaches identified in the literature. A NARX neural network [61] and a polytopic model [54] were applied to the data obtained in the laboratory. The proposed CNN was also compared with two other types of NNs that allow solving time series problems, i.e., the long short-term memory NN (LSTM-NN) and the wavelet artificial neural network (WANN). LSTM-NN uses the current and previous states of the NN to model time-series problems with high accuracy [62]. The

hyper-parameters of the LSTM-NN (one hidden layer with 35 neurons, a learning rate of 0.04, a GDF of 0.99 and a L_2 regularization value of 10^{-4}) were tuned by using a grid search algorithm. The WANN decomposes the converter signals in different components (those with a Hurst exponent higher than 0.5, as explained in [63]) by means of a discrete wavelet transform. These components are used in the training process.

After measuring and pre-processing the data, the next step is to perform the BOA to tune the convolutional layer parameters and the training hyper-parameters. A total of 30 WCNNs were trained by selecting 500 epochs per training. Table 3.5 summarizes the values of the tuned hyper-parameters and Table 3.6 shows the fixed parameters.

Table 3.5. Hyper-parameters of the WCNN

Hyper-parameter	Minimum	Maximum	Tuned Value
Number of filters	1	15	11
Filter width	1	15	3
Filter height	1	15	10
Learning Rate	0.001	0.1	0.02661
Gradient decay factor	0.8	0.99	0.8006

Table 3.6. Training parameters of the WCNN

Hyper-parameter	Tuned Value
Minibatch size	128
Number of epochs	500
Validation frequency	15 epochs
L_2 regularization	10^{-4}
Pool size	5
Solver	Adam

Figure 3.24 shows a 3D mesh depicting the effect of the hyper-parameters analyzed in the BOA on the WCNN loss function. It shows that the lowest values of the loss function (RMSE) are achieved when the learning rate is between 0.015 and 0.04, when 10 or more filters are considered and their size (width x height) is below 50.

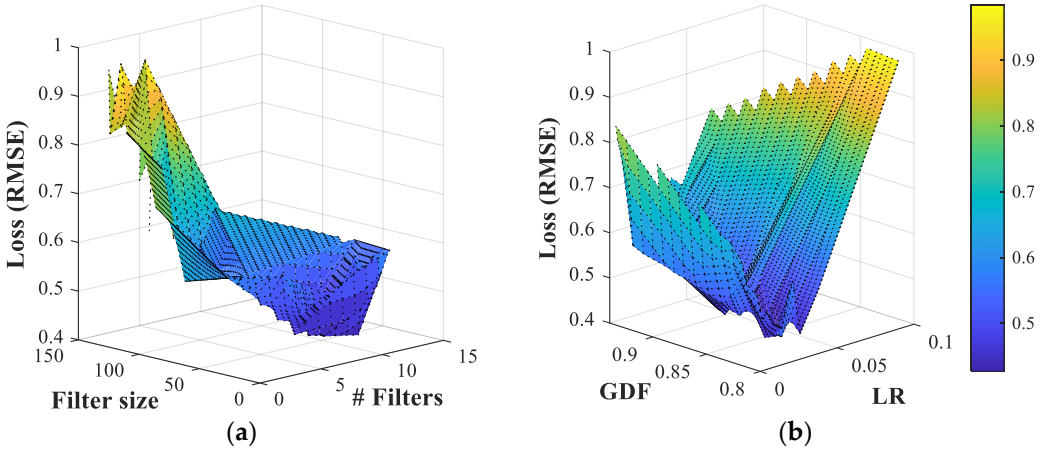

Figure 3.24. RMSE value of the BOA depending on (a) number and size of filters and (b) GDF and learning rate.

The total number of epochs was set to 3000 with a validation frequency of 15 epochs and the loss function was calculated by means of the RMSE. The training procedure was done by using the Deep Learning Toolbox of Matlab® and it was carried out by means of a GeForce RTX 2080 Super GPU.

Based on the methodology presented in Figure 3.19, the final step is to predict the output values of the WCNN from the test dataset and to calculate the RMSE and R^2 values. This dataset contains experiments that were not used during the training process. The obtained results are presented in Table 3.7, which shows that the WCNN has a greater accuracy than the other modeling approaches. The difference between the RMSE values is significant, thus proving the greater accuracy of the trained WCNN. Furthermore, the coefficient of determination of the predictions using the WCNN is around 0.99 for both variables, which is desirable for this type of problem. It is seen that by applying the DWT to the measured data, the training time is considerably reduced and the accuracy slightly increases when compared to the results of a conventional CNN. The accuracy attained with the proposed WCNN compensates for the longer training time with respect to the WANN and polytopic models.

Table 3.7. RMSE and coefficient of determination

Method	**RMSE**		**R^2**		***Time elapsed***
	I_{in}	V_{out}	I_{in}	V_{out}	
Proposed WCNN	0.0093	0.0077	0.9965	0.9956	515 s
Proposed CNN without DWT	0.0094	0.0082	0.9958	0.9931	1332 s
LSTM-NN	0.0136	0.0130	0.9854	0.9684	4092 s
WANN	0.0184	0.0145	0.9720	0.9706	205 s
NARX NN [61]	0.0202	0.144	0.9748	0.9680	9503 s

Polytopic [54]	0.217	0.198	0.9669	0.9651	57 s

Figure 3.25 shows how the WCNN and the comparison approaches replicate the output variables of the system when the converter operates under steady-state and the input voltage is set to 270 V. It can be seen that the proposed WCNN reproduces accurately the input current and output voltage of the converter, including the ripple and commutation frequency. Despite that the other compared methods can replicate the mean value of the signals, they cannot estimate the ripple and commutation frequency of the converter.

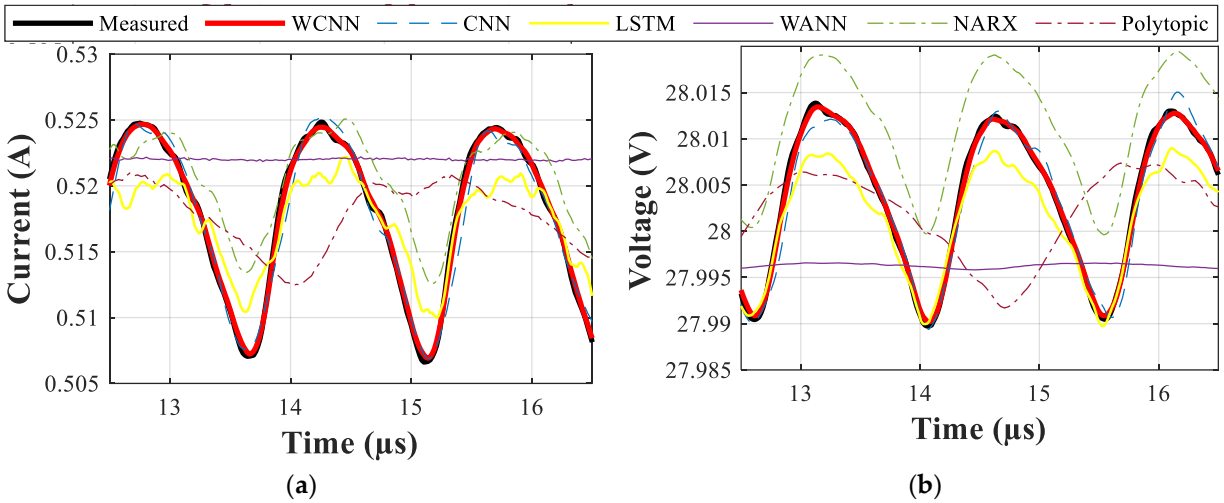

Figure 3.25. Steady state measurement and estimation of (a) Input current, (b) Output voltage.

Figure 3.26 compares the estimation and the actual output of the converter under a load connection. The DC-DC converter input voltage is 270 V and it is initially consuming 264.2 W, when a sudden load change occurs, so that the new consumption is 148.8 W. Even though Figure 3.26 shows a similar transient response between the estimated and experimental data, it is necessary to look more closely into the response of the converter just after a perturbation. Figure 3.27 compares the transient response of the converter. The CNN estimation of the immediate transient response is similar to the actual measured response, whereas the estimation made by the other methods is less accurate.

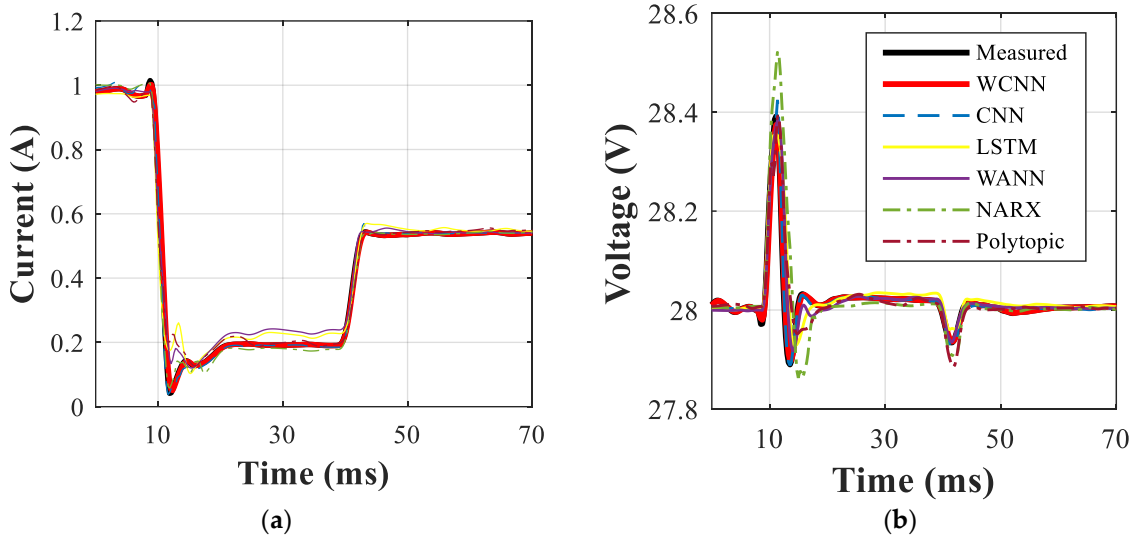

Figure 3.26. Transient response measurement and estimation of (a) Input current, (b) Output voltage.

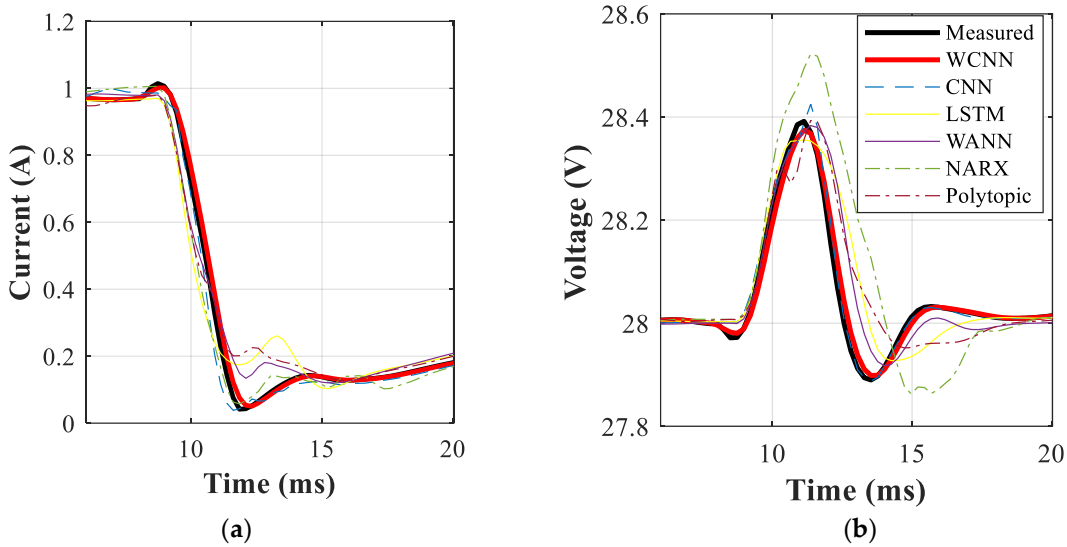

Figure 3.27. Instant transient response measurement and estimation of (a) Input current, (b) Output voltage.

Finally, the robustness of the estimations made by the WCNN is shown in Figure 3.28 by comparing the estimated and experimental values of all experiments from the test dataset. It shows a scatter plot, where the *x*-axis refers to the measured data and the *y*-axis refers to the estimated data. These graphs confirm the results presented in Table 3.7, since the predicted values show high accuracy when the WCNN is tested with new data. Furthermore, the slope for the two output variables of the WCNN is close to 1, which implies a high correlation between the estimation and experimental data. The presented results compare the robustness between the normal CNN and the one with the wavelet decomposition.

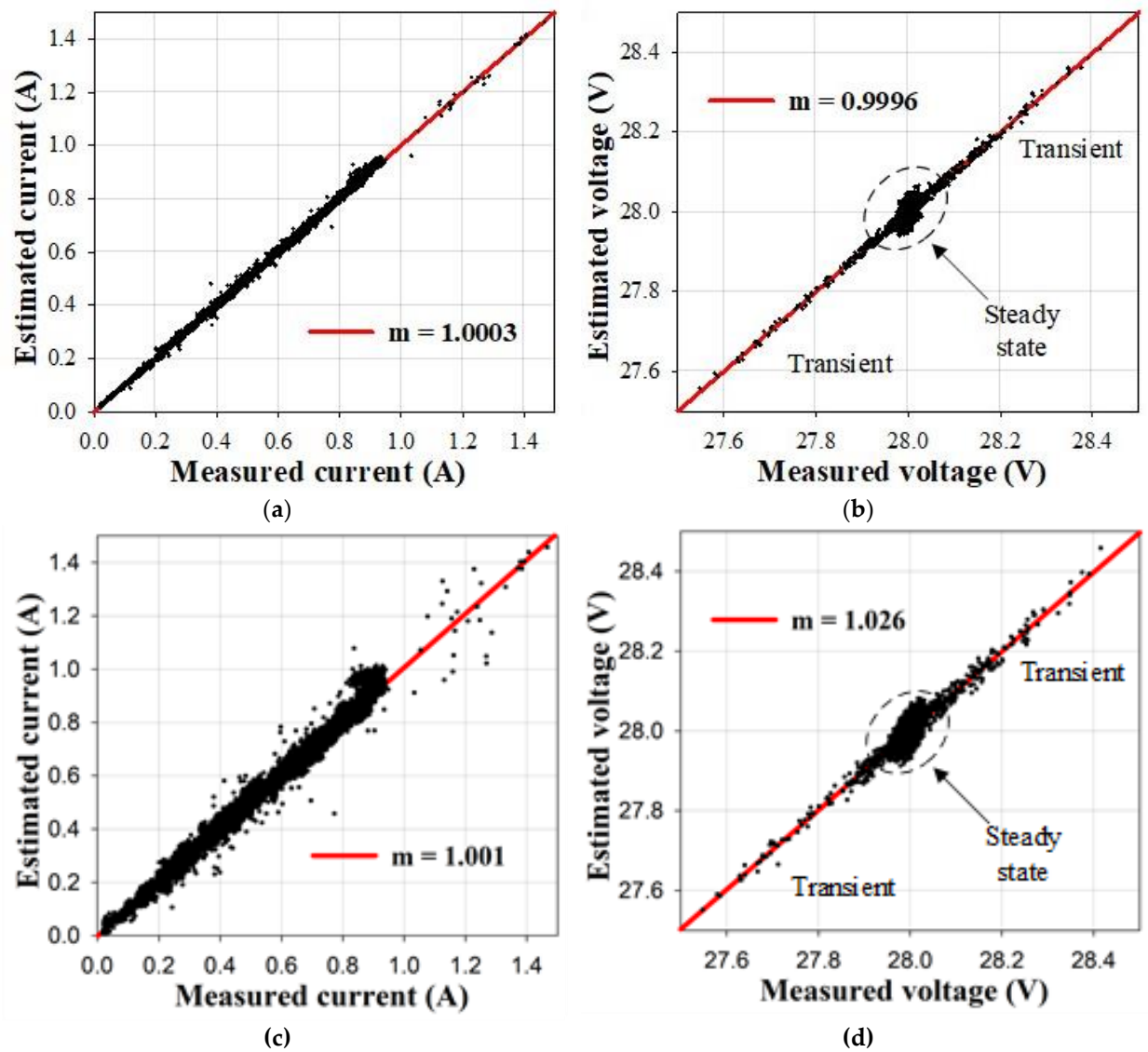

Figure 3.28. Scatter plot comparing measured and estimated signals. (a) input current estimation with DWT, (b) output voltage estimation with DWT, (c) input current estimation without DWT, (d) output voltage estimation without DWT.

These results prove that by applying a wavelet decomposition to the data, the accuracy of the CNN is enhanced while reducing the training time. It is also noted that the performance of the CNN approach (with and without DWT) is considerably better than the other strategies.

3.6 Long Short Term Memory Neural Network (LSTM NN)

In a traditional recurrent neural network, the gradient of the error function is back propagated and scaled by a factor different to unity. This implies a decay in the gradient at each iteration, leading to an inaccurate training of the network [91]. To overcome this problem, LSTM-NNs were first introduced in 1997 [92] as a necessity to overcome the long-term dependency problem, which is associated with the gradient decay that occurs in traditional RNNs. LSTM networks aim to preserve the backpropagation error across time and the layers of the RNN. It is useful because it allows the network to discard the irrelevant information for the training stage, and the weights are updated according to memory units protected from perturbations. This topology allows the NN to keep learning even if there are many time steps. A great advantage of LSTM-NNs, compared to traditional RNNs, is that they keep learning at every time step, even in case of numerous time steps.

The LSTM cell consists of memory blocks that are able to store, write, read or forget information by means of gates that open and close, depending on the corresponding weights [93]. Figure 3.29 shows the complexity of the LSTM cell when compared with a normal cell, as the ones in NARX NNs. In Figure 3.29 *h* refers to the cell value, *c* represents the cell memory state, *x* the input value and *σ* the sigmoid function. In order to understand Figure 3.29, it is important to mention that there is a module (or cell) for each step of the time series. In general, it is a chain where the future output depends on past inputs and outputs.

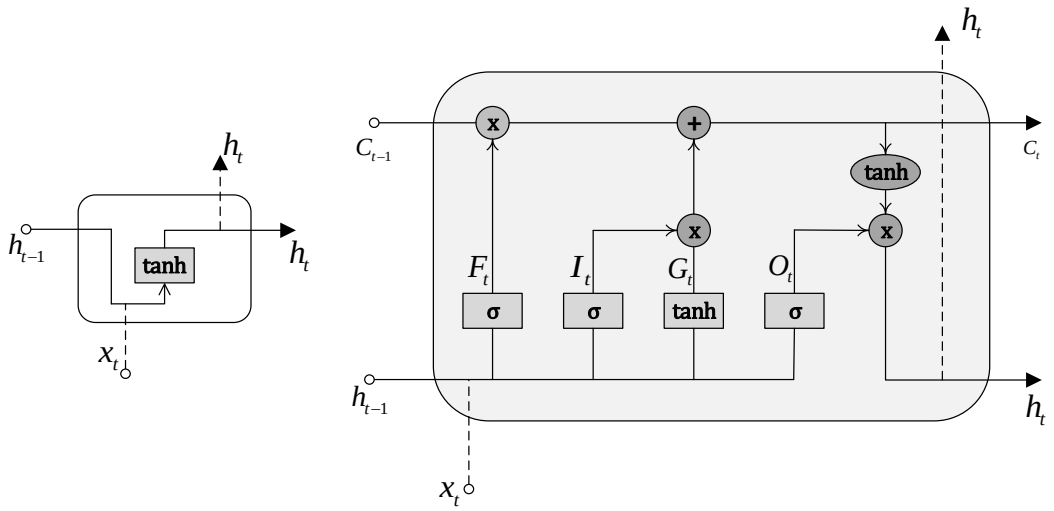

Figure 3.29. **Cell structure (a) Traditional RNN; (b) LSTM.**

From Figure 3.29 it is evident that in a standard RNN, the cell only uses one gate, which is an activation function (usually tanh). On the right side, the LSTM cell has four gates that interact

between each other. Figure 3.29 shows the input, forget, output and input modulation gates of a LSTM cell. The first three are controlled by the sigmoid function σ, and they generate an output between 0 and 1 based on the significance of the h_{t-1} input value [93], whereas the input modulation gate uses the 'tanh' activation function. Pointwise operations are applied inside the cell in order to connect the four gates and to obtain the output values.

The structure of the LSTM allows the network to learn the long range temporal dependencies from the dataset used to train [94]. This characteristic is especially useful for the system identification of the DC/DC power converters because the previous time steps affect the outputs of the black-box system. To understand how the LSTM generates an output, it is necessary to explain each step of the process from the moment that the information enters to the cell.

1. Input and recurrent data pass through the forget gate, where the sigmoid function determines the output value. This number is between 0 and 1, and when it is zero, the cell completely forgets the data.

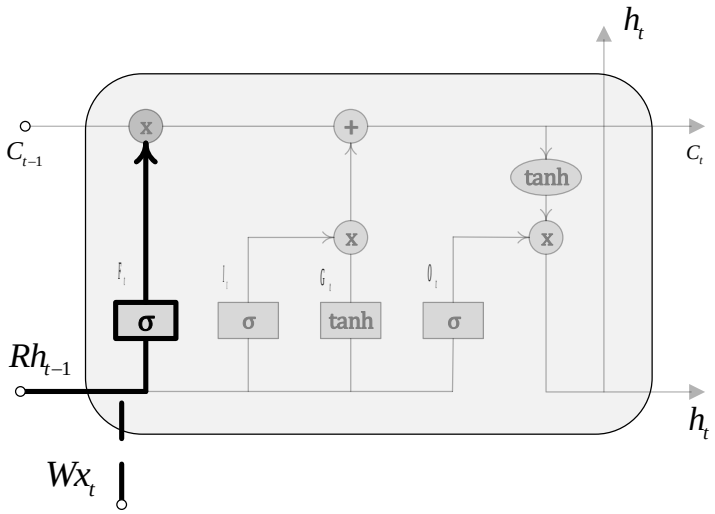

Figure 3.30. Forget gate operation in LSTM cell.

$$F_t = \sigma\left(W_f x_t + R_f h_{t-1} + b_f\right) \tag{71}$$

where W are the weights of the respective gate, R the recurrent weights and b the bias values.

2. Now, the data is sent to the input gate, which decides which values will be updated. At the same time, an activation function (tanh), like the one in the simple recurrent network, creates new possible values to be added. Then, the two vectors are multiplied to create an update of the state.

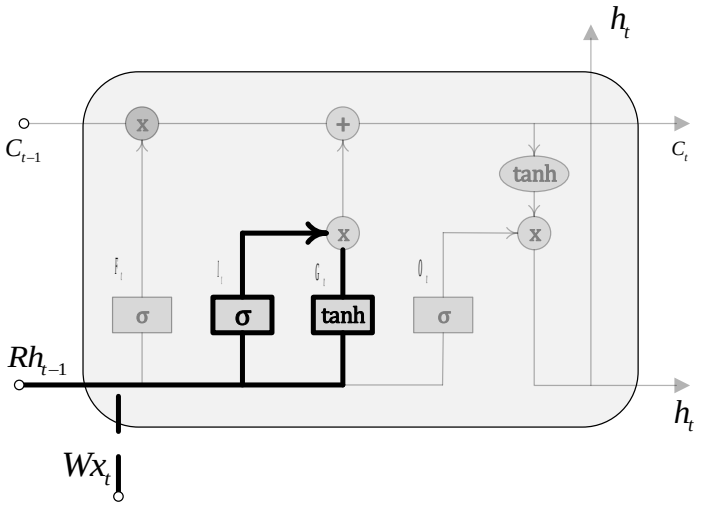

Figure 3.31. Input gate operation in LSTM cell.

$$I_t = \sigma\left(W_i x_t + R_i h_{t-1} + b_i\right) \tag{72}$$

$$G_t = \tanh\left(W_g x_t + R_g h_{t-1} + b_g\right) \tag{73}$$

3. The next step is to update the old cell state into a new one. This is done by multiplying the old state by the output of the forget gate found in the first step and by adding the new information calculated in step two to this result.

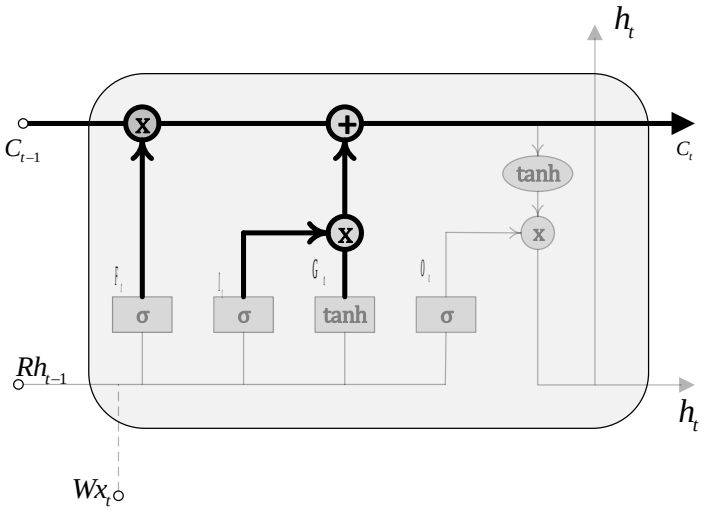

Figure 3.32. Cell operation at LSTM cell.

$$c_t = F_t \cdot c_{t-1} + I_t \cdot G_t \tag{74}$$

4. The final step is to calculate the output, which is determined by the cell state. As in the first two steps, the input and recurrent data pass through a gate with a sigmoid function,

while the cell state goes through an output activation function (tanh). Both results are multiplied to obtain the output.

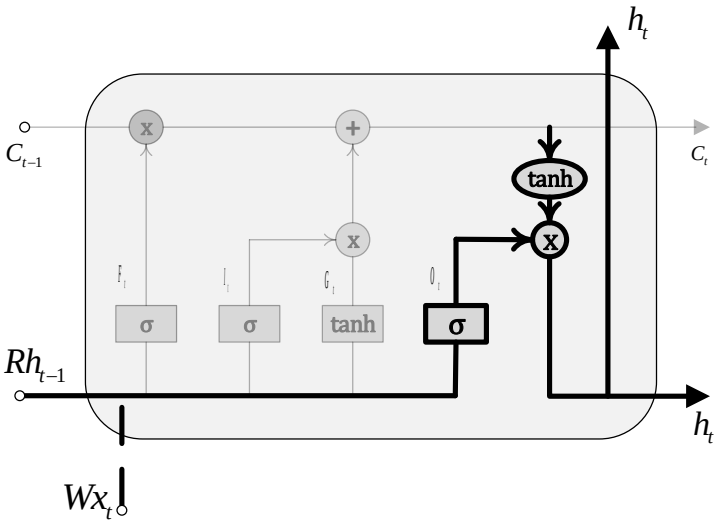

Figure 3.33. Output gate operation in LSTM cell.

$$O_t = \sigma\left(W_o x_t + R_o h_{t-1} + b_o\right) \tag{75}$$

$$h_t = O_t \cdot \tanh\left(c_t\right) \tag{76}$$

Finally, by using the updated hidden states, it is possible to calculate the predicted output values as,

$$y_t = W_{fc} h_t + b_{fc} \tag{77}$$

where W_{fc} and b_{fc} are the weights and bias of the fully-connected layer, respectively.

The structure of the LSTM allows the network to learn the long range temporal dependencies from the dataset used to train the NN [94]. This characteristic is especially useful for the system identification of DC-DC power converters, because the previous time steps affect the outputs of the black-box system. All processes described in Figure 3.29 are just for one cell or block. Figure 3.34 shows the general perspective of the hidden layer of the network, where the input layer refers to the inputs of the system and hidden units are the neurons.

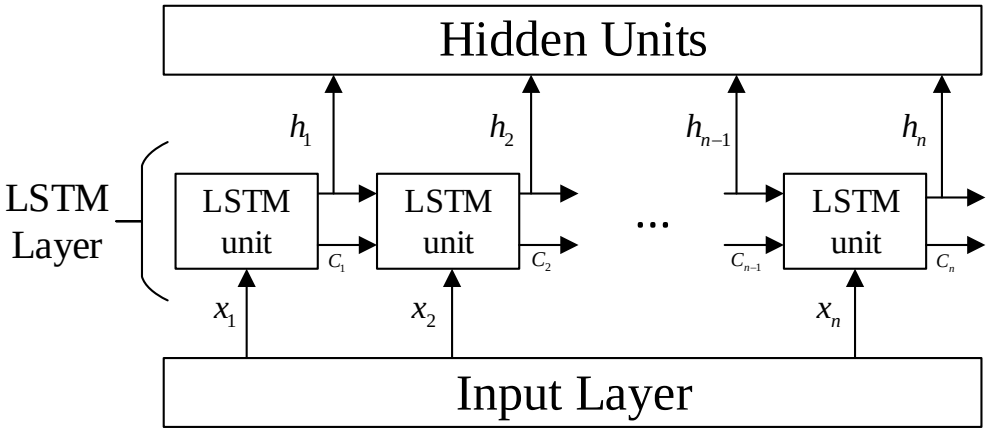

Figure 3.34. LSTM blocks connections.

The number of LSTM cells in Figure 3.34 corresponds to the number of time steps of the dataset. The input x_j of the black-box system is sent to the LSTM cell, the x_j vector consisting of the input values of the system at the time step *j.* The h_j term is the output of the LSTM cell and contains the weights of the neurons at the *j-th* time step, while c_j represents the updated cell state. The overall structure of the NN consists of four layers, the Sequence Input Layer, Hidden Layer (LSTM), Fully Connected Layer and the Regression Output Layer.

3.6.1 Proposed algorithm

This section proposes an offline system identification methodology whose main objective is to obtain a model of DC-DC power converters when there is no prior information about its topology or electrical characteristics. It is based on the well-known deep learning algorithm named LSTM-NN. To enhance the accuracy of the model, a set of hyper-parameters of the NN is defined by applying an optimization algorithm.

Figure 3.35 describes the proposed methodology for obtaining a NN that describes the behavior of the converter. It shows that the tuning of the hyper-parameters of the NN is a key point. The learning rate (LR), which refers to how fast the weights of the NN are adjusted, is tuned by means of the *LR Range Test*. The next step is to apply the Bayesian optimization algorithm (BOA) to determine the value of each hyper-parameter using the pre-processed training and validation datasets. If the lowest value of the root mean square error (RMSE) is below the defined threshold, the combination of hyper-parameters is stored, otherwise, the set of hyper-parameters are redefined and the process starts again. After having a proper hyper-parameters configuration, the network is trained again for *N* iterations and then, the determination coefficient R^2 and the root mean square error (RMSE) are calculated using the preprocessed test dataset to measure the

accuracy of the model. It is important to mention that in order to accelerate the process, the LR Range Test and the BOA, just consider a fraction of the total number of iterations (*N*) .

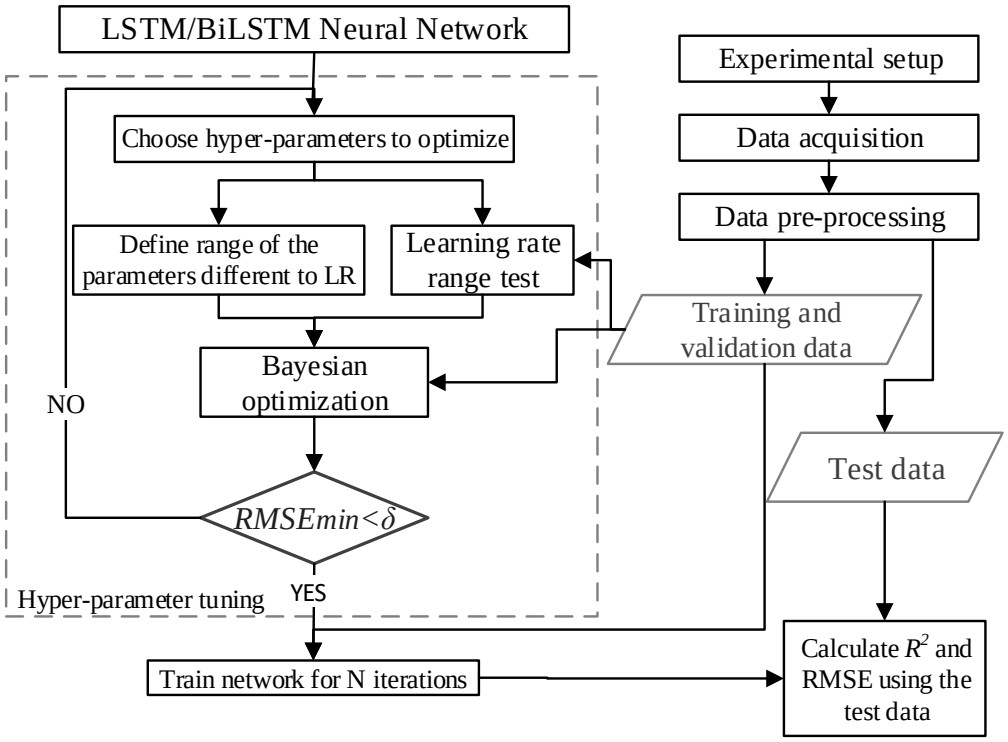

Figure 3.35. Proposed algorithm to train LSTM neural networks.

In Section 3.7 the hyper-parameter tuning process is explained thoroughly.

3.6.2 Step down DC-DC converter (input voltage and load change)

Section 3.5.4 presented the black-box modelling of the 270 V –to– 28 V step-down converter using a dataset that considered load changes at the output of the converter. This section presents the modelling of the same converter by considering changes in the input voltage and also in the output load. Considering the nature of the 270 HVDC, where the voltage delivered is always 270 V with minor perturbations [90], the input voltage of the step-down converter (black-box) is set as constant for all the experiments and the level might change in the 240 V to 300 V interval. The block diagram of the experimental setup is shown in Figure 3.36, where it can be appreciated that the power supply is controlled from the computer.

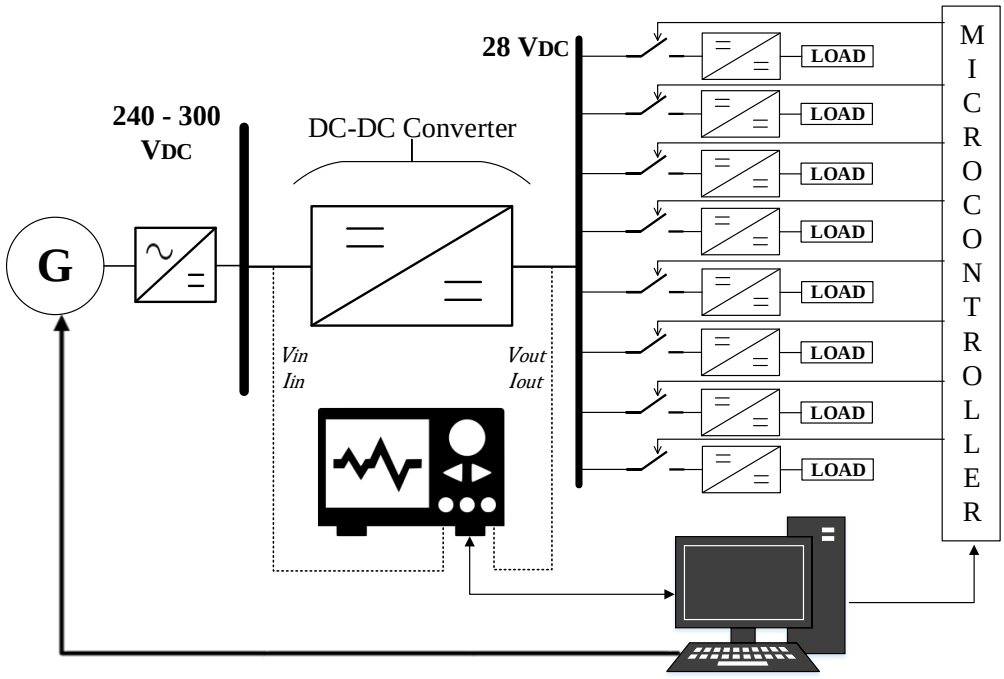

Figure 3.36. Block diagram of experimental setup

The converters used in this setup are the ones detailed in Table 3.3 and Table 3.4. The data acquisition setup is shown in Figure 3.37. It shows that the input voltage is generated by an AC power supply (Figure A.2) and this voltage is controlled by means of a script in Python.

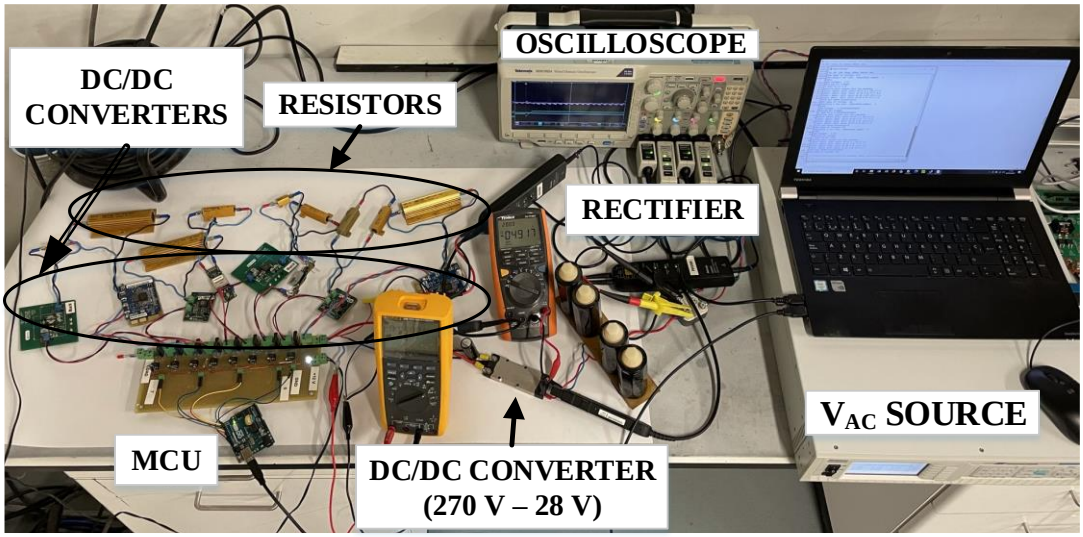

Figure 3.37. Data acquisition setup of step down converter. Power supply controlled externally

A total of 1512 experiments were conducted, where 1000 of them were used to train the neural networks and the remaining 512 experiments to test their accuracy.

3.6.2.1 Results

This section presents the results of the LSTM modeling algorithm when it is applied to the data collected from the step-down converter in the laboratory. The performance of the model is compared against that of five state-of-the-art modeling techniques. Two of them are feed-forward neural networks that are used in regression problems such as the NARX and wavelet neural networks (WNN). The first one is based on [61] and the hyper-parameters are tuned by means of a grid search, while for the WNN, the procedure used is the one presented in [63], where the signals are subjected to a wavelet decomposition and the most representative components are selected to train the network. On the other hand, two other approaches are the polytopic model [54] and the state space averaging model [55]. In case of polytopic modeling, the general model of the DC-DC converter is generated as a combination of multiple models, which are obtained based on the operating points of the DC-DC converter. In case of the state space average model, a simple buck converter was considered to obtain the modeling transfer function. The last technique is a simple 1D CNN, which is often used to classify time-series, since this deep neural network is able to identify complex signal patterns by applying filters.

Figure 3.38 shows the data set dealt with, including the training, validation and test data sets, as a scatter graph where each point represents an experiment. The *x*-axis refers to the delivered power and the *y*-axis to the input voltage of the converter. The grey and white areas in Figure 3.38 refer to the DCM and CCM of the DC-DC converter, respectively.

After obtaining the experimental results, the next step is to tune the hyper-parameters of the LSTM-NN. To determine the optimum LR range, the LR range test was applied, thus obtaining the RMSE for each LR value. Figure 3.39 shows the RMSE evolution when it is tested under different learning rates. The same phenomenon is seen in Figure 3.54.

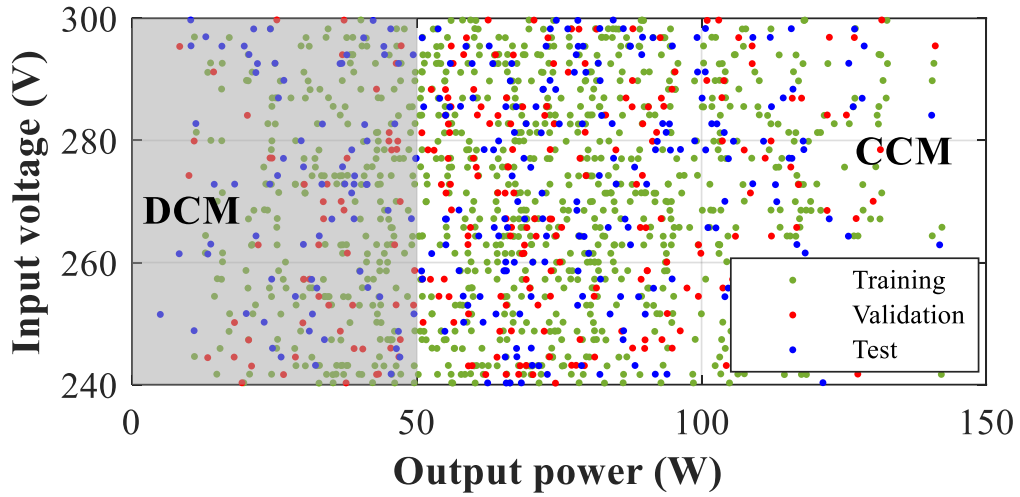

Figure 3.38. Training, validation and test data sets plotted in the space defined by the output power and the input voltage of the converter.

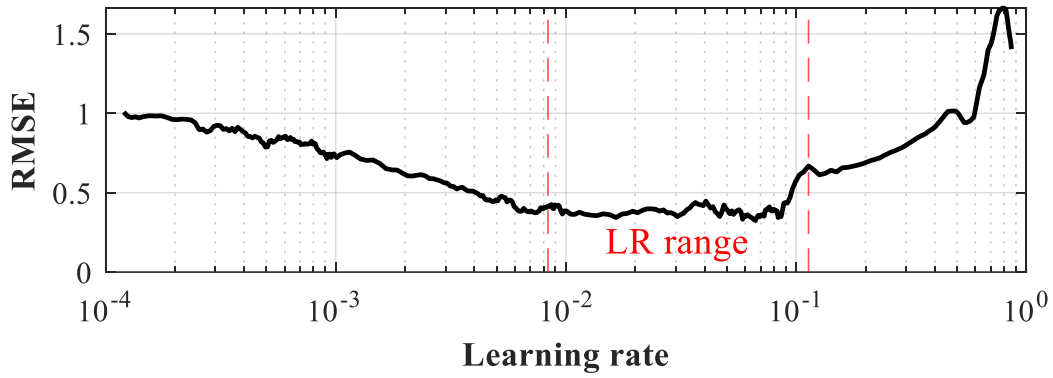

Figure 3.39. Learning rate test using the LSTM.

The next step is to apply the BOA to the measured data. The Bayesian optimization algorithm was applied to 30 LSTM-NNs with different hyper-parameter configurations, while each LSTM-NN was trained for 80 epochs. The algorithm was programmed in Matlab® using the Deep Learning Toolbox, and the training process was carried out using a GeForce RTX 2080 Super GPU. Table 3.8 shows the minimum, maximum and tuned values of the hyper-parameters used in the Bayesian optimization. The boundaries of the other hyper-parameters are set based on their typical values and the complexity that a large value can add to the training process [95], [96].

Table 3.8. Bayesian optimization range

Hyper-parameter	Minimum	Maximum	Optimal
Neurons	5	100	96
Learning rate	Given by the LR range test		0.01415
Gradient decay factor (GDF)	0.8	0.99	0.9799
L_2 regularization	1e-10	1e-2	9.06e-7

The next step is to train the LSTM-NN with the tuned hyper-parameters. The number of epochs was set to 300 with a validation frequency of 15. Table 3.9 presents the RMSE and coefficient of determination (R^2) mean values of the predictions of 512 different experiments from the test dataset. It shows the performance of the trained LSTM-NN and compares their results to the ones obtained with the other methods. The stopping criteria of the NARX-NN, polytopic model and the state-space averaging method are found in references in Table 3.9. In case of the WNN and the 1D CNN, a high epoch number is set, and the training process stops when the RMSE value increases for five consecutive epochs. Table 3.9 proves that the deep learning approach is more accurate considering that the RMSE is lower and the R^2 is closer to 1, compared to the other analyzed modeling techniques. The polytopic and the state-space average models present low precision because they do not perform well when the converter changes from one conduction mode to another. Even though the proposed approach is not the fastest method, it takes a relatively short training time.

Table 3.9. RMSE and coefficient of determination (R^2)

Method	RMSE		R^2		Elapsed time
	I_{in}	V_{out}	I_{in}	V_{out}	
LSTM	0.0185	0.0172	0.991	0.985	1718.63 s
NARX-NN [61]	0.0401	0.0342	0.948	0.902	117915 s
WCNN	0.0277	0.0241	0.966	0.930	842 s
Polytopic model [54]	0.0392	0.0366	0.910	0.844	427.0 s
State-space averaging method [55], [66]	0.0547	0.0360	0.849	0.774	233.2 s
1D CNN	0.0295	0.0212	0.960	0.948	2607.07 s

Figure 3.40, Figure 3.41, Figure 3.42 and Figure 3.43 compare the estimations of the proposed method with measurements and the state-of-the-art approaches. Each figure includes four plots. While (a) and (b) refer to the inputs applied to the model, (c) and (d) show the outputs (estimations). Figure 3.40 and Figure 3.41 present waveforms of the ripple during steady state in CCM (V_{in} = 270 V, P = 94.5 W), and in DCM (V_{in} = 247 V, P = 22.3 W), respectively.

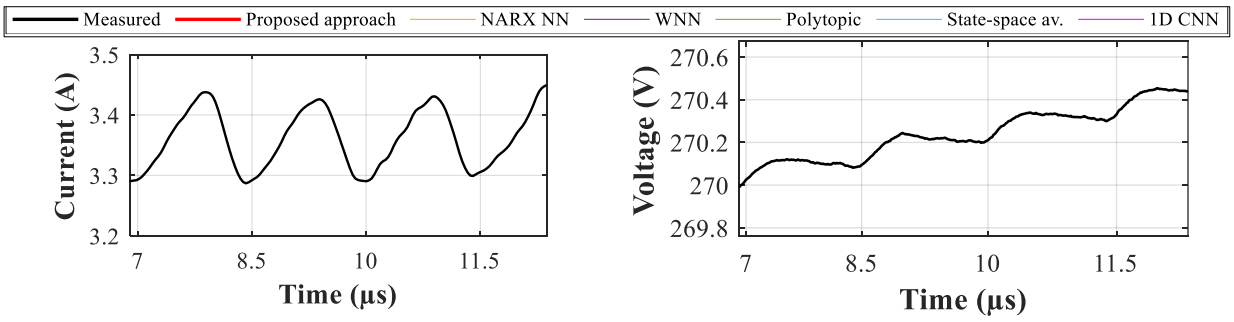

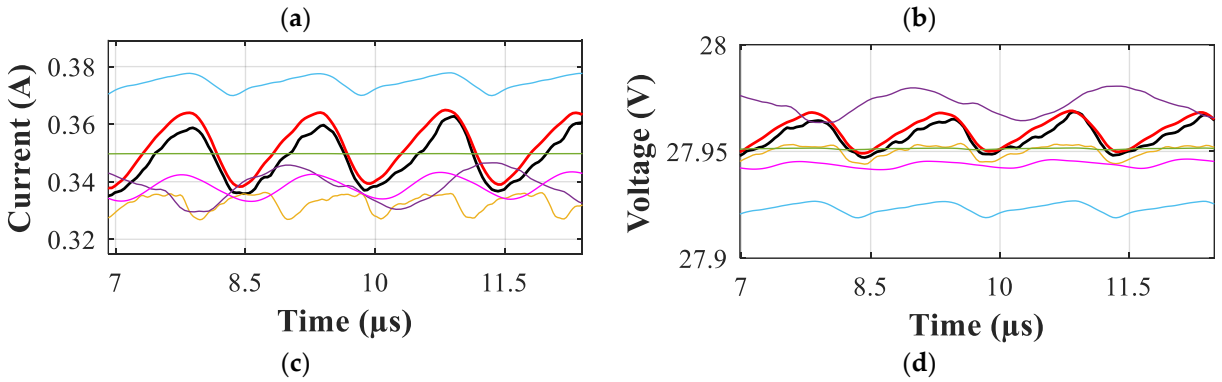

Figure 3.40. Steady state comparison in CCM (a) Output current. (b) Input voltage. (c) Input current. (d) Output voltage.

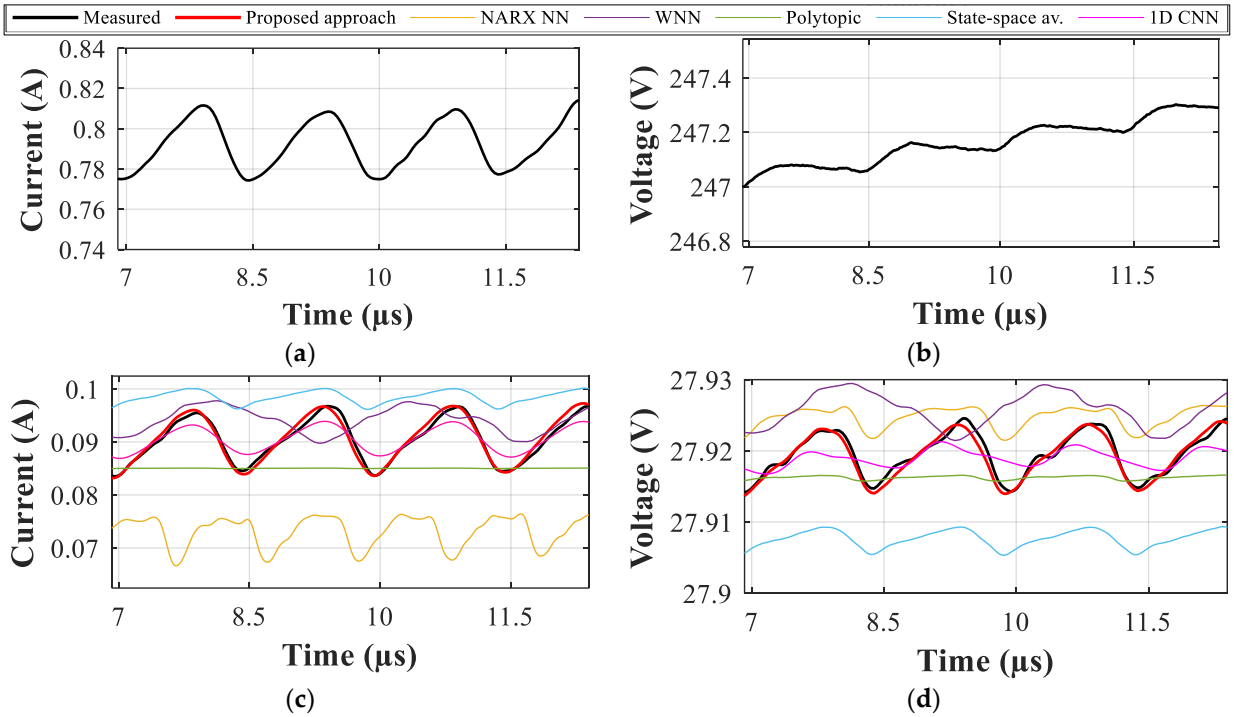

Figure 3.41. Steady state comparison in DCM. (a) Output current. (b) Input voltage. (c) Input current. (d) Output voltage.

The LSTM approach is the only one able to replicate the waveforms in steady state (ripple, frequency, mean value) with high fidelity in both CCM and DCM, the other methods present an inferior performance. The irregular distortion observed in the measured ripples of the signals is caused because measurements of DC-DC converters are often corrupted with high-frequency noise, which results from the switching characteristics of the converter and the sensor over-amplification of the noise [97]. Figure 3.42 and Figure 3.43 present the transient response of the converter, the first one considers a load disconnection (V_{in} = 252 V, $P_{initial}$ = 116 W, P_{final} = 34.81 W) while the second one shows a load connection (V_{in} = 288 V, $P_{initial}$ = 46.08 W, P_{final} = 97.34 W).

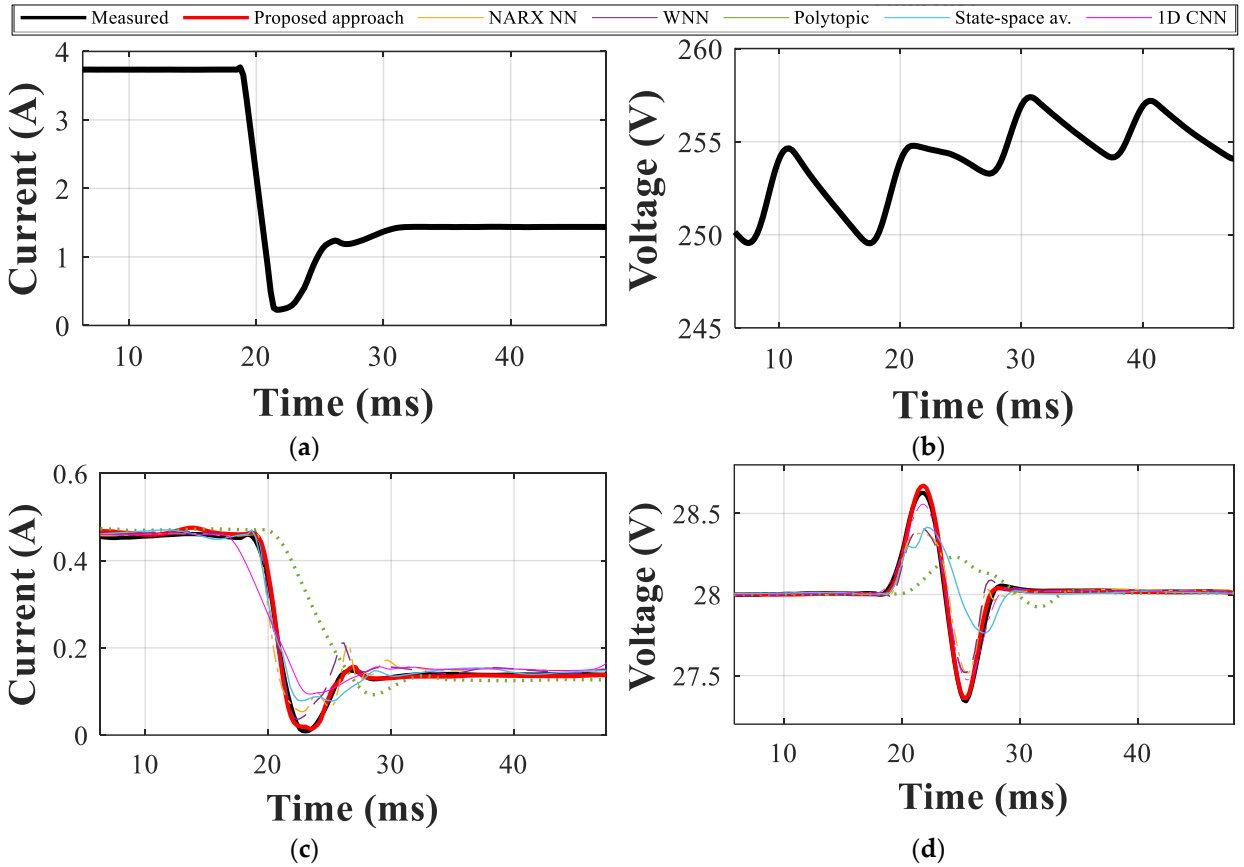

Figure 3.42. Transient response during a load disconnection. (a) Output current. (b) Input voltage. (c) Input current. (d) Output voltage.

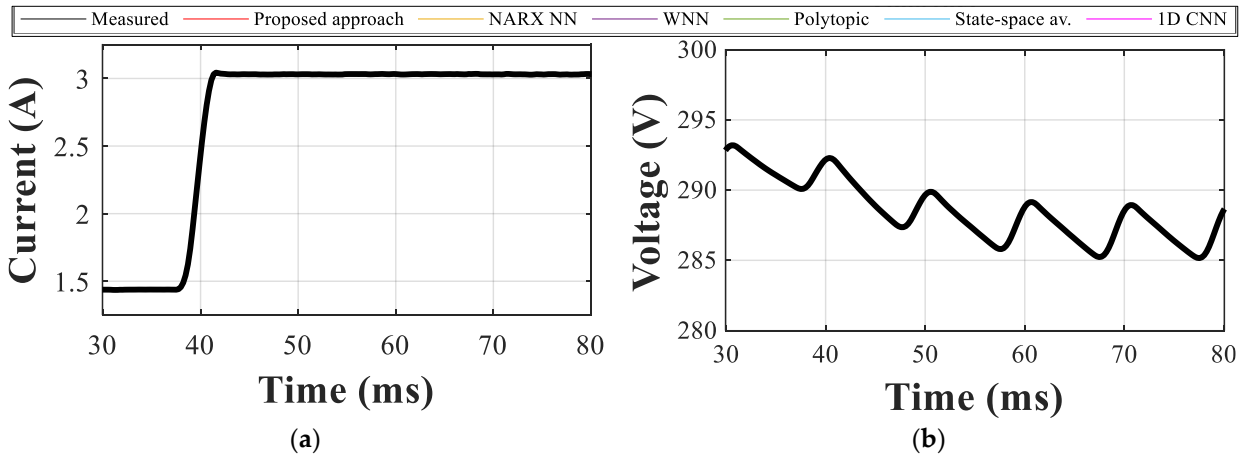

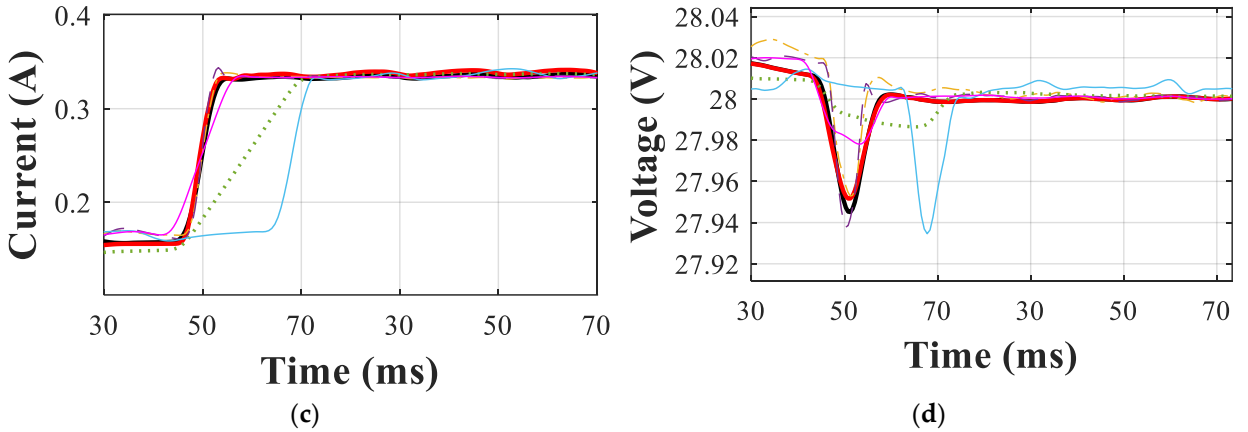

Figure 3.43. Transient response during a load connection. (a) Output current. (b) Input voltage. (c) Input current. (d) Output voltage.

The estimated transient response for all models is similar. However, the LSTM-NN is the only one capable of replicating the overshoot of the signals. To better appreciate this effect, Figure 3.44 shows a closer look to the first perturbation.

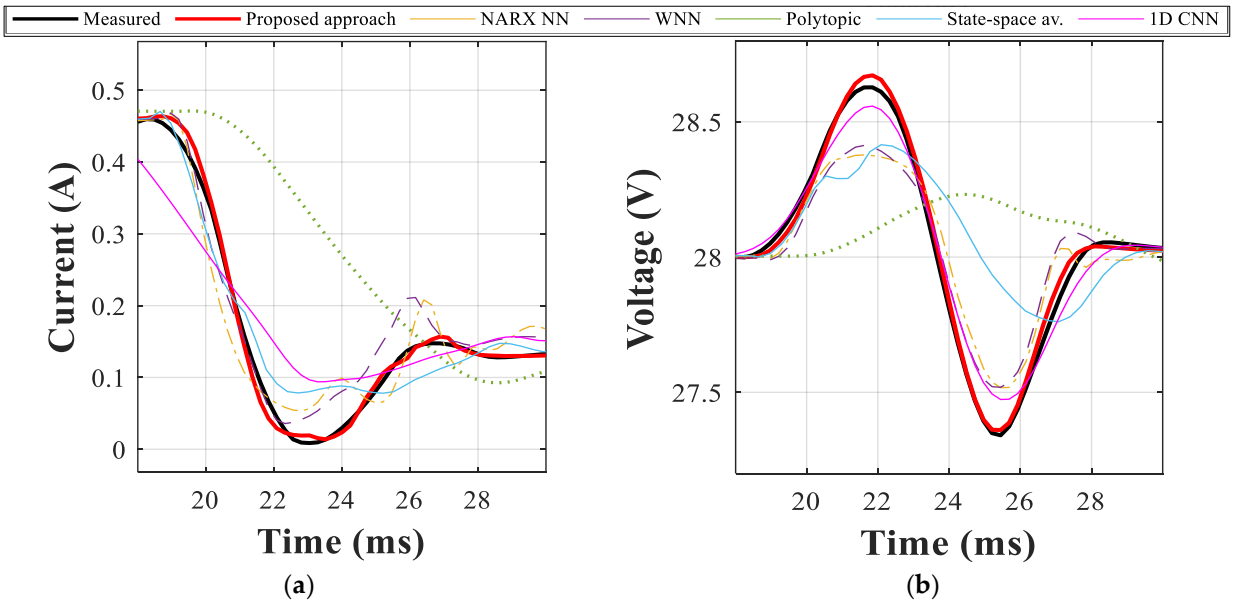

Figure 3.44. Instantaneous response of the converter during a load disconnection. (a) Input current. (b) Output voltage.

Results presented in Figure 3.44 show that the LSTM approach replicates the instant transient response of the converter with high precision and outperforms the other approaches.

Finally, Figure 3.45 shows a scatter plot comparing the measured and estimated currents in order to prove the robustness of the LSTM methodology. The points of the graphs were calculated by using the test dataset (512 experiments) and the output values of the model obtained in the study. The plot in Figure 3.45 (a) is separated in three regions. The white region refers to the CCM of the converter, the light grey region to the DCM and the dark grey region is an area where the

operating mode can be either CCM or DCM depending on the input voltage value. The graphs show a good generalization ability of the neural network since the dispersion between measured and estimated values is very low and the slope is almost 1 in both cases, which implies a high correlation and accuracy. The few anomalies observed in the estimations of the current (i.e. I_{meas} = 0.19 A and I_{est} = 0.276 A) occur when the converter changes its operation from CCM to DCM and the model fails to replicate with high accuracy the overshoot of the instantaneous transient response. This phenomenon was only observed in 7 of the 102 cases (6.86%), and it does not affect the steady state estimation or the estimated response time.

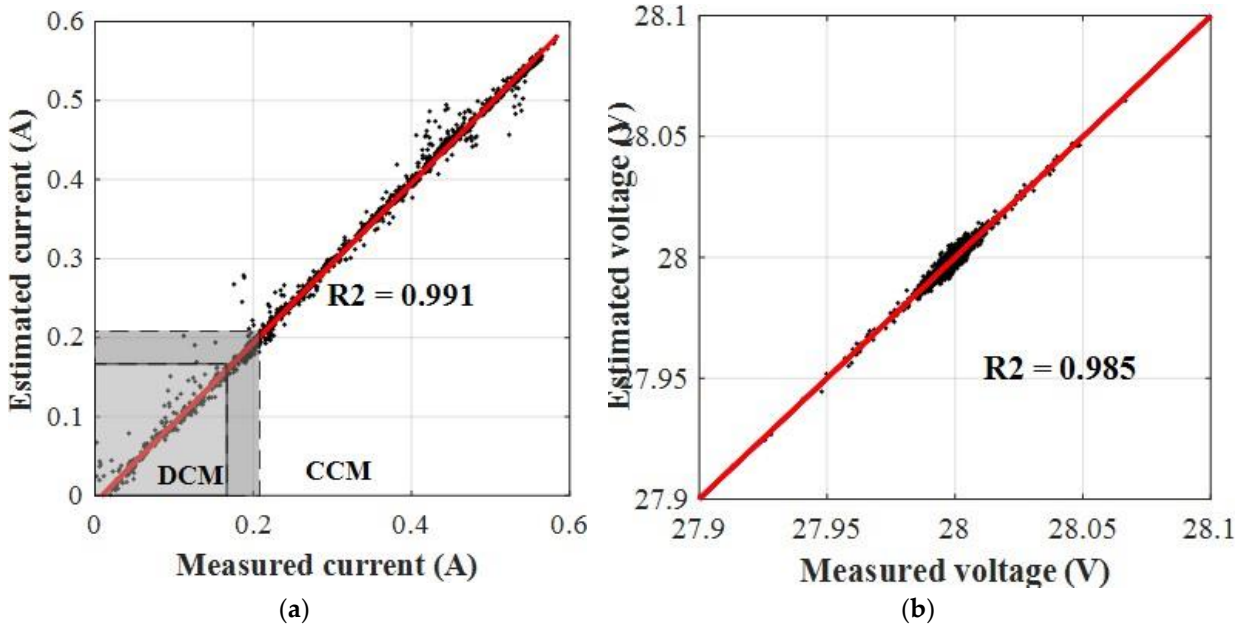

Figure 3.45. Scatter plot of experimental versus estimations. (a) Input current. (b) Output voltage.

3.6.3 Bidirectional converter used in electric vehicles

The system to be evaluated in this subsection is a mild hybrid electric vehicle (MHEV), this topology being used by major manufacturers such as Audi, Toyota, Nissan or Honda, among others [98]. This type of vehicle improves fuel efficiency by supplying power to the electric motor in certain situations or by applying regenerative braking. MHEVs require a higher voltage (48 V) to feed the electrical systems of the vehicle in order to reduce conduction losses [99], [100]. The MHEV is a transition technology that is placed in the middle point between the conventional 12 V supply system and the 48 V system proposed by some manufacturers of premier cars [101].

The black-box identification technique focuses on the dual-voltage architecture that considers two batteries and a DC-DC bidirectional converter, the last one being the device to be modeled.

Understanding the working principle and the topology of the electrical system of the MHEV is fundamental in order to obtain an accurate model of the power converter. Figure 3.46 shows the dual architecture of this electrical system and its main components. It can be seen that at the 48 V side there is a battery, a starter generator, a drive (DC-AC or AC-DC depending whether the electric machine works as a motor or as a generator, respectively) and loads, whereas at the 12 V side there is a battery and a set of low voltage loads. Figure 3.46 does not specify the topology of the DC-DC converter since it may change depending on the manufacturer of the automobile and its requirements [101]. However, for the purpose of this study, this is indifferent, since the proposed black-box approach is able to model the bidirectional converter despite its topology.

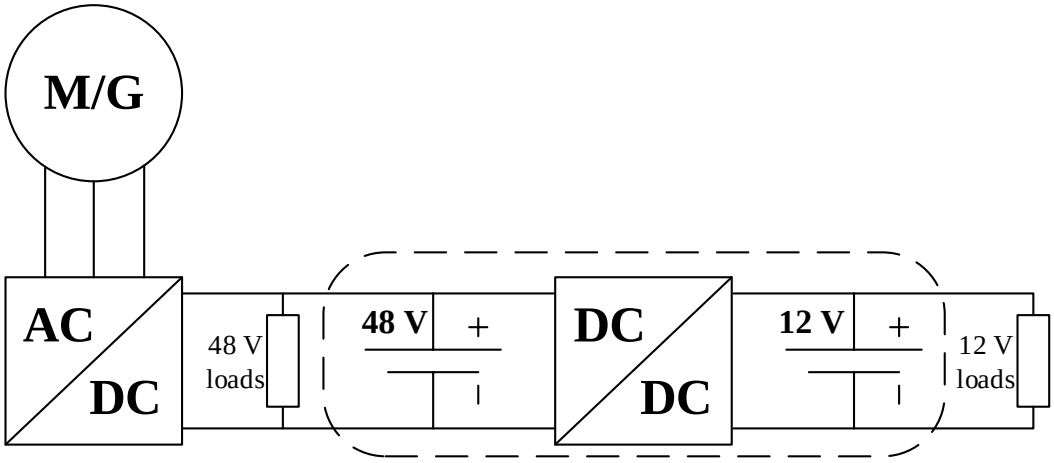

Figure 3.46. MHEV electrical system.

Each battery is in charge of stabilizing its own network. When the belt-driven starter generator (BISG) is operating as a generator, the converter works in the buck mode, the two batteries are charged and the power is supplied to the loads. When the BISG operates as a motor, the DC/DC converter operates in the boost mode and the power flows from the 12 V side to the 48 V side [100]. Some manufacturers include a starter on the low voltage side in order to start the motor in case of failure of the 48 V network.

The experimental setup pursues replicating the voltage conversion stage that occurs in MHEVs. To this end, the setup shown in Figure 3.46 was implemented in the laboratory. It includes three main elements, the 48 V battery, the DC-DC bidirectional power converter and the 12 V battery. The objective is to obtain a rich dataset based on the measurements at the input and output terminals of the converter, allowing an accurate training of the LSTM-NN. The first step of the experimental stage is to choose an adequate set of batteries and a proper converter. These elements were selected considering the characteristics, ratings and specifications of the elements that can be found in commercial MHEVs [98]. The chosen converter was the LM5170-Q1 48 V -

to- 12 V DC-DC buck-boost converter manufactured by Texas Instruments. This converter is suitable for real MHEV applications and it can be controlled externally by means of its current or a voltage source. The evaluation module of the converter was used to perform the experiments, since it allows the user to modify different parameters based on the required measurements. The bidirectional converter has an inner current control loop and an outer voltage control loop. The first one receives two external signals that determine the direction and magnitude of the current flowing through the converter. It uses a Type-II compensator to stabilize the loop for the buck and boost operations. The outer voltage loop is controlled by a digital circuit, which also regulates the output voltage of the converter. Both loops are interconnected, since the output error signal of the voltage loop is an input signal for the current loop. Table 3.10 shows the characteristics of the converter and Figure 3.47 presents the circuit board.

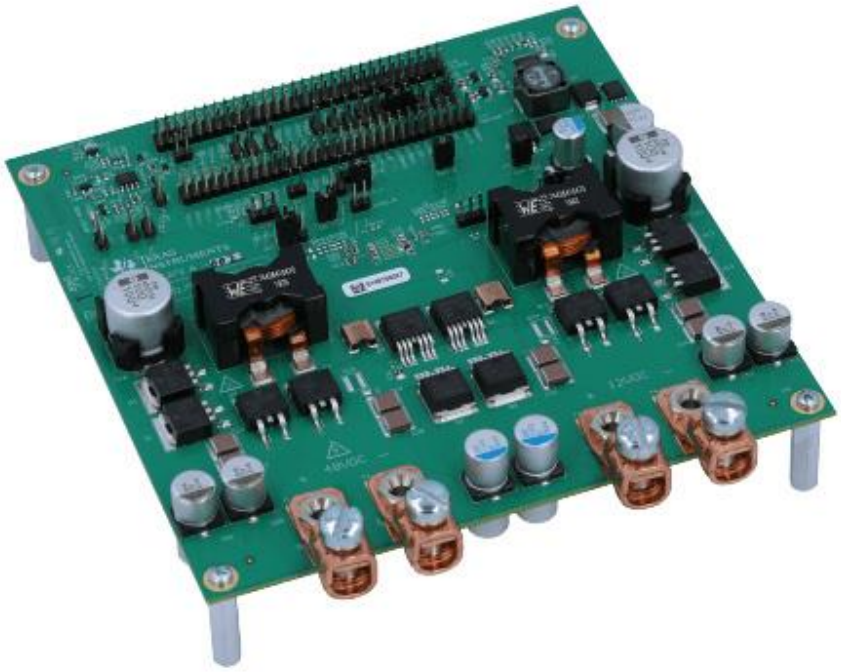

Figure 3.47. LM5170-Q1 evaluation module.

Table 3.10. LM5170-Q1 bidirectional power converter specifications

Parameter	Value
Input voltage range	6 V – 75 V
Typical input voltage	48 V
Output voltage range	3 V – 48 V
Typical output voltage	12 V
Maximum power	720 W
Switching frequency	100 kHz

Peak efficiency	> 97%

The MD-BB0 Li-Ion 48 V battery pack from Torrot was used, which is intended for automotive applications. Although it is not specifically designed for MHEVs, the characteristics shown in Table 3.11 are quite similar to the 48 V batteries of commercially available MHEVs. On the other hand, the T4 12 V lead acid battery from Augi was used, which is widely applied in vehicles. Table 3.11 summarizes the specifications of the batteries dealt with in this work.

Table 3.11. Battery specifications

Parameter	48 V Battery	12 V Battery
Nominal discharge current	6.28 A	Not specified
Maximum discharge current	50 A	440 A
Nominal charge current	6.28 A	Not specified
Maximum charge current	12 A	Not specified
Rated capacity	31.9 Ah	64 Ah

After selecting the equipment, the following step is to define an experimental setup based on the type of data needed to train and test the neural networks. As already mentioned, the training stage of the neural network requires a rich dataset that includes different operating points and transient responses of the bidirectional converter. Thus, several conditions must be measured and acquired based on the maximum rating and response time of the converter. An automatic acquisition system was implemented in order to collect the training and test datasets in a fast and efficient way.

Figure 3.48 shows the schematic of the setup implemented in the laboratory where the oscilloscope and the bidirectional converter are fully controlled by a computer and a DAQ device. A Python script synchronizes the control signals of the converter and the data acquisition system. This code sends a current command to the control loops of the bidirectional converter. Based on this value, it adjusts the measurement settings of the oscilloscope (trigger, coupling and time scale). The maximum and minimum values of the current command are fixed based on the power rating of the batteries and the converter. The number of iterations is defined by the user and indicates the number of experiments of the dataset. Each experiment contains five signals: time, input voltage, input current, output voltage and output current of the bidirectional converter. It is not necessary to connect loads to any of the batteries, as the converter provides the direction and magnitude of the current.

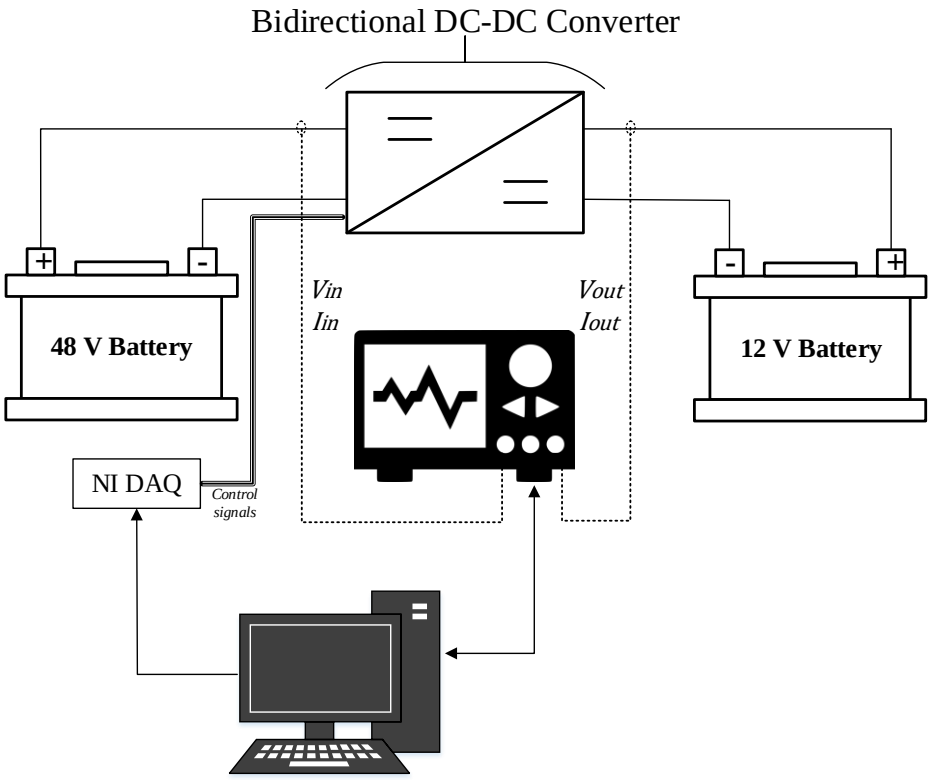

Figure 3.48. Experimental setup of bidirectional converter.

It is necessary to pre-process the input data in order to filter the noise and to avoid overfitting, thus increasing the training speed of the neural network. The pre-processing consists of an interpolation and the application of a simple moving average filter. First, the interpolation is applied to reduce the number of points of each experiment of the dataset. Next, the moving average filter is applied to eliminate the high-frequency noise from the measurements. The number of points taken in the moving average is chosen in order to keep the main characteristics of the transient response. The last step of this stage is to divide the processed data set into the training, validation and test sets. This partition is done based on the information available on the dataset, because it directly affects the results of the training of the neural network. The same pre-processing strategy must be applied to these three subsets.

The 48 V –to– 12 V DC-DC bidirectional converter model is validated by the test data set to predict the output values provided by the NN, which are compared against the actual values, and the error between both signals is calculated. This is done to validate the NN by testing the obtained model under conditions other than those considered in the training data. It verifies the robustness of the model and assures that the trained neural network does not present overfitting issues. The accuracy of the predictions is calculated by means of the root mean squared error and the

coefficient of determination, which are two indicators used to evaluate modeling and fitting problems [102]. RMSE values as low as possible and R^2 values close to 1 are desirable.

Figure 3.49 shows the experimental setup implemented in the laboratory, from which the experimental data was acquired. This setup has the same configuration as that in Figure 3.48.

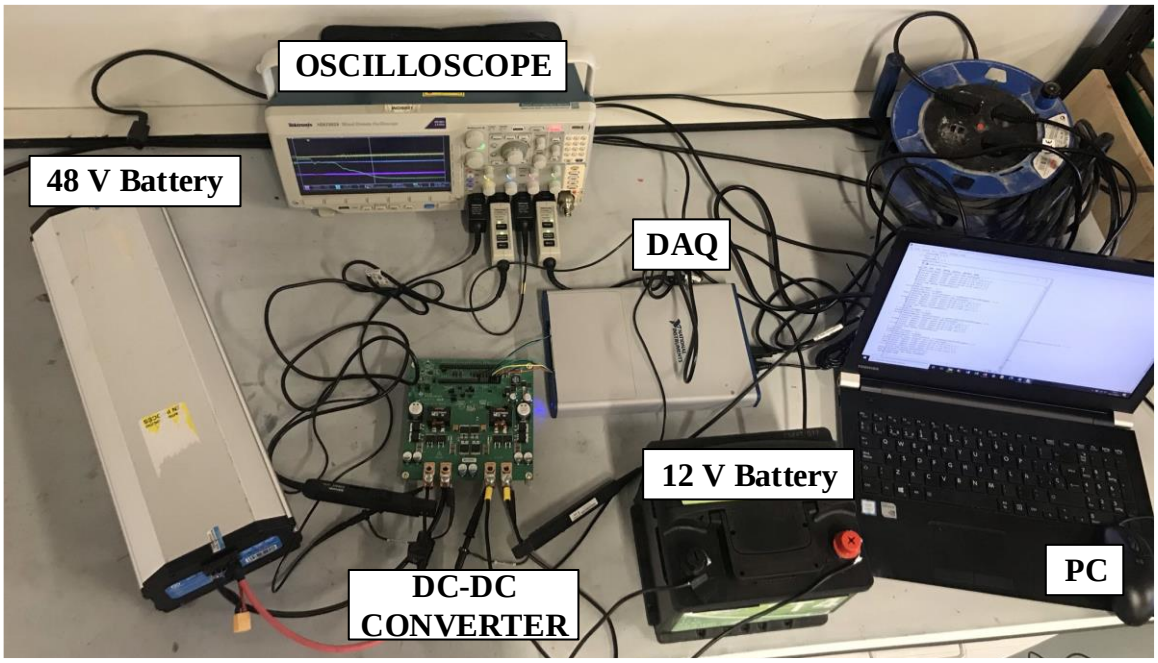

Figure 3.49. Experimental setup of the MHEV electrical system.

The equipment used to acquire the data consists of a 4 channel oscilloscope (Figure A.2), two high-frequency current probes (Figure A.2) and two high-frequency voltage probes (Figure A.2). A total of 1000 different experiments were performed by controlling the current flowing through the power converter. The sampling frequency of the oscilloscope was set to 2.5 MHz and 10^5 points were acquired, resulting in a period of 0.4 microseconds. The pre-processing consisted of reducing the number of points of every experiment to 5000 and then applying a 10-points moving average filter. Figure 3.50 presents an example of the four signals acquired in each experiment. In this case it is well appreciated the transient response of the bidirectional converter.

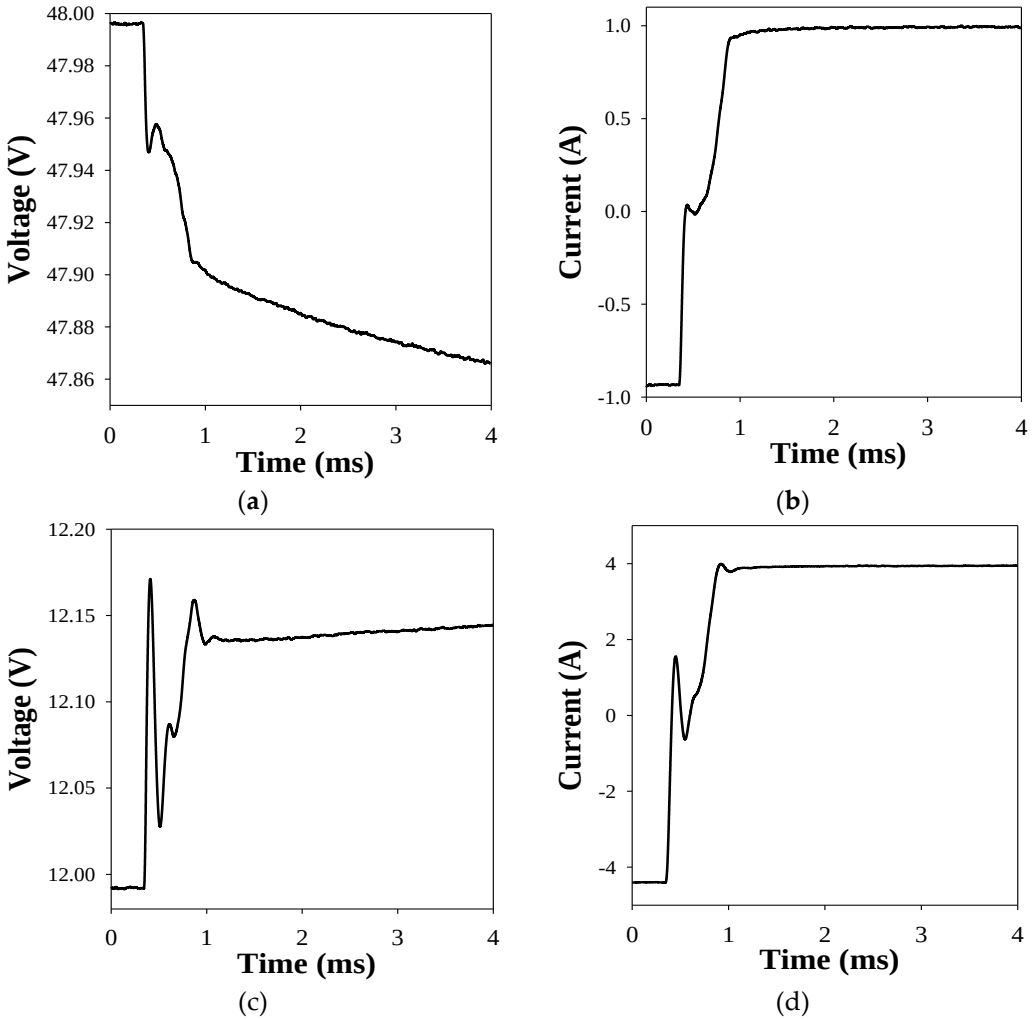

Figure 3.50. Bidirectional converter measurements per experiment. (a) Input voltage, (b) Input current, (c) Output voltage and (d) Output current.

3.6.3.1 Results

A total of 750 experiments was assigned to the training dataset, whereas the validation and test datasets contain 125 experiments each. The next step is to tune the hyper-parameters of the NN. Table 3.12 presents the minimum and maximum bounds of the variables to be tuned by the Bayesian optimization algorithm. A total number of 30 NNs were trained by the BOA, each training process runs for 100 epochs.

Table 3.12. Bayesian optimization range

Hyper-parameter	Minimum	Maximum
Neurons	5	150
Learning rate (LR)	0.001	0.1

Gradient decay factor (GDF)	0.8	0.99
L_2 regularization value	1e-10	1e-2

The BOA took 12 minutes to train the 30 neural networks. It was found that the optimal point has the following hyper-parameters: 29 neurons, *LR* = 0.03426, *GDF* = 0.974 and L_2 = 0.00169. Subsequently, the LSTM-NN was trained with these hyper-parameters for 1000 epochs using the 'adam' solver (MATLAB). Figure 3.51 shows the evolution of the training progress.

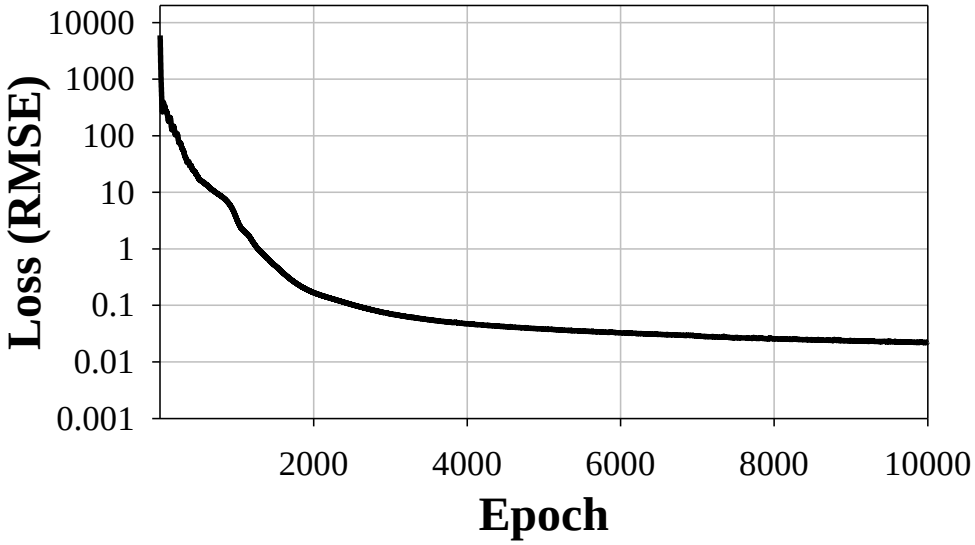

Figure 3.51. Training progress.

The following step consists of validating the NN when tested under different conditions than the ones used during the training stage. Table 3.13 shows the RMSE and R^2 values obtained after evaluating 125 experiments from the test dataset. It also compares these values to the ones obtained by means of the predictions made using the other three methods. The LSTM-NN outperforms the other three techniques because the RMSE is lower and the R^2 coefficient is closer to 1.

Table 3.13. Results and comparison with other methods

Method	RMSE		R^2		Time elapsed
	I_{in}	V_{out}	I_{in}	V_{out}	
LSTM-NN	0.1204	0.0023	0.9995	0.9998	274 s
NARX-NN [61]	1.4043	0.0067	0.9761	0.9877	12458 s
Polytopic model [54]	1.3740	0.0126	0.9522	0.9565	26 s
State-space averaging method [55], [66]	1.4410	0.0222	0.9465	0.9539	312 s

To better understand the accuracy of the proposed model, Figure 3.52 shows the actual and predicted outputs of two experiments of the test dataset. Figure 3.52 a) and b) show an experiment in which the converter changes its operating mode from boost to buck, whereas in Figure 3.52 c) and d) the operating mode changes in the opposite way. In both cases, the estimation of the LSTM-NN is close to the measurements. Figure 3.52 also shows that the accuracy of the transient response is better than those estimated by the other three models. The LSTM-NN model accurately replicates the steady state and transient response values, while the other methods exhibit some discrepancies. It is worthy to note that the estimation of the current at the 12 V side of the power converter is slightly less accurate than the estimation of the voltage. This might be because the transient response of the output current is wider than the one for the voltage, depending on the experiment.

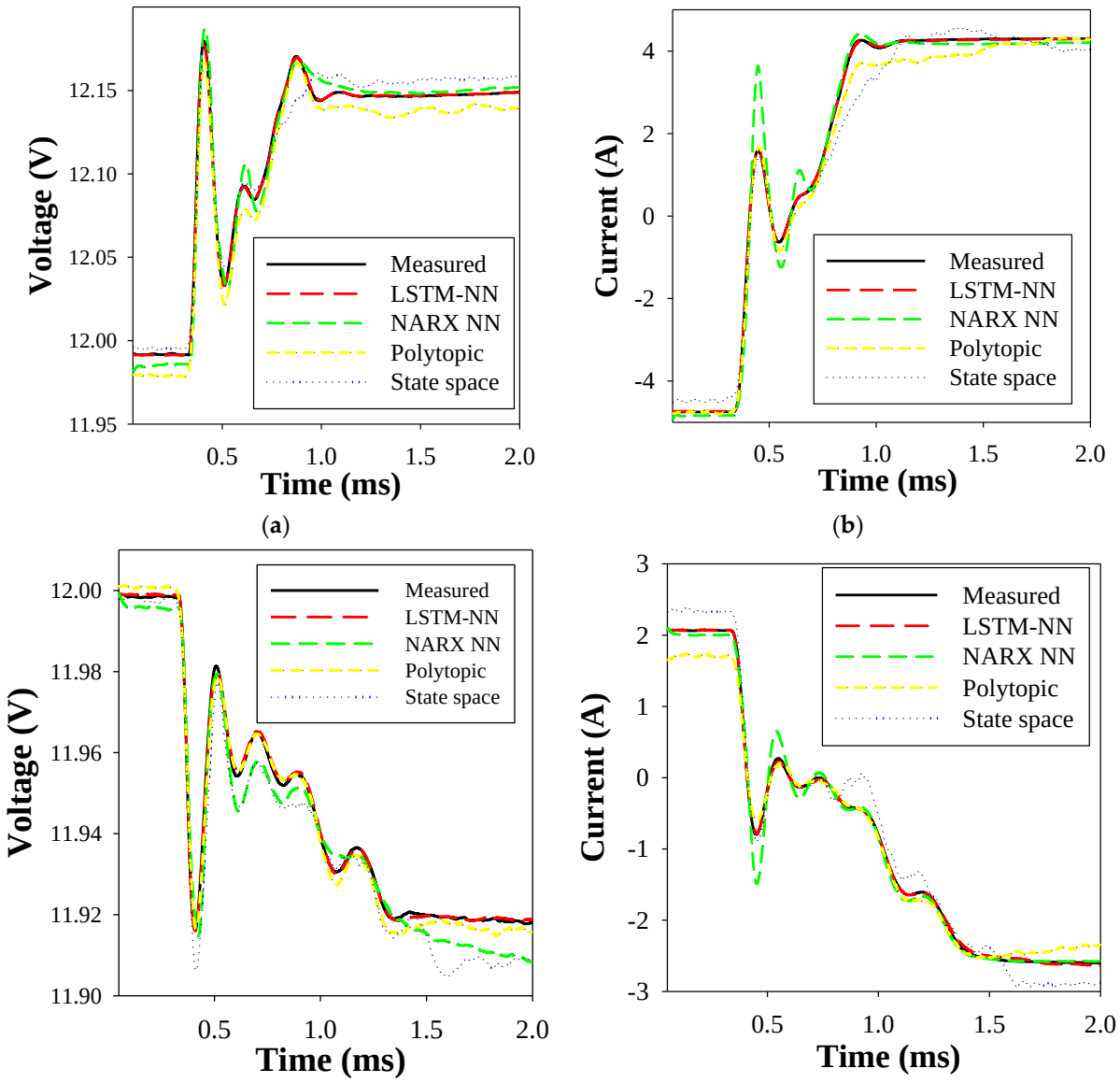

(c) (d)

Figure 3.52. Transient response measurement and estimation of (a) Output voltage (boost mode to buck mode), (b) Output current (boost mode to buck mode), (c) Output voltage (buck mode to boost mode), (d) Output current (buck mode to boost mode).

Figure 3.53 plots the estimations done by the four methods against the experimental measurements corresponding to a broad range of operating conditions. Such results prove the robustness of the proposed model since the slope is very close to unity. The LSTM-NN outperforms the other three approaches, since the dispersion of the points is much smaller and the coefficients of determination are greater.

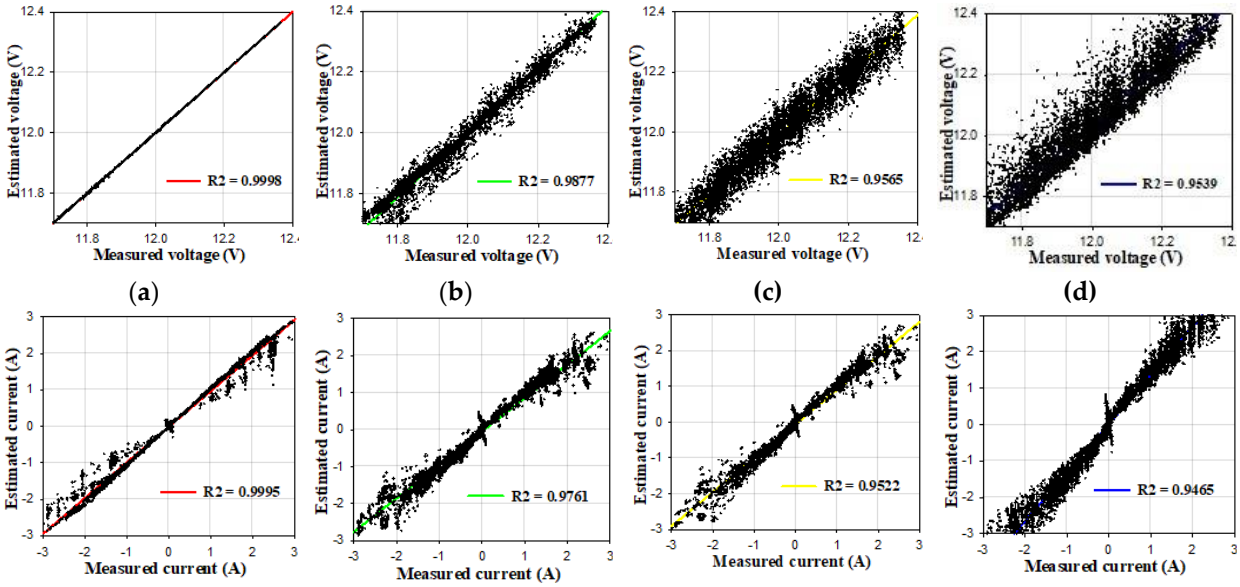

Figure 3.53. Scatter plot comparing measured and estimated signals. (a) output voltage (LSTM-NN), (b) output voltage (NARX), (c) output voltage (Polytopic), (d) output voltage (State space), (e) output current (LSTM-NN), (f) output current (NARX), (g) output current (Polytopic), (h) output current (State space).

The results presented in this section proved the effectiveness of the modeling approach proposed in this thesis, as well as the accurateness in comparison with other methods found in the technical literature.

3.7 Hyper-parameter tuning

A fundamental part in the process of training neural networks is to find the appropriate hyper-parameters. This can be done using different algorithms whose objective is to find a network configuration that minimizes the error. A strategy that combines two different methods is proposed to find the network that fits the best the data.

3.7.1 Learning rate (LR) range test

The learning rate is one of the most important hyper-parameters to tune in a neural network. If it is too small it takes more time to train and it can produce overfitting. If the LR is large the training may diverge. Therefore, the LR range test introduced in [95] is used to find a correct value or range of values where the LR of the training should be in order to improve accuracy and decrease the training cost of the neural network.

The test is simple and consists of training a set of neural networks while the learning rate increases at each iteration. The initial LR is set to a small value, and it increases linearly until the training diverges. The values of the loss function, RMSE and accuracy are stored for each iteration. Figure 3.54 shows the corresponding graphs.

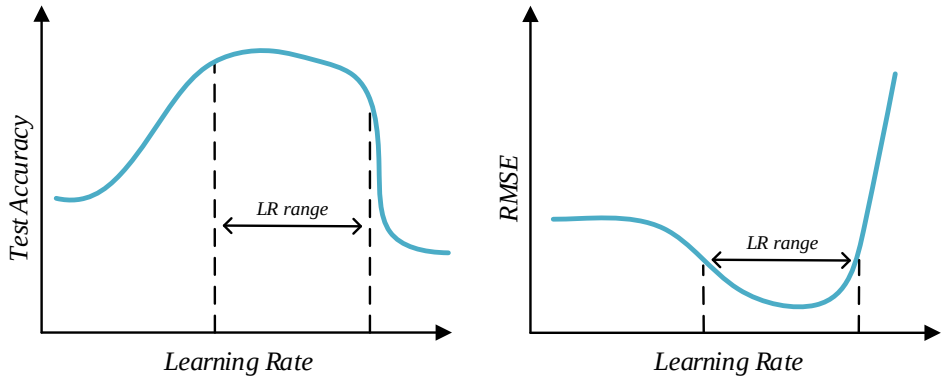

Figure 3.54. Loss and accuracy vs. Learning rate.

To select the appropriate bounds or the Learning Rate itself the following assumptions are considered [95].

- The minimum LR bound corresponds to a tenth of the maximum bound.
- The maximum bound is chosen according to the divergence of the training.

For this project purpose, the training of each network will only consider the first 50 epochs. The learning rate range is used as an input for the Bayesian Optimization Algorithm, which is explained in the next section.

3.7.2 Bayesian optimization

Taking into account that traditional methods such as grid search and random search require a several number of iterations (training) to find a proper configuration of the neural network, for large datasets or complex structures, each iteration may take a long time and the cost of evaluating the objective function using the aforementioned methods is too high. Therefore, the Bayesian Optimization Algorithm arises as a solution which finds a suitable set of hyper-parameters after training fewer networks [87]. This method uses a probabilistic surrogate model of an unknown objective function $f(x)$ and the optimization problem is the following [88]:

$$x^* = \arg\max_{x \in X} f(x) \tag{78}$$

Where X is the space of possible values of the hyper-parameters to be tuned and x^* is the optimal solution. The function of the model can be considered as a stochastic Gaussian process because it combines the distribution of each hyper-parameter.

The Bayesian optimization is a sequential method, which means that it considers the past evaluation results to select a new set of parameters that may outperform the last ones in the surrogate function. The main objective is to update $f(x)$ at each iteration to reduce the uncertainty of the model and obtain a more accurate result. The last iteration is not necessarily the best one, but it helps to build the probabilistic model and to get closer to a more accurate solution. The algorithm steps are illustrated in Figure 3.55.

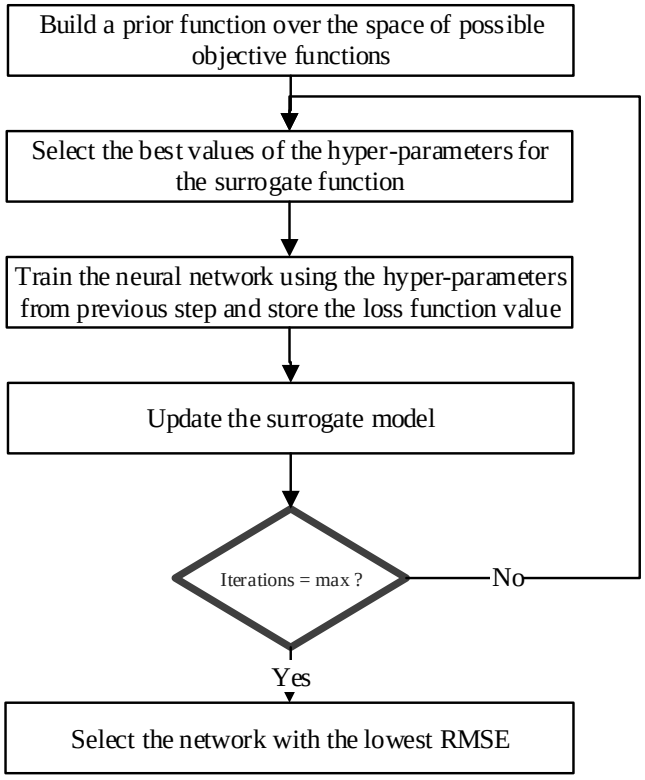

Figure 3.55. Bayesian optimization algorithm.

The key elements of Bayesian optimization are the model of the function and the Acquisition function. The first refers to the surrogate function, which for the case of LSTM NN hyper-parameters is a Gaussian process, as mentioned before. The second one refers to a function that is optimized in order to find the location of the next observation. It is done by evaluating the candidate points in the surrogate function. The chosen Acquisition function was the Expected Improvement per Second Plus (*EIpS*). Choosing the correct functions gives a good balance between exploration (large uncertainty in the surrogate model) and exploitation (model prediction is high), which is desirable.

4 OTHER APPLICATIONS OF THE PROPOSED METHODS

4.1 Parameter estimation of a power factor correction converter

4.1.1 Motivation

Power factor corrector (PFC) converters are devices aimed to increase the power quality of a distribution system by improving the power factor and decreasing the total harmonic distortion (THD) [103], [104]. They are mainly used in applications feeding a large number of electronic loads. PFC converters are found in different applications, including low power industrial sectors, residential and commercial distribution systems. These electronic loads generate harmonic currents and inject reactive power to the electrical system, thus resulting in a low power factor and high total harmonic distortion (THD) [105]. In these scenarios, the inclusion of a PFC converter is necessary in order to fulfill the requirements of the international power quality standards, such as the IEEE Std. 519 [106]. In particular, boost PFCs are widely used in household appliances, laptop adapters, on-board chargers and aircraft power supplies, among others [107]. When supplying switching-mode power converters such as the boost PFC, it is required to add an electromagnetic interference (EMI) filter at its input in order to attenuate the conducted EMI disturbances generated by the electronic equipment towards the power line [108] and fulfill the stringent requirements of EMI-related international standards. Companies of the aforementioned sectors typically integrate the boost PFC and EMI filters to systems that include many other power devices and components from different manufacturers. These companies need accurate models of their devices to perform several tasks, such as the design of controllers, predictive maintenance, calculation of the energy consumption, etc. [109]. However, manufacturers of power devices often do not provide enough information regarding the topology or the inner components characteristics due to confidentiality reasons [14]. To generate accurate discrete models of power electronics devices used during the design and optimization stages, engineers are required to know the values or parameters of the constitutive components in advance [19]. Therefore, it is highly appealing to develop a method to estimate these values in order to develop models to replicate the behavior of power electronics devices with high accuracy.

At the recent knowledge, there are no studies dealing with the topic of parameter identification of a boost PFC with an input EMI filter. The technical literature reveals that most of the works conducted on EMI filters, either identify the filter from of a simplified transfer function [110] or perform an electromagnetic analysis of the filter components [111], [112], thus not being practical to obtain the actual values of the filter parameters. It is straightforward to deduce that there is an imperious need to non-intrusively identify all parameters of the electronic device at once from the

input/output voltages/currents, because the input/output terminals are often the only accessible points.

4.1.2 Boost power factor correction converter

The boost PFC analyzed in this section is an AC-DC converter used to obtain an output DC voltage from an AC source with a high power factor [113]. This converter is widely used because it is capable of supplying power to multiple loads, while continuously regulating the output voltage [114], being desirable in many industry applications. The boost PFC is a switched mode power converter (SMPC) that applies a pulse width modulation (PWM) strategy to convert the electrical power efficiently. A side effect of this conversion is related to the generated high-frequency switching harmonics, which induce the parasitic characteristics of the different elements in the circuit. They also generate electromagnetic interference (EMI), which is a disturbance affecting electric and electronic circuits by conduction, electromagnetic induction or electrostatic coupling, which tends to degrade the behaviour of the affected circuits. Then, to mitigate this interference and to satisfy the EMI standard, it is necessary to add an EMI filtering stage at the input of the boost PFC converter.

Figure 4.1 shows the block diagram of the power converter to be identified. It is divided into four different stages, each one including different physical and non-physical parameters to be identified. These four stages are the EMI filter, the single-phase AC-DC rectifier, the DC-DC boost converter and the control loop of the SMPC converter.

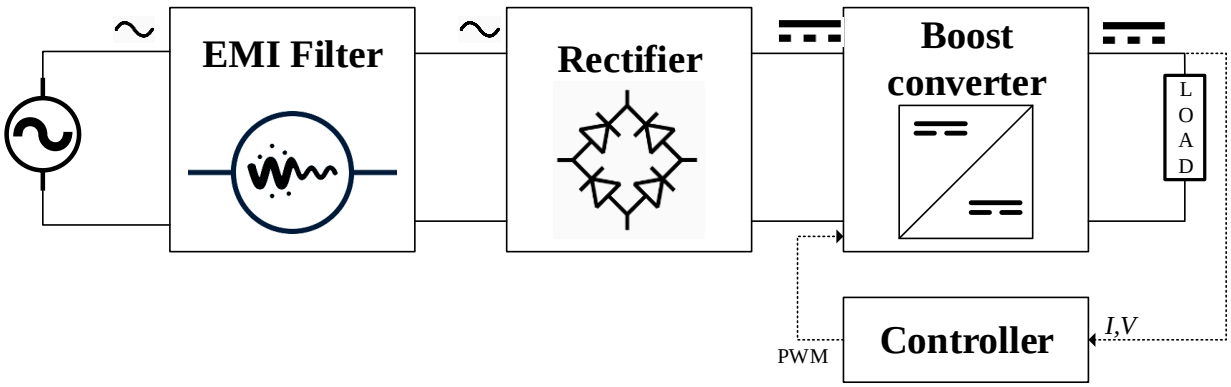

Figure 4.1. Block diagram of the boost PFC which includes an EMI filter.

The topologies of the EMI filter and the boost PFC converter are based on commercially available components. The first one is the power line filter model 10VN1, manufactured by Corcom. It consists of an EMI filter that is used between the power line and the electronic equipment to attenuate the conducted EMI disturbances generated by the electronic equipment towards the power line [108]. An EMI/RFI power line filter is analyzed, which is designed for providing

differential- and common-mode attenuation for digital equipment such as switching power supplies, over the 10 kHz – 30 MHz frequency range. Figure 4.2 shows the circuit of the EMI filter used as the input stage of the boost PFC. It is seen that there are 12 unknown parameters to be identified, corresponding to the passive elements of the circuit. Normally, the values of the coupled inductors (i.e. L_1 and L_2) and the capacitors with common ground (i.e., C_3 and C_4) are identical, thus reducing the number of parameters to be estimated and simplifying the identification process.

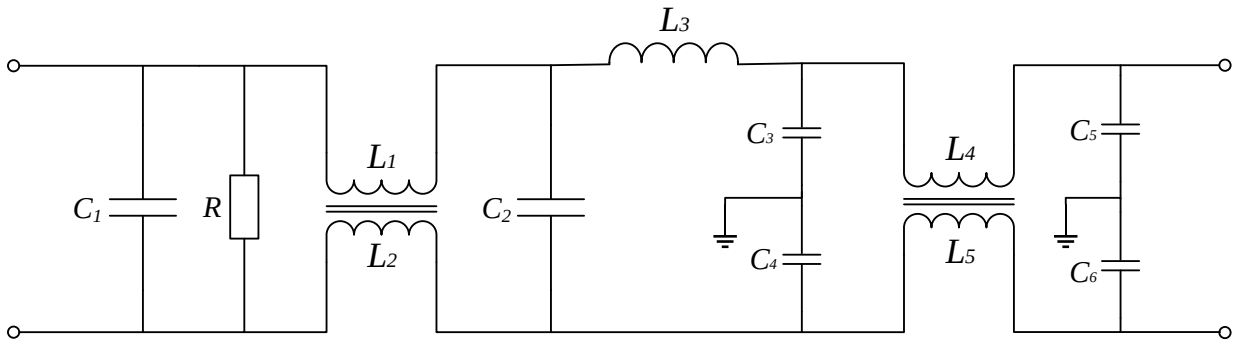

Figure 4.2. EMI filter to be identified.

The AC-DC boost PFC converter consists of a single-phase rectifier connected to a step-up high-frequency switching DC-DC boost converter that is regulated by means of two control loops (voltage and current). The boost PFC converter studied in this thesis is the evaluation module model ISA102V2 manufactured by ST, which is an 80 W high performance transition mode PFC board based on the L6562A controller. The AC-DC conversion is done by means of a full wave diode bridge with an output capacitor for smoothing the rectified voltage. The rectifier feeds a boost converter with a classic topology that includes the parasitic resistance of the capacitor and the inductor. Due to the high-switching frequencies of the transistors, it is also important to consider the parasitic resistance of these elements.

Figure 4.3 presents the circuit of the boost PFC and the elements to be estimated. Regarding the rectifier, the exponential model of the diode was used, since it accurately represents its behaviour [43]. It relates the current that flows across the diode to its voltage drop as,

$$I = I_s \cdot \left(e^{qV/(NkT_m)} - 1 \right) \tag{79}$$

where I and I_s refer to the diode current and saturation current, respectively, V is the voltage drop across the terminals of the diode, q is the elementary charge of an electron, k is the Boltzmann constant and T_m is the working temperature.

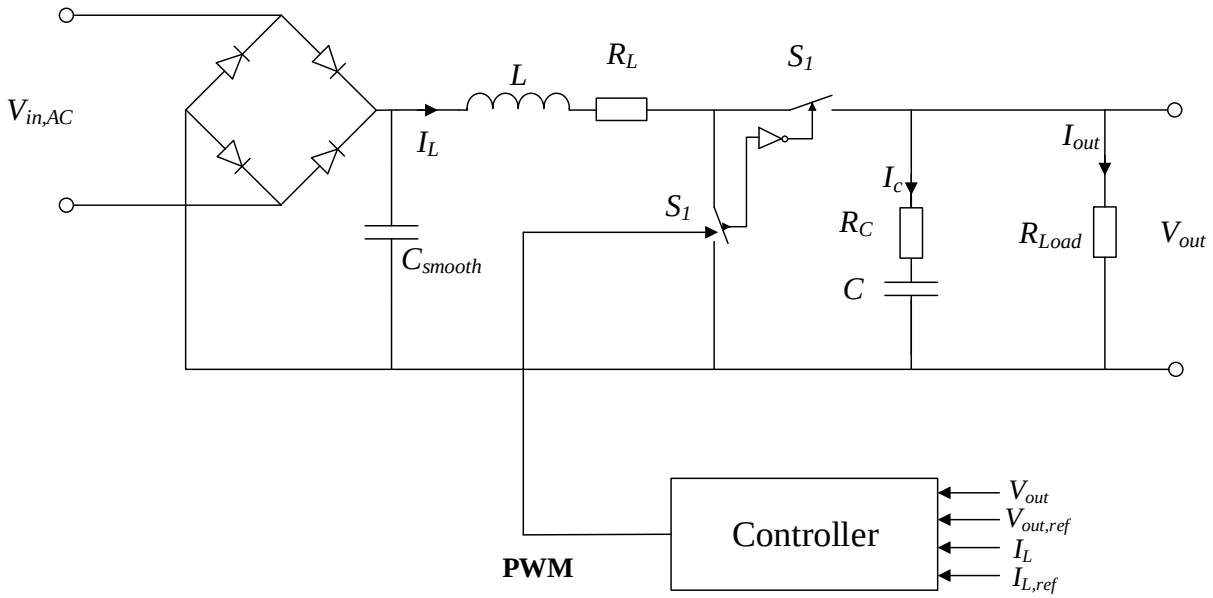

Figure 4.3. Boost PFC converter to be identified.

The controller of the DC-DC converter has two main objectives. The first one is to maintain a power factor close to 1 by using an inner current control loop, so the input voltages and currents should be almost in phase. The second objective is to deliver a constant output voltage by means of an outer voltage control loop [115]. It regulates the output voltage to a given reference value. Both loops apply a PI compensation, thus, creating a robust control scheme of the boost PFC converter.

Figure 4.4 presents the block diagram of the controller along with its circuitry. Regarding the parameters to be estimated, the current control is a PI compensator, which is normally implemented in the microcontroller unit of the converter and can be modelled as a transfer function. Figure 4.4 indicates that the reference value of the inductor current is given by the output generated by the outer voltage loop, showing the interconnection between both control loops. The compensation of the outer voltage control loop is performed by a type 3 operational amplifier, as shown in Figure 4.4. (b). This type of compensation provides two poles and two zeros, being used when a phase boost greater than 90 degrees is needed [39]. The reference voltage is specified by design, and the values of the resistors and capacitors must be identified.

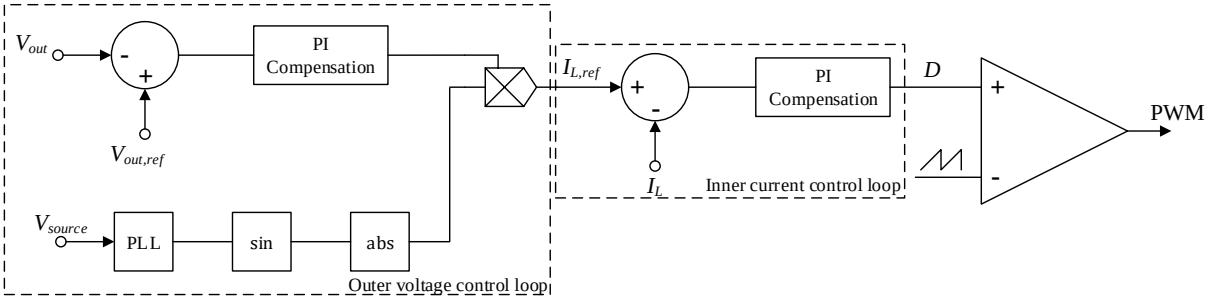

(**a**)

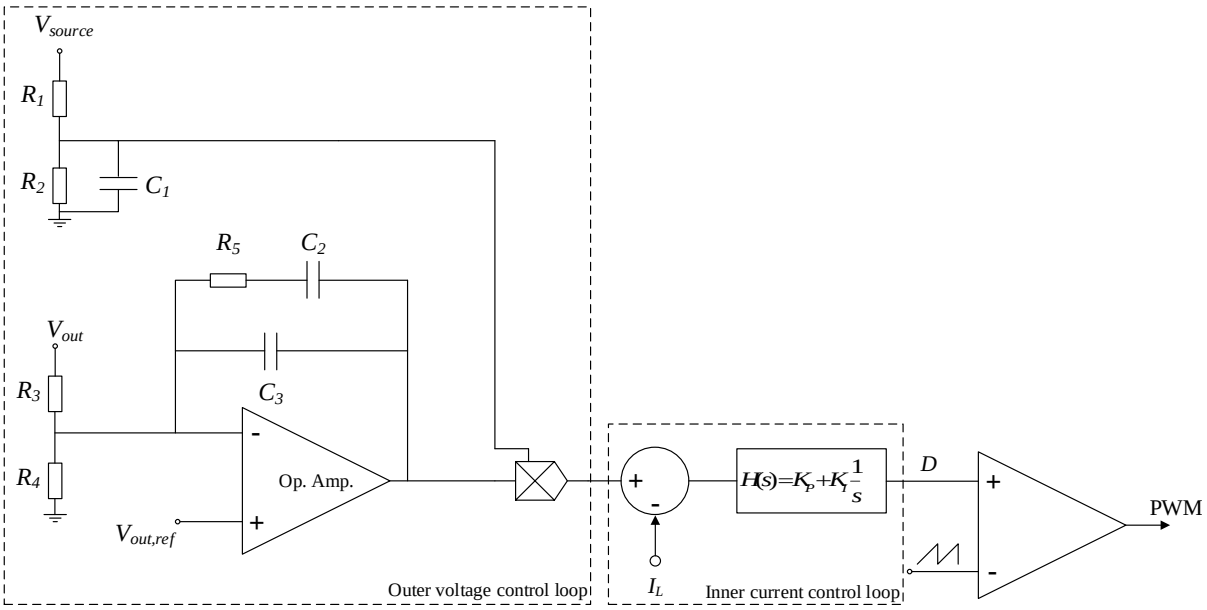

(**b**)

Figure 4.4. Boost PFC controller. (a) Block scheme. (b) Circuit.

Given the topologies of the four blocks presented in this section, there are 33 unknown values to be estimated. They correspond to the parameters of the EMI filter $(R, C_1, C_2, C_3, C_4, C_5, C_6, L_1, L_2, L_3, L_4, L_5)$, the single phase rectifier $(I_S, N, T_m, R_{diode}, C_{smooth})$, the boost converter $(C, R_C, L, R_L, R_{S1}, R_{S2})$ and the control loops $(R_1, R_2, R_3, R_4, R_5, C_1, C_2, C_3, K_P, K_I)$. The following Sections present the proposed methodology to identify these sets of parameters and the data acquisition procedure.

4.1.3 Methodology

Given the complexity of the circuit and the extensive number of variables to be identified, it is necessary to define a methodology that allows the identification of all the parameters with high accuracy and without comprising the total simulation time. Identifying all parameters at once may lead to an incorrect solution because it is very likely that the optimization approach finds a local minimum that differs from the actual parameters of the converter.

Figure 4.5 shows the proposed algorithm, which aims to identify certain sets of parameters separately in order to reduce uncertainty and obtain better results.

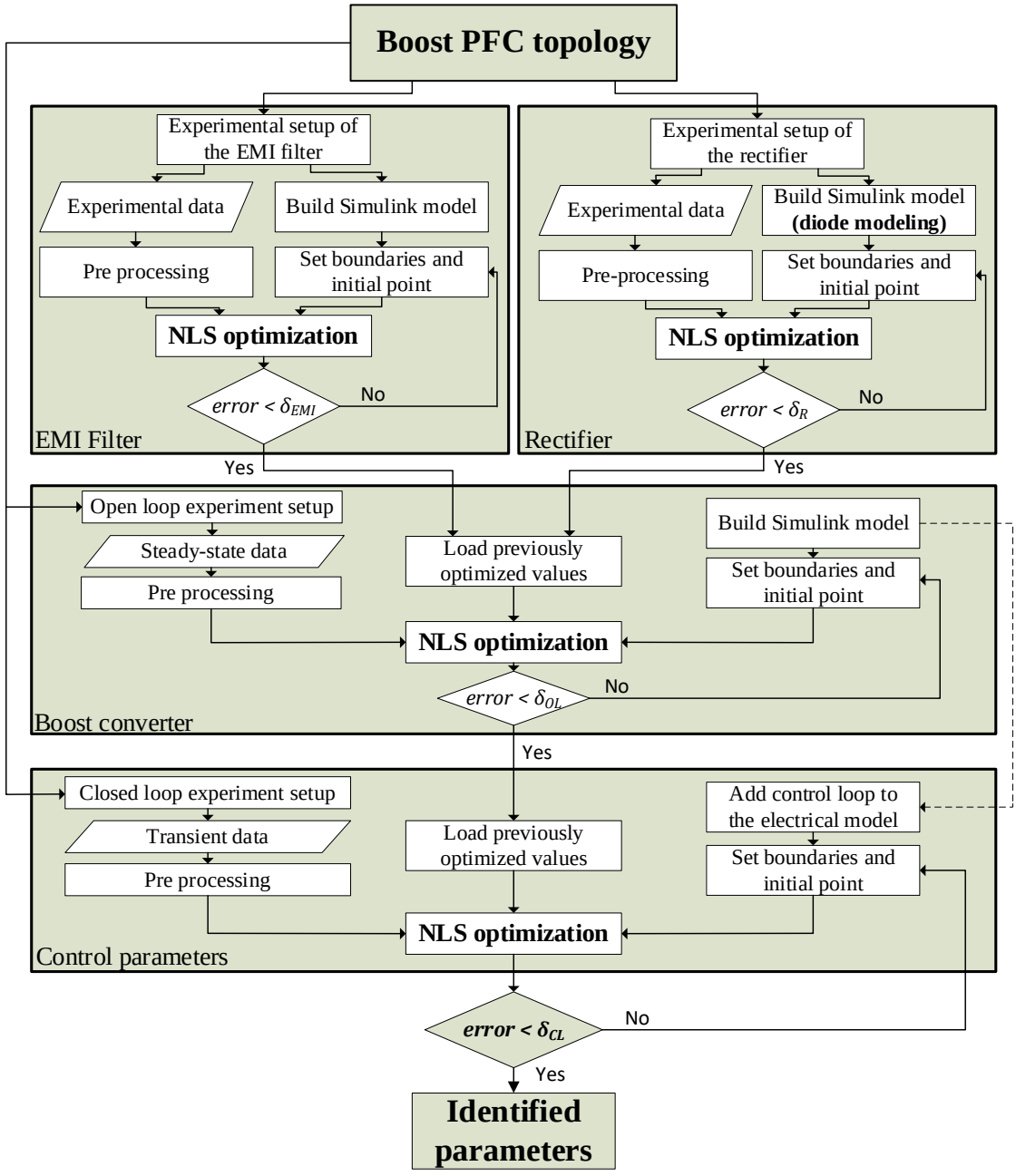

Figure 4.5. Proposed methodology to identify the parameters of the boost PFC converter.

The algorithm is divided in four different parts, which correspond to the four blocks of the diagram shown in Figure 4.1 (EMI filter, rectifier, boost converter and controller). The first step of the methodology consists in defining the circuit topology of all components and to specify the variables to be estimated. The next step is to identify the parameter values of the EMI filter and the rectifier, these being independent processes, which can run in parallel. The third stage

corresponds to the open loop parameter estimation of the boost converter, where the previously identified values and topologies of the EMI filter and rectifier are used. Finally, the control or closed loop parameters of the converter are estimated using the NLS algorithm and the previously obtained parameters. A thoroughly explanation of each optimization stage is given as follows:

- EMI filter: This stage aims to identify the 12 values of the passive elements of the EMI filter. Firstly, the experimental setup and the data to be acquired in the laboratory are defined. To force a sufficient rich response of the EMI filter that enables identifying its parameters, a capacitor was connected at the output terminals in parallel with the resistive load when a periodic square waveform voltage was applied to the input terminals by means of an AC source. To perform the identification process, the voltage and current at the input and output terminals are needed. To simulate the high output impedance of the function generator used to generate the square waveform, a resistance R_{in} in series with an inductance L_{in} was added to the Simulink® model, and the values of such parameters were identified jointly with the parameters of the filter. To enhance the performance of the identification process, the data is divided into two sets, which are used in the optimization process, i.e., the data centered in the rising edge of the periodic square waveform, and in the falling edge of the period. This is done to avoid using a complete period of the signals by focusing on the intervals that contain the relevant information.

- Rectifier: The identification process of the parameters of the single-phase rectifier is independent from the other elements of the boost PFC converter, since it just uses the acquired signals at the input and output terminals of the rectifier. This process aims to estimate the diode and the output capacitor parameters. The complexity of this stage depends on the diode model that is considered, which in this case is the exponential, as described by (1).

  The parameter estimation process uses the data of three different experiments of the rectifier (by changing the load connected at the output terminals) in order to obtain an accurate representation of the exponential model. Therefore, the TRRNLS optimization algorithm identifies the values by fitting the curves of three operating points of the rectifier.

- Boost converter (open loop): The third stage of the proposed methodology is the estimation of the boost converter electrical components. The available data are the currents and voltages at the input terminals of the EMI filter and at the output of the boost converter. Therefore, the previously estimated parameters of the EMI filter and the rectifier are required in this

optimization process. The parasitic components must be considered in order to obtain accurate results.

The data used in this stage is based on the steady state behavior of the converter when it is connected to a certain load. The timespan is chosen in order to increase the simulation speed without compromising accuracy. Thus, the parameters can be estimated by analyzing a small number of periods (i.e., 2 or 3).

- Control parameters (closed loop): The last stage consists in identifying the boost PFC control loop values. It also re-estimates the value of the capacitor of the converter because it affects the transient response of the outer voltage loop [115]. It uses the estimated values of the previous stages and adds the voltage and current control loops to the Simulink model. The experimental setup is the same as in the open loop identification stage. However, the converter is subjected to a load change at the output terminal to obtain its transient response. The timespan of the data acquired is chosen depending on the time that the converter requires to reach the steady state. In this stage the NLS algorithm requires more time compared to the other stages, because it uses a model with a higher complexity and the dataset is larger.

As shown in Figure 4.5, each stage of the proposed algorithm includes a data pre-processing step which is fundamental to run the optimization process. This step consists of resizing, filtering and synchronizing the raw data according to the data generated by the Simulink models. The resizing consists of reducing the number of points of the data measured without losing relevant information. It is done by means of an interpolation and it directly affects the computational burden of the process. After resizing the data, the next step is to eliminate the high-frequency noise by applying a low-pass finite impulse response filter as it is the moving average. The number of considered points depends on the type of data. Finally, the time vector of the measured signals is modified in order to synchronize the data generated from the simulations with the experimental data, which is essential for curve fitting purposes.

Another important aspect to consider is the definition of the seed point and the upper and lower boundaries of the variables to be identified. The selection of the initial point is based on a-priori knowledge of the different elements of boost PFC converters and the boundaries are set to cover six orders of magnitude, i.e., a typical initial value of the inductor in a boost converter is 1 µH, so that the lower and upper boundaries are set to 1 nH and 1 mH, respectively.

After each TRRNLS optimization loop, the error value is compared to a fixed value δ that is selected at each stage of the proposed algorithm. This value is set to 0.01 for all stages. If the

error value is higher than the defined threshold, the initial point and the constraints are modified by multiplying the obtained values by a random number between 0.75 and 1.25 and the NLS optimization starts again. This is done to assure that the process reaches a different local minimum than the last one. The algorithm advances to the next step when the error value is lower than δ, otherwise it iterates. Equation (5) defines the error, which is calculated based on the experimental and estimated values of the signals used in the optimization process.

$$error = \sum_{i=1}^{Sig} Mean\left(\left| \frac{x_{i,norm,\exp} - x_{i,norm,est}}{x_{i,norm,\exp}} \right| \right) \tag{80}$$

where *x* refers the signals that are fitted in the TRRNLS optimization. The values are normalized to have the voltages and currents of similar magnitudes, which allows a proper comparison

4.1.4 Experimental setup

The EMI filter and boost PFC used in the laboratory for the parameter estimation process are the Corcom 10VN1 and the STMicroelectronics STEVAL-ISA102V2, respectively. The maximum rated voltage of the filter is 250 VAC, its rated current is in the range 6-10 A and the operating frequency could be 50 Hz or 60 Hz. The circuit board and the specifications of the boost PFC are listed in Figure 4.6 and Table 4.1, respectively.

Figure 4.6. STEVAL-ISA102V2 circuit board (Boost PFC converter).

Table 4.1. STMicroelectronics STEVAL-ISA102V2 Boost PFC converter specifications.

Parameter	Value
Line voltage range	88 to 265 VAC
Output voltage	400 VDC

Rated output power	80 W
Switching frequency	35 kHz
Minimum efficiency	92%

The equipment used to measure the voltages and currents of the different devices consisted of a 4 channel oscilloscope (Tektronix MDO3024 200 MHz 2.5 GS/s; Tektronix, Beaverton, OR, USA), two high-frequency current probes (Tektronix TCP0030A 0.001-20 A 120 MHz; Tektronix, Beaverton, OR, USA) and two high-frequency differential probes (Tektronix THDP200; Tektronix, Beaverton, OR, USA).

Figure 4.7 presents the experimental setup used to acquire the necessary data for the parameter estimation process. Figure 4.7 (a) shows the setup used for the EMI filter identification stage of the proposed methodology, while the experimental setup presented in (b) is used for the identification of the other stages of the methodology.

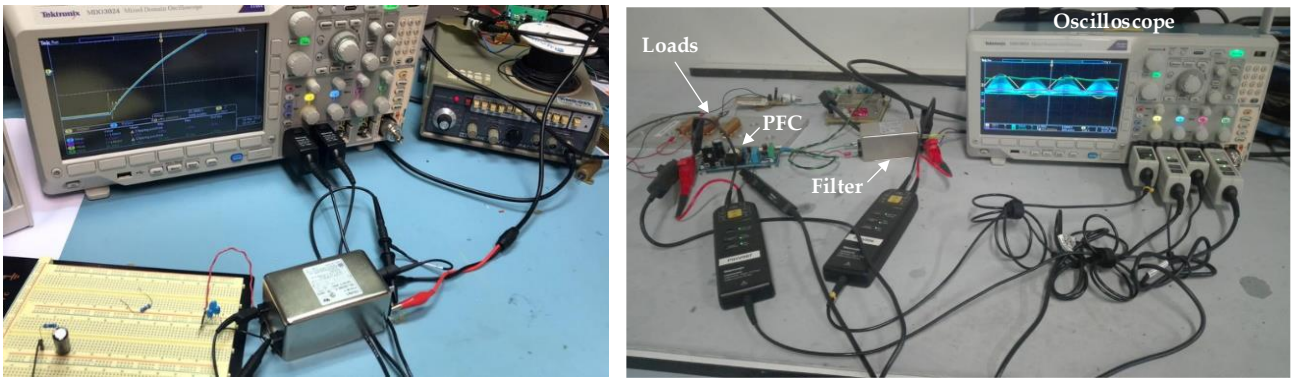

(**a**) (**b**)

Figure 4.7. Experimental setup meant for the: (a) Corcom 10VN1 EMI filter parameter estimation; (b) STMicroelectronics STEVAL-ISA102V2 AC-DC boost PFC converter connected to the EMI filter.

4.1.5 Results

This section presents the experimental results obtained with the EMI filter and the boost PFC converter.

4.1.5.1 EMI filter parameter identification

According to the methodology presented in Figure 4.5, the parameter identification of the EMI filter is the first stage of the process. To this end, the data is acquired based on the procedure explained in Subsection 4.1.3. The periodic square wave voltage applied to the filter has an amplitude of 2 V and a frequency of 50 Hz, while the load consists of an 11 µF capacitor connected in parallel to an 11 Ω resistor. Table 4.2 presents the minimum, maximum, initial and optimal

(identified) values of the TRRNLS optimization algorithm. It also shows the theoretical values given by the manufacturer. The simulation time was approximately of 8 hours and 42 minutes, using an Intel® Xeon® CPU, ES.1650 v2 3.50 GHz, with 64 GB of RAM memory.

Table 4.2. Optimization conditions of the NLS identification algorithm of the EMI filter and comparison of actual and identified parameters.

Parameter	Minimum (*lb*)	Maximum (*ub*)	Initial	Actual (datasheet)	Identified	Error
R	1 Ω	1 MΩ	1 kΩ	270 kΩ	260.15 kΩ	3.67%
C_1	1 nF	1 mF	1 µF	0.68 µF	0.62 µF	8.82%
C_2	1 nF	1 mF	1 µF	0.47 µF	0.45 µF	4.26%
C_3	1 nF	1 mF	1 µF	0.01 µF	0.0103 µF	3%
C_4	1 nF	1 mF	1 µF	0.01 µF	0.0103 µF	3%
C_5	1 nF	1 mF	1 µF	0.0055 µF	0.0047 µF	14.5%
C_6	1 nF	1 mF	1 µF	0.0055 µF	0.0047 µF	14.5%
L_1	10 nH	10 mH	10 µH	6.36 mH	6.42 mH	0.94%
L_2	10 nH	10 mH	10 µH	6.36 mH	6.42 mH	0.94%
L_3	10 nH	10 mH	10 µH	0.06 mH	0.059 mH	1.7%
L_4	10 nH	10 mH	10 µH	1.47 mH	1.35 mH	8.16%
L_5	10 nH	10 mH	10 µH	1.47 mH	1.35 mH	8.16%

Figure 4.8 and Figure 4.9 show the experimental and estimated signals at the input and output terminals of the EMI filter, as well as the Bode magnitude and phase plots of the filter. The estimation is done by simulating the electrical model using the identified parameters presented in Table 4.2. The results show a good agreement between experimental and simulated results considering the identified parameters. It is also appreciated that the frequency response is almost the same for both cases.

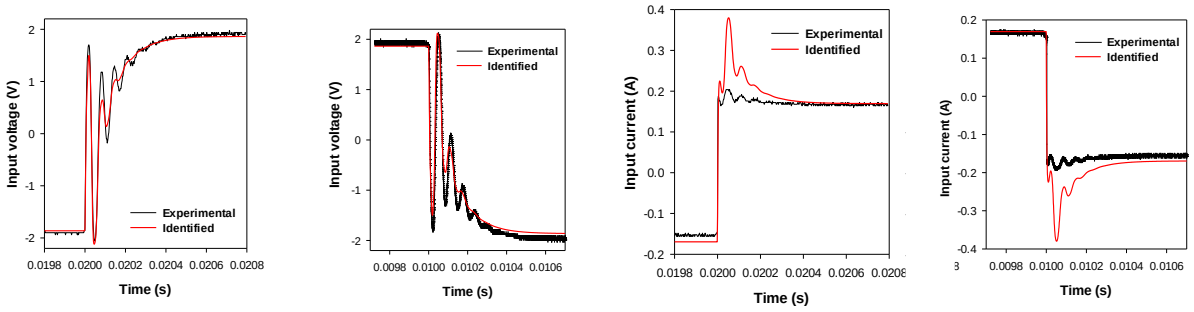

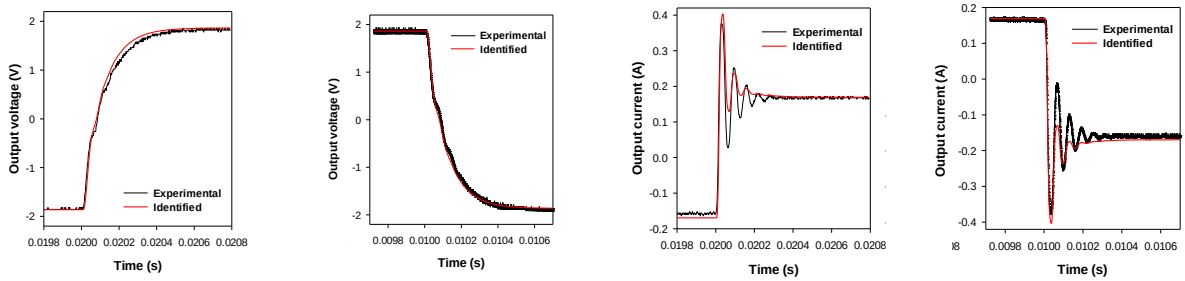

(e) (f) (g) (h)

Figure 4.8. EMI filter. Experimental versus simulated data using the identified parameters. (a) Rising edge input voltage; (b) Falling edge input voltage; (c) Rising edge input current; (d) Falling edge input current; (e) Rising edge output voltage; (f) Falling edge output voltage; (g) Rising edge output current; (h) Falling edge output current.

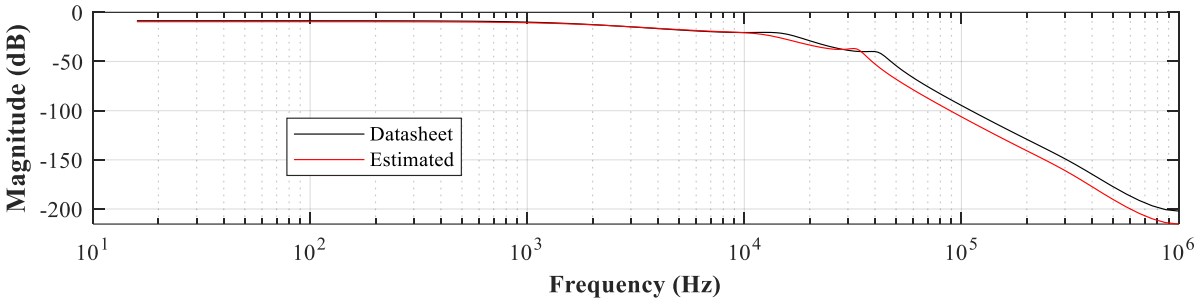

(a)

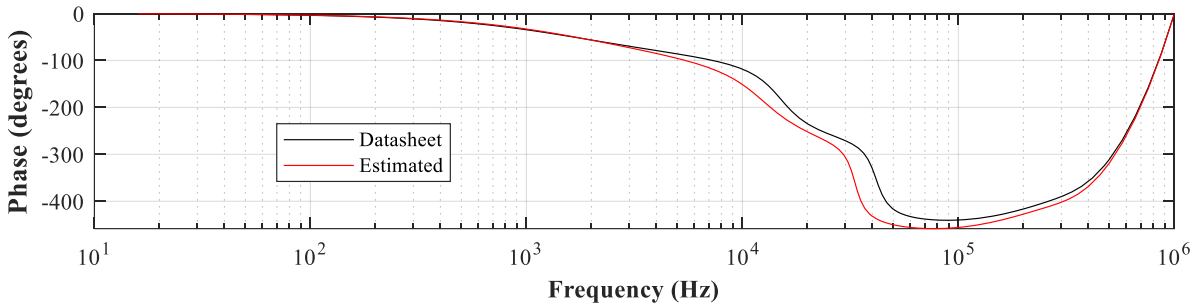

(b)

Figure 4.9. Comparison of the actual and the estimated bode plot of the EMI filter: (a) Magnitude; (b) Phase.

4.1.5.2 Rectifier parameter estimation

Similarly to the process described in Chapter 2, the rectifier parameters were estimated. Since the single phase rectifier is integrated in the evaluation module of the boost PFC used in this section, the data acquired in this stage is based on the experimental setup presented in Figure 4.7 (b). However, the EMI filter is not used and the voltage and current probes are placed at the input of the boost PFC and at the smoothing capacitor. The rectifier is fed with an input signal of 230 V and 50 Hz. The rectifier must be tested under different operating points due to the requirements of the exponential model of the diode,so that the output loads were selected to 3.9 kΩ, 1.95 kΩ and 7.8 kΩ. The simulation time was about 1 hour and 7 minutes, which is relatively fast considering this type of problem.

Table 4.3 presents the main values of the TRRNLS optimization procedure and compares the optimal point to the actual values of the rectifier. It is important to mention that some values are not provided by the manufacturer.

Table 4.3. Optimization conditions of the NLS identification algorithm of the single-phase rectifier and comparison of actual and identified parameters.

Parameter	Minimum (*lb*)	Maximum (*ub*)	Initial	Actual (datasheet)	Identified	Error
I_S	1 pA	1 mA	1 µA	-	4.86 mA	-
T_m	270 K	350 K	300 K	-	328.2 K	-
N	0	2	1	-	0.1494	-
R_{diode}	1 µΩ	1 Ω	1 mΩ	-	12 mΩ	-
C_{smooth}	1 nF	1 mF	1 µF	0.22 µF	0.2112 µF	4%

Since there is not available data regarding the theoretical values of the rectifier parameters, it is necessary to compare the measured output voltage and current with the estimated ones, as done in Figure 4.10. It is seen that the estimation reproduces with high fidelity the amplitude, mean value and frequency of the output signals of the single-phase rectifier. Figure 4.10 (c) shows that the high-frequency switching characteristics of the output current are also replicated with accuracy. Figure 4.11 shows the estimation of the forward I-V curve of the diode, which is calculated by using the identified parameters, and it is compared with the forward I-V curve provided by the manufacturer.

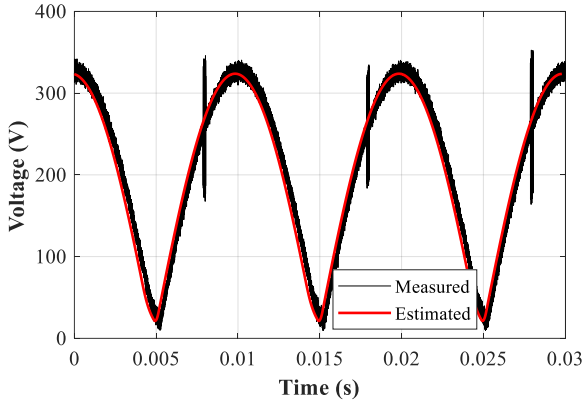

(a)

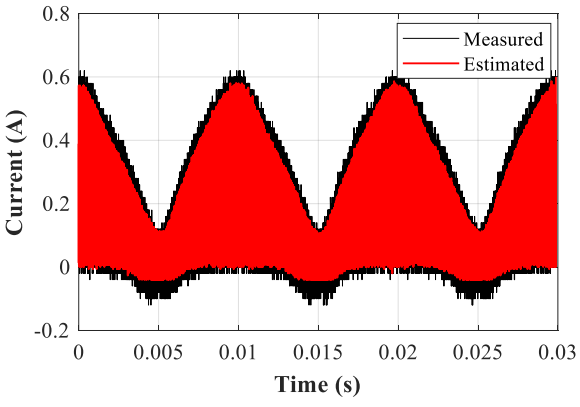

(b)

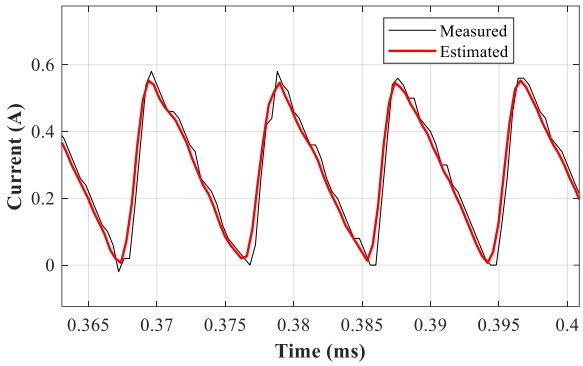

(c)

Figure 4.10. Measured and estimated waveforms of the rectifier. (a) Output voltage; (b) Output current; (c) Output current switching characteristics.

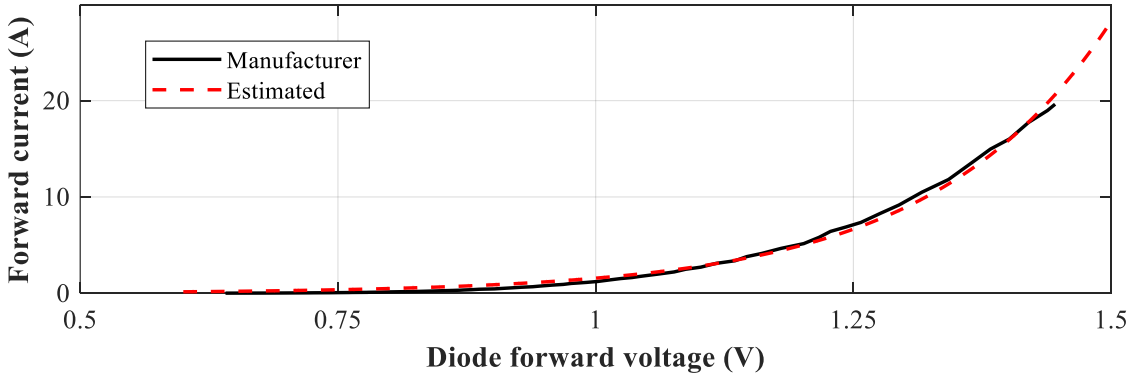

Figure 4.11. Manufacturer and estimated I-V curves of the rectifier diodes

4.1.5.3 Boost PFC converter parameter identification

After identifying the parameters of the input filter and the AC-DC rectifier, the next stage of the proposed methodology is the identification of the steady state parameters of the boost PFC converter. This process is carried out and the data is measured using the setup presented in Figure 4.7 (b). A load of 3.9 kΩ was connected to the output of the converter and the timespan of the measurements was set to to three times the switching period of the boost converter. The duty cycle value was fixed to 0.12 because the control loop is not considered in this stage.

Table 4.4 presents the values of the initial point and boundaries of the variables, as well as the comparison between the estimated and actual values of the passive elements. The simulation lasted for about 2 hours and 56 minutes.

Table 4.4. Optimization conditions of the NLS identification algorithm of the boost converter and comparison of actual and identified parameters.

Parameter	Minimum (lb)	Maximum (ub)	Initial	Actual (datasheet)	Identified	Error
C	1 nF	1 mF	1 µF	47 µF	33.2 µF	29.4%
R_C	1 µΩ	1 Ω	1 mΩ	19.4 mΩ	20.02 mΩ	3.20%
L	10 nH	10 mH	10 µH	0.7 mH	0.701 mH	0.14%
R_L	1 µΩ	1 Ω	1 mΩ	-	9.72 mΩ	-
R_{S1}	1 µΩ	1 Ω	1 mΩ	860 mΩ	882.8 mΩ	2.65%
R_{S2}	1 µΩ	1 Ω	1 mΩ	-	114.2 mΩ	-

The results presented in Table 4.4 show a high accuracy in the identification of the parameters of the boost converter except for the capacitor. However, as it was mentioned above, this parameter also affects the transient behaviour of the converter, thus, it is re-identified in the next stage of the process.

Figure 4.12 presents the measurement and steady-state estimation of the input and output signals of the converter. It is appreciated that the estimated curves fit the acquired data with high precision and the ripple of the signals is the same.

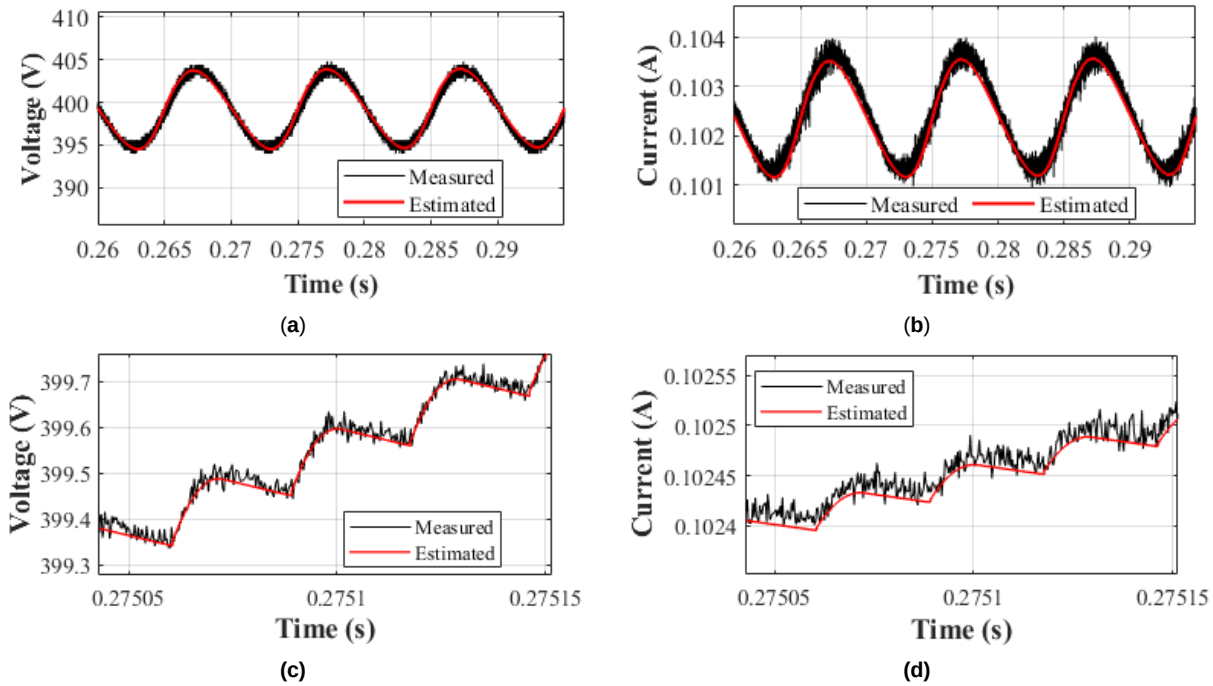

Figure 4.12. Experimental versus simulated data of the boost converter: (a) Output voltage (timespan is three periods of AC source frequency); (b) Output current (the timespan is three periods of AC source frequency); (c) Output voltage (the timespan is three periods of the PWM switching frequency); (d) Output current (the timespan is three periods of the PWM switching frequency).

4.1.5.4 Control loop parameter identification

The last stage of the identification procedure consists in finding the parameters related to the outer voltage and inner current control loop. It uses the models and identified values of the EMI filter, the rectifier and the boost converter in order to estimate the controller parameters. The experimental setup presented in Figure 4.7 (b) is used to acquire the data. A sudden load change is applied to capture the transient response of the boost PFC. The output load of the converter changes from 3.9 kΩ to 1.95 kΩ and the timespan of the measurements is defined according to the time that the converter needs to reach the steady state. As mentioned in the previous subsection, the value of the boost converter capacitor is also identified in this stage, and its initial or seed value is the estimated value in the previous stage.

Table 4.5 shows the initial, minimum, maximum, estimated and theoretical values of the controller parameters. The actual proportional and integral constants are not specified because they are not given by the manufacturer. The time required in this optimization was 7 hours and 46 minutes.

Table 4.5. Optimization conditions of the NLS identification algorithm of the control loop and comparison of actual and identified parameters.

Parameter	Minimum (lb)	Maximum (ub)	Initial	Actual (datasheet)	Identified	Error
C	1 µF	100 µF	33.2 µF	47 µF	44.2 µF	5.96%
R_1	10 Ω	10 MΩ	10 kΩ	2 MΩ	1.973 MΩ	1.35%
R_2	10 Ω	10 MΩ	10 kΩ	15 kΩ	14.82 kΩ	1.2%
R_3	10 Ω	10 MΩ	10 kΩ	2 MΩ	2.05 MΩ	2.5%
R_4	10 Ω	10 MΩ	10 kΩ	12.7 kΩ	12.002 kΩ	5.50%
R_5	10 Ω	10 MΩ	10 kΩ	22 kΩ	22.36 kΩ	1.64%
C_1	1 nF	1 mF	1 □F	10 nF	9.38 nF	6.2%
C_2	1 nF	1 mF	1 µF	2200 nF	2069.5 nF	4.7%
C_3	1 nF	1 mF	1 µF	150 nF	148.3 nF	1.13%
K_P	10^{-6}	10^{6}	1	-	0.0892	-
K_I	10^{-6}	10^{6}	1	-	1258.5	-

The results in Table 4.5 show that the identified value of the boost PFC capacitor is more accurate than the estimation in the previous stage, while the values of the outer voltage control loop are identified with high precision.

Figure 4.13 compares the measured and estimated curves when a load change occurs. It is appreciated that the signals simulated with the identified parameters are able to replicate the behaviour of the boost PFC converter.

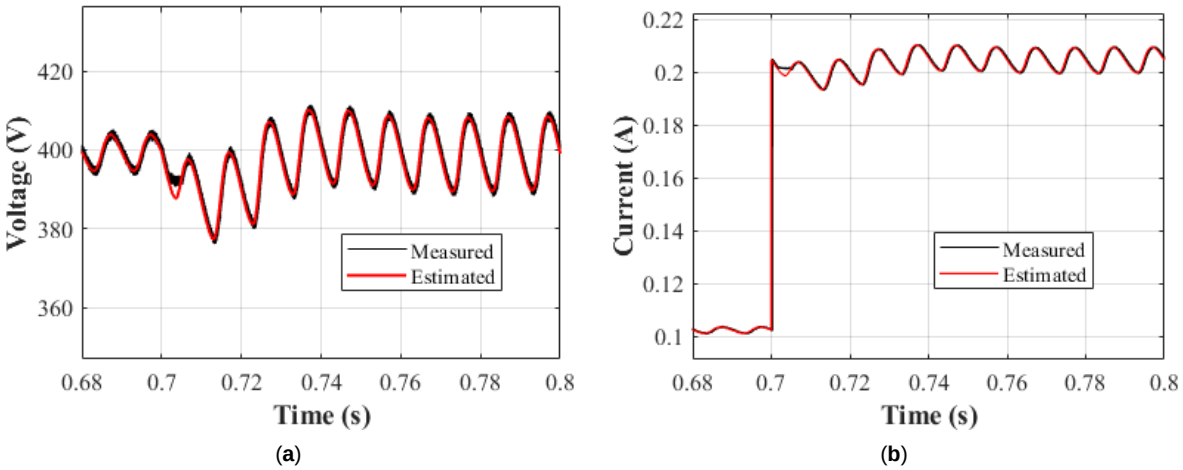

(a) (b)

Figure 4.13. Measured and simulated transient response of the boost PFC. (a) Input voltage. (b) Input current.

The average relative error of the estimated parameters is 4.473 %, which has been calculated based on the error values presented from Table 4.2 to Table 4.5. Finally, the error of the fitting process is 0.00082, which has been calculated by applying Equation (80) to the signals displayed in Figure 4.13 (a) and (b). Note that this value is more than ten times below the defined threshold $\delta = 0.01$.

4.2 Prognostics of DC-DC Converters used in electric vehicles

4.2.1 Motivation

Electrical machines are being broadly applied in different fields, including electric automobiles, aviation, trains, ships, or industry among others, playing a key role in these applications. However, faults in electrical machines have damaging effects, posing at risk the safety of the involved applications [116]. Therefore, the application of condition monitoring strategies is a must. It is based on applying different methods to identify changes in a system because of fault development or the degradation of the state of health (SoH), thus generating an alarm to indicate the occurrence of a failure [117]. To apply effective on-line condition monitoring approaches it is necessary to develop methods for detecting degraded or anomalous operational modes in the early stage, much before the development of important faults, while minimizing false alarm events [118], [119].

Therefore, predictive maintenance of electrical machines and drives is gaining popularity in different fields, from electric traction to industrial activities. There are several reasons, from the high capital cost and central importance electrical machines play in the process, to the heavy economic losses that unexpected faults can generate because of needed machine or parts replacements, loss of production due to its unavailability, or property damage to property and people injuries [120]. The imperious requirement of manufacturing more competitive equipment, together with the progress of digital technologies, has facilitated the acquisition of operational data, which can be processed by means of artificial intelligence methods to extract valuable information to apply data-driven diagnosis and maintenance approaches [121].

Power converters often operate in closed-loop systems, and thus, any change in one of their components will modify the operating point of other constituents and the resultant thermal stress, thus affecting overall system reliability. This change tends to accelerate the aging process of the affected part and the remaining components of the converter. It is generally accepted that electronic components exhibit a bathtub failure curve. It includes three stages, i.e., an initial infant mortality stage followed by a constant failure rate region and ending in the wear-out period. However, several deviations with respect to the bathtub curve have been reported [122]. It is known that capacitors and power switches are the power converter components with the highest failure rate [123], [124], capacitors accounting for around 30% failures in power converters [125]. Reliability plays a key role in power electronic systems, especially for those applications in which availability is a critical parameter, so that even under faulty conditions the application should be able to operate [126].

Capacitors are among the most critical components of power converters. They have a huge influence in the final cost, performance, and size of such electronic systems, although they exhibit the highest degradation rates and shorter lifespans among all power converter components [127]. Therefore, condition monitoring plays a key role to estimate the health status of capacitors and to apply predictive maintenance tasks for ensuring stability in the operation of power converter systems. The equivalent series resistance (ESR) and the capacitance of the capacitor are two widely used parameters for evaluating the health status of capacitors. Unlike the ESR, the capacitance of a capacitor is suitable for health monitoring of various types of capacitors. Therefore, it is more preferable for large-scale systems [127].

This section presents the design, implementation, and experimental validation of a novel method for fault prognosis for power converters using a deep learning-based parameter identification approach. The parameter identifier uses the TRRNLS method described in chapter 2 in order to compute real-time estimates of the analyzed parameters (capacitance and ESR) [128]. Since the capacitor is perhaps the most critical element in power converters, the evolution of two parameters, i.e., the ESR and the capacitance is used to determine and forecast the future condition of the capacitor and thus, of the power converter.

4.2.2 Powertrain of an electric vehicle

The powertrain of electric vehicles consists of various power converters that are in charge of delivering the power generated by the battery pack to the electric motor and the electronic loads of the vehicle [129]. The architecture of the electrical system may change depending on the specific characteristics of the vehicles. Nevertheless, there are specific components that can be found in most electric and hybrid electric vehicles [130]. Figure 4.14 shows a block diagram of a typical powertrain of an electric vehicle, which includes the different elements involved in the energy conversion process. Typically, there are three types of converters in the electrical system. These are a DC-DC high voltage bidirectional converter, a DC-DC low voltage bidirectional converter and a three-phase inverter that feeds the electric motor. However, in technologies that also consider a fuel cell as an energy source, another converter is included.

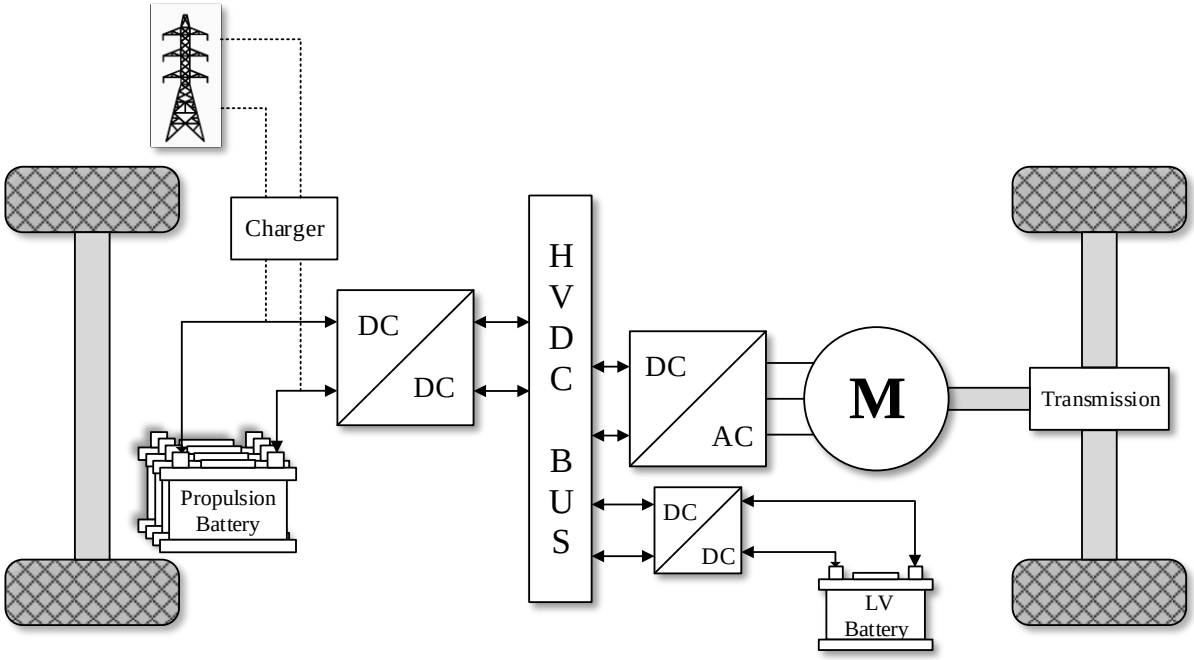

Figure 4.14. Powertrain of an electric vehicle.

DC-DC converters used in electric vehicles must meet certain conditions in order to guarantee a proper operation of the vehicle and to offer a reliable and efficient conversion process [129]. Some of these essential requirements include light weight, small volume, high efficiency, low electromagnetic interference, low ripple or control of the current flowing through the converter, among others [129]. Thus, switched mode power converters arise as a solution, since they are capable of fulfilling these requirements with high performance. These types of converters are widely used in multiple applications and provide high reliability to the electrical system of the vehicle.

Since power converters play a key role in the propulsion of electric vehicles, it is necessary to estimate their health status in real time in order to guarantee a correct operation of the powertrain and prevent possible failures. A brief analysis of the DC-DC converters used in these vehicles is necessary to better understand the possible failures that they may incur. The most critical power electronics element of the powertrain shown in Figure 4.14 is the bidirectional power converter, because it feeds the electrical machine that propels the automobile. Figure 4.15 presents the typical architecture of a DC-DC bidirectional converter used in automotive applications [131]. It is seen that the converter links the energy storage system to the electric motor of the vehicle, while allowing the current to flow in both directions. Among the elements of the converter shown in Figure 4.15, the transistors and the electrolytic capacitor are the most likely to fail [132], being the capacitor the main reason for power system breakdowns [132]. The degradation of these capacitors results in an undesired voltage ripple that affects the efficiency of the power converter.

The continuous operation of a degraded capacitor may lead to an irreversible damage of the DC-DC converter. Thus, this study focuses on the prognostics of the faultiest element of the bidirectional converter, which is the electrolytic capacitor.

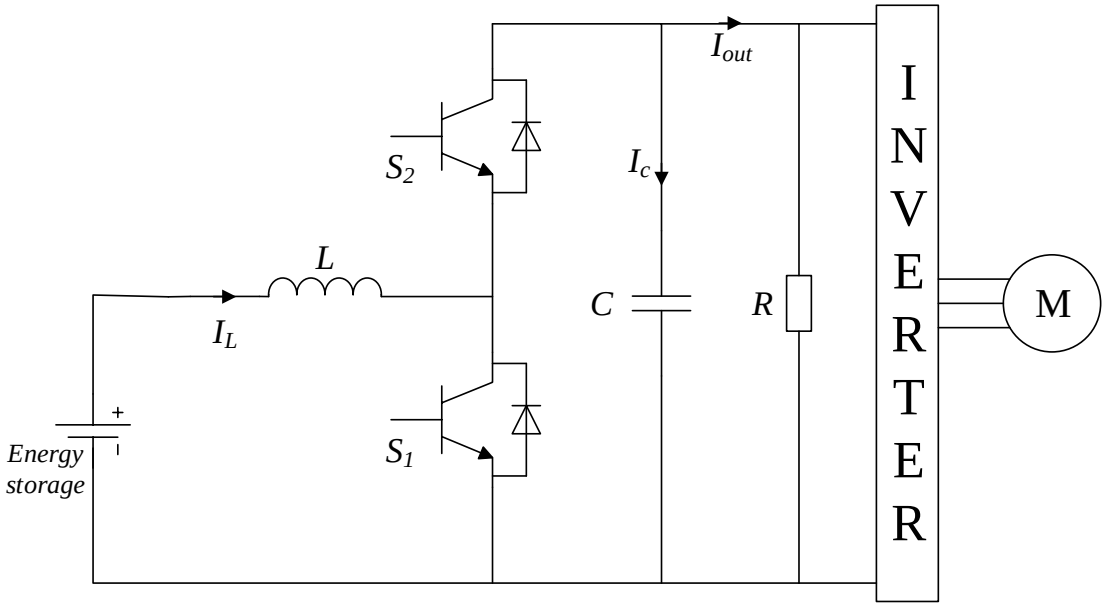

Figure 4.15. Typical topology of a bidirectional DC-DC converter used in electric vehicles.

4.2.2.1 Electrolytic capacitor

Capacitors are well known for being a component that protects the drives and distribution systems from the perturbations generated by heavy dynamic loads like the motor of an electric vehicle. However, electrolytic capacitors are also recognized for being the originators of failures in important power supply systems, such as actuators, avionics equipment, or power electronics devices, among others [133]. Therefore, the prognostics and state-of-health estimation of these elements becomes imperative in power systems that rely on their proper operation.

Normally, the electrolytic capacitor is modelled with four passive elements, which are the capacitance, equivalent series resistance (ESR), equivalent series inductance (ESL) and the leakage resistance. However, this problem only considers the capacitance *C* and ESR in the state-of-health estimation of the electrolytic capacitor, since these parameters are the ones with a greater impact on the capacitor performance [133].

Figure 4.16 presents the simplified electrical model of an electrolytic capacitor. The degradation of this type of capacitor results in a decrease of the capacitance and an increase of the ESR, which eventually affects the performance of the electrolytic capacitor. According to the standard MIL C 62 F, the capacitor is considered as faulty when the value of the capacitance drops 20%

below the value obtained in the manufacturing process, and/or when the ESR increases above 280% its initial value.

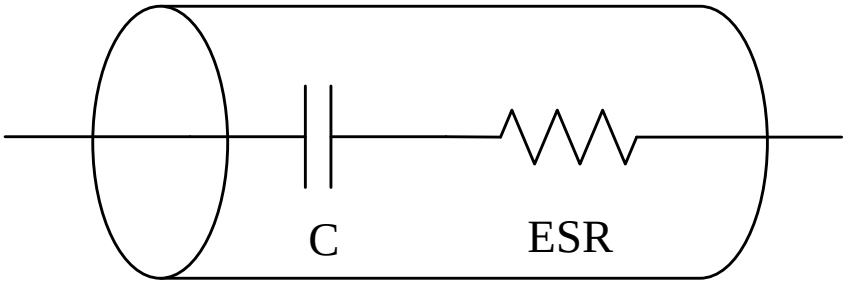

Figure 4.16. Simple electrical model of an electrolytic capacitor.

The main factors that contribute to the degradation process of electrolytic capacitors are the temperature, vibration, overvoltage, humidity, pressure and a high current ripple [134]. This study aims to analyze the overvoltage effect on the degradation of the capacitor. Charging the electrolytic capacitor with a voltage above its rated value leads to the evaporation of the electrolyte, an increase of the internal pressure as well as of the leakage current [133]. The electrical overstress of the capacitor results in an increase of its internal temperature because the current flow rises drastically, and consequently, the electrolyte evaporates and the ESR increases. In addition, the internal pressure of the capacitor increases due to the chemical reactions that occur when it is subjected to charging cycles at a high voltage. The following subsection presents the accelerated aging tests carried out to degrade the electrolytic capacitor.

4.2.2.2 Accelerated aging tests

This section aims to explore the effects of high voltage in the electrolytic capacitors used in DC-DC converters. When the operating voltage of the converter is above the rated voltage of the capacitor, the capacitor tends to degrade, and it may lead to an irreversible damage that alters the converter behaviour. Thus, an aging test is proposed in order to charge and discharge the capacitor in recurrent cycles. To this end, it is necessary to apply a periodic square signal for several hours, with an amplitude higher than the nominal voltage of the capacitor. The expected outcome of this aging test is an increase of the ESR and a decrease of the capacitance with time. Although the aging test of the electrolytic capacitor does not involve the converter, once the degradation process has been completed, a comparison contrasting the DC-DC converter performance with the initial values of the capacitor and with the degraded capacitor is done.

The accelerated aging test proposed in this section is based on the experiment detailed in [133]. A DC power supply feeds the electrolytic capacitor by applying a voltage 20% higher than the

nominal value specified by the manufacturer, until the capacitor is fully charged. Then, the power supply switches off and the capacitor is discharged through a resistor connected to it. This cycle repeats for several times until the capacitance is below a predetermined value. Meanwhile, the values of the capacitance and the ESR are measured constantly in order to have a rich dataset. Figure 4.17 presents the accelerated aging experimental setup.

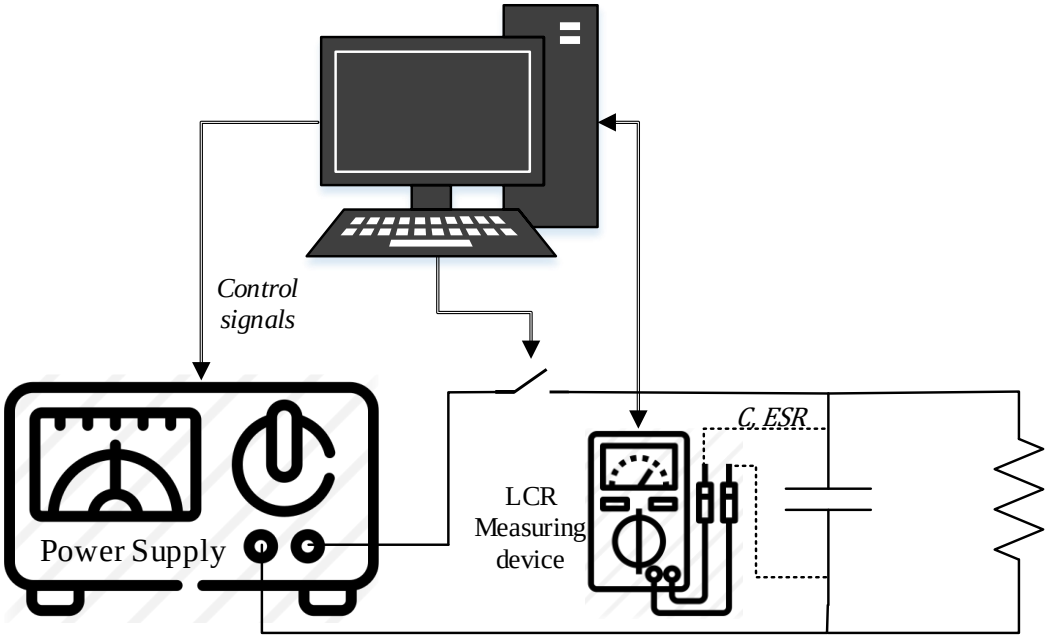

Figure 4.17. Accelerated aging test data acquisition system.

Figure 4.17 shows that the experiment is controlled by a computer, which is in charge of sending orders to the equipment involved in the data acquisition process. Concretely, it controls the voltage delivered by the power supply, the RLC measuring equipment and a switch that connects or disconnects the capacitor from the DC power supply. The data is acquired every 30 minutes. In order to have an accurate measurement of the electrolytic capacitor parameters, it is necessary to disconnect the power supply.

The data acquisition system shown in Figure 4.17 was implemented in the laboratory. The electrolytic capacitor used in the degradation process has a nominal capacitance of 220 µF, an ESR of 300 mΩ, a rated voltage of 7.56 V and it is manufactured by Panasonic. This capacitor can be found at the output of different DC-DC converters such as the TPS40200EVM-002 step-down converter manufactured by Texas Instruments. In order to discharge the capacitor, a 100 Ω resistor was connected in parallel to the electrolytic capacitor. Figure 4.18 shows the experimental setup implemented in the laboratory.

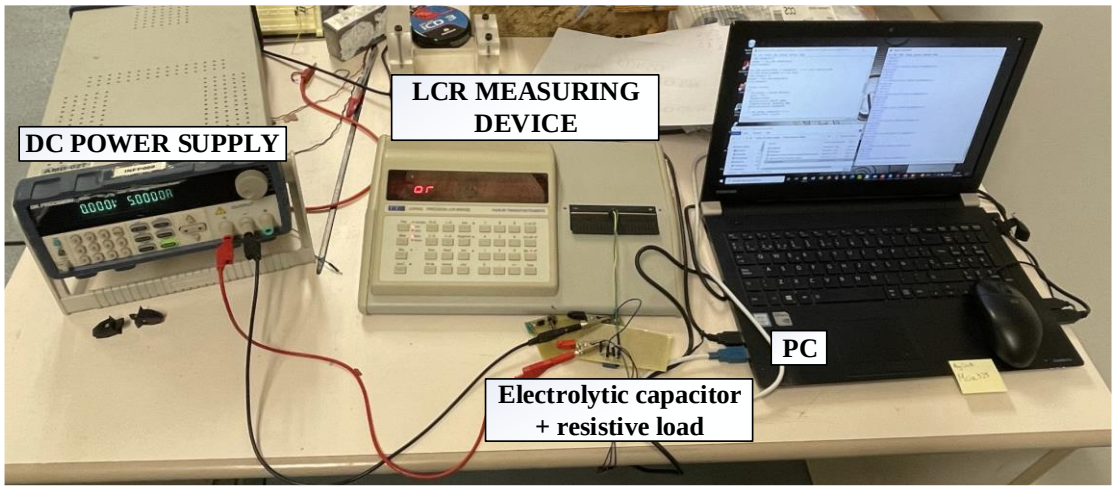

Figure 4.18. Experimental setup of the accelerated aging test.

The DC power supply used in this process is the BK Precision 9205 (BK Precision Corporation, Yorba Linda, CA, USA), while the measuring device is the LCR400 Precision LCR Bridge, manufactured by Thurlby Thandar Instruments. The voltage applied to the capacitor is 7.56 V, which is 1.2 times higher than its nominal voltage. The switching frequency of the power supply is 0.2 Hz, which implies that the capacitor is charged during 2.5 seconds and discharged during the same amount of time. Figure 4.19 shows the voltage waveform during the charging and discharging processes.

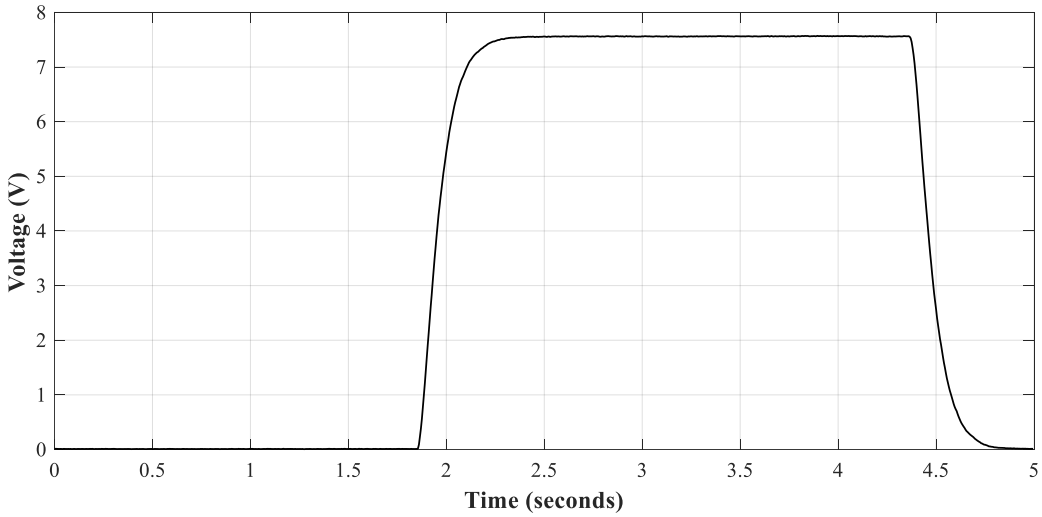

Figure 4.19. Charging and discharging cycle of electrolytic capacitor.

4.2.3 Proposed methodology

The proposed prognostics methodology combines a white-box parameter estimation method and a neural network structure. The first one is used to determine the capacitance and ESR value of the electrolytic capacitor, while the second one aims to forecast the future values of these

parameters. The importance of this approach is that during the whole process, it just requires the signals measured at the input and output terminals of the DC-DC power converter. Figure 4.20 presents the proposed procedure.

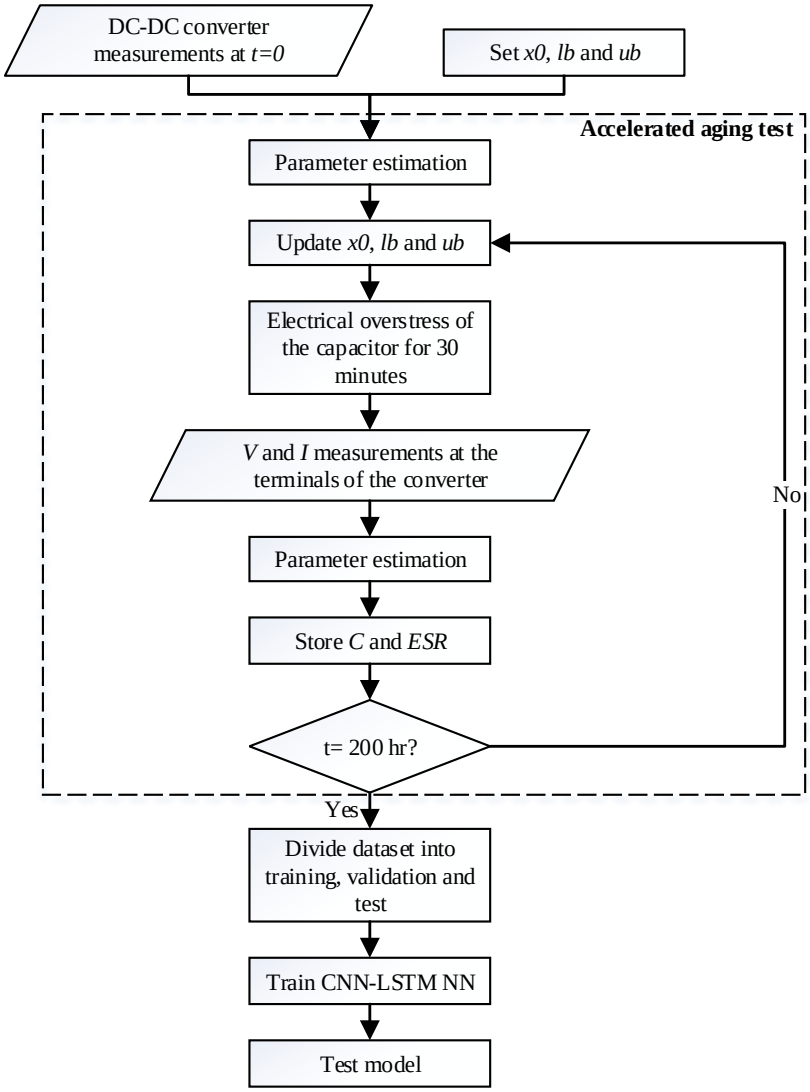

Figure 4.20. Proposed methodology.

As depicted in Figure 4.20, the first step is to measure the signals and to estimate the parameters of the power converter when it operates under healthy conditions. These parameters are estimated based on an optimization method, where the variables are initialized with an initial value (x_0) and the maximum (*lb*) and minimum (*ub*) values are set. Then, the degradation process of the electrolytic capacitor starts, and every 30 minutes the parameters are identified based on the non-invasive measurements of the converter. This is done until the accelerated aging test reaches a certain limit time. At the end of each iteration, the capacitance and ESR values are stored, while the initial, minimum and maximum values of the parameters are updated for the next identification

loop. The values of the capacitance and resistance are also measured using a specialized device to validate the accuracy of the parameter estimation method.

Once the degradation test has finished, the next step is to obtain a model that is able to predict the future values of the capacitor parameters. To this end, the stored data is split into three different datasets, i.e., the training, validation and test sets. The first two ones are used to train the CNN-LSTM neural network, whereas the test data set is used to determine the accuracy of the predictions made by the model.

4.2.4 Proposed CNN-LSTM architecture

The deep learning method used to forecast the values of the capacitance and the ESR of the electrolytic capacitor is based on the approaches proposed in Chapter 3. It combines a one dimensional convolutional neural network and a long short-term memory neural network. Recurrent neural networks such as LSTM are widely used in the analysis of time-series because they are able to learn the sequential dependencies of the data and use them to predict future values [87]. On the other hand, CNNs are widely used in image classification problems since they are capable of obtaining complex features of data that contain significant information [77]. However, over the last years, the CNNs are being used in time-series related problems since they allow finding relationships between the different time dependencies of the data with a good accuracy. This forecasting technique integrates a one dimensional CNN with a LSTM-NN in order to predict the future values of the capacitance and ESR of the electrolytic capacitor. The main advantage of combining convolutional and LSTM layers is that the model learns the long term dependencies of the complex features of the time-series, which allows the neural network to replicate with high accuracy the behaviour of the training data [135].

The inputs and outputs of the neural network must be defined. This study proposes as input the *n* previous steps of the variable to be predicted (*C* or ESR), while the output considers the *m* future steps of this variable. For instance, if *n* is set to 15 and *m* to 5, the CNN-LSTM NN estimates the next 5 values of the variable *x* based on the last 15 values. The number of samples used to train the model is given by the total length *l* of the dataset and the selected *n* and *m* values, which can be calculated as follows,

$$samples = l - (m + n) + 1 \tag{81}$$

where the timespan of the first, second and third samples are, respectively, (t_1, t_{m+n}), (t_2, t_{m+n+1}) and (t_{l-m-n}, t_l).

Figure 4.21shows the neural network architecture proposed in this work. It is seen that the input data enters the convolutional layer, where the complex features are extracted. Then, the resulting maps input the pooling layer and the obtained output is the input of the LSTM layer, which generates the variable values for the next *m* time steps.

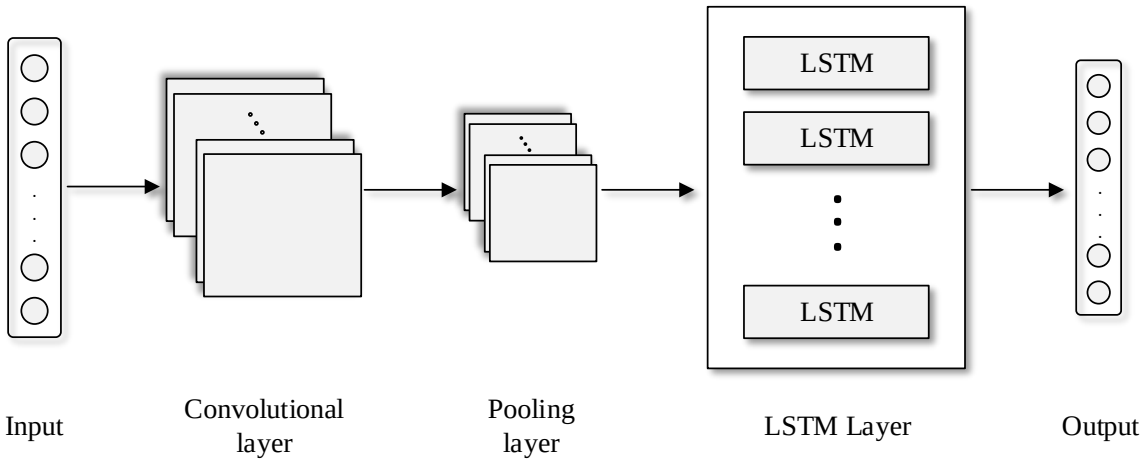

Figure 4.21. CNN-LSTM NN architecture.

4.2.5 Results

This section presents the implementation of the methodology proposed in Figure 4.20 to a real DC-DC converter, the results of the accelerated aging tests and the forecasting of the future values of the capacitance *C* and ESR. The proposed prediction method is compared against four approaches that are used to model time-series related problems. These methods are the nonlinear autoregressive exogenous neural network (NARX NN), a single LSTM NN and a one dimensional CNN.

The DC-DC converter used is the Texas Instruments TPS40200EVM-002. Despite the fact of not being a bidirectional converter, the chosen device has the same working principle and passive elements as the step-down mode of a bidirectional converter. Also, this evaluation module results in the degradation process of the capacitor since it is not packaged, which allows the connection and disconnection of the capacitor. The electrolytic capacitor used in the accelerated aging test is the Panasonic EEEFK0J221AP, with nominal values $C = 220\,\mu H, ESR = 360\,m\Omega$ with a tolerance of ± 20%.

According to the proposed methodology, the first step is to estimate the converter parameters before the aging process starts. To this end, the TRRNLS algorithm is applied using the signals acquired from the converter under steady state and when a load change occurs. Figure 4.22 presents the experimental setup used to acquire the data of the DC-DC converter.

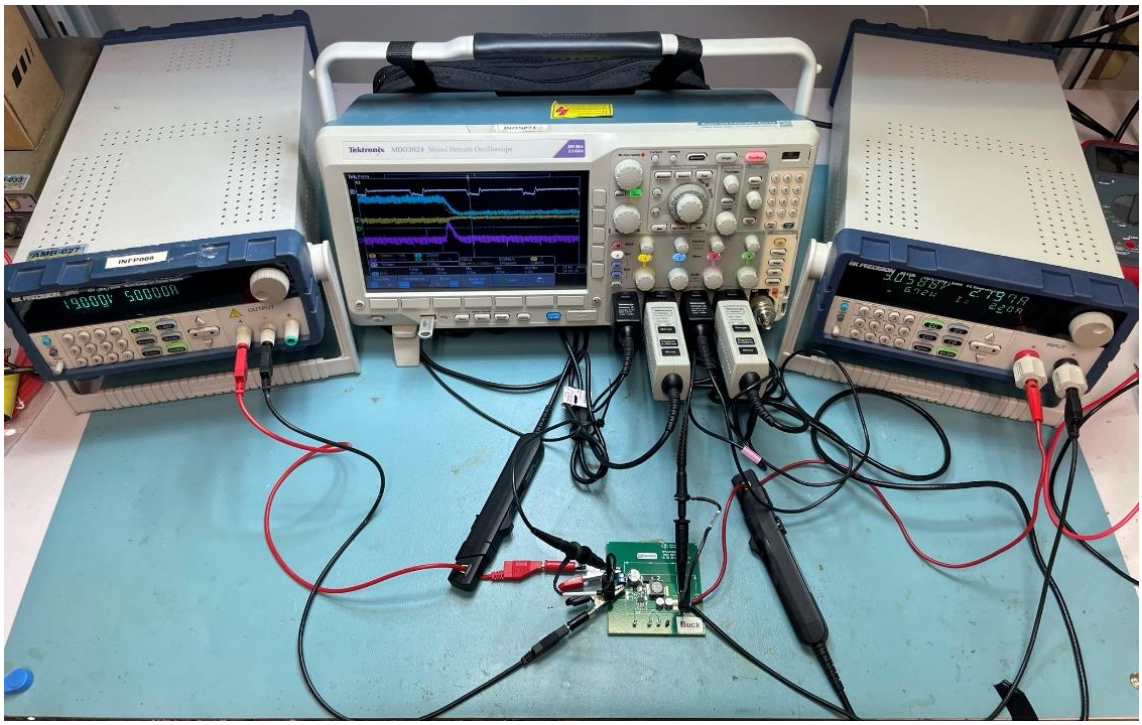

Figure 4.22. Experimental setup to acquire data from DC-DC converter.

Once the data have been measured and pre-processed, the parameters of the DC-DC converter are estimated using the optimization method presented in this section. The parameter estimation algorithm was programmed in Matlab and Simulink. Seven parameters for the steady state data and four parameters from the data acquired from the transitory were identified. The average error in the estimation of all parameters was 3.55%. The results from the estimations were C = 208.23 μF and ESR = 429.5 mΩ, whereas the values obtained using the LCR measuring device were C = 207.58 and ESR= 427.2 mΩ. This represents a relative error of 0.31% and 0.54 %, respectively.

Once the parameters have been estimated, the accelerated aging test begins. The test lasted for 391 hours and measurements were performed every 30 minutes. It is important to mention that the electrolytic capacitor parameters were identified at each iteration based on the input and output signals. They were also measured using a LCR measuring device. Figure 4.23 presents the evolution of the capacitance and ESR during the degradation process. One curve refers to the actual value of these parameters, while the other curve shows the estimations done by means of the TRRNLS algorithm.

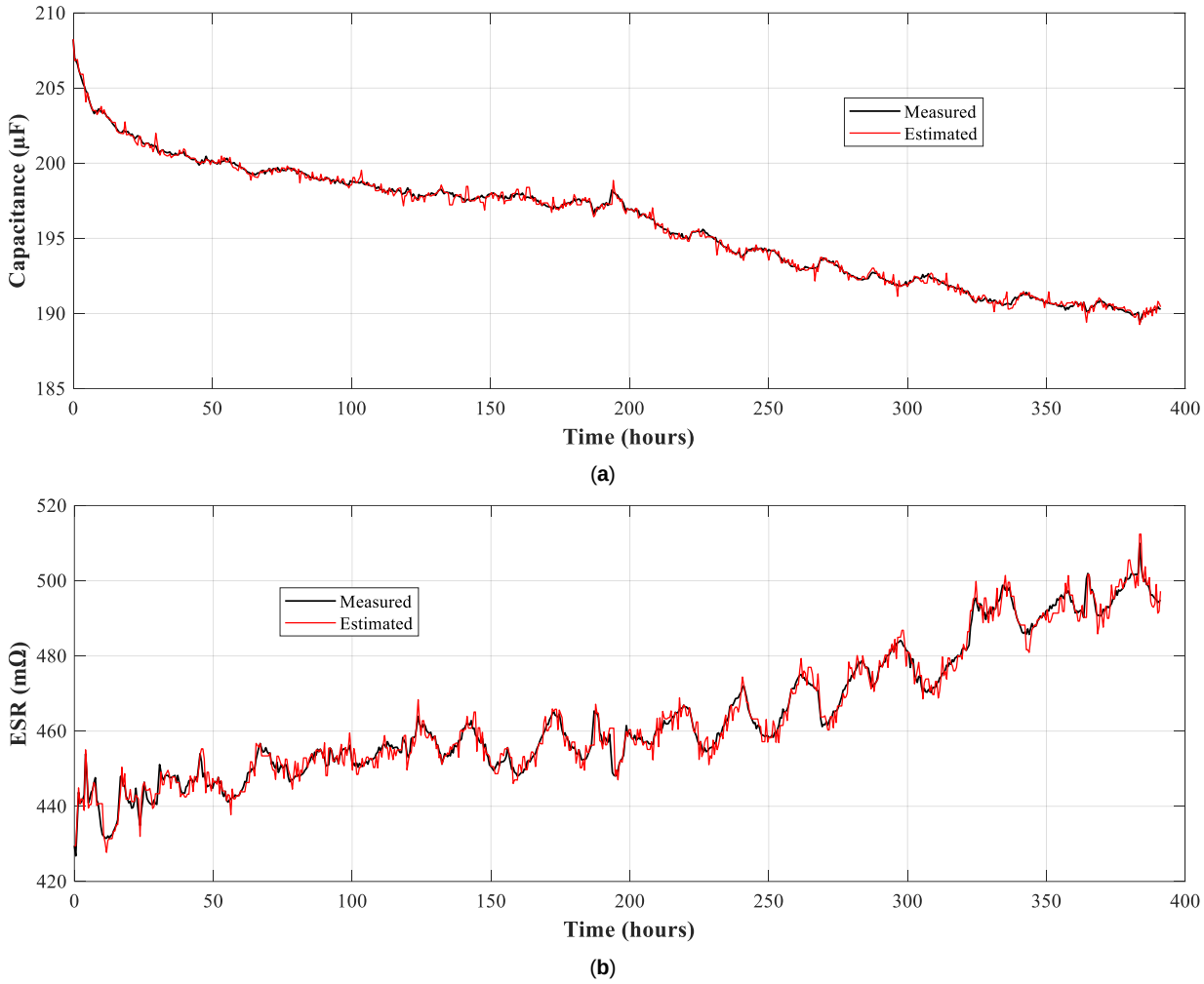

Figure 4.23. Measured and estimated values during the accelerated aging test. (a) Capacitance; (b) ESR.

Figure 4.23 proves that the proposed optimization algorithm is capable of estimating the capacitor parameters with high accuracy during the accelerated aging test. The total number of estimated values was 753, which corresponds to the number of measurements performed during the aging process. The average estimation error is 0.08% for the capacitance and 0.37% for the ESR, which in both cases is considerably low.

The next step is to split the estimated data during the accelerated aging test into training, validation and test sets in order to train the model. The training set considers 70% of the original dataset, corresponding to 527 time steps or 275 hours. The size of the validation set is a tenth part of the original time-series, which comprises 75 steps in the interval from 275 to 313.5 hours. Finally, the test set is formed by the last 20% data of the capacitor, comprising the last 77.5 hours of the aging test.

As mentioned above, once the data has been divided, the next step is to tune the set of hyper-parameters that enhances the accuracy of the model. To this end, a random search algorithm

was applied, where 100 neural networks were trained for 10 epochs each. Table 4.6 presents the boundaries of the search algorithm and the tuned values.

Table 4.6. Random search algorithm to set the parameters of the CNN-LSTM NN

Parameter	Minimum	Maximum	Optimal
Kernel size	1	15	4
LSTM neurons	1	100	31
n	20	100	56
m	1	40	12

Once the hyper-parameters have been tuned, the CNN-LSTM neural network is trained based on the strategy detailed in the previous section. The total number of epochs dealt with was 32, the model reaching convergence after 12.2 seconds.

Figure 4.24 and Table 4.7 summarize the results obtained after training the CNN-LSTM neural network and compare these results against those obtained by applying other approaches. The model accuracy is obtained using the test dataset, which includes data that have not been used in the training process. All models were programmed and trained using Python and it was carried out by means of a GeForce RTX 2080 Super GPU.

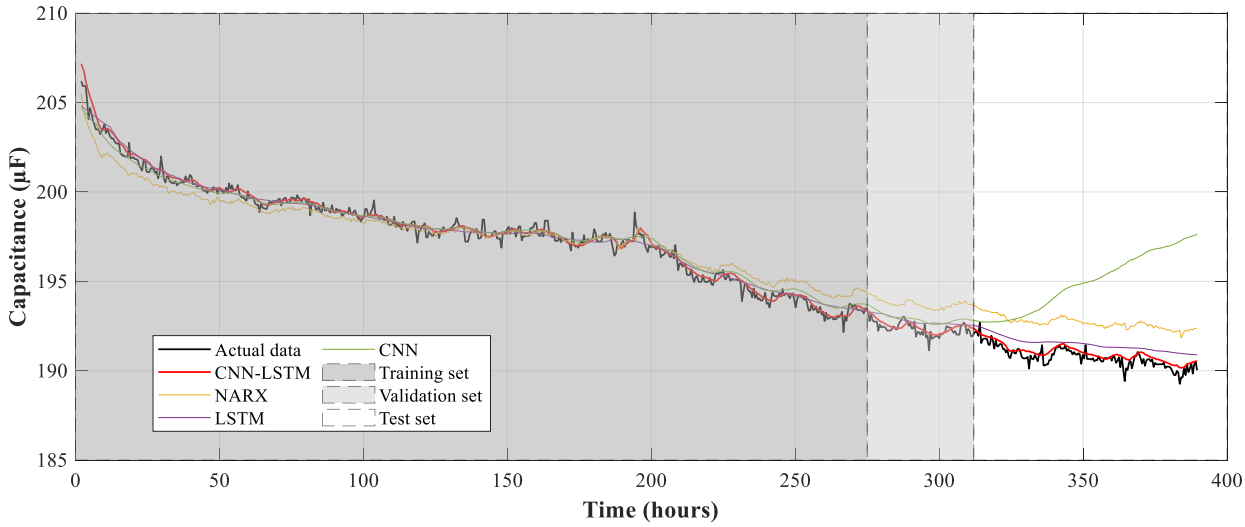

(a)

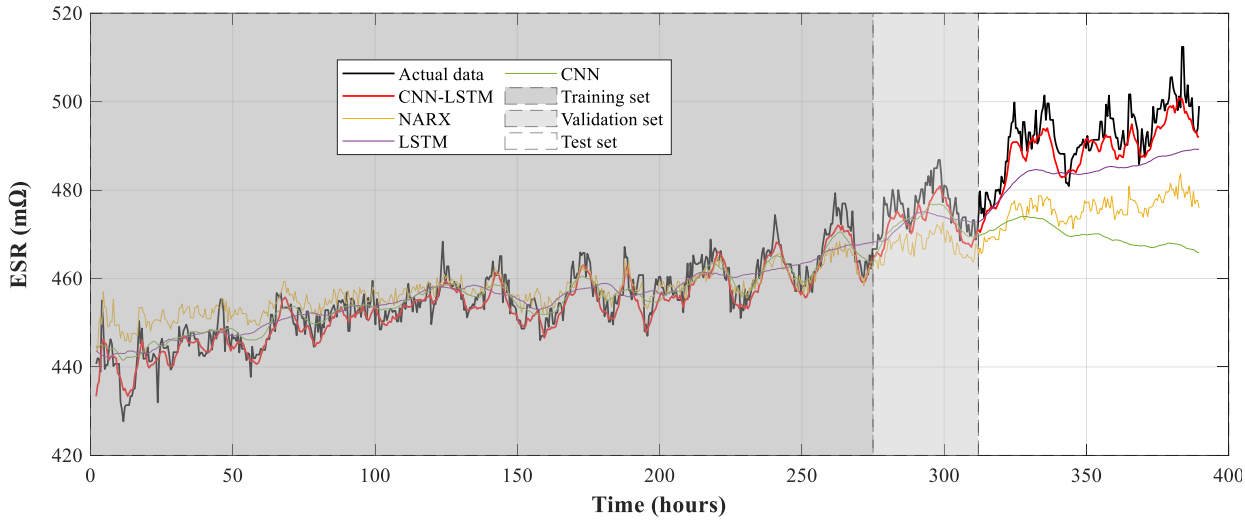

(b)

Figure 4.24. Prediction of the future values of (a) Capacitance; (b) Equivalent series resistance of the electrolytic capacitor.

Table 4.7. CNN-LSTM performance and comparison with other methods

Method	Capacitance		ESR		Time elapsed
	RMSE	R^2	RMSE	R^2	
CNN-LSTM	0.00042	0.995	0.0016	0.9901	12.2 seconds
NARX	0.00080	0.825	0.0055	0.846	66 seconds
LSTM	0.00056	0.9612	0.0035	0.944	8.03 seconds
CNN	0.00121	0.774	0.0094	0.790	12.8 seconds

From the results presented in Table 4.7, it is evident that the proposed methodology is able to predict the future outputs of the capacitance and ESR of the electrolytic capacitor. Results attained with the CNN-LSTM approach present a coefficient of determination that is almost 1 for the two predicted variables. On the other hand, the CNN-LSTM neural network outperforms the other approaches, since it presents a lower value of the RMSE and a value of the determination coefficient R^2 closer to 1 in the predictions made using the test dataset. The higher accuracy of the proposed method is also appreciated in Figure 4.24, because the model is capable of replicating the behavior of the electrolytic capacitor, even when it is tested with a set of data that was not used in the training process. The training time of the proposed methodology is longer than that of the LSTM approach, but lower than that of the CNN neural network. However, the elapsed time is relatively low considering that the proposed model consists of two hidden layers with different architecture.

Finally, a comparison between the measured and estimated voltages and currents of the DC-DC converter is performed with a 1.5 Ω resistive load. To this end, experimental data are acquired

from the laboratory setup once the accelerated aging test has finished. The estimation of these waveforms is done by taking the predicted values of C and ESR at the last time step from simulations of the converter considering the predicted values of parameters C and ECR. Figure 4.25 presents the four waveforms, where it is evident that the model replicates accurately the response of the converter.

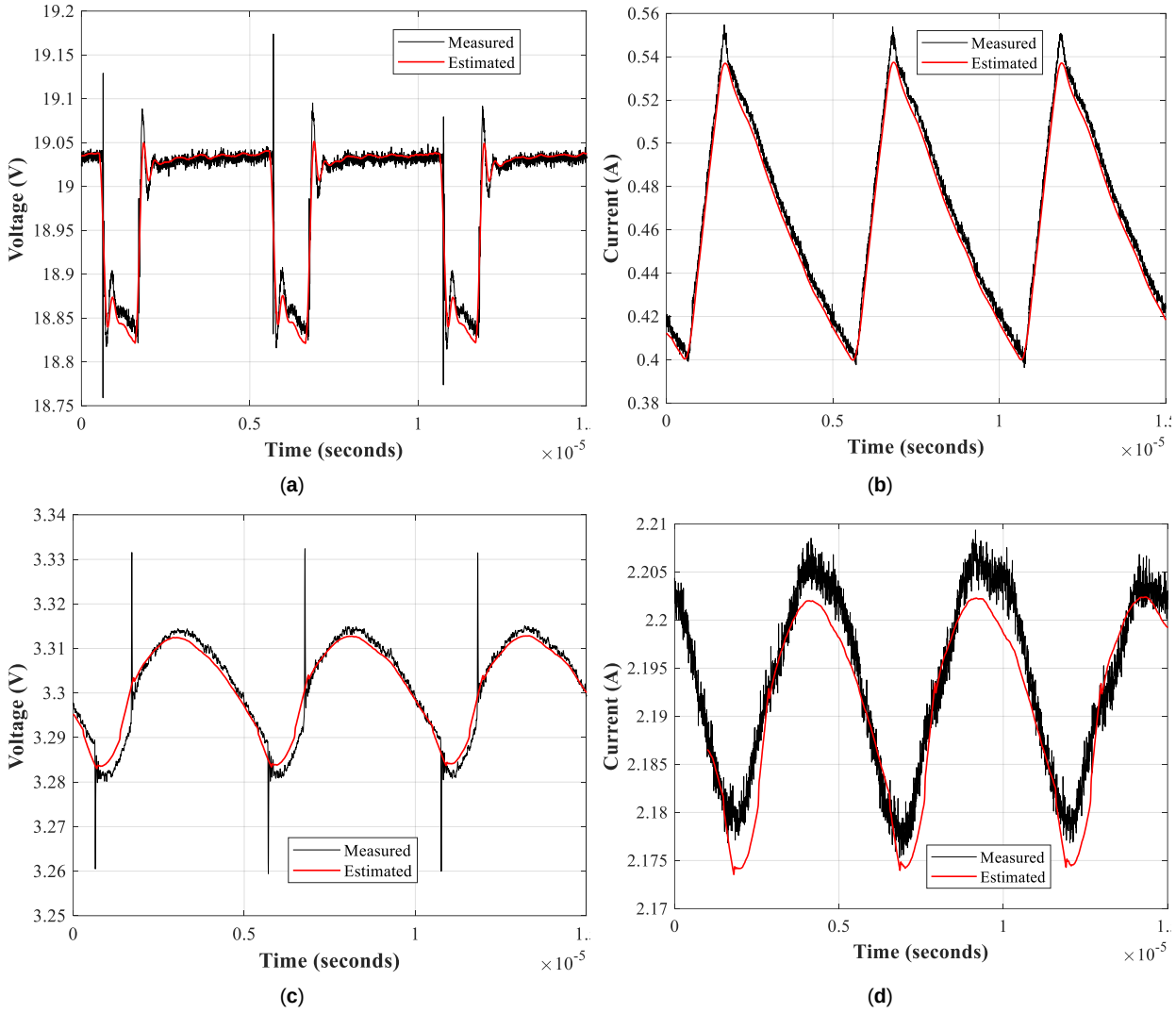

Figure 4.25. Measured and estimated signals (a) Input voltage; (b) Input current; (c) Output voltage; (d) Output voltage.

5 CONCLUSIONS

5.1 General conclusion

The main objective of this thesis was to design and implement methodologies that generate models able to replicate the behavior of power converters. As it has been shown through this document, white-box and black-box approaches were proposed and tested using real data. It is worth noting that the methodologies and algorithms presented in this thesis can be applied to obtain black-box or white-box models of many other devices such as power supplies, rectifiers or filters among others.

The second chapter proposed two parameter identification methods for DC-DC power converters based on non-invasive on-line measurements of the voltages and currents at the input/output terminals of the converters. To this end, three types of commercially available DC-DC converters have been analyzed, namely buck, boost and buck-boost converters. The first method presents the calculation of the analytical equations of the converters. These equations along with the measured data are used to obtain the parameters of the circuit. However, this approach is limited since it requires measuring the inductor current and it is not able to estimate the parameters of the control loop. The second parameter estimation method proposed in chapter 2 is based on solving an optimization problem by applying the non-linear least squares algorithm, and in particular, the trust-region reflective least squares solver. The presented results are based on experimental data acquired from the input/output terminals of the converters, considering both steady state and transient operating conditions. Such results prove that it is feasible to identify all model parameters with accuracy, including those related to the passive, parasitic and control loop elements, thus allowing to generate accurate discrete simulation models of the converters.

The third chapter has proposed an offline black-box modelling approach of switched mode DC-DC converters used in electric vehicles and aircrafts. To this end, three methodologies based on different neural networks were proposed. The NNs were trained as they use an optimization algorithm to tune a set of hyper-parameters that enhances the accuracy of the model. The results presented in this chapter are based on experimental setups, where multiple experiments considering different situations were carried out to train the neural networks. Such results show that the deep learning approach has a higher accuracy when compared with existing methods in the literature. It was proven that the output prediction matches well with the actual output values given that the coefficient of determination R^2 is 0.99, so that the neural network is able to predict the step-down converter steady-state and transient waveforms under CCM and DCM operating conditions.

Finally, the last chapter presented two different applications of the white-box and black-box identification methodologies proposed in this thesis. Firstly, an accurate modeling of power factor correction converters is presented. It proposes a parameter identification strategy of a boost PFC converter integrating an EMI filter at the input stage. This approach uses the trust-region nonlinear least squares optimization algorithm, the topology of the circuits and non-intrusive measurements at the input and output terminals of the device. More than 30 parameters were identified with high precision, and the behavior of the AC-DC converter was replicated with high accuracy. On the other hand, the second part of Chapter 4 proposed a methodology for identifying the state-of-health of the DC-DC converters that feed propulsive electric machines for hybrid electric vehicles. The methodology performs an offline and non-invasive estimation of the converter parameters by using the signals acquired at the input and output terminals of the converter. The proposed approach can estimate the actual and future values of the capacitance and ESR of the electrolytic capacitors used in DC-DC converters. To this end, the electrolytic capacitor of the converter was aged by applying an accelerated aging test, which was based on applying an electrical overstress to the electrolytic capacitor. It is noted that the same methodology can be extended to other factors that may degrade this component, such as temperature, pressure, etc. With the data obtained in this test, a deep learning model was trained in order to predict the future health condition of the electrolytic capacitor, and thus, the DC-DC converter state-of-health. This prognostic approach results in the prevention of failures in the powertrain of the electric vehicle, given the negative impact of a faulty electrolytic capacitor in a power system.

5.2 Contributions

This thesis contributes to the state-of-the-art in several ways. Chapter 2 has covered knowledge gaps in the area of parameter identification of power converters. First, it proposes a parameter identification approach which is able to identify the full set of parameters of the converter (between 15 and 18, depending on the converter topology) from experimental data, including the parameters of the passive and parasitic components and those of the PWM control loop. Second, the proposed strategy does not require solving any differential equation governing the behavior of the converter, thus being quite immune to signal noise. Third, the suggested solution allows determining simultaneously all converter parameters from only two measurements performed under steady state and transient conditions. Finally, these measurements are based on acquiring the terminal input/output voltages and currents of the converter, the acquisition procedure being non-invasive and independent of the converter topology.

On the other hand, chapter 3 presents three methodologies to obtain an accurate and replicable offline data-driven model of switched mode DC-DC power converters used in real applications. It uses nonlinear autoregressive exogenous neural networks, long short-term memory neural networks and convolutional neural networks to generate a model, whose hyper-parameters are tuned by means of an optimization algorithm. The black-box approaches proposed in this thesis are different from the solutions found in the technical literature and contribute to the state-of-the art in several aspects. First, it allows reproducing the steady state and transient behaviors of the power converter by acquiring the input-output voltages and currents, that is, by means of time-domain measurements. This is advantageous since it simplifies the requirements of the measuring equipment and avoids transformations from the frequency to the time domain and vice versa, which is required in many other approaches [46], [50]. Second, the measurements are non-invasive and independent of the converter topology, and it does not require to continuously apply an excitation signal to the converter, which is the case of the Hammerstein model [53]. Third, this modelling approach is very robust and accurate, since it is able to reproduce the dynamics of the DC-DC converter under different operating points and under the continuous and discontinuous conduction modes (CCM and DCM). Other approaches [50], [53], [54] require different models depending on the operating point, and some others are unable to integrate the CCM and DCM in just one model. Fourth, the proposed approaches are based on real cases, since the data is acquired from converters used in electric vehicles and aircrafts. These converters are identified with high accuracy by having connected realistic constant power loads, while most of previous works have simple setups and converters where the industrial application is not clear [50], [55], [56]. Fifth, it outperforms other neural network models because it does not consider a fixed length

of the data, and the computational burden is lower [69]. Finally, the obtained model can be easily integrated in an electrical simulation environment because it consists of just one model that generates an output based on matrix operations.

There does not exist a bibliography related to the parameter identification of an AC-DC boost PFC converter with an EMI filter. Therefore, it is not possible to compare the proposed methodology with an existing approach. However, the methodology proposed in section 4.1 contributes to the state-of-the-art in several aspects. First, it proposes a strategy to estimate more than 30 parameters based on non-intrusive measurements at the input and output terminals of the different elements of the PFC converter. Second, the different elements of the control loops (voltage and current) are identified, which allows to reproduce with high accuracy the transient behaviour of the converter. Third, estimating all the parameters of a widely used device, such as a AC-DC PFC, results in the design and maintenance of systems supplying multiple electronics loads. Finally, the experimental setup to perform the data acquisition is relatively simple because it is not necessary to apply internal excitations to the circuit or perform invasive measurements in the inductor of the boost converter.

In Section 4.2 the proposed prognostics methodology combines white-box parameter estimation and a neural network structure. Whereas the parameter estimation stage is used to determine the capacitance and the ESR value of the electrolytic capacitor, the deep learning neural network is applied to forecast the future values of these parameters. The effectiveness of the method is proved from theoretical analysis, simulation, and experimental verification, respectively. The proposed method is advantageous over other approaches since it only requires measurements at the input/output terminals of the converter to identify the parameters of the capacitor (capacitance and ESR), thus being non-invasive and general, since it can be applied to different power converter topologies. In addition, the CNN-LSTM neural network topology has not yet been applied in this field, outperforming other state-of-the-art approaches found in the technical literature.

5.3 Future work

This thesis filled an existing gap related to the modelling of power electronic converters. However, there is knowledge that still needs to be explored.

Firstly, the identification of power converters based on grey-box models results appealing since it can use neural networks and other deep learning approaches in order to estimate the parameters of power converters. Normally, a grey-box model consists of a linear or non-linear model with partially known theoretical structure, where the unknown parts can be derived from experimental data. A grey-box approach is useful because the topology of the converter could be identified by means of a classification problem. Thus, the parameters of the converter can be identified with few information about its structure, for example, if it is a step-down or step-up converter.

Related to the converters used in the identification process, the proposed algorithms could be tested with different DC-DC and AC-DC converters. Given the numerous types of commercially available power converters, it is useful to prove the robustness of the methods with data from converters with other topologies. For instance, white-box and black-box modelling of isolated DC-DC converters such as fly-back or forward. Furthermore, the experimental data could be more realistic if a real power source is used. This can be achieved by mimicking the output impedance and voltage of the power source. For the case of the aircraft distribution network, it would be convenient to use a synchronous machine generator with eight pole-pairs as the ones used in airplanes.

Regarding the prognostics of the power electronic converters, other ageing tests could be added to the study. These tests depend on the external agents that affect the long-time performance of the converters, for instance the temperature or the pressure. A rigorous accelerated aging test must be performed and the proposed neural network should be able to estimate the remaining useful life of the converter. Also, the prognostics can be expanded to other elements that may affect the proper operation of the converters, such as the inductors or the transistors.

Finally, an advance in computation capacity and artificial intelligence algorithms is expected in the upcoming years. Therefore, the black-box approaches presented in this thesis might be enhanced and may lead to more complex and accurate models of the power converters. A growth in the computation capacity means that models could be trained with more data or in a lower time.

BIBLIOGRAPHY

[1] B. K. Bose, “Power electronics-a technology review,” *Proc. IEEE*, vol. 80, no. 8, pp. 1303–1334, 1992.

[2] J. A. Rosero, J. A. Ortega, E. Aldabas, and L. Romeral, “Moving towards a more electric aircraft,” *IEEE Aerosp. Electron. Syst. Mag.*, vol. 22, no. 3, pp. 3–9, Mar. 2007.

[3] J.-R. Riba, Á. Gómez-Pau, and M. Moreno-Eguilaz, “Experimental Study of Visual Corona under Aeronautic Pressure Conditions Using Low-Cost Imaging Sensors,” *Sensors*, vol. 20, no. 2, p. 411, Jan. 2020.

[4] B. K. Bose, “Power Electronics, Smart Grid, and Renewable Energy Systems,” *Proc. IEEE*, vol. 105, no. 11, pp. 2011–2018, Nov. 2017.

[5] B. K. Bose, *Power electronics and motor drives : advances and trends*. Elsevier/Academic Press, 2006.

[6] J. Rabkowski, D. Peftitsis, and H. P. Nee, “Recent Advances in Power Semiconductor Technology,” in *Power Electronics for Renewable Energy Systems, Transportation and Industrial Applications*, vol. 9781118634035, Wiley-IEEE Press, 2014, pp. 69–106.

[7] H. Balakrishnan, M. Moreno-Ezuilaz, J. R. Riba, S. Bogarra, and A. Garcia, “DC-DC Buck Converter Parameter Identification Based on a White-Box Approach,” in *Proceedings - 2018 IEEE 18th International Conference on Power Electronics and Motion Control, PEMC 2018*, 2018, pp. 242–247.

[8] J.-R. Riba, M. Moreno-Eguilaz, S. Bogarra, and A. Garcia, “Parameter Identification of DC-DC Converters under Steady-State and Transient Conditions Based on White-Box Models,” *Electronics*, vol. 7, p. 393, Dec. 2018.

[9] Qian Shen, L. Ren, C. Gong, and Huizhen Wang, “A unified feature parameter extraction strategy based on system identification for the Buck converter with linear or nonlinear loads,” in *IECON 2016 - 42nd Annual Conference of the IEEE Industrial Electronics Society*, 2016, pp. 388–393.

[10] M. Ahmeid *et al.*, “Real-Time Parameter Estimation of DC–DC Converters Using a Self-Tuned Kalman Filter,” *IEEE Trans. Power Electron.*, vol. 32, no. 7, pp. 5666–5674, Jul. 2017.

[11] V. Nguyen *et al.*, “Active EMI Reduction Using Chaotic Modulation in a Buck Converter with Relaxed Output LC Filter,” *Electronics*, vol. 7, no. 10, p. 254, Oct. 2018.

[12] Y. Zhang *et al.*, “Improved Step Load Response of a Dual-Active-Bridge DC–DC Converter,” *Electronics*, vol. 7, no. 9, p. 185, Sep. 2018.

[13] H. Balakrishnan, M. Moreno-Ezuilaz, J.-R. Riba, S. Bogarra, and A. Garcia, “DC-DC Buck Converter Parameter Identification Based on a White-Box Approach,” in *2018 IEEE 18th*

International Power Electronics and Motion Control Conference (PEMC), 2018, pp. 242–247.

[14] V. Valdivia, “Behavioral Modeling and Identification of Power Electronics Converters and Subsystems Based on Transient Response,” Universidad Carlos III de Madrid, 2013.

[15] A. Bréard, R. Moulla, and C. Vollaire, “Metamodel of Power Electronic Converters Using Learning SVR Method Coupling With Wavelet Compression,” *IEEE Trans. Electromagn. Compat.*, vol. 58, no. 2, pp. 588–598, Apr. 2016.

[16] V. Valdivia, A. Barrado, A. Lazaro, M. Sanz, D. Lopez Del Moral, and C. Raga, “Black-box behavioral modeling and identification of DC-DC converters with input current control for fuel cell power conditioning,” *IEEE Trans. Ind. Electron.*, vol. 61, no. 4, pp. 1891–1903, 2014.

[17] O. Nelles, *Nonlinear System Identification. From Classical Approaches to Neural Networks and Fuzzy Models.* Springer-Verlag Berlin Heidelberg, 2001.

[18] G. Rojas-Dueñas, J.-R. Riba, and M. Moreno-Eguilaz, “Non-Linear Least Squares Optimization for Parametric Identification of DC-DC Converters,” *IEEE Trans. Power Electron.*, vol. 36, no. 1, pp. 654–661, Jun. 2021.

[19] J. A. Oliver, R. Prieto, V. Romero, and J. A. Cobos, “Behavioural Modelling of DC-DC Converters for Large-Signal Simulation of Distributed Power Systems,” *Twenty-First Annu. IEEE Appl. Power Electron. Conf. Expo. 2006. APEC ’06.*, no. 1, pp. 1204–1209, 2006.

[20] Y. Wehbe, L. Fan, and Z. Miao, “Least squares based estimation of synchronous generator states and parameters with phasor measurement units,” *2012 North Am. Power Symp. NAPS 2012*, 2012.

[21] M. M. Fawzi Saber Algreer, “Microprocessor Based Signal Processing Techniques for System Identification and Adaptive Control of DC-DC Converters,” Newcastle University, 2012.

[22] B. H. Lin, J. T. Tsai, and K. L. Lian, “A Non-Invasive Method for Estimating Circuit and Control Parameters of Voltage Source Converters,” *IEEE Trans. Circuits Syst. I Regul. Pap.*, pp. 1–11, Aug. 2019.

[23] M. Algreer, M. Armstrong, and D. Giaouris, “Active Online System Identification of Switch Mode DC–DC Power Converter Based on Efficient Recursive DCD-IIR Adaptive Filter,” *IEEE Trans. Power Electron.*, vol. 27, no. 11, pp. 4425–4435, Nov. 2012.

[24] L. Tomesc, B. Betea, and P. Dobra, “Determining the Frequency Response of a DC-DC Converter thru System Identification,” *IFAC Proc. Vol.*, vol. 46, no. 6, pp. 149–152, Jan. 2013.

[25] L. Ren and C. Gong, “Modified hybrid model of boost converters for parameter identification

of passive components," *IET Power Electron.*, vol. 11, no. 4, pp. 764–771, Apr. 2018.

[26] G. M. Buiatti, A. M. R. Amaral, and A. J. M. Cardoso, "An unified method for estimating the parameters of non-isolated DC/DC converters using continuous time models," *Telecommun. Energy Conf. 2007. INTELEC 2007. 29th Int.*, pp. 334–341, 2007.

[27] H. Gietler, C. Unterrieder, A. Berger, R. Priewasser, and M. Lunglmayr, "Low-complexity, high frequency parametric system identification method for switched-mode power converters," *Conf. Proc. - IEEE Appl. Power Electron. Conf. Expo. - APEC*, pp. 2004–2009, 2017.

[28] X. Li, X. Ruan, Q. Jin, M. Sha, and C. K. Tse, "Approximate Discrete-Time Modeling of DC-DC Converters With Consideration of the Effects of Pulse Width Modulation," *IEEE Trans. Power Electron.*, vol. 33, no. 8, pp. 7071–7082, Aug. 2018.

[29] M. Al-Greer, M. Armstrong, M. Ahmeid, and D. Giaouris, "Advances on system identification techniques for DC-DC switch mode power converter applications," *IEEE Trans. Power Electron.*, vol. 34, no. 7, pp. 6973–6990, Jul. 2019.

[30] M. Kumar and R. Gupta, "Stability and Sensitivity Analysis of Uniformly Sampled DC-DC Converter with Circuit Parasitics," *IEEE Trans. Circuits Syst. I Regul. Pap.*, vol. 63, no. 11, pp. 2086–2097, Nov. 2016.

[31] Texas Instruments, "TPS61089-PWR742 Evaluation Module. User's Guide," Dallas, 2016.

[32] S. A. Billings, *Nonlinear system identification: NARMAX methods in the time, frequency, and spatio-temporal domains*. wiley, 2013.

[33] T. M. Le, B. Fatahi, H. Khabbaz, and W. Sun, "Numerical optimization applying trust-region reflective least squares algorithm with constraints to optimize the non-linear creep parameters of soft soil," *Appl. Math. Model.*, vol. 41, pp. 236–256, Jan. 2017.

[34] Mathworks, "Least-Squares Fitting." Matlab, p. 5, 2019.

[35] M. Ahsan and M. A. Choudhry, "System identification of an airship using trust region reflective least squares algorithm," *Int. J. Control. Autom. Syst.*, vol. 15, no. 3, pp. 1384–1393, Jun. 2017.

[36] T. F. Coleman and Y. Li, "An Interior Trust Region Approach for Nonlinear Minimization Subject to Bounds," *SIAM J. Optim.*, vol. 6, no. 2, pp. 418–445, May 1996.

[37] L. Wu *et al.*, "Parameter extraction of photovoltaic models from measured I-V characteristics curves using a hybrid trust-region reflective algorithm," *Appl. Energy*, vol. 232, pp. 36–53, Dec. 2018.

[38] M. K. Kazimierczuk, *Pulse-Width Modulated DC-DC Power Converters*. Chichester, West Sussex: John Wiley & Sons, Ltd., 2008.

[39] S. W. Lee, "Application Report Demystifying Type II and Type III Compensators Using Op-

Amp and OTA for DC/DC Converters," Dallas, USA, 2014.

[40] Texas Instruments, "Using the TPS40200. User's Guide," Texas, 2009.

[41] Texas Instruments, "TPS61089EVM-742 Boost Converter Evaluation Module for TPS61089 | TI.com." [Online]. Available: http://www.ti.com/tool/TPS61089EVM-742. [Accessed: 05-Feb-2020].

[42] F. De Stasi, "Application Report: Working with inverting buck-boost converters," Dallas, Texas, 2019.

[43] B. Pelz, A. Belkadi, and G. Moddel, "Avoiding erroneous analysis of MIM diode current-voltage characteristics through exponential fitting," *Meas. J. Int. Meas. Confed.*, vol. 120, pp. 28–33, May 2018.

[44] Semikron, "SKD 30/16 A1 ." [Online]. Available: http://shop.semikron.com/es/Productos-y-Tienda/Grupo-de-Productos/Puentes-Rectificadores/Power-Bridge-Rectifiers/SKD-30-16-A1.html. [Accessed: 05-Feb-2020].

[45] A. C. Cameron and F. A. G. Windmeijer, "An R-squared measure of goodness of fit for some common nonlinear regression models," *J. Econom.*, vol. 77, no. 2, pp. 329–342, Apr. 1997.

[46] L. Arnedo, R. Burgos, F. Wang, and D. Boroyevich, "Black-box terminal characterization modeling of DC-to-DC converters," in *Conference Proceedings - IEEE Applied Power Electronics Conference and Exposition - APEC*, 2007, pp. 457–463.

[47] A. Naziris, G. Guarderas, A. Frances, R. Asensi, and J. Uceda, "Large-signal black-box modelling of bidirectional battery charger for electric vehicles," in *Conference Proceedings - IEEE Applied Power Electronics Conference and Exposition - APEC*, 2019, vol. 2019-March, pp. 3195–3198.

[48] S. K. Ki and R. Todd, "Black-box modelling of a permanent magnet generator for aerospace systems," in *IET Conference Publications*, 2016, vol. 2016, no. CP684.

[49] Petrone, R., Zheng, Z., Hissel, D., Péra, M. C., Pianese, C., Sorrentino, M., … Yousfi-Steiner, "A review on model-based diagnosis methodologies for PEMFCs," *Int. J. Hydrogen Energy*, vol. 38, no. 17, pp. 7077-7091., 2013.

[50] L. Arnedo, R. Burgos, D. Boroyevich, and F. Wang, "System-Level Black-Box Dc-to-Dc Converter Models," in *Conference Proceedings - IEEE Applied Power Electronics Conference and Exposition - APEC*, 2009, pp. 1476–1481.

[51] H. Ali, H. Liu, X. Zheng, P. Gao, and H. Zaman, "Frequency response based behavioral modeling verification for three phase AC-DC converter," in *Proceedings IECON 2017 - 43rd Annual Conference of the IEEE Industrial Electronics Society*, 2017, vol. 2017-Janua, pp. 4908–4912.

[52] M. Amara, C. Vollaire, M. Ali, and F. Costa, “Black box EMC modeling of a three phase inverter,” in *EMC Europe*, 2018, pp. 1–6.

[53] F. Alonge, R. Rabbeni, M. Pucci, and G. Vitale, “Identification and Robust Control of a Quadratic DC/DC Boost Converter by Hammerstein Model,” *IEEE Trans. Ind. Appl.*, vol. 51, no. 5, pp. 3975–3985, Sep. 2015.

[54] A. Frances, R. Asensi, and J. Uceda, “Blackbox Polytopic Model with Dynamic Weighting Functions for DC-DC Converters,” *IEEE Access*, vol. 7, pp. 160263–160273, 2019.

[55] L. Wang *et al.*, “Electromagnetic Transient Modeling and Simulation of Power Converters Based on a Piecewise Generalized State Space Averaging Method,” *IEEE Access*, vol. 7, pp. 12241–12251, 2019.

[56] A. Nabinejad, A. Rajaei, and M. Mardaneh, “A Systematic Approach to Extract State-Space Averaged Equations and Small-Signal Model of Partial-Power Converters,” *IEEE J. Emerg. Sel. Top. Power Electron.*, vol. 8, no. 3, pp. 2475–2483, Sep. 2020.

[57] F. Alonge, F. D’Ippolito, and T. Cangemi, “Identification and robust control of dc/dc converter Hammerstein model,” *IEEE Trans. Power Electron.*, vol. 23, no. 6, pp. 2990–3003, 2008.

[58] L. Arnedo, “System Level Black-Box Models for DC-DC Converters,” Virginia Polytechnic Institute and State University, 2008.

[59] A. Luchetta *et al.*, “MLMVNNN for Parameter Fault Detection in PWM DC-DC Converters and Its Applications for Buck and Boost DC-DC Converters,” *IEEE Trans. Instrum. Meas.*, vol. 68, no. 2, pp. 439–449, Feb. 2019.

[60] Y. Cheng, J. Wu, H. Zhu, S. W. Or, and X. Shao, “Remaining Useful Life Prognosis Based on Ensemble Long Short-Term Memory Neural Network,” *IEEE Trans. Instrum. Meas.*, pp. 1–1, Oct. 2020.

[61] G. Rojas-Duenas, J.-R. Riba, K. Kahalerras, M. Moreno-Eguilaz, A. Kadechkar, and A. Gomez-Pau, “Black-Box Modelling of a DC-DC Buck Converter Based on a Recurrent Neural Network,” in *2020 IEEE International Conference on Industrial Technology (ICIT)*, 2020, pp. 456–461.

[62] Y. Yu, X. Si, C. Hu, and J. Zhang, “A review of recurrent neural networks: Lstm cells and network architectures,” *Neural Computation*, vol. 31, no. 7. MIT Press Journals, pp. 1235–1270, 01-Jul-2019.

[63] B. Doucoure, K. Agbossou, and A. Cardenas, “Time series prediction using artificial wavelet neural network and multi-resolution analysis: Application to wind speed data,” *Renew. Energy*, vol. 92, pp. 202–211, Jul. 2016.

[64] Y. Jin, C. Shan, Y. Wu, Y. Xia, Y. Zhang, and L. Zeng, “Fault Diagnosis of Hydraulic Seal

Wear and Internal Leakage Using Wavelets and Wavelet Neural Network," *IEEE Trans. Instrum. Meas.*, vol. 68, no. 4, pp. 1026–1034, Apr. 2019.

[65] P. Qashqai, K. Al-Haddad, and R. Zgheib, "Modeling Power Electronic Converters Using A Method Based on Long-Short Term Memory (LSTM) Networks," in *IECON Proceedings (Industrial Electronics Conference)*, 2020, vol. 2020-October, pp. 4697–4702.

[66] M. Baumann, C. Weissinger, and H. G. Herzog, "System identification and modeling of an automotive bidirectional DC/DC converter," in *2019 IEEE Vehicle Power and Propulsion Conference, VPPC 2019 - Proceedings*, 2019.

[67] S. M. Ghamari, H. Mollaee, and F. Khavari, "Robust self-tuning regressive adaptive controller design for a DC–DC BUCK converter," *Meas. J. Int. Meas. Confed.*, vol. 174, p. 109071, Apr. 2021.

[68] Z. Y. Xue, K. S. Xiahou, M. S. Li, T. Y. Ji, and Q. H. Wu, "Diagnosis of Multiple Open-Circuit Switch Faults Based on Long Short-Term Memory Network for DFIG-Based Wind Turbine Systems," *IEEE J. Emerg. Sel. Top. Power Electron.*, vol. 8, no. 3, pp. 2600–2610, Sep. 2020.

[69] T. Ergen and S. S. Kozat, "Online Training of LSTM Networks in Distributed Systems for Variable Length Data Sequences," *IEEE Trans. Neural Networks Learn. Syst.*, vol. 29, no. 10, pp. 5159–5165, Oct. 2018.

[70] A. Rahrooh and S. Shepard, "Identification of nonlinear systems using NARMAX model," *Nonlinear Anal. Theory, Methods Appl.*, vol. 71, no. 12, pp. e1198–e1202, Dec. 2009.

[71] Z. Boussaada, O. Curea, A. Remaci, H. Camblong, and N. M. Bellaaj, "A nonlinear autoregressive exogenous (NARX) neural network model for the prediction of the daily direct solar radiation," *Energies*, vol. 11, no. 3, 2018.

[72] E. H. K. Fung, Y. K. Wong, H. F. Ho, and M. P. Mignolet, "Modelling and prediction of machining errors using ARMAX and NARMAX structures," *Appl. Math. Model.*, vol. 27, no. 8, pp. 611–627, 2003.

[73] J. A. Freeman and D. M. Skapura, *Neural Networks: Algorithms, Applications, and Programming Techniques (Computation and Neural Systems Series)*. Addison-Wesley, 1991.

[74] A. Suratgar, M. Tavakoli, and A. Hoseinabadi, "Modified Levenberg–Marquardt method for neural networks training," *World Acad Sci Eng Technol*, pp. 46–48, 2005.

[75] D. Hunter *et al.*, "Selection of Proper Neural Network Sizes and Architectures — A Comparative Study," *IEEE Trans. Ind. Informatics*, vol. 8, no. 2, pp. 228–240, 2012.

[76] L. Cun *et al.*, "Handwritten Digit Recognition with a Back-Propagation Network," *Proc. Adv. Neural Inf. Process. Syst.*, pp. 396–404, 1989.

[77] W. Rawat and Z. Wang, “Deep convolutional neural networks for image classification: A comprehensive review,” *Neural Computation*, vol. 29, no. 9. MIT Press Journals, pp. 2352–2449, 01-Sep-2017.

[78] I. Arel, D. Rose, and T. Karnowski, “Deep machine learning-A new frontier in artificial intelligence research,” *IEEE Comput. Intell. Mag.*, vol. 5, no. 4, pp. 13–18, Nov. 2010.

[79] J. B. Yang, M. N. Nguyen, P. P. San, X. L. Li, and S. Krishnaswamy, “Deep convolutional neural networks on multichannel time series for human activity recognition,” *IJCAI Int. Jt. Conf. Artif. Intell.*, vol. 2015-Janua, no. Ijcai, pp. 3995–4001, 2015.

[80] F. Ciancetta, G. Bucci, E. Fiorucci, S. Mari, and A. Fioravanti, “A New Convolutional Neural Network-Based System for NILM Applications,” *IEEE Trans. Instrum. Meas.*, pp. 1–1, 2020.

[81] Y. Xie, C. Li, Y. Lv, and C. Yu, “Predicting lightning outages of transmission lines using generalized regression neural network,” *Appl. Soft Comput. J.*, vol. 78, pp. 438–446, May 2019.

[82] M. Liu, W. Wu, Z. Gu, Z. Yu, F. F. Qi, and Y. Li, “Deep learning based on Batch Normalization for P300 signal detection,” *Neurocomputing*, vol. 275, pp. 288–297, Jan. 2018.

[83] S. Ioffe and C. Szegedy, “Batch normalization: Accelerating deep network training by reducing internal covariate shift,” in *32nd International Conference on Machine Learning, ICML 2015*, 2015, vol. 1, pp. 448–456.

[84] H. Liu, X. Mi, and Y. Li, “Smart deep learning based wind speed prediction model using wavelet packet decomposition, convolutional neural network and convolutional long short term memory network,” *Energy Convers. Manag.*, vol. 166, pp. 120–131, Jun. 2018.

[85] W. Li, A. Monti, and F. Ponci, “Fault detection and classification in medium voltage dc shipboard power systems with wavelets and artificial neural networks,” *IEEE Trans. Instrum. Meas.*, vol. 63, no. 11, pp. 2651–2665, Nov. 2014.

[86] S. Ruder, “An overview of gradient descent optimization algorithms,” Sep. 2016.

[87] F. He, J. Zhou, Z. kai Feng, G. Liu, and Y. Yang, “A hybrid short-term load forecasting model based on variational mode decomposition and long short-term memory networks considering relevant factors with Bayesian optimization algorithm,” *Appl. Energy*, vol. 237, pp. 103–116, Mar. 2019.

[88] B. Shahriari, K. Swersky, Z. Wang, R. P. Adams, and N. De Freitas, “Taking the human out of the loop: A review of Bayesian optimization,” *Proceedings of the IEEE*, vol. 104, no. 1. Institute of Electrical and Electronics Engineers Inc., pp. 148–175, 01-Jan-2016.

[89] S. Pang *et al.*, “Interconnection and Damping Assignment Passivity-Based Control Applied to On-Board DC-DC Power Converter System Supplying Constant Power Load,” *IEEE*

Trans. Ind. Appl., vol. 55, no. 6, pp. 6476–6485, Nov. 2019.

[90] M. Tariq, A. I. Maswood, C. J. Gajanayake, and A. K. Gupta, “Modeling and Integration of a Lithium-Ion Battery Energy Storage System with the More Electric Aircraft 270 v DC Power Distribution Architecture,” *IEEE Access*, vol. 6, pp. 41785–41802, 2018.

[91] X. Ma, Z. Tao, Y. Wang, H. Yu, and Y. Wang, “Long short-term memory neural network for traffic speed prediction using remote microwave sensor data,” *Transp. Res. Part C Emerg. Technol.*, vol. 54, pp. 187–197, May 2015.

[92] S. Hochreiter and J. Schmidhuber, “Long Short-Term Memory,” *Neural Comput.*, vol. 9, no. 8, pp. 1735–1780, Nov. 1997.

[93] S. Wang, X. Wang, S. Wang, and D. Wang, “Bi-directional long short-term memory method based on attention mechanism and rolling update for short-term load forecasting,” *Int. J. Electr. Power Energy Syst.*, vol. 109, pp. 470–479, Jul. 2019.

[94] I. Sutskever, O. Vinyals, and Q. V Le, “Sequence to Sequence Learning with Neural Networks,” 2014.

[95] L. N. Smith, “A disciplined approach to neural network hyper-parameters: Part 1 -- learning rate, batch size, momentum, and weight decay,” Mar. 2018.

[96] A. H. Victoria and G. Maragatham, “Automatic tuning of hyperparameters using Bayesian optimization,” *Evol. Syst.*, May 2020.

[97] K. Lakomy *et al.*, “Active Disturbance Rejection Control Design with Suppression of Sensor Noise Effects in Application to DC-DC Buck Power Converter,” *IEEE Trans. Ind. Electron.*, 2021.

[98] McKinsey & Company, “Mild hybrids—a multi-billion euro growth opportunity alongside e-mobility?,” Aug. 2020.

[99] S.-R. Lee, B.-Y. Choi, J. Lee, and C.-Y. Won, “48 V to 12 V soft-switching interleaved buck and boost converter for mild-hybrid vehicle application,” *undefined*, 2016.

[100] S. Nazari, J. Siegel, and A. Stefanopoulou, “Optimal Energy Management for a Mild Hybrid Vehicle with Electric and Hybrid Engine Boosting Systems,” *IEEE Trans. Veh. Technol.*, vol. 68, no. 4, pp. 3386–3399, Apr. 2019.

[101] T. Kim and S. Kwak, “A Flexible Voltage Bus Converter for the 48-/12-V Dual Supply System in Electrified Vehicles,” *IEEE Trans. Veh. Technol.*, vol. 66, no. 3, pp. 2010–2018, Mar. 2017.

[102] F. Karim, S. Majumdar, H. Darabi, and S. Chen, “LSTM Fully Convolutional Networks for Time Series Classification,” *IEEE Access*, vol. 6, pp. 1662–1669, Dec. 2017.

[103] M. Bodetto, A. E. Aroudi, A. Cid-Pastor, J. Calvente, and L. Martínez-Salamero, “Design of AC-DC PFC high-order converters with regulated output current for low-power

applications," *IEEE Trans. Power Electron.*, vol. 31, no. 3, pp. 2012–2025, Mar. 2016.

[104] X. Ren, Y. Wu, Z. Guo, Z. Zhang, and Q. Chen, "An Online Monitoring Method of Circuit Parameters for Variable On-Time Control in CRM Boost PFC Converters," *IEEE Trans. Power Electron.*, vol. 34, no. 2, pp. 1786–1797, Feb. 2019.

[105] J. Bayona, N. Gélvez, and H. Espitia, "Design, Analysis, and Implementation of an Equalizer Circuit for the Elimination of Voltage Imbalance in a Half-Bridge Boost Converter with Power Factor Correction," *Electronics*, vol. 9, no. 12, p. 2171, Dec. 2020.

[106] J. Bao, J. Liu, Z. Huang, W. Liu, and H. Li, "An Online Parameter Identification for Ultracapacitor Model by Using Recursive Least Square with Multi-forgetting Factor," in *2018 13th World Congress on Intelligent Control and Automation (WCICA)*, 2018, pp. 962–966.

[107] H. Xu, D. Chen, F. Xue, and X. Li, "Optimal design method of interleaved boost PFC for improving efficiency from switching frequency, boost inductor, and output voltage," *IEEE Trans. Power Electron.*, vol. 34, no. 7, pp. 6088–6107, Jul. 2019.

[108] J.-L. Kotny, X. Margueron, and N. Idir, "High-Frequency Model of the Coupled Inductors Used in EMI Filters," *IEEE Trans. Power Electron.*, vol. 27, no. 6, pp. 2805–2812, Jun. 2012.

[109] J. Riba, M. Moreno-eguilaz, S. Bogarra, and A. Garcia, "Parameter Identification of DC-DC Converters under Steady-State and Transient Conditions Based on White-Box Models," *Electronics*, vol. 7, no. 393, 2018.

[110] C. Labarre and F. Costa, "Circuit analysis of an EMI filter for the prediction of its magnetic near-field emissions," *IEEE Trans. Electromagn. Compat.*, vol. 54, no. 2, pp. 290–298, Apr. 2012.

[111] N. Wang, Z. Yan, J. Tang, Z. Ning, B. Xiao, and H. Wang, "Study on Prediction Models of EMI Filter with Near-field Coupling Effect," in *2018 12th International Symposium on Antennas, Propagation and EM Theory, ISAPE 2018 - Proceedings*, 2019.

[112] B. Narayanasamy, F. Luo, and Y. Chu, "Modeling and Stability Analysis of Voltage Sensing based Differential Mode Active EMI Filters for AC-DC Power Converters," in *2018 IEEE Symposium on Electromagnetic Compatibility, Signal Integrity and Power Integrity, EMC, SI and PI 2018*, 2018.

[113] R. Zhang *et al.*, "Line Frequency Instability of One-Cycle-Controlled Boost Power Factor Correction Converter," *Electronics*, vol. 7, no. 9, p. 203, Sep. 2018.

[114] A. Singh, A. Mallik, and A. Khaligh, "A Comprehensive Design and Optimization of the DM EMI Filter in a Boost PFC Converter," in *IEEE Transactions on Industry Applications*, 2018, vol. 54, no. 3, pp. 2023–2031.

[115] G. Chu, C. K. Tse, S. C. Wong, and S. C. Tan, “A unified approach for the derivation of robust control for boost PFC converters,” *IEEE Trans. Power Electron.*, vol. 24, no. 11, pp. 2531–2544, 2009.

[116] S. Ma, W. Cai, W. Liu, Z. Shang, and G. Liu, “A lighted deep convolutional neural network based fault diagnosis of rotating machinery,” *Sensors (Switzerland)*, vol. 19, no. 10, p. 2381, May 2019.

[117] D. Martinez, H. Henao, and G. A. Capolino, “Overview of Condition Monitoring Systems for Power Distribution Grids,” in *Proceedings of the 2019 IEEE 12th International Symposium on Diagnostics for Electrical Machines, Power Electronics and Drives, SDEMPED 2019*, 2019, pp. 160–166.

[118] Y. Wei, D. Wu, and J. Terpenny, “Robust Incipient Fault Detection of Complex Systems Using Data Fusion,” *IEEE Trans. Instrum. Meas.*, pp. 1–1, 2020.

[119] J. Martínez, J. R. Riba, and M. Moreno-Eguilaz, “State of health prediction of power connectors by analyzing the degradation trajectory of the electrical resistance,” *Electron.*, vol. 10, no. 12, p. 1409, Jun. 2021.

[120] L. Frosini, “Monitoring and diagnostics of electrical machines and drives: A state of the art,” in *Proceedings - 2019 IEEE Workshop on Electrical Machines Design, Control and Diagnosis, WEMDCD 2019*, 2019, pp. 169–176.

[121] D. Gonzalez-Jimenez, J. Del-Olmo, J. Poza, F. Garramiola, and P. Madina, “Data-driven fault diagnosis for electric drives: A review,” *Sensors*, vol. 21, no. 12. MDPI AG, p. 4024, Jun-2021.

[122] M. K. Alam and F. H. Khan, “Reliability analysis and performance degradation of a boost converter,” in *IEEE Transactions on Industry Applications*, 2014, vol. 50, no. 6, pp. 3986–3994.

[123] S. Yang, A. Bryant, P. Mawby, D. Xiang, L. Ran, and P. Tavner, “An industry-based survey of reliability in power electronic converters,” *IEEE Trans. Ind. Appl.*, vol. 47, no. 3, pp. 1441–1451, May 2011.

[124] S. Yang, D. Xiang, A. Bryant, P. Mawby, L. Ran, and P. Tavner, “Condition monitoring for device reliability in power electronic converters: A review,” *IEEE Transactions on Power Electronics*, vol. 25, no. 11. pp. 2734–2752, 2010.

[125] M. G. Pecht and M. Kang, *Prognostics and Health Management of Electronics*. Chichester, UK: John Wiley and Sons Ltd, 2018.

[126] W. Yuan, T. Wang, D. Diallo, and C. Delpha, “A fault diagnosis strategy based on multilevel classification for a cascaded photovoltaic grid-connected inverter,” *Electron.*, vol. 9, no. 3, p. 429, Mar. 2020.

[127] H. L. Dang and S. Kwak, “Review of health monitoring techniques for capacitors used in power electronics converters,” *Sensors (Switzerland)*, vol. 20, no. 13. MDPI AG, pp. 1–22, Jul-2020.

[128] J. Poon, P. Jain, C. Spanos, S. K. Panda, and S. R. Sanders, “Fault Prognosis for Power Electronics Systems Using Adaptive Parameter Identification,” *IEEE Trans. Ind. Appl.*, vol. 53, no. 3, pp. 2862–2870, May 2017.

[129] M. Al, J. Van, and H. Gualous, “DC/DC Converters for Electric Vehicles,” *Electr. Veh. - Model. Simulations*, Sep. 2011.

[130] W. Zhuang *et al.*, “A survey of powertrain configuration studies on hybrid electric vehicles,” *Appl. Energy*, vol. 262, p. 114553, Mar. 2020.

[131] M. S. Perdigão, J. P. F. Trovão, J. M. Alonso, and E. S. Saraiva, “Large-Signal Characterization of Power Inductors in EV Bidirectional DC-DC Converters Focused on Core Size Optimization,” *IEEE Trans. Ind. Electron.*, vol. 62, no. 5, pp. 3042–3051, May 2015.

[132] C. S. Kulkarni, G. Biswas, and X. Koutsoukos, “A prognosis case study for electrolytic capacitor degradation in DC-DC converters,” in *PHM Conference*, 2009.

[133] J. R. Celaya, C. Kulkarni, G. Biswas, and K. Goebel, “Towards prognostics of electrolytic capacitors,” *AIAA Infotech Aerosp. Conf. Exhib. 2011*, 2011.

[134] N. Agarwal, M. W. Ahmad, and S. Anand, “Quasi-Online Technique for Health Monitoring of Capacitor in Single-Phase Solar Inverter,” *IEEE Trans. Power Electron.*, vol. 33, no. 6, pp. 5283–5291, Jun. 2018.

[135] D. Qin, J. Yu, G. Zou, R. Yong, Q. Zhao, and B. Zhang, “A Novel Combined Prediction Scheme Based on CNN and LSTM for Urban PM2.5 Concentration,” *IEEE Access*, vol. 7, pp. 20050–20059, 2019.

[136] “SaberRD.” [Online]. Available: https://www.synopsys.com/verification/virtual-prototyping/saber/saber-rd.html. [Accessed: 27-Jan-2020].

[137] “Workstation de medios Dell Precision Tower 5810 | Dell.” [Online]. Available: https://www.dell.com/ve/empresas/p/precision-t5810-workstation/pd. [Accessed: 27-Jan-2020].

[138] “Model 9205, Multi-Range Programmable DC Power Supplies - B&K Precision.” [Online]. Available: https://www.bkprecision.com/products/power-supplies/9205-600w-multi-range-60v-25a-dc-power-supply.html. [Accessed: 05-Feb-2020].

[139] “MDO3000 | Tektronix.” [Online]. Available: https://www.tek.com/oscilloscope/mdo3000-mixed-domain-oscilloscope. [Accessed: 05-Feb-2020].

APPENDIX

A. Materials and resources

This section explains the different materials and resources considered for the proper development of this research work. They cover software, electronics, hardware equipment and test facilities.

A.1. Software

The software to be used for this project purposed is listed:

- MATLAB®: Mathematical environment for programming and developing different models and algorithms.
- Simulink: It is a part of Matlab® and is used to simulate circuits and use other tools.
- Synopsys SaberRD®: Integrated environment for designing and analysing power electronic systems and multi-domain physical systems [136].
- PSIM®: Electronics simulation software.
- Microsoft Word®: Text editor.
- Microsoft Visio ®: Diagrams creator.
- Sigmaplot®: Graph creator.

A.2. Hardware

This project requires a powerful work station in order to run the proposed algorithms and methods. The main specifications are the following:

- Processor: Intel® Xeon® CPU E5-1650 v2 @3.50 GHz
- Installed RAM: 64 GB
- Operative system: Windows 10
- Hard drive disk: 1400 GB
- GPU: NVIDIA GeForce RTX 2080

Figure A.1 shows the work station.

Figure A.1. Dell Precision 5810 work station. Source: [137]**.**

A.3. Measurement equipment

Experiments are performed by means of a DC power supply (BK Precision 9205; BK Precision Corporation, Yorba Linda, CA, USA). Input/output voltages and currents were acquired by using of a four channel oscilloscope (Tektronix MDO3024 200 MHz 2.5 GS/s; Tektronix, Beaverton, OR, USA), two high-frequency current probes (Tektronix TCP0030A 0.001-20 A 120 MHz; Tektronix, Beaverton, OR, USA) and two high-frequency voltage probes (Tektronix TPP0250 250 MHz; Tektronix, Beaverton, OR, USA).

Figure A.2 show the equipment used in the laboratory to acquire the signals from the devices.

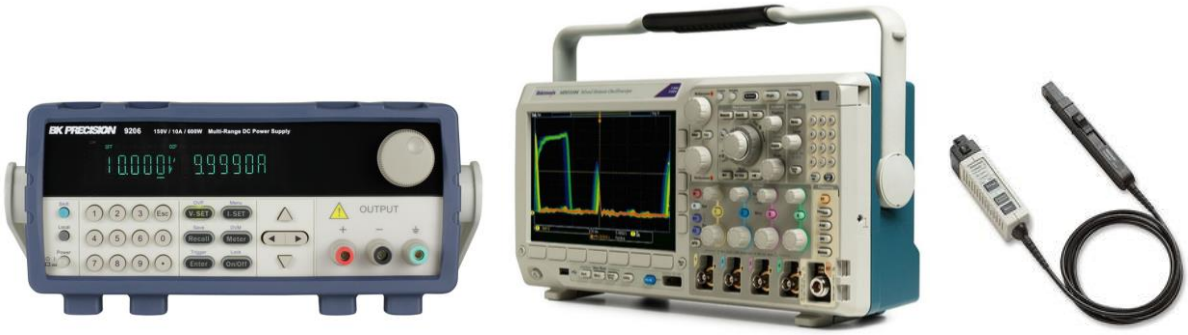

Figure A.2. Measurement equipment. Source: [138], [139]**.**